Topological Majorana fermions models and new applications

Fan Yang

INSTITUT POLYTECHNIQUE DE PARIS

NNT : 2020IPPAX041

Thèse de doctorat

Modèles topologiques de Majorana fermions et nouvelles applications

Thèse de doctorat de l'Institut Polytechnique de Paris
préparée à l'École Polytechnique

École doctorale n°626
École Doctorale de l'Institut Polytechnique de Paris (ED IP Paris)
Spécialité de doctorat : Physique de la matière condensée

Thèse présentée et soutenue à Palaiseau, le 21 septembre 2020, par

FAN YANG

Composition du Jury :

M. Nicolas Regnault Professeur, LPA, ENS and Princeton University	Président
M. Johannes Knolle Professeur, Technical University of Munich	Rapporteur
M. Yuval Oreg Professeur, Weizmann Institute of Science	Rapporteur
M. Pasquale Calabrese Professeur, SISSA and INFN, Sezione di Trieste	Examinateur
M. Benoit Douçot Professeur, LPTHE, Sorbonne Université	Examinateur
M. Ion Garate Professeur agrégé, Université de Sherbrooke	Examinateur
M. Pascal Simon Professeur, LPS, Université Paris-Saclay	Examinateur
Mme. Karyn Le Hur CPHT, École Polytechnique	Directeur de thèse

Abstract

We present a theoretical study of topological models hosting Majorana fermions which are their own anti-particles, with relevant probes of quantum entanglement and experimental protocols for quantum engineering in cQED. In the first part, by proximity effects we address the topological superconducting wire systems, where Majorana fermions emerge as zero-energy modes at the edges. By varying strengths of inter-wire couplings and changing fluxes of orbital magnetic fields, we show an interplay between topological p-wave superconductivity and quantum Hall states. For the remaining two parts of the thesis, we focus on Kitaev spin liquids that can be exactly solved in a Majorana fermion representation. We present a solution for tunable square and brickwall ladder systems. We introduce valence bond fluctuations to characterize phase transitions between Abelian and non-Abelian phases, and find a general relation with the entanglement entropy. To simulate these many-body Majorana states, we propose a driven superconducting box circuit with generalizations to coupled box ensembles. There, a variety of models can be implemented including the toric code, the random Ising chain as well as the SYK Majorana model.

Résumé

Nous présentons une étude théorique des modèles topologiques révélant des fermions de Majorana qui sont leurs propres anti-particules, avec des sondes de l'intrication quantique et des protocoles expérimentaux d'ingénierie quantique en cQED. Dans la première partie, par des effets de proximité, nous abordons le supraconducteur topologique dans des systèmes de fil, où les fermions de Majorana émergent comme modes à énergie nulle sur les bords. En faisant varier les forces des couplages inter-fils et l'évolution des flux dus aux champs magnétiques orbitaux, nous montrons une interaction entre la supraconductivité topologique des ondes p et les états Hall quantiques. Pour les deux autres parties de la thèse, nous nous concentrons sur les liquides de spin de Kitaev qui peuvent être résolus exactement dans une représentation de fermions de Majorana. Nous présentons une solution dans des géométries de type échelle. Nous introduisons les fluctuations des liens de valence pour caractériser les transitions de phase entre les phases abélienne et non abélienne, et trouver une relation générale avec l'entropie d'enchevêtrement. Pour simuler ces états Majorana à plusieurs corps, nous proposons un circuit en caisson supraconducteur puis des généralisations pour des ensembles de boîtes couplées. Là, une variété de modèles peut être implémentée, y compris le code torique, la chaîne d'Ising aléatoire ainsi que le modèle SYK Majorana.

Contents

Acknowledgement

Three years of PhD in condensed matter physics has been a fascinating adventure for me, thanks to the supervision of Karyn. She is an inspiring and dedicated advisor, who loves to do novel research with young students in a broad range of topics. With her help, I benefited from the freedom of choosing directions and the opportunity to open the toolbox of a theorist. The consumption rate of pens and brushes for our whiteboard calculations is unforgettable. Passion, meanwhile, the most meaningful thing I have learned from Karyn, doubtlessly enables so many brilliant physicists like her to push forward the field of topological matter at lightening speed.

At the end of each stressful year, Denis Bernard and Stéphane Munier, my tutors from LPT and CPHT, were always ready to offer me supportive and constructive advice. I am grateful to have them as witnesses to the ups and downs of my endeavors.

I much enjoyed the time spent with my collaborators: Ariane Soret, Loïc Henriet, Kirill Plekhanov from CPHT, Vivien Perrin, Alexandru Petrescu, Ion Garate from Université de Sherbrooke and Ephraim Bernhardt from ENS. Specialized in different subfields, they brought new perspectives into the projects both numerically and analytically. I have also learnt a lot of Majorana physics from the discussion with Loïc Herviou.

Years ago, I met Silke Biermann from CPHT upon her summer research visit to Peking University. By that time, I was an undergraduate student in Materials Chemistry. From Silke, I got to know Paris with its lively French academic environment. After coming here, the flexibility of the system allowed me to try different fields from High Energy Physics (Master) to Condensed Matter (PhD). It would have been im-

possible without the generosity and vision of the professors I met: Hong Jiang, Yiqin Gao, Baruch Rosenstein, Pascal Paganini, Antoine Georges, Alexandre Zabi, Jesper Jacobsen, Nicolas Regnault and Slava Rychkov. I always feel lucky to be supported by them in my pursuit of a path with multiple interests.

During my stay in CPHT, I would like to thank the company of colleagues for their sharing of lunch and coffee time: Tal Goren, Philipp W Klein, Julian Legendre, Joel Hutchinson and Hepeng Yao. I appreciate the administrative help of Fadila Debbou, Malika Lang, Florence Auger in making my foreign life convenient and travels abroad smooth. Danh Pham-Kim played the key figure in keeping hardwares and softwares around me efficient. Also, I am impressed by the genuine efforts of our lab director Chazottes Jean-René in organizing wonderful annual events, particularly the PhD day and spring picnics.

I cherish the memorable weekends and excursions with friends in Paris: Yifan Chen, Kang Yang, Peng Chen, Jiaxing Qiao, Dongsheng Ge, Xinyang Wang, Yi Pan, Yue Feng, Zicheng Qian, Xiujun Zheng, Yao Xu, Songyuan Li, Yi Zhang, Zhengying Liu and Yanliang Guo. Meanwhile, I can never forget the hospitality of the ones on my visits to Germany and Canada: Botao Wang, Junhui Zheng, Ke Liu, Félix Rose, Flore Kunst, Chengshu Li and Chunxiao Liu.

Although the first draft of this thesis was written during the spring outbreak of the COVID-19 pandemic, my mentality has been taken good care of by the musicians: Mozart, Schubert, Debussy, Philip Glass, Zhou Shen, IU, FINNEAS, Billie Eilish and Taylor Swift.

In the end, I wish to express the gratitude to the precious ones who grow old with me: my parents, my grandparents and my childhood friends Tiantian Wang, Chaoxian Hua, Yan Zhou, Yitong Guo. It's nice to have a family.

Introduction

In the last decades, Majorana fermions have revived interests in the field of condensed matter due to possible applications in quantum information as protected qubits [1–7] and surface codes with $\mathcal{Z}_2$ variables [8–12]. On one hand, they emerge as Majorana zero-energy modes (MZMs) at the topological defects (for instance, at the edges) in a variety of topological systems with particle-hole symmetry. These are p-wave superconductors, the superconducting analogues of quantum Hall phases [13–15]. On the other hand, Majorana fermions are closely related to $\mathcal{Z}_2$ quantum spin liquids [16, 17]. The Kitaev spin model on the honeycomb lattice [18] represents an important class of models in this category, and can be solved exactly in a Majorana fermion representation. The model shows three gapped spin liquid phases and an intermediate gapless phase which can be identified as a semi-metal of Majorana fermions.

The quest of topological phases initially started from the quantum Hall effect [19, 20], and since then has evolved towards variants on the honeycomb lattice with effectively a zero magnetic flux in a unit cell [21]. These quantum Hall systems are characterized by a robust, unidirectional charge flow at the sample boundaries [22, 23], as well as by the emergence of fractional charges in the case of Laughlin states [24–27]. Recently, one theoretical approach to study the connections between topological superconductors and quantum Hall phases is to view two-dimensional systems as arrays of coupled one-dimensional wires [28–30]. This so-called wires construction approach comes with the benefit that it allows to investigate interaction effects (such as fractionalization) [31–33] that go beyond mean-field theory, via the Luttinger liquid paradigm [34, 35].

The search for quantum spin liquids in the Mott regime [36–41], however, has remained a great challenge in relation with the discovery of quantum materials [42–50]. Quantum spin liquids show interesting topological and entanglement properties [51–54] which can be used for applications in quantum information [55]. The Kitaev honeycomb model [18] demonstrates the significance of $\mathcal{Z}_2$ gauge fields on the low-energy properties. It is also important to mention exact constructions of chiral spin liquids [56] and spin liquid states in ladder systems [57].

Starting from the low-dimensional analogues, one may envision to simulate Kitaev spin liquids from constructing four-site Majorana boxes in circuit quantum electrodynamics (cQED) networks. Notably, a system of three transmons has been realized recently [58], with possible applications in topological phases [59, 60]. These boxes could be used in variable geometries from quantum impurity systems to tunable ladder and plaquette models. Ensembles of square-plaquette models have been realized in ultra-cold atoms [61] to emulate an Anderson Resonating Valence Bond spin-liquid state [38, 62], and have been shown theoretically to be related to d-wave superconductivity (superfluidity) in the Hubbard model close to the Mott state [63]. The design of such Majorana boxes addresses challenging questions regarding the choice of couplings. Experiments in superconducting cQED architectures [64] and in ultra-cold atoms [65] report progress in engineering four-body interactions inspired by theoretical efforts [66, 67].

In these contexts, the goals of this thesis are two folds: first, to explore the topological and entanglement properties of Majorana fermions in topological superconducting wires and Kitaev spin liquids; second, to design feasible physical platforms towards the quantum engineering of many-body Majorana states.

In Chapter 1, we review a series of basic topological concepts starting from the classification of topological phases for non-interacting fermions based on non-spatial symmetries, to the illustration of central models hosting Majorana fermions: p-wave superconductors in $d = 1, 2$ and the Kitaev honeycomb model. By bulk-boundary

correspondence, the Majorana edge modes are protected by the bulk gap and their properties can be further derived from topological invariants of the bulk via index theorem. A summary of the potential experimental realizations of these topological Majorana fermion models is given at the end of this chapter.

In Chapter 2, we go on to present a theoretical study of the interplay between topological p-wave superconductivity, orbital magnetic fields and quantum Hall phases in coupled wire systems. First, related to the Paper 4, we analyze hybrid systems consisting of a Kitaev chain coupled to a Luttinger liquid. By tuning the magnetic field and the carrier density, we identify quantum Hall and charge density wave phases, as well as regimes in which superconductivity is induced in the second chain by proximity effect. It allows us to consider two-dimensional systems made of weakly coupled ladders. We manage to engineer a $p + ip$ superconductor and fulfill a generalization of the $\nu = 1/2$ fractional quantum Hall phase, following the previous work on the two-leg spinful ladder [68]. The analytical findings will be compared with numerical exact diagonalization.

In Chapter 3, related to the Paper 3, we introduce valence bond fluctuations to characterize quantum spin liquids and the entanglement properties of them. Applying analytical approaches, we find an identical scaling law between valence bond fluctuations and entanglement entropy in the two-dimensional Kitaev spin model and in one-dimensional chain analogues. We also show how these valence bond fluctuations can locate, via the linear scaling prefactor, the quantum phase transitions between the three gapped and the gapless Majorana semi-metal phases in the honeycomb model. We then study the effect of a uniform magnetic field along the [111] direction opening a gap in the intermediate phase which becomes topological. We still obtain a robust signal to characterize the transitions towards the three gapped phases. Our analytical results will be compared with density matrix renormalization (DMRG) simulations.

In Chapter 4, related to the Paper 1, we derive a generalized phase diagram for the Kitaev square ladder system. As a reminiscence of the two-dimensional model,

we identify three gapped spin liquid phases and one gapless phase that extends to a plane. Based on unit cells of the ladder geometry, in the Paper 2, we design a driven superconducting box with four spins-1/2 (qubits). Within one box or island, we introduce a generalized nuclear magnetic resonance protocol to realize our models. Coupling boxes allows us to realize Kitaev spin liquids in various geometries with applications in the toric code. We show how to produce a Néel state of fluxes as a result of the π flux ground state and address the role of local impurity fluxes leading to random Ising models. We present an implementation of the Sachdev-Ye-Kitaev Majorana model in coupled ladder systems. The comparison of the analytical results with numerical simulations will be addressed, including time-average measurements of spin correlation functions, together with the effects of dissipation.

Below is a list of articles that were published during the preparation of the thesis.

- 4. F.Y., Vivien Perrin, Alexandru Petrescu, Ion Garate and Karyn Le Hur, *From topological superconductivity to quantum Hall states in coupled wires*, Phys. Rev. B **101**, 085116 (2020), arXiv:1910.04816

- 3. F.Y., Kirill Plekhanov and Karyn Le Hur, *Valence bond fluctuations in the Kitaev spin model*, Phys. Rev. Research **2**, 013005 (2020), arXiv:1901.03973

- 2. F.Y., Loïc Henriet, Ariane Soret and Karyn Le Hur, *Engineering quantum spin liquids and many-body Majorana states with a driven superconducting box circuit*, Phys. Rev. B **98**, 035431 (2018), arXiv:1801.05698

- 1. Karyn Le Hur, Ariane Soret, and F.Y.[1], *Majorana spin liquids, topology, and superconductivity in ladders*, Phys. Rev. B **96**, 2015109 (2017), arXiv:1703.07322

[1] Authors in alphabetical order

Chapter 1

Background

In this chapter, we give a general introduction to the emergence of Majorana fermions and their basic properties in the context of condensed matter.

We begin in Sec. 1.1 with a brief review of classification theories for the fully gapped system of non-interacting fermions [69, 70]. On the classification table, topological classes with different non-spatial symmetries host intrinsic topological invariants. We adopt the K-theory approach [71] to derive two complex symmetry classes. Then in Sec. 1.2, allowing additional particle-hole symmetry, the real part of the classification table covers a systematic identification of topological superconductors (TSCs) in various dimensions. In contrast to its birth in particle physics, here a Majorana fermion particle emerges as the gapless excitation of Bogoliubov quasiparticles and is protected by the bulk gap. In order to obtain topological invariants, again we apply the K-homology method. Two important low-dimensional examples are followed: the Kitaev p-wave superconducting chain [72] and the spinless $p + ip$ chiral superconductors [14]. From the bulk-boundary correspondence, both models give rise to Majorana zero-energy modes (MZMs) at topological point defects. Sec. 1.3 is dedicated to a new type of topological states embedded in a $\mathcal{Z}_2$ gauge field - the Kitaev spin liquids [18]. Remarkably, on the honeycomb geometry, the low-temperature energy spectrum can be exactly solved in the Majorana fermion representation. We further explore excitations of vortices in different phases that obey either Abelian or

non-Abelian statistics. Experimental realizations of Majorana modes in three aforementioned models are summarized in Sec. 1.4.

1.1 Topology in quantum matter

In the first section, we aim to present a simple mathematical formulation for the tenfold classification of topological states in systems composed of non-interacting fermions [69, 70]. We constrain ourselves to single-particle Hamiltonians that, at a mean-field level, serve as effective descriptions of a wide variety of topological materials. Notable examples include spin-orbit-induced topological insulators [73–75], topological superconductors [3, 76], superfluids [77], semimetals [78, 79] and nodal superconductors [80, 81].

Historically, concepts of topology have been introduced to go beyond the Landau-Ginzburg-Wilson framework [82, 83], where spontaneous symmetry breaking is employed to classify different phases of matter. In topological systems, however, symmetries play a drastically different role and are responsible for the absence of a local order parameter. Meanwhile, when certain symmetries are present, topologically non-trivial states cannot be adiabatically deformed to trivial states unless the system undergoes a quantum phase transition. They are called *symmetry protected topological* (SPT) phases [84] and reveal the short-range entanglement.

1.1.1 Tenfold classification with symmetries

Now, we focus on fermionic SPT phases classified by three non-spatial symmetries: the time reversal ($\mathcal{T}$), particle-hole ($\mathcal{P}$) and chiral ($\mathcal{C}$) symmetries. Given a set of complex fermion annihilation and creation operators satisfying the anti-commutation relation $\{\psi_\mu, \psi_\nu^\dagger\} = \delta_{\mu\nu}$, it is convenient to put them onto a d-dimensional lattice and add internal degrees of freedom $\mu = (j, \sigma)$. Here, j denotes the lattice site and σ indicates extra quantum numbers, for instance, the spins $\sigma = \pm 1/2$. A matrix notation is useful to manifest the linear transformations of fermionic operators under

different non-spatial symmetries,

$$\begin{aligned}
\mathcal{T}\psi_\mu\mathcal{T}^{-1} &= (U_T)_\mu{}^\nu\psi_\nu, \quad \mathcal{T}i\mathcal{T}^{-1} = -i, \\
\mathcal{P}\psi_\mu\mathcal{P}^{-1} &= (U_P^*)_\mu{}^\nu\psi_\nu^\dagger, \\
\mathcal{C}\psi_\mu\mathcal{C}^{-1} &= (U_C^*)_\mu{}^\nu\psi_\nu^\dagger.
\end{aligned} \tag{1.1}$$

The matrix element $U_\mu{}^\nu$ is related to the symmetry operator $\mathcal{U}(=\mathcal{T},\mathcal{P},\mathcal{C})$ acting on the fermionic Fock space. We adopt the Einstein summation convention over the repeated indices (ν). To preserve the anti-commutation relation of fermionic operators: $\mathcal{U}\{\psi_\mu,\psi_\nu^\dagger\}\mathcal{U}^{-1} = \delta_{\mu\nu}$, from Eq. (1.1) the matrix U has to be unitary: $UU^\dagger = \mathbb{1}$. Then, $\mathcal{T}$ becomes an anti-unitary operator and $\mathcal{P}$ unitary. Meanwhile, $\mathcal{P}$ interchanges the particle and hole channels. $\mathcal{C}$ can be viewed as a combination of the two operations above: $\mathcal{C} = \mathcal{T}\cdot\mathcal{P}$ with $U_C = U_P^* U_T$.

We go on to consider an arbitrary single-particle Hamiltonian that shares a second-quantized form $\mathcal{H} = \psi^\dagger H\psi = \psi_\mu^\dagger H^{\mu\nu}\psi_\nu$. When the system is invariant under the symmetry operation $\mathcal{U}\mathcal{H}\mathcal{U}^{-1} = \mathcal{H}$, one obtains

$$U_T^\dagger H^* U_T = H, \quad U_P^\dagger H^t U_P = -H, \quad U_C^\dagger H U_C = -H. \tag{1.2}$$

Without loss of generality, we assume $\mathrm{Tr}\, H = \mathrm{Tr}\, U_C = 0$. For a Hermitian system, the transformation rules in Eq. (1.2) take an alternative form in momentum space

$$\begin{aligned}
\mathcal{T}H(k)\mathcal{T}^{-1} &= H(-k), \\
\mathcal{P}H(k)\mathcal{P}^{-1} &= -H(-k), \\
\mathcal{C}H(k)\mathcal{C}^{-1} &= -H(k).
\end{aligned} \tag{1.3}$$

Here, the Fourier transform is defined on the d-dimensional lattice with volume $V = L^d$: $\psi_j(r) = 1/(\sqrt{V})\sum_k e^{ikr}\psi_j(k)$ and $H^{\mu\nu}(k) = \sum_r e^{-ikr}H^{\mu\nu}(r)$.

From Schur's lemma we can infer that two successive operations $\mathcal{U}^2$ produces $U_T^* U_T = e^{i\theta_T}\cdot\mathbb{1}, U_P^* U_P = e^{i\theta_P}\cdot\mathbb{1}, U_C^2 = e^{i\theta_C}\cdot\mathbb{1}$. These phase factors are determined as follows: first, the unitarity of the $U_{T(P)}$ matrix indicates $U_{T(P)}^t = e^{i\theta_{T(P)}}U_{T(P)}$ and

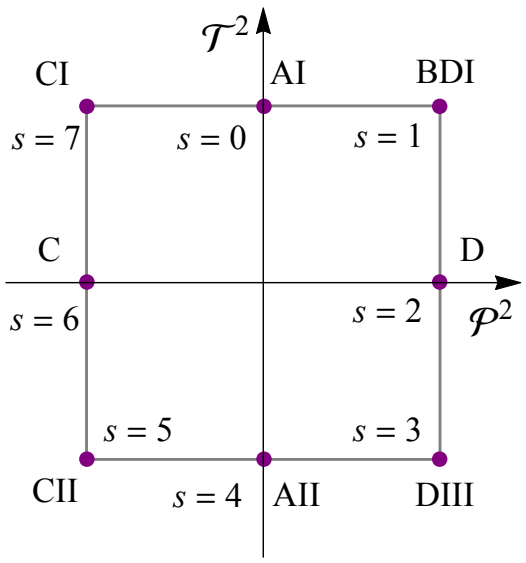

Figure 1.1: Eight-hour clock for the real symmetry classes labelled by index s. $\mathcal{T}$, $\mathcal{P}$ symmetries have the value $\pm$ along two axes. Adapted from Ref. [85].

$e^{2i\theta_{T(P)}} = 1$; second, a redefinition $U_C \to U'_C = e^{-i\theta_C/2}U_C$ leads to $(U'_C)^2 = \mathbb{1}$. Hence, in the presence of symmetries the system satisfies

$$\mathcal{T}^2 = \pm 1, \quad \mathcal{P}^2 = \pm 1, \quad \mathcal{C}^2 = 1. \tag{1.4}$$

And we denote $\mathcal{U}^2 = 0$ when the given symmetry is absent. Since $\mathcal{C} = \mathcal{T}\cdot\mathcal{P}$, there are $3^2 = 9$ possibilities for the behaviours of the Hamiltonian under CPT transformations. One more possibility arises when both time reversal and particle-hole symmetries are missing but the chiral symmetry is present: $\mathcal{T}^2 = \mathcal{P}^2 = 0, \mathcal{C}^2 = 1$. Fig. 1.1, Table 1.1 and Table 1.2 show the tenfold symmetry classes [86–88] for fully gapped non-interacting fermionic systems.

Table 1.1: Complex symmetry classes of tenfold way for non-interacting fermionic Hamiltonians. Index δ is called the topological dimension defined by $\delta = d - D$ with d the spatial dimension and $D + 1 = d - d_{\text{defect}}$ the co-dimension of defects. The case $D = 0$, $\delta = d$ corresponds to a fully gapped bulk system. We also label the two complex symmetry classes A and AIII by index $s = 0, 1$ respectively.

δ	$\mathcal{T}^2$	$\mathcal{P}^2$	$\mathcal{C}^2$	0	1	2	3	4	5	6	7
A	0	0	0	$\mathbb{Z}$	0	$\mathbb{Z}$	0	$\mathbb{Z}$	0	$\mathbb{Z}$	0
AIII	0	0	+	0	$\mathbb{Z}$	0	$\mathbb{Z}$	0	$\mathbb{Z}$	0	$\mathbb{Z}$

Table 1.2: Real symmetry classes of tenfold way for non-interacting fermionic Hamiltonians. Index s stands for eight classes imbedded with $\mathcal{T}$, $\mathcal{P}$ symmetries in Fig. 1.1. $K(s;d,D)$ represents the homomorphism $\pi_D(\mathcal{R}_{d-s}) = \pi_0(\mathcal{R}_{\delta-s})$.

$(\delta - s) \mod 8$	0	1	2	3	4	5	6	7
$K(s;d,D)$	$\mathbb{Z}$	0	0	0	$2\mathbb{Z}$	0	$\mathbb{Z}_2^{(2)}$	$\mathbb{Z}_2^{(1)}$

1.1.2 K-theory approach

From Table 1.1 and Table 1.2, the non-trivial topological phases of ten symmetry classes are classified by a topological invariant of type $\mathbb{Z}, 2\mathbb{Z}, \mathbb{Z}_2^{(1)}, \mathbb{Z}_2^{(2)}$ in different spatial dimensions. Next, we show a derivation of them using K-homology and Clifford algebras [71].

Before proceeding to theoretical aspects, it may be useful to introduce the notion of topological defects. In Table 1.1 and Table 1.2, two gapped phases with different topological numbers cannot be connected to each other by continuous deformations. Physically, on a d-dimensional lattice with a finite size, they are separated by an interface that carries a gapless mode. Equivalently, it can be viewed as putting a topological defect (of dimension d_{defect}) into a gapped bulk system. To encircle the defect, the gapless mode then lives on a sphere S^D. The spatial dimension of the sphere can be easily read: $D = d - d_{\text{defect}} - 1$ (e.g. a point defect on a two-dimensional bulk surface is surrounded by a line). Now, the defect Hamiltonian can be expressed as $H(k,r)$, with $(k,r) \in \text{BZ}^d \times \mathcal{M}^D$. On the other hand, as we shall see later, the topological dimension δ which determines the classification of topological phases is given by $(d - D)$. Throughout the manuscript, we often encounter the most simple case: a gapped bulk system in d-dimensions and the topological defect becomes its boundary of a dimension $d_{\text{defect}} = d - 1$. The gapless edge mode appearing on the interface between the system and its boundary, thus lives on a space with a fixed dimension $D = d - d_{\text{defect}} - 1 = 0$. Then, the defect Hamiltonian becomes an edge Hamiltonian $H(k,r) = H_{\text{edge}}(k)$. Since $(k,r) \in \text{BZ}^d \times \mathcal{M}^0$, we have localized zero-

energy edge modes in the one-dimensional topological system or one gapless edge mode with fixed chirality in the two-dimensional topological system (see Table 1.5). Meanwhile, in this case we get a topological dimension $\delta = d - D = d$. The formulation of the defect Hamiltonian helps us to consider broader types of topological defects and go to higher dimensions: for instance, in Section 1.2.3, we will address the point defects inside the 2D $p+ip$ superconductor that support Majorana zero-energy modes.

In general, the defect Hamiltonian takes a Dirac form (illustrated by specific examples afterwards),

$$H(k, r) = \vec{k} \cdot \vec{\Gamma} + m\Gamma_0(r). \tag{1.5}$$

It can be derived from low-energy excitations around the gapless Dirac point $\vec{k}_0$. Here, $\vec{k}$ denotes the deviation of momentum from the gapless point. $\vec{\Gamma}$, on the other hand, become Dirac matrices with d components (one for each bulk dimension). They satisfy the Clifford relation $\{\Gamma_\mu, \Gamma_\nu\} = 2\delta_{\mu\nu}$. The second mass term in Eq. (1.5) represents the contribution from the gap in the bulk. $\Gamma_0(r)$ should anticommute with any component of $\vec{\Gamma}$ in the kinetic term. If different defect Hamiltonians can be transformed into one another without closing the gap, they belong to the same class. One thus reformulates the original classification problem into an algebraic one: to identify the disconnected components that live on the intrinsic classifying space of a given defect Hamiltonian.

It is convenient to apply the method of K-homology. The universality class in Table 1.1 and Table 1.2 incorporates 2 types for complex Clifford algebras and 8 types for real Clifford algebras. All are re-labelled by index s (see also Fig. 1.1). We denote their classifying spaces as $\mathcal{C}_q$ and $\mathcal{R}_q$ with $q = d - s$. The disconnected components in a general manifold S^D are given by homotopy groups $\pi_D(\mathcal{C}_q)$ and $\pi_D(\mathcal{R}_q)$. In the following, we illustrate a few bulk examples ($D = 0$) related to two complex symmetry classes, the structures of which we encounter frequently hereafter. The derivation of real symmetry classes is left to Section 1.2 and we will see Majorana

fermion emerges naturally as the gapless boundary mode.

- **Class A in $d = 1, 2$.** The first complex symmetry class A describes topological band insulators without CPT symmetries. For $d = 2$, the most simple case comes from a two-band model of Nambu spinors. Its Bloch Hamiltonian can be expressed in terms of Pauli matrices

$$H(k) = R_0(k) \cdot \mathbb{1} + \vec{R}(k) \cdot \vec{\sigma}, \quad \Psi(k) = \begin{pmatrix} \psi_\uparrow(k) \\ \psi_\downarrow^\dagger(k) \end{pmatrix}, \tag{1.6}$$

and with the convention $\vec{\sigma} = (\sigma^x, \sigma^y, \sigma^z)$,

$$\sigma^x = \begin{pmatrix} 0 & 1 \\ 1 & 0 \end{pmatrix}, \quad \sigma^y = \begin{pmatrix} 0 & -i \\ i & 0 \end{pmatrix}, \quad \sigma^z = \begin{pmatrix} 1 & 0 \\ 0 & -1 \end{pmatrix}. \tag{1.7}$$

Notably, the system has $U(1)$ spin-rotation symmetry around z-axis. The energy spectrum reads $\epsilon_\pm(k) = R_0(k) \pm |\vec{R}(k)|$. We now choose a typical set of parameters: $R_0(k) = 0, \vec{R}(k) = (\sin k_x, \sin k_y, -\mu/2 - \sum_{\mu=x,y} \cos k_\mu)$, and focus on one of the Dirac points $\vec{k}_0 = (0, 0)$. The associated gap $\epsilon_\pm(\vec{k}_0) = \pm|\mu/2 + 2|$ closes at the chemical potential $\mu = -4$. An expansion around $\vec{k}_0$ then gives us the desired form of the defect Hamiltonian

$$H(k, r) = k_x \sigma^x + k_y \sigma^y + m\sigma^z, \tag{1.8}$$

with $m = -(\mu + 4)/2$ and $(k, r) \in \mathrm{BZ}^2 \times S^0$. The Pauli matrices can be viewed as Clifford generators in Eq. (1.5). Separated by a gapless mode, two phases with $m > 0$ and $m < 0$ are topologically distinct. More generally, let us enlarge the Fock space and consider N copies of band insulators that are decoupled from each other,

$$H(k, r) = k_x \sigma^x \otimes \mathbb{1}_N + k_y \sigma^y \otimes \mathbb{1}_N + \sigma^z \otimes M, \quad \Psi_j(k) = \begin{pmatrix} \psi_{j,\uparrow}(k) \\ \psi_{j,\downarrow}^\dagger(k) \end{pmatrix}, \tag{1.9}$$

with $M = \mathrm{diag}(m_1, \ldots, m_N)$ and $j = 1, \ldots, N$. The defect Hamiltonian respects $U(N)$ spin-rotation symmetry. Apparently, for $m_j \neq 0$ the type of topological

phases is determined by the sign of the effective mass. It is convenient to normalize the masses by a unitary transformation: $UMU^\dagger = \mathrm{diag}(\mathbb{1}_n, -\mathbb{1}_{N-n})$. When n is fixed, there are only two types of phases with either positive or negative mass. The simply connected part is identified in this way as $U(N)/(U(n) \times U(N-n))$. Taking into account all possible values of n, the entire classifying space of class A ($s = 0$) in $d = 2$ becomes

$$\mathcal{C}_2 = \bigcup_{0 \le n \le N} \frac{U(N)}{U(n) \times U(N-n)}, \tag{1.10}$$

with disconnected components $\pi_0(\mathcal{C}_2) = \mathbb{Z}$. We recover the integer topological number in Table 1.1. For $d = 1$, a similar argument can be made by looking at the defect Hamiltonian with one less dimension

$$H(k, r) = k_x \sigma^z \otimes \mathbb{1}_N + M. \tag{1.11}$$

To obey the Clifford algebra, the mass generator satisfies $\{\sigma^z \otimes \mathbb{1}_N, M\} = 0$. M can be an arbitrary superposition of σ^x and σ^y matrices. In the Nambu spinor space, it takes the form

$$M = \begin{pmatrix} 0 & U^\dagger \\ U & 0 \end{pmatrix} \tag{1.12}$$

where matrix U is Hermitian and $U \in U(N)$. The classifying space then reads

$$\mathcal{C}_1 = U(N), \tag{1.13}$$

with the homotopy group $\pi_0(\mathcal{C}_1) = 0$. Class A in $d = 1$ becomes a trivial phase.

- **Class AIII in $d = 0, 1$.** The second complex symmetry class AIII is embedded with chiral symmetry. From the transformation rules (1.4) and (1.2), one gets $U_C^\dagger = U_C^{-1} = U_C$ and the anti-commutation relation $\{H, U_C\} = 0$. It means in $d = 0$, the mass generator Γ_0 in the defect Hamiltonian shares the same form as the unitary matrix U_C. It lives on the classifying space $\mathcal{C}_1 = U(N)$ for class

AIII ($s = 1$). The trivial topology $\pi_0(\mathcal{C}_1) = 0$ agrees with the classification Table 1.1. Now we move to $d = 1$ and study the model of the Su-Schrieffer-Heeger (SSH) chain. It captures the physics of *trans*-polyacetylene [89, 90]. The single-particle lattice Hamiltonian takes the form

$$\mathcal{H} = \sum_j t_1 a_j^\dagger b_j + t_2 b_j^\dagger a_{j+1} + \text{h.c.}, \tag{1.14}$$

with real hopping amplitudes $t_1 = t(1+\delta)$, $t_2 = t(1-\delta)$ and $t > 0$. The operator $a_j^\dagger (b_j^\dagger)$ creates one spinless fermion in the j-th unit cell of sublattice $A(B)$. In momentum space $k \in]-\pi, \pi]$, the two-band Bloch Hamiltonian becomes

$$H(k) = R(k) \cdot \vec{\sigma}, \quad \Psi(k) = \begin{pmatrix} a_k \\ b_k \end{pmatrix}, \tag{1.15}$$

where $R(k) = (t(1-\delta) + t(1+\delta)\cos k, t(1+\delta)\sin k, 0)$. The chiral symmetry (1.3) is manifest in the operator $\mathcal{C} = \sigma^z$. From the energy dispersion $\epsilon_\pm(k) = \pm t\sqrt{2(1+\delta^2+(1-\delta^2)\cos k)}$, the gap closes at $k_0 = \pi$ when $\delta = 0$. Two phases with $\delta > 0$ and $\delta < 0$ are topologically distinct. As before, we derive the defect Hamiltonian of N decoupled SSH chains from an expansion around the gapless point

$$H(k, r) = -t(1+\delta)k\sigma^y \otimes \mathbb{1}_N - 2t\sigma^x \otimes M, \tag{1.16}$$

where $M = \text{diag}(\delta_1, \ldots, \delta_N)$. The sign of the effective mass δ_j determines the topology of the phase. For class AIII ($s = 1$) in $d = 1$, one obtains the same classifying space as class A ($s = 0$) in $d = 2$: $\mathcal{C}_0 \simeq \mathcal{C}_2$ in Eq. (1.10). The topological invariant becomes an integer $\pi_0(\mathcal{C}_0) = \mathbb{Z}$. Furthermore, it reveals *Bott periodicity* [91, 92] of the (mod 2) pattern in complex symmetry classes (see also Table 1.1),

$$\mathcal{C}_{q+2} \simeq \mathcal{C}_q, \qquad q = d - s. \tag{1.17}$$

In general, Bott periodicity can be proven by solving an extension problem in Clifford algebras [71, 93, 94]. Next, we elaborate on the case of complex symmetry

classes. We leave the discussion of real symmetry classes to Section 1.2.1. By contrast, there a different (mod 8) periodic pattern is revealed as shown in Table 1.2.

Proof of Eq. (1.17). For complex symmetry classes, the defect Hamiltonian (1.5) is composed of Γ matrices that obey a complex Clifford algebra $Cl_{\tilde{q}}$. The index $\tilde{q}$ denotes the number of Γ matrices or equivalently, the number of Clifford generators $\{e_\mu\}$. The anti-commutation relation is satisfied

$$\{e_\mu, e_\nu\} = 2\delta_{\mu\nu}, \quad \mu, \nu = 1, \ldots, \tilde{q}. \tag{1.18}$$

The algebra is complex in the sense that the vector space can now be represented by these generators as $\{C_{n_1 n_2 \cdots} e_1^{n_1} e_2^{n_2} \cdots\}$ with $C_{n_1 n_2 \cdots} \in \mathbb{C}$ and $n_\mu = 0, 1$. First, let us consider the effect of spatial dimension d and set $s = 0$ (class A). From the example of 2D band insulators (1.9), the Clifford algebra is extended from Cl_d to Cl_{d+1} with the addition of the mass term $m\Gamma_0(r)$. Then, the number of different ways for this extension $\pi_0(\mathcal{C}_d)$ becomes the number of topological phases. Each of them hosts a non-equivalent mass. We now take into account the following relation in complex Clifford algebra

$$Cl_{d+2} \simeq Cl_d \otimes \mathbb{C}(2). \tag{1.19}$$

Here, the complex algebra of 2×2 matrices $\mathbb{C}(2)$ can be ignored in the extension procedure. An equivalence relation for the classifying space is obtained: $\mathcal{C}_{d+2} \simeq \mathcal{C}_d$. Now, one can add the chiral symmetry and take $s = 1$ (class AIII). In the example of 1D SSH chains (1.16), the chiral symmetry operator ($\mathcal{C} = \sigma^z \otimes \mathbb{1}_N$) plays the same role as an extra Clifford generator: $\{H(k, r), \mathcal{C}\} = 0$. Consequently, the vector space (or the space dimension) is enlarged by one, and the extension problem turns into $Cl_{d+1} \to Cl_{d+2}$ or $Cl_{d-s+2} \to Cl_{d-s+3}$. Combined with the relation (1.19), we complete the proof of Bott periodicity (1.17) for complex symmetry classes.

In the end, if we allow arbitrary co-dimension for the topological defect ($D \neq 0$), the new continuous map of finding topologically distinct phases becomes $\mathrm{Map}(S^D, \mathcal{C}_q)$.

Table 1.3: Topological invariants of the tenfold symmetry classification [69].

Type	$\mathcal{C}^2 = 0$	$\mathcal{C}^2 = 1$
$\mathbb{Z}$	Chern number (Ch)	Winding number (ν)
$\mathbb{Z}_2^{(1)}$	Chern-Simons (CS)	Fu-Kane (FK)
$\mathbb{Z}_2^{(2)}$	Fu-Kane (FK)	Chern-Simons (CS)

Due to the fact $\mathcal{C}_{q-1} \simeq \mathrm{Map}(S^1, \mathcal{C}_q)$, one verifies

$$\pi_D(\mathcal{C}_q) = \pi_0(\mathcal{C}_{q-D}) = \pi_0(\mathcal{C}_{\delta-s}), \tag{1.20}$$

where $\delta = d - D$ stands for the topological dimension. It is worthwhile to note that the same argument can be applied to real symmetry classes [95].

1.1.3 Topological invariants

Non-trivial topological phases in classification Table 1.1 and Table 1.2 are associated with topological invariants that can be measured in experiments. Physically, topological invariants detect the adiabatic changes in wave functions when we move them around the base manifold of the defect Hamiltonian. When the wave functions are not smooth everywhere, an obstruction arises and leads to a nonzero topological invariant. Table 1.3 summarizes the case of strong topological invariants, for which the phase space one considers is compactified: $(k, r) \in \mathrm{BZ}^d \times \mathcal{M}^D \to S^{d+D}$.

In this section, we cover the invariants related to the $\mathbb{Z}$-classified topology.

- **Chern number.** One can start from a general defect Hamiltonian that holds N bands with $N_-(N_+)$ bands below (above) the Fermi level. The energy bands are linked to a set of normalized eigenstates: $H(k,r)|\tilde{u}_\pm^\mu(k,r)\rangle = \epsilon_\pm^\mu(k,r)|\tilde{u}_\pm^\mu(k,r)\rangle$ where $\mu|_\pm = 1, \ldots, N_\pm$. For convenience, we adopt a short-handed notation for the occupied eigenfunctions: $|u^\mu(k,r)\rangle = |\tilde{u}_-^\mu(k,r)\rangle$. The winding of them around the base manifold can then be described by the Berry curvature

$$\mathcal{F} = d\mathcal{A} + \mathcal{A}^2, \tag{1.21}$$

built from the Berry connection

$$\mathcal{A}^{\mu\nu}(k,r) = \langle u^{\mu}(k,r)|du^{\nu}(k,r)\rangle. \tag{1.22}$$

In Table 1.3, topological number $\mathbb{Z}$ is characterized by the Chern number when the chiral symmetry is absent

$$\mathrm{Ch}_n = \frac{1}{n!}\left(\frac{i}{2\pi}\right)^n \int_{\mathrm{BZ}^d\times\mathcal{M}^D} \mathrm{Tr}(\mathcal{F}^n), \tag{1.23}$$

with $2n = d+D$. For a second-quantized defect Hamiltonian $H(k,r)$, it is more convenient to use an alternative expression in terms of Q matrix

$$\mathrm{Ch}_n = -\frac{1}{2^{2n+1}n!}\left(\frac{i}{2\pi}\right)^n \int_{\mathrm{BZ}^d\times\mathcal{M}^D} \mathrm{Tr}[Q(dQ)^{2n}], \tag{1.24}$$

where Q is a Hermitian matrix constructed from the spectral projector

$$Q(k,r) = \mathbb{1} - 2P(k,r), \quad P(k,r) = |u^{\mu}(k,r)\rangle\langle u^{\mu}(k,r)|. \tag{1.25}$$

By definition, one verifies that $Q(k,r)|\tilde{u}^{\mu}_{\pm}(k,r)\rangle = \pm|\tilde{u}^{\mu}_{\pm}(k,r)\rangle$. Hence, matrix $Q(k,r)$ shares the same set of eigenfunctions as $H(k,r)$ with normalized eigenvalues ±1. The two share a similar matrix structure as well. For a two-band insulator belonging to class A in $d = 2$ (1.6), one can extract Chern numbers from Eq. (1.24) and Eq. (1.25): $\mathrm{Ch}_1 = 0$ for $\mu < -4$ and $\mathrm{Ch}_1 = 1$ for $-4 < \mu < 0$. Indeed, by varying the chemical potential the system goes from a trivial phase to the topological regime and the gap closes at the critical point. Experimentally, without an external magnetic field, the non-zero Chern number gives rise to an anomalous quantum Hall response that can be described by a quantized Hall conductance σ_{xy} [21, 96]. We call 2D materials of this type *Chern insulators*.

- **Winding number.** In the presence of chiral symmetry, $\mathbb{Z}$-classified topology is given by the winding number. First noticing $\mathrm{Tr}\, U_C = 0$ and $U_C^2 = 1$, one can always find a basis where U_C is diagonalized with evenly distributed eigenvalues

$\{\pm 1\}$. Constrained by the chiral symmetry $\{H, U_C\} = 0$, the energies of the system come in pairs: $\epsilon_+^\mu = -\epsilon_-^\mu$ and $|\tilde{u}_+^\mu\rangle = U_C|\tilde{u}_-^\mu\rangle$. Meanwhile, the defect Hamiltonian now shares a block off-diagonal form

$$H(k,r) = \begin{pmatrix} 0 & D(k,r) \\ D^\dagger(k,r) & 0 \end{pmatrix}. \tag{1.26}$$

The $D(k,r)$ matrix has a dimension $N_- \times N_-$ with $N_- = N_+ = N/2$. Accordingly, the Q matrix in Eq. (1.25) inherits the structure of $H(k,r)$

$$Q(k,r) = \begin{pmatrix} 0 & q(k,r) \\ q^\dagger(k,r) & 0 \end{pmatrix}. \tag{1.27}$$

Due to the fact $Q^2 = \mathbb{1}_N$, $q(k,r) \in U(N_-)$. When $d+D = 2n+1$, the homotopy group for the classifying space becomes non-trivial: $\pi_{d+D}(U(N_-)) = \mathbb{Z}$. It can be captured by the winding number in terms of $Q(k,r)$ matrix

$$\nu_{2n+1}[q] = \int_{\mathrm{BZ}^d \times \mathcal{M}^D} \frac{(-1)^n n!}{(2n+1)!} \left(\frac{i}{2\pi}\right)^{n+1} \mathrm{Tr}[(q^{-1}dq)^{2n+1}]. \tag{1.28}$$

Let us go back to 1D SSH chain (1.15) in Class AIII. One immediately identifies $q(k,r) = [t(1-\delta) + t(1+\delta)e^{-ik}]/|\epsilon_\pm(k)|$ and the winding number reads $\nu_1 = i/(2\pi)\int_{\mathrm{BZ}} dk q^{-1}\partial_k q$. For $\delta > 0$, $\nu_1 = 1$ and for $\delta < 0$, $\nu_1 = 0$. In the topological regime $\delta > 0$, the non-zero winding number is manifest in the physical obversable - geometric *Zak phase* [97, 98], a Berry's phase the particle picks up after moving around the Brillouin zone.

For the remaining topological invariants in Table 1.3, Chern-Simons and Fu-Kane invariants, we leave the discussion to Section 1.2. As mentioned before, we will address the topological classification of real symmetry classes by changing into the representation of real Majorana fermions.

1.2 Origin of Majorana fermions

In 1937, one year before his mysterious disappearance on the ship from Palermo to Naples, Ettore Majorana proposed the Majorana representation of the Dirac equation

for relativistic particles [99]. Since a spin-1/2 Majorana fermion is its own antiparticle, he became the first to point out its influence on neutrino physics. Around twenty years later, remarkably, the Majorana equation arose naturally in the Bardeen-Cooper-Schrieffer (BCS) description of the superconducting order in solids [100–102]. Since then, the search for Majorana fermions has blossomed in a broad range of fields, including nuclear, particle and condensed matter physics [4].

Not only its wide stretch is impressive, in modern times realizing Majorana fermion in topological quantum matter has been viewed as an important step towards future fault-tolerant quantum computation [15]. Due to non-trivial topology in band structures, a Majorana particle manifests itself as a nonlocal zero-energy mode that is robust against quantum decoherence. In the following, we present a short review on the emergence of Majorana fermion in different contexts with a focus on uncovering its topological nature in relation to topological superconductors [14, 72]. The appearance of Majorana fermions in quantum spin liquids [18] will be covered in Section 1.3.

1.2.1 From particle physics to topological matter

In particle physics, Majorana fermions are embodied in a real symmetrical solution to the Dirac equation [103]

$$(\gamma^\mu p_\mu - m)\Psi = 0. \tag{1.29}$$

The four-momentum is defined as $p_\mu = \eta_{\mu\nu}p^\nu = (i\partial_t, -\vec{p})$ with a Minkowski metric $\eta_{\mu\nu} = (+1, -1, -1, -1)$. And we set $\hbar = c = 1$. In the Weyl representation, the 4×4 Dirac matrices γ^μ take the form

$$\gamma^\mu = \begin{pmatrix} 0 & \sigma^\mu \\ \tilde{\sigma}^\mu & 0 \end{pmatrix}, \quad \sigma^\mu = (\mathbb{1}, -\vec{\sigma}), \quad \tilde{\sigma}^\mu = (\mathbb{1}, \vec{\sigma}). \tag{1.30}$$

And they satisfy the Clifford algebra $\{\gamma^\mu, \gamma_\nu\} = 2\delta^\mu_\nu$. Multiplying Eq. (1.29) from the left with the operator $(\gamma^\nu p_\nu + m)$, one recovers the energy-momentum relation for a relativistic particle: $E^2 = p^2 + m^2$. It is more convenient to express the wave function

in the basis of two-component chiral fields $\Psi = (\psi_L, \psi_R)^t$, where ψ_L and ψ_R stand for the left-handed $(\frac{1}{2}, 0)$ and right-handed $(0, \frac{1}{2})$ Weyl spinors. The Dirac equation (1.29) is then transformed into a pair of coupled equations

$$\begin{pmatrix} i\partial_t + \vec{p}\cdot\vec{\sigma} & -m_D \\ -m_D & i\partial_t - \vec{p}\cdot\vec{\sigma} \end{pmatrix} \begin{pmatrix} \psi_L \\ \psi_R \end{pmatrix} = 0. \tag{1.31}$$

Furthermore, by separating the time-dependent part from the wave function $\Psi(t,x) = e^{-iEt}\Phi(x)$, one can replace the differential operator: $i\partial_t \to E$ and take complex conjugation of Eq. (1.31). Charge conjugation (c) symmetry or particle-hole ($\mathcal{P}$) symmetry immediately follows: there exists a solution $\Phi^c(x)$ with energy $(-E)$. More precisely, [1]

$$\Psi^c(t,x) = e^{+iEt}\Phi^c(x), \quad \Phi^c(x) = \mathcal{P}\Phi(x) = (-i\gamma^2)\cdot\Phi^*(x). \tag{1.32}$$

Starting from here, we can construct a real Majorana solution $\Psi(t,x)$ that encodes particle-antiparticle correspondence

$$\Psi^c(t,x) = \Psi(t,x). \tag{1.33}$$

The effects are two folds. First, the time-dependence should vanish and Majorana fermion becomes a zero-energy mode: $E = 0$. Meanwhile, one identifies:

$$\begin{pmatrix} \psi_L^c(x) \\ \psi_R^c(x) \end{pmatrix} = \begin{pmatrix} i\sigma^y\psi_R^*(x) \\ -i\sigma^y\psi_L^*(x) \end{pmatrix} = \begin{pmatrix} \psi_L(x) \\ \psi_R(x) \end{pmatrix}. \tag{1.34}$$

Substituting it into the Weyl representation (1.31), we obtain the decoupled Majorana equation

$$(i\partial_t - r\vec{p}\cdot\vec{\sigma})\psi_r(x) - irm_r\sigma^y\psi_r^*(x) = 0, \tag{1.35}$$

with the index $r = +/-$ for R/L. Here, we allow different masses for two chiral fields: $m_D \to m_{R/L}$. It is interesting to compare Majorana fermion with its Dirac

[1] The γ^2 matrix can be traced back to the operation: $(\vec{p}\cdot\vec{\sigma})^* = \sigma^y(\vec{p}\cdot\vec{\sigma})\sigma^y$.

counterpart. Both are constructed from the same set of Weyl spinors and carry spin-1/2. Yet, apart from the zero-energy constraint, Majorana fermion also has no charge. It lies in the fact that the Majorana equation (1.35) breaks the global U(1) gauge symmetry: $\psi_r(x) \to e^{-i\alpha}\psi_r(x)$. The coupling to an electromagnetic field is no longer allowed: $p_\mu \to p_\mu - qA_\mu$. With a nonzero potential A_μ, one infers the charge should be neutral: $q = 0$.

Going beyond a mathematical reformulation of the Dirac equation, Majorana fermions have a deep impact on neutrino physics. In the well-known seesaw mechanism [104–107], the mass term in the Lagrangian of a single-flavour neutrino (among all three flavours) takes the form

$$\mathcal{L}_m = \frac{1}{2}\begin{pmatrix}\bar{\nu}_L^c & \bar{\nu}_R\end{pmatrix}\begin{pmatrix}m_L & m_D \\ m_D & m_R\end{pmatrix}\begin{pmatrix}\nu_L \\ \nu_R^c\end{pmatrix}. \tag{1.36}$$

Here, $\nu_{R/L}^{(c)}$ stand for Weyl spinors (previously $\psi_{R/L}^{(c)}$ in Eq. (1.34)) and antineutrinos are described by $\bar{\nu} = \nu^\dagger\gamma^0$. The non-observation of ν_R implies $m_R \gg (m_L, m_D)$. Assuming $m_L \simeq 0$, from the diagonalisation one gets an extra light neutrino ν_e with mass $m_{\nu_e} \sim m_D^2/m_R$. It agrees with experiments that neutrinos are much lighter than charged Dirac leptons. It also gives us a hint that neutrinos in $\mathcal{L}_m$ (1.36) could be Majorana particles. A direct evidence would arise from the neutrinoless double beta decay process [108, 109]: ${}^N_Z A \longrightarrow {}^{N-2}_{Z+2}A + 2\beta^-$. Being its own antiparticle $\bar{\nu}_e = \nu_e$, in the intermediate process the antineutrino must be absorbed by a neutron. Similar processes can occur in proton decays [110] and it leads to a selection rule with respect to the baryon and lepton numbers: $\Delta(B-L) = \pm 2$. Supersymmetry further predicts Majorana fermions as dark matter candidates [111], and it motivates on-going deep underground experiments [112, 113] that are designed to detect weak interactions among massive particles.

The concept of Majorana fermion was transferred from nuclear to condensed matter physics first by the establishment of theory on superconductivity [100–102]. To describe the wave function of spin-1/2 electrons in solids, one can resort to a four-

component Nambu spinor

$$\Psi_r = \begin{pmatrix} c_{\uparrow,r} \\ c_{\downarrow,r} \\ c^\dagger_{\downarrow,r} \\ -c^\dagger_{\uparrow,r} \end{pmatrix} = \begin{pmatrix} \Psi_r \\ i\sigma^y \Psi^*_r \end{pmatrix} \sim \begin{pmatrix} \Psi_{R,r} \\ \Psi^c_{L,r} \end{pmatrix}, \tag{1.37}$$

with r the site index. Here, the Nambu spinor Ψ_r becomes a Majorana field operator (1.34). And the particle-hole symmetry can be easily verified: $\Psi^c_r = (i\gamma^2)\Psi^*_r = \Psi_r$. To understand the emergent superconducting order at the mean field level [4], the BCS formalism postulates a Bogoliubov-de Gennes (BdG) Hamiltonian [114]:

$$\mathcal{H}_{\text{BdG}} \propto \int d^d r \Psi^\dagger_r H_{\text{BdG}}(r) \Psi_r, \quad H_{\text{BdG}}(r) = \begin{pmatrix} h_0(r) \cdot \mathbb{1}_N & \Delta(r) \cdot \mathbb{1}_N \\ \Delta^*(r) \cdot \mathbb{1}_N & -\sigma^y h^*_0(r) \sigma^y \end{pmatrix}. \tag{1.38}$$

While $h_0(r)$ contains the kinetic energy and the chemical potential, $\Delta(r)$ embodies the effective pairing between two opposite spins on the same site. The pairing term originates from the attractive interaction $V n_{\uparrow,r} n_{\downarrow,r}$ with $V < 0$, and physically changes the total number of electrons by an even integer. The effect is in resemblance to the double beta decay process ($\Delta L = \pm 2$). From the Majorana equation (1.35), we further notice $\Delta(r)$ generates a mass for the Majorana particle.

Yet quite different from particle physics where Majorana fermion appears in weak interactions, later it has been found that Majorana fermions with zero energy can stay as robust boundary states in topological superconductors. The effective picture is given by class D with only particle-hole symmetry, one of real symmetry classes on the classification Table 1.2. For the remaining of this section, we move on to elucidate the topological structure of this symmetry class and comment briefly on the emergence of MZMs. Concrete examples will follow in Sections 1.2.2, 1.2.3 and 1.3.

As has been previously shown, the particle-hole constraint [115] can be incorporated naturally into a generic BdG Hamiltonian in the basis of Nambu spinors

$$\mathcal{H} = \frac{1}{2} \Psi^\dagger_\mu H^{\mu\nu} \Psi_\nu, \quad \Psi^\dagger = (\psi^\dagger_1, \ldots, \psi^\dagger_N, \psi_1, \ldots, \psi_N). \tag{1.39}$$

Here, τ^α ($\alpha = x, y, z$) a new set of Pauli matrices acts on the Nambu spinor space. And $\Psi^\dagger$ and Ψ are no longer independent from each other: $\Psi^\dagger = (\tau^x\Psi)^t$. Substituting it into Hamiltonian (1.39), we obtain $\mathcal{H} = (1/2)(\tau^x\Psi)^t H(\tau^x\Psi)^* = -(1/2)\Psi^\dagger\tau^x H^t\tau^x\Psi + (1/2)\,\mathrm{Tr}(\tau^x H\tau^x)$. According to the transformation rule (1.2), the BdG Hamiltonian is now endowed with intrinsic particle-hole symmetry ($\mathcal{P} = \tau^x$)

$$\tau^x H^t\tau^x = -H, \quad \mathrm{Tr}(\tau^x H\tau^x) = 0. \tag{1.40}$$

With these two constraints, one can derive a compact BCS form

$$H = \begin{pmatrix} \xi & \Delta \\ -\Delta^* & -\xi^t \end{pmatrix}. \tag{1.41}$$

Compared with Eq. (1.38), now the kinetic term ξ and the pairing term Δ become $N \times N$ matrices and satisfy: $\xi = \xi^\dagger, \Delta = -\Delta^t$. Symmetry classes in classification Table 1.2 are interpreted by real Clifford algebra. It is then natural to change into a real Majorana basis ($\mu = 1, \ldots, N$)

$$\gamma_\mu = \Psi_\mu + \Psi_\mu^\dagger, \quad \gamma_{\mu+N} = -i(\Psi_\mu - \Psi_\mu^\dagger), \tag{1.42}$$

where $\gamma_\mu^\dagger = \gamma_\mu$ and the anti-commutation relation $\{\gamma_\mu, \gamma_\nu\} = 2\delta_{\mu\nu}$ is satisfied.[2] The Hamiltonian takes the new form in terms of a real anti-symmetric matrix

$$\mathcal{H} = \frac{i}{4}\gamma_\mu^t A^{\mu\nu}\gamma_\nu, \tag{1.43}$$

with $A^* = A$ and $A^t = -A$. It is always possible to find an orthogonal matrix S and block diagonalize the Hamiltonian:

$$\eta = S^{-1}\gamma, \quad Q = S^{-1}AS = \begin{pmatrix} 0 & \epsilon_1 & & & \\ -\epsilon_1 & 0 & & & \\ & & 0 & \epsilon_2 & \\ & & -\epsilon_2 & 0 & \\ & & & & \ddots \end{pmatrix}, \tag{1.44}$$

[2] Unfortunately, we used the same notation for the Dirac matrices (1.30). Yet it is not difficult to distinguish them according to the context.

and

$$\mathcal{H} = (i/2)\sum_{\mu=1}^{N} \epsilon_\mu \eta_{2\mu-1}\eta_{2\mu}, \tag{1.45}$$

with $\epsilon_\mu \geq 0$. When pairings are present in topological systems, MZMs can occur in several forms. For instance, two boundary Majorana modes can be decoupled from a chain, and it gives rise to a $\mathbb{Z}_2^{(1)}$ topological invariant [72] in the bulk. A single gapless Majorana mode can also be formed at the edge of a gapped two-dimensional material that carries a nonzero Chern number [14, 18].

Hence, it is necessary to clarify the types of topological states in class D. For simplicity, we consider the case $d_{\text{defect}} = d - 1$ such that $\delta = d$.

- **Class D in $d = 1, 2$.** One starts from a generic defect Hamiltonian in $d = 1$ with a Dirac structure: $H(k, r) = k\Gamma_1 + m\Gamma_0(r)$. Consistent with the BCS form (1.41), we choose a basis such that

$$H(k, r) = k\tau^z \otimes \mathbb{1}_N + m\Gamma_0(r). \tag{1.46}$$

  The particle-hole symmetry is respected if $\mathcal{P}H(k, r)\mathcal{P}^{-1} = -H(-k, r)$, and one identifies $\mathcal{P} = \mathcal{K}$. Accordingly, $\Gamma_0(r)$ should anti-commute with both Γ_1 and $\mathcal{P}$. From the hermiticity $\Gamma_0^* = \Gamma_0^t$ and $(\tau^\alpha)^t = -\tau^y\tau^\alpha\tau^y$, there are two components in the mass term:

$$\Gamma_0(r) = \tau^y \otimes \Delta_1(r) + \tau^x \otimes i\Delta_2(r). \tag{1.47}$$

  Here, $\Delta_{1,2}$ are the real symmetric and anti-symmetric parts of the $N \times N$ matrix $\Delta = \Delta_1 + \Delta_2$ and $\Delta^t = \Delta_1 - \Delta_2$. Moreover, one notices the normalization of Clifford generators $\{\Gamma_\mu, \Gamma_\nu\} = 2\delta_{\mu\nu}$. It indicates $\mathbb{1}_N = (\Delta_1)^2 - (\Delta_2)^2 = \Delta \cdot \Delta^t$. Therefore, Δ is orthogonal. The classifying space of 1D defect Hamiltonian in class D ($s = 2$) becomes

$$\mathcal{R}_{(d-s) \bmod 8} = \mathcal{R}_7 = O(N), \tag{1.48}$$

with disconnected components $\pi_0(\mathcal{O}(N)) = \mathbb{Z}_2^{(1)}$. From Table 1.3, it is characterized by a Chern-Simons topological invariant.

Now we go to the case $d = 2$. One more Clifford generator should be added to the kinetic term: $H(k, r) = k_x\Gamma_1 + k_y\Gamma_2 + m\Gamma_0(r)$. Similarly, by carefully choosing the basis one can reach a simplified form of the defect Hamiltonian

$$H(k, r) = k_x\tau^x \otimes \mathbb{1}_N + k_y\tau^z \otimes \mathbb{1}_N + m\Gamma_0(r), \tag{1.49}$$

with $\mathcal{P} = \mathcal{K}$. Again, to meet the anti-commutation relations with $\Gamma_{1,2}$ and $\mathcal{P}$, the Dirac mass generator is constrained to one component

$$\Gamma_0(r) = \tau^y \otimes \Delta_1(r), \tag{1.50}$$

with $\Delta_1(r)$ a real symmetric matrix. By analogy to 2D Chern insulators (1.9) in complex symmetry class A, we can find an orthogonal matrix $S \in O(N)$ such that the mass term is diagonalized: $M = S^{-1}\Delta_1 S = \mathrm{diag}(m_1, \ldots, m_N)$. Topologically distinct masses are fully determined by $\mathrm{sgn}(m_i)$. The classifying space is then expanded by a set of orthogonal matrices $\{S(n, N-n)\}$ that are different from each other in the number of positive eigenvectors (n) and the number of negative eigenvectors $(N-n)$. It follows

$$\mathcal{R}_0 = \bigcup_{0\le n\le N} \frac{O(N)}{O(n) \times O(N-n)}. \tag{1.51}$$

Thus, the topological state of class D in $d = 2$ belongs to the type: $\pi_0(\mathcal{R}_0) = \mathbb{Z}$. In the absence of chiral symmetry, from Table 1.3 it is characterized by a nonzero Chern number (1.24).

At the end of this section, for completeness we present a brief demonstration of the Bott periodicity in classification Table 1.2 of real symmetry classes

$$\mathcal{R}_{q+8} \simeq \mathcal{R}_q, \qquad q = d - s. \tag{1.52}$$

Similarly, it can be proven by solving the extension problem of real Clifford algebra [69, 71].

Proof of Eq. (1.52). A set of elements $\{e_{\mu=1,2,\ldots,m+n}\}$ embedded with real coefficients generates real Clifford algebra $Cl_{m,n}$. And it has the structure

$$\begin{aligned} &\{e_\mu, e_\nu\} = 0, \quad \mu \neq \nu; \\ &(e_\mu)^2 = \mathrm{sgn}(\mu - m + \epsilon), \quad \epsilon = 0^-. \end{aligned} \tag{1.53}$$

Formally, we address the matrix representation of $\{e_\mu\}$ and $Cl_{m,n}$ is then described by m real anti-symmetric and n real symmetric matrices. Finding the topologically non-equivalent masses is simplified to the search for the extension procedure of associated real Clifford algebra. The type $Cl_{m,n} \to Cl_{m,n+1}$ is denoted by $\mathcal{R}_{m,n}$. One can establish the equality $\mathcal{R}_{m,n} = \mathcal{R}_{m-n}$ from the isomorphism: $Cl_{m+1,n+1} \simeq Cl_{m,n} \otimes \mathbb{R}(2)$ for $Cl_{m,n}$ shares the same representation with $Cl_{m,n} \otimes \mathbb{R}(2)$. As an example, we can see how the extension problem works for class D. In the case $d = 2$, it is useful to introduce another isomorphism $Cl_{0,m+2} = Cl_{m,0} \otimes \mathbb{R}(2)$, that is illustrated by

$$e_\mu = e'_\mu \otimes (i\tau^y) \quad (\mu = 1, 2, \ldots, m), \quad e_{m+1} = \mathbb{1} \otimes \tau^z, \quad e_{m+2} = \mathbb{1} \otimes \tau^x, \tag{1.54}$$

with $(e'_\mu)^2 = -1$. From the two isomorphisms, the extension algebra $Cl_{0,2} \to Cl_{1,2}$ one identifies in the defect Hamiltonian (1.49) with a mass term (1.50), is equivalent to $Cl_{0,0} \to Cl_{0,1}$. We successfully recover the classifying space $\mathcal{R}_0$ in Eq. (C.2). For the case $d = 1$, the Dirac form of the defect Hamiltonian in Eq. (1.46) and Eq. (1.47) is assigned a classifying space $\mathcal{R}_{-1} : Cl_{0,1} \to Cl_{0,2}$. Now, the *Morita equivalence* in the real Clifford algebra can be employed

$$Cl_{m+8,n} \simeq Cl_{m,n} \otimes \mathbb{R}(16). \tag{1.55}$$

It leads to $\mathcal{R}_{-1} = \mathcal{R}_7 : Cl_{8,1} \to Cl_{8,2}$. And the Bott periodicity (1.52) is validated.

If the topological defect $m\Gamma_0(r)$ lives in arbitrary dimension ($r \in S^D, D \neq 0$), the same argument used for complex symmetry classes (1.20) can be applied. One obtains

the homotopy group for the classification problem

$$\pi_D(\mathcal{R}_{d-s}) = \pi_0(\mathcal{R}_{\delta-s}), \quad \delta = d - D, \tag{1.56}$$

from the mapping $\mathcal{R}_{q-1} = \mathrm{Map}(S^1, \mathcal{R}_q)$ [95].

Once topological defects support potential MZMs, we can characterize the states by topological invariants and further study interaction effects. Related aspects will be covered in following sections based on models in integrable systems.

1.2.2 p-wave superconducting chain

Let us begin with the p-wave superconducting chain first proposed by Kitaev [72]. It is the most simple scenario of MZMs. The lattice Hamiltonian allows pairings between spinless fermions on neighbouring sites

$$\mathcal{H} = -\mu \sum_{j=1}^{N} c_j^\dagger c_j + \sum_{j=1}^{N-1} \left(-t c_j^\dagger c_{j+1} + \Delta c_j^\dagger c_{j+1}^\dagger + \mathrm{h.c.} \right). \tag{1.57}$$

Here, $c_j/c_j^\dagger$ annihilates/creates a spinless fermion on site j. We set the hopping amplitude t to be real and the chemical potential μ uniform. The pairing parameter Δ is also taken as real for any phase factor $\Delta = |\Delta| e^{i\theta}$ can be absorbed by the gauge transformation $c_j^\dagger \to e^{-i\theta/2} c_j^\dagger$. The particle number conservation or the $U(1)$ symmetry is broken once $\Delta \neq 0$. The topology of the superconducting chain can be analysed with periodic boundary conditions (PBCs) as well as open boundary conditions (OBCs).

For PBCs, in momentum space one builds the BdG form

$$\mathcal{H} = \frac{1}{2} \sum_k \Psi_k^\dagger H(k) \Psi_k, \quad \Psi_k = \begin{pmatrix} c_k \\ c_{-k}^\dagger \end{pmatrix}, \tag{1.58}$$

in terms of Pauli matrices

$$H(k) = \vec{h}(k) \cdot \vec{\sigma} = (-2t \cos k - \mu) \cdot \sigma^z - 2\Delta \sin k \cdot \sigma^y. \tag{1.59}$$

The lattice spacing is set to $a = 1$. The pairing term $(-2\Delta \sin k)$ changes its sign under $k \to -k$, so the model behaves as a p-wave superconductor. The Bloch Hamiltonian is restrained by the particle-hole symmetry: $\mathcal{P} = \sigma^x \mathcal{K}$, thus it belongs to the real symmetry class D. As is shown in the energy spectrum $E_\pm(k) = \pm|\vec{h}(k)| = \pm h = \pm\sqrt{(2t\cos k + \mu)^2 + (2\Delta \sin k)^2}$, the gap closes at $k^* = 0, \pi$ if the chemical potential satisfies $\mu = -2t, +2t$. The topological phase falls into the regime $|\mu| < |2t|$ and is characterized by the CS invariant of $K(s = 2; d = 1, D = 0) = \mathbb{Z}_2^{(1)}$ type (referring to Fig. 1.1, Table 1.2 and Table 1.3). Before addressing formally the topological invariant, we can first draw an intuitive picture from the BCS Hamiltonian [76]. The eigenfunctions can be constructed explicitly

$$|\tilde{u}_\pm(k)\rangle = \begin{pmatrix} \alpha_k \\ \beta_k \end{pmatrix} = \begin{pmatrix} h_x - ih_y \\ \pm h - h_z \end{pmatrix} \cdot \frac{1}{\sqrt{2h(h \mp h_z)}}, \tag{1.60}$$

and we obtain a diagonalized Hamiltonian $\mathcal{H} = \sum_k E_+ a_k^\dagger a_k$ with $a_k = \langle u_+(k)|\Psi(k)\rangle = \alpha_k^* c_k + \beta_k^* c_{-k}^\dagger$. The ground state forbids the occupation of the fermionic particle $a_k|\mathrm{GS}\rangle = 0$, hence it is proportional to $\prod_{0<k<\pi}(1 + \varphi(k) c_{-k}^\dagger c_k^\dagger)|0\rangle$. The wave-function $\varphi(k) = \beta_k^*/\alpha_k^* = (h - h_z)/(h_x + ih_y)$ reveals a Cooper pair formed at opposite momenta. The topological regime $|\mu| < |2t|$ corresponds to a weakly paired phase. From the perspective of band structures, when $|\Delta| \ll t$, the lower band has a dispersion $E_- = -2t\cos k - \mu$. For $\mu < |2t|$, the BCS pairing term $-2i\Delta \sin(k) c_{-k}^\dagger c_k^\dagger + h.c.$ can open a gap at the two Fermi points which are described by a linear spectrum and help the Cooper pairs to develop [14]: in real space, they become loosely bound with $|\varphi(r)| \sim |r|^{-1}$. Whereas when $|\mu| > |2t|$, the gapless points disappear and the bulk gap can no longer be formed. Thus, $|\varphi(r)|$ decays exponentially over the distance, suggesting the strong pairing nature of a BEC-like condensate.

For a chain with open boundaries, it is more convenient to use the Majorana fermions representation (1.42)

$$\gamma_{A,j} = c_j^\dagger + c_j, \quad \gamma_{B,j} = i(c_j^\dagger - c_j), \tag{1.61}$$

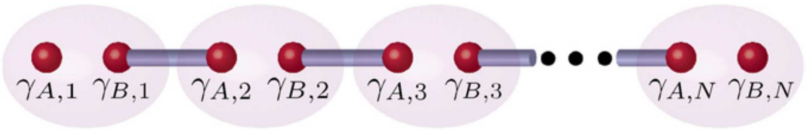

Figure 1.2: Pairing of the Kitaev p-wave superconducting chain in the limit $t = \Delta \neq 0$, $\mu = 0$. Two MZMs appear at the edges of the chain and the ground state becomes doubly degenerate. From Ref. [76].

and recast the Hamiltonian into the form

$$\mathcal{H} = -\frac{i}{2}\sum_j \left[\mu\gamma_{A,j}\gamma_{B,j} + (t+\Delta)\gamma_{B,j}\gamma_{A,j+1} - (t-\Delta)\gamma_{A,j}\gamma_{B,j+1}\right]. \tag{1.62}$$

In the topological regime $|\mu| < |2t|$, we look at the special case $t = \Delta, \mu = 0$ where only the second term remains. As shown in Fig. 1.2, it gives rise to nearest-neighbor pairings of Majorana fermions in the bulk and on the edges, two modes $\gamma_{A,1}$ and $\gamma_{B,N}$ are decoupled from the rest of the chain. From the symmetry argument in Eq. (1.32) and Eq. (1.33), the Majorana edge mode is self-conjugate and thus pinned at zero energy $E = 0$. Switching on $t \neq \Delta$, $\mu \neq 0$, MZMs persist since the topology is protected against any continuous deformation of the Hamiltonian that does not close the bulk gap.[3] Given an ensemble of chains, it is then promising to build robust qubits out of these MZMs that are trapped at far ends.

To characterize topologically distinct phases more rigorously, we now resort to the CS invariant [69]

$$\mathrm{CS}_{2n-1}[\mathcal{A}] = \frac{1}{(n-1)!}\left(\frac{i}{2\pi}\right)^n \int_{\mathrm{BZ}^d\times\mathcal{M}^D}\int_0^1 dt\,\mathrm{Tr}(\mathcal{A}\mathcal{F}_t^{n-1}) \in \frac{1}{2}\mathbb{Z}, \tag{1.63}$$

where $2n-1 = d+D$ and $\mathcal{F}_t = td\mathcal{A} + t^2\mathcal{A}^2$. For class D, the $\mathbb{Z}_2^{(1)}$ topology is trivial unless $\mathrm{CS}_{2n-1}[\mathcal{A}]$ takes the value of a half integer. It is rather important to point out that CS_{2n-1} depends on the specific gauge chosen for the Berry connection (1.22). In other words, considering the form of the eigenfunction $|\tilde{u}_-(k)\rangle$ in Eq. (1.60) is not

[3] On the other hand, in realistic setups, as long as the length of the chain $L = Na$ becomes large enough compared to the superconducting coherence length (which remains finite in the topological phase), the overlap of the wave-functions of two MZMs can be safely ignored.

unique, the value of CS_{2n-1} is not fixed. A more well-defined quantity is given by the $U(1)$ gauge invariant Wilson loop

$$W_{2n-1} = \exp(2\pi i \mathrm{CS}_{2n-1}[\mathcal{A}]). \tag{1.64}$$

In 1D, one can simplify the integral (1.63) by incorporating particle-hole symmetry and analysing the matrix structure in real Majorana basis. First, it is easy to find the following symmetry between Berry connections [4]

$$\mathcal{A}_-^{\mu\nu}(k) = \mathcal{A}_+^{\mu\nu}(-k). \tag{1.65}$$

Accordingly,

$$\mathrm{CS}_1 = \left(\frac{i}{2\pi}\right)\int_0^\pi dk\,\mathrm{Tr}[\mathcal{A}_-(k) + \mathcal{A}_+(k)] = \left(\frac{i}{2\pi}\right)\int_0^\pi dk\,\mathrm{Tr}\,U^\dagger\partial_k U. \tag{1.66}$$

In the second equality, eigenfunctions are recast into a unitary matrix form: $U_\alpha^\mu(k) = u_\alpha^\mu(k)$ where $\alpha = \pm$ denotes the band index and $\mu = 1, 2$ encodes the dimension of the BdG Hamiltonian. From the Jacobi's formula, $\mathrm{Tr}\,U^\dagger\partial_k U = \partial_k \ln(\det U)$. One obtains the gauge invariant Wilson loop (1.64) or equivalently the Majorana number [5]

$$\mathcal{M} = W_1 = \frac{\det U(0)}{\det U(\pi)} = \mathrm{sgn}(\mathrm{Pf}[A(0)]\,\mathrm{Pf}[A(\pi)]). \tag{1.67}$$

Here, $A(k)$ denotes the real anti-symmetric matrix representation of the Hamiltonian in the Majorana basis (1.62). Owing to the $\sqrt{2}$ degeneracy of a single Majorana mode, we adopt the Fourier transform: $\gamma_j = \sqrt{2N^{-1}}\sum_k e^{ikx_j}\gamma_k$ with $\gamma_k^\dagger = \gamma_{-k}$ and $\{\gamma_k, \gamma_{k'}\} = \delta_{k,-k'}$. It leads to

$$\mathcal{H} = \frac{i}{2}\sum_k \Gamma^t(k)A(k)\Gamma(-k), \quad \Gamma(-k) = \begin{pmatrix}\gamma_{A,-k}\\ \\ \gamma_{B,-k}\end{pmatrix} \tag{1.68}$$

[4] It can be deduced by noticing $|u_-(k)\rangle$ and $|u_+(-k)\rangle$ are related to each other through the particle-hole transformation: $|u_+(-k)\rangle = \mathcal{P}|u_-(k)\rangle = \sigma^x|u_-^*(-k)\rangle$, due to $H(-k)\mathcal{P}|u_-(k)\rangle = -\mathcal{P}H(k)|u_-(k)\rangle = E_+(-k)\mathcal{P}|u_-(k)\rangle$.

[5] The final expression is related to a change of basis from Eqs. (1.42) to (1.44): $\Psi \xrightarrow{\Lambda} \gamma \xrightarrow{S^{-1}} \eta$. Hence, $\mathcal{M}$ can be calculated with the orthogonal matrix S: $\mathcal{M} = [\det S(0)]\cdot[\det S(\pi)]^{-1}$. Since $|\det S(k)| = 1$, $\mathcal{M} = \pm 1$. Moreover, in Majorana representation (1.44) the Pfaffian of the off-diagonal matrix $Q = S^T A S$ takes a positive sign: $\mathrm{Pf}[Q] = \prod_{\mu=1}^N \epsilon_\mu = \epsilon_1 > 0$. It follows that $\mathrm{sgn}(\mathrm{Pf}[S^T A S]) = \mathrm{sgn}(\mathrm{Pf}[A]\det[S]) = +1$, thus validating Eq. (1.67).

where

$$A(k) = 2i\Delta \sin k \cdot \sigma^x - i(-2t\cos k + \mu)\cdot \sigma^y. \tag{1.69}$$

The Majorana number $\mathcal{M} = \mathrm{sgn}(\mu^2 - 4t^2)$ becomes (-1) in the topological phase ($|\mu| < |2t|$) and $(+1)$ in the strong paired phase ($|\mu| > |2t|$).

An alternative interpretation of the topological invariant can be made when one imposes the time-reversal symmetry on the spinless fermion operators

$$\mathcal{T} c_j \mathcal{T}^{-1} = c_j, \quad \mathcal{T} c_j^\dagger \mathcal{T}^{-1} = c_j^\dagger. \tag{1.70}$$

In momentum space, one identifies $\mathcal{T} = \mathcal{K}, \mathcal{C} = \sigma^x$ such that the Hamiltonian (1.59) respects all three symmetries (1.3). Since $\mathcal{T}^2 = \mathcal{P}^2 = 1$, the p-wave superconducting chain now belongs to class BDI of type $\mathbb{Z}$ characterized by a winding number ν (see Fig. 1.1, Table 1.2 and Table 1.3). As along as the system holds a weak superconducting order, that is to say, the energy scale of pairing lies much below all the others ($|\Delta| \ll |t|, |\mu|$), the Majorana number can be interpreted by the winding number [4]

$$\mathcal{M} = (-1)^\nu. \tag{1.71}$$

Similar to the SSH chain, one can calculate ν from the definition (1.28) or equivalently by counting the number of gapless Fermi points over the right half of the first Brillouin zone $]0, \pi]$ when $\Delta = 0$. [6] For the topological regime $|\mu| < |2t|$, there is one gapless point in the band structure with an energy dispersion $(-2t\cos k - \mu)$. It leads to $\nu = 1$ and $\mathcal{M} = -1$. In the strong paired phase $|\mu| > |2t|$, $\nu = 0, \mathcal{M} = 1$. The result is consistent with our previous analysis of the CS invariant.

Next, we address briefly the interaction effects on MZMs [116, 117]. It gives an ideal example how the ten-fold classification of non-interacting fermions collapses. Consider an ensemble of time-reversal (TR) invariant Kitaev superconducting chains (class BDI) that are placed in parallel with left and right boundaries. Depending

[6] The other half is retrieved by the particle-hole transformation (1.3) with $\mathcal{P} = \sigma^x\mathcal{K}$: $h_{x,y}(k) = -h_{x,y}(-k), h_z(k) = h_z(-k)$.

Table 1.4: The $\mathbb{Z}_8$ classification of the BDI Majorana chains under the effects of interactions (index $\epsilon = (-1)^\nu$). The last column shows the one-to-one correspondence with respect to the Altland-Zirnbauer classes or the ten-fold way. More details can be found in Ref. [116].

ν mod 8	0	1	2	3	4	5	6	7
ϵ	+	−	+	−	+	−	+	−
a	+	+	−	−	+	+	−	−
$\mathcal{T}^2$	+	+	+	−	−	−	−	+
Cartan label	AI	BDI	D	DIII	AII	CII	C	CI

on the presence or absence of bulk gaps, there are M_f Majorana zero-energy modes dangling at each end. It corresponds to a total winding number $\nu = M_f$. Inside the Hilbert space of one chain, Majorana fermions come in pairs $(\gamma_{j,A}, \gamma_{j,B})$ by the construction from c_j and $c_j^\dagger$ (1.61). Apart from the time-reversal symmetry (1.70), an extra symmetry emerges - the fermion number parity $\mathcal{G}_f = \prod_{j=1}^N (1 - 2n_j) = \prod_{j=1}^N (-i\gamma_{j,A}\gamma_{j,B})$, under which the spinless fermionic operators transform according to

$$\mathcal{G}_f c_j \mathcal{G}_f^{-1} = -c_j, \quad \mathcal{G}_f c_j^\dagger \mathcal{G}_f^{-1} = -c_j^\dagger. \tag{1.72}$$

Thus, $[\mathcal{T}, \mathcal{G}_f] = 0$ and $\mathcal{T}^2 = \mathcal{G}_f^2 = 1$. However, if we reconstruct along one boundary the Hilbert space of complex fermions from an even number of MZMs which are no longer paired to one another, the relation between the symmetry generators $\mathcal{T}$ and $\mathcal{G}_f$ should be modified:

$$\mathcal{T}\mathcal{G}_f = a\mathcal{G}_f\mathcal{T}, \tag{1.73}$$

with $a = \pm 1$ and $\mathcal{T}^2 = \pm 1$, $\mathcal{G}_f^2 = 1$. Meanwhile, an odd number of MZMs involved lifts the degeneracy of the ground state from 1 to 2. It results in eight different topological invariants. For one-dimensional interacting systems, as shown in Table 1.4, the class BDI collapses from $\mathbb{Z}$ to $\mathbb{Z}_8$.

1.2.3 Spinless $p+ip$ superconductor

MZMs can also be realized in a spinless $p+ip$ superconductor in two dimensions, in accordance with the *bulk-edge correspondence* [118, 119]. Depending on the geometry of the defects, Table 1.5 lists the types of fermionic boundary modes related to the set of symmetry classes that we encounter throughout the thesis. Index theorem [120–124] allows one to count the number of edge modes from topological invariants of the bulk. For instance, in the presence of chiral symmetry, the topological index of a point defect in class $\mathbb{Z}$ is identical to the winding number

$$\mathrm{ind}_{\mathbb{Z}} = \nu_{2d-1}, \tag{1.74}$$

with d the dimension of the bulk. In the BDI Majorana chain, it has been shown that the $\mathbb{Z}$-topological index is non-trivial in the topological phase ($|\mu| < |2t|$) with $\nu = 1$. Besides, the emergent zero-energy Majorana bound states with fixed chirality are robust against any chiral symmetric perturbations.

When the particle-hole symmetry is the only symmetry present (for instance, in a $p+ip$ superconductor), the point defect is then embedded with a $\mathbb{Z}_2^{(1)}$-topological index. It determines the parity of MZMs around the defect and is related to the CS invariant [85]

$$\mathrm{ind}_{\mathbb{Z}_2}^{(1)} = 2\mathrm{CS}_{2d-1} \mod 2. \tag{1.75}$$

A non-trivial half-integer CS invariant thus gives rise to an odd number of MZMs. They cannot be grouped into pairs all together and are gapped out with opposite energies ($\pm\epsilon$) under particle-hole symmetric perturbations.

To see the emergence of these protected MZMs, in the following we construct explicitly a defect Hamiltonian for a $p+ip$ superconductor on a square lattice

$$H(k,r) = [-2t(\cos k_x + \cos k_y) - (\mu(r) - 4t)]\sigma^z - 2\Delta(\sin k_x \sigma^y - \sin k_y \sigma^x). \tag{1.76}$$

We adopt the same Nambu basis for spinless fermions as defined in Eq. (1.58) with 2D momentum $k = (k_x, k_y)$. Along $\hat{x}$ and $\hat{y}$ directions, the strengths of the hopping

Table 1.5: Topological defects in low dimensions with different symmetry classes. The topological dimension of defects is denoted by $d_{\text{defect}} = 0$ for a point defect and $d_{\text{defect}} = 1$ for a line defect. Adapted from Ref. [69].

d_{defect}	Symmetry	Topological classes	Edge modes	Sec.
0	AIII	$\mathbb{Z}$	chiral Dirac at $\epsilon = 0$	2.2.2
0	BDI	$\mathbb{Z}$	chiral Majorana at $\epsilon = 0$	1.2.2
0	D	$\mathbb{Z}_2^{(1)}$	Majorana at $\epsilon = 0$	1.2.3
1	D	$\mathbb{Z}$	gapless chiral Majorana	1.3.3

t and pairing Δ terms share the same form as the p-wave superconducting chain (1.57) except that on $\hat{y}$ direction the pairing channel becomes imaginary ($-i\Delta$). In our convention, when we expand the Hamiltonian (1.76) around $k^* = (0, 0)$ with an effective mass $m = 1/(2t)$,

$$H(k, r) = \vec{h}(k, r) \cdot \vec{\sigma} = \left[\frac{k^2}{2m} - \mu(r)\right] \sigma^z - 2\Delta(k_x \sigma^y - k_y \sigma^x), \tag{1.77}$$

the off-diagonal term that produces the pair $c_{-k}c_k$ reads $[-2i\Delta(k_x + ik_y)]$, referring to a $p_x + ip_y$ superconductor. The defect Hamiltonian (1.77) respects particle-hole symmetry with $\mathcal{P} = \sigma^x \mathcal{K}$ and belongs to class D.

For the moment, if we consider a uniform chemical potential $\mu(r) = \mu$ in the bulk, the topology can be clarified in a similar way as the 1D chain. Built from the eigenfunctions (1.60), the ground state has the structure $\prod_{k_x \geq 0, k_y \geq 0} (1 + \varphi(k) c^\dagger_{-k} c^\dagger_k)|0\rangle$ with a Cooper-pair wave-function $\varphi(k) = (h - h_z)/(h_x + ih_y)$. When $\mu > 0$, $|\psi(r)|$ exhibits a power-law decay r^{-1} characteristic of a weak pairing phase, whereas when $\mu < 0$, $|\psi(r)|$ decays exponentially manifesting strongly bound Cooper pairs over the space. The non-trivial topology falls into the former weakly paired regime. It is convenient to evaluate the Chern number in terms of the unit vector $\vec{n}(k) = \vec{h}(k)/h$, which represents a mapping or compactification from $T^2 = \text{BZ}^2 \times \mathcal{M}^0$ to S^2. By identifying $Q(k) = \vec{n}(k) \cdot \vec{\sigma}$, the Chern number expression (1.24) can be rewritten into

$$\text{Ch}_1 = \frac{1}{4\pi} \int dk^2 \left[\vec{n} \cdot (\partial_{k_x} \vec{n} \times \partial_{k_y} \vec{n})\right]. \tag{1.78}$$

It is easy to check $\mathrm{Ch}_1 = -1$ for $\mu > 0$ and $\mathrm{Ch}_1 = 0$ for $\mu < 0$. [7]

Next, to physically build the edge modes [14, 76, 125], we resort to the continuum limit and confine our system onto a disk as depicted in Fig. 1.3a. The chemical potential has a distribution

$$\mu(r): \quad \begin{cases} > 0, & R_1 < r < R_2; \\ < 0, & \text{otherwise.} \end{cases} \tag{1.79}$$

The shaded green annulus region corresponds to the bulk that has a non-trivial Chern number $\mathrm{Ch}_1 = -1$. When the radii of the inner circle R_1 and the outer circle R_2 become sufficiently large, the system can support two gapless chiral Majorana edge modes with opposite chirality. For a finite-size system, however, these edge modes always remain gapped. Instead of line defects, it is then reasonable to consider point defects inside the system that can be created by quantum fluxes. In Fig. 1.3a, we insert an $l \cdot \Phi$ flux to the internal trivial region ($r < R_1$) with $l \in \mathbb{Z}$ and $\Phi = hc/2e$ (h - Planck's constant) one quantum of magnetic flux. It induces a vortex with a superconducting pairing phase $\phi = 2\pi l$. Accordingly, in polar coordinates (r, θ) the pairing amplitude is changed from Δ to $\Delta e^{-il\theta}$.

By a change of variables, we can write down the Hamiltonian for the edge modes

$$\mathcal{H}_{\text{edge}} = \int dr^2 \left[-\Delta e^{-i(l-1)\theta} \psi \left(\partial_r + \frac{i}{r} \partial_\theta \right) \psi + \text{h.c.} \right] - \mu(r) \psi^\dagger \psi. \tag{1.80}$$

If one is interested in low-energy excitations around $k^* = (0, 0)$, the kinetic energy $k^2/(2m)$ can be safely neglected. Before diagonalizing the edge Hamiltonian, it is convenient to absorb the phase factor θ associated with the angular momentum by a gauge transform: $\psi \to \widetilde{\psi} = e^{-i(l-1)\theta/2} \psi$. Notably, for the new fermion field $\widetilde{\psi}$ the boundary condition has been modified

$$\widetilde{\psi}(\theta + 2\pi) = (-1)^{(l-1)} \widetilde{\psi}(\theta). \tag{1.81}$$

[7] One quick way is to look at the wrapping of $\vec{n}$ around the unit sphere S^2 when $|k|$ goes from 0 to ∞. When $|k|$ is fixed, n_x and n_y covers a circle on the sphere at a height n_z. For $\mu > 0$, by increasing $|k|$ the circle moves from the south pole to the north pole and sweeps the sphere exactly once. In contrast, for $\mu < 0$, the circle follows the trajectory: the north pole $\to$ the equator $\to$ the north pole. It results in net zero contribution to the Chern number.

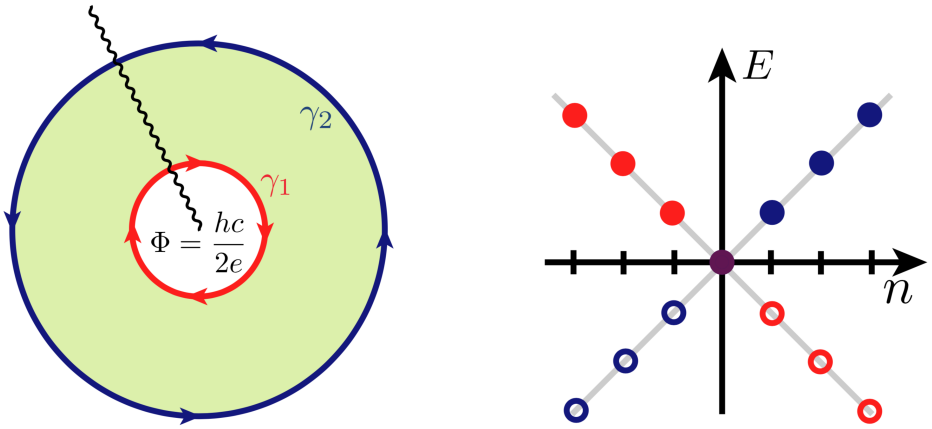

(a) (b)

Figure 1.3: (a) Geometry of a $p_x + ip_y$ superconductor on a disk. The green annulus with $\mu > 0$ denotes the topological region ($R_1 < r < R_2$). When the value of the magnetic flux threading the center region ($r < R_1$) picks an odd multiple of flux quantum $\Phi = hc/(2e)$, there arise two MZMs γ_1 and γ_2 trapped at the inner and outer edges of the disk. (b) Energy spectrum of edge modes with integer angular momentum n for the geometry of (a). From Ref. [76].

When l is odd, we keep the periodic boundary condition; otherwise, we tackle the anti-periodic boundary condition. Bearing it in mind, we then find two sets of solutions for $\mathcal{H}_{\text{edge}} = (1/2)\int dr \widetilde{\Psi}^\dagger(r) H(r) \widetilde{\Psi}(r)$. The new basis takes the form $\widetilde{\Psi}(r) = (\widetilde{\psi}_r, \widetilde{\psi}_r^\dagger)^t = \sum_n \widetilde{\Psi}_n(r)$ and

$$\widetilde{\Psi}_n(r) = \begin{cases} e^{in\theta} e^{\int_{R_1}^r dr' \mu(r')/(2\Delta)} \begin{pmatrix} 1 \\ 1 \end{pmatrix}, & r \to R_1; \\ \\ e^{in\theta} e^{-\int_{R_2}^r dr' \mu(r')/(2\Delta)} \begin{pmatrix} i \\ -i \end{pmatrix}, & r \to R_2. \end{cases} \tag{1.82}$$

The energies of these edge wave-functions read

$$E|_{r\to R_1} = \frac{2n\Delta}{R_1}, \quad E|_{r\to R_2} = -\frac{2n\Delta}{R_2}. \tag{1.83}$$

Without loss of generality, we assume $\Delta \leq 0$. The angular momentum n is subject to the boundary requirement (1.81). When l is odd, under periodic boundary condition, n takes integer values and the energy spectrum is plotted in Fig. 1.3b with red (blue) dots denoting the inner (outer) edge. For a physical state, $E \geq 0$. We

see immediately two degenerate zero-energy modes (purple dots) appearing at zero angular momentum. They correspond to two MZMs $\gamma_1 = \widetilde{\Psi}_0(R_1)$ and $\gamma_2 = \widetilde{\Psi}_0(R_2)$ localized at the edges (shown in Fig. 1.3a). Conversely, when l becomes even, n has to take half-integer values to fulfil the anti-periodic boundary condition. The degenerate modes then get separated from $n = 0$ to $n = \pm 1/2$ and acquire finite energy in the spectrum. On the edges, only two gapped chiral Majorana modes can be observed. The second scenario is consistent with the flux-free case $l = 0$.

The existence of MZMs in a $p + ip$ superconductor reveals a $\mathbb{Z}_2$ symmetry pattern associated with the vorticity l. We proceed to obtain $\mathbb{Z}_2$-topological index from the CS_3 invariant (1.75). It complements our previous analysis on more general grounds [18, 85, 125]. Consider an arbitrary Hamiltonian $H_{\mathcal{C}}(k)$ of class D in $d = 2$ endowed with non-zero Chern number $\mathcal{C} = \mathrm{Ch}_1$. When exposed to a vortex of quantum fluxes, the defect Hamiltonian can be described by

$$\widetilde{H}(k,\phi) = \begin{pmatrix} e^{-i\phi M_z/2} H_{\mathcal{C}}(k) e^{i\phi M_z/2} & 0 \\ 0 & H_{-\mathcal{C}}(k) \end{pmatrix}. \tag{1.84}$$

Here, $\phi = l \cdot \tan^{-1}(y/x)$ denotes the superconducting pairing phase that winds around the vortex by $l \cdot 2\pi$. Matrix M_z embodies the rotation around $\hat{z}$ axis perpendicular to the lattice. To make $\widetilde{H}(k,\phi)$ invariant under the transform $\phi \to \phi + 2\pi$, a slight modification of the matrix form is allowed

$$M_z = \begin{pmatrix} 2 & 0 \\ 0 & 0 \end{pmatrix} = \sigma^z + 1. \tag{1.85}$$

Meanwhile, in Eq. (1.84), a copy of the original Hamiltonian with opposite Chern number is added. On the base manifold $T^2 \times S^1$, $H_{-\mathcal{C}}(k)$ helps to cancel the weak topologies from the non-zero Chern number. The latter preclude the possibility of a global continuous basis being built for the CS invariant. By definition (1.63),

$$2\mathrm{CS}_3[\widetilde{H}(k,\phi)] = \left(\frac{i}{2\pi}\right)^2 \int_{\mathrm{BZ}^2 \times S^1} \mathrm{Tr}\left[\widetilde{\mathcal{A}} d\widetilde{\mathcal{A}} + \frac{2}{3}\widetilde{\mathcal{A}}^3\right]. \tag{1.86}$$

The Berry connection $\widetilde{\mathcal{A}}$ can be evaluated in the continuous gauge: $|\widetilde{u}(k,\phi)\rangle = e^{i\phi M_z/2}|\widetilde{u}(k)\rangle$. And $|\widetilde{u}(k)\rangle$ denotes a set of occupied states of the vortex-free Hamiltonian. Taking into account that $\widetilde{H}(k,\phi=0)$ hosts total zero Chern number, the integral (1.86) can be simplified to [8]

$$2\mathrm{CS}_3[\widetilde{H}(k,r)] = \left(\frac{i}{2\pi}\right)^2 \int_{\mathrm{BZ}^2\times S^1} (-i)\,\mathrm{Tr}\left[\mathcal{F}[H_{\mathcal{C}}(k)]\right] \wedge d\phi = \mathrm{Ch}_1 \times l. \tag{1.87}$$

We get a topological index: $\mathrm{ind}^{(1)}_{\mathbb{Z}_2} = \mathrm{Ch}_1 \times l \mod 2$. For a $p_x + ip_y$ superconductor, $\mathrm{Ch}_1 = -1$. The parity of the localized MZMs is then equal to the parity of the vorticity l of quantum fluxes.

1.3 Kitaev spin liquids

In this section, we address a new type of topological states accompanied by an emergent Ising gauge field - Kitaev spin liquids [18]. At low temperatures, the gauge field is deconfined and takes the value 0 or 1 belonging to the group $\mathcal{Z}_2$. [9] The ground state wave functions are captured by a matter Majorana field associated to an energy spectrum which can be either gapped or gapless. Corresponding excitations exhibit the mutual statistics of Abelian and non-Abelian anyons. Another important feature of the model is revealed in the presence of a uniform magnetic field. The intermediate gapless phase becomes gapped and carries a non-zero spectral Chern number. It gives rise to a gapless chiral Majorana edge mode with central charge $c = 1/2$ and is responsible for a half-integer thermal Hall effect.

Historically, the concept of quantum spin liquids (QSLs) was first introduced by Anderson in 1973 as a possible ground state for the spin-1/2 Heisenberg antiferro-

[8] It follows that $\widetilde{\mathcal{A}} = \langle\widetilde{u}(k)|d|\widetilde{u}(k)\rangle = \widetilde{\mathcal{A}}^0 + iQd\phi$ with $\widetilde{\mathcal{A}}^0$ the Berry connection of $\widetilde{H}(k,\phi=0)$ and $2Q = \langle\widetilde{u}(k)|M_z|\widetilde{u}(k)\rangle$. Inside the integral, due to exactly opposite contributions from $H_{\pm\mathcal{C}}(k)$ parts that do not involve $d\phi$ all vanish. It leads to $\mathrm{Tr}[\cdots] = (-i)\,\mathrm{Tr}[2Q\widetilde{\mathcal{F}}^0 - d(Q\widetilde{\mathcal{A}}^0)] \wedge d\phi$. Here, the Berry curvature reads $\widetilde{\mathcal{F}}^0 = d\widetilde{\mathcal{A}}^0 + (\widetilde{\mathcal{A}}^0)^2$. The total derivative in the trace can be further discarded. Upon integration, by particle-hole symmetry M_z in Eq. (1.85) is equivalent to an identity matrix in the subspace of $H_{\mathcal{C}}(k)$. Hence, $2Q$ matrix projects $\widetilde{\mathcal{F}}^0$ onto $\mathcal{F}[H_{\mathcal{C}}(k)]$ the Berry curvature of the original copy.

[9] We choose a different character to distinguish it from the type $\mathbb{Z}_2$ on the classification Table 1.2.

magnet on a triangular lattice [62]. Similar to classical spin liquids in frustrated magnets [16, 17], the system preserves spin rotational symmetry. But it also shows long-range entanglement through resonating valence bonds (RVBs). Later, Anderson brought the idea of RVB to life as a hidden mechanism for undoped high-T_c cuprate superconductors [38]. If Anderson's postulate is true, doping a QSL material with electrically charged holes would induce superconductivity. Since then, intensive efforts in the pursuit of QSLs in Mott insulators have been realized. The spins are confined in periodic crystals and become quantum via short-ranged interactions. Although Anderson's initial hypothesis of a QSL ground state on the triangular lattice remains hard to prove [126], in 2006 Kitaev found an exact solution to a $\mathcal{Z}_2$ QSL on the honeycomb lattice. Symmetric Heisenberg exchanges are reduced to three nearest-neighbour anisotropic Ising interactions. Most encouragingly, the model can potentially describe a variety of quantum materials including iridates and α-$RuCl_3$ [127–129]. In Section 1.4.2, we will give a short review of current theoretical and experimental progresses on the material α-$RuCl_3$.

1.3.1 Exact spectrum and phase diagram

We begin with the phase diagram of the spin-1/2 Kitaev honeycomb model. As depicted in Fig. 1.4, the lattice Hamiltonian takes the form

$$\mathcal{H} = -\sum_{\langle ij\rangle_\mu} J_\mu \sigma_i^\mu \sigma_j^\mu, \quad \mu = x, y, z. \tag{1.88}$$

Here, we assume three ferromagnetic Ising couplings $J_\mu > 0$. The subscript $\langle ij\rangle_\mu$ represents two nearest-neighbour sites, forming a bond each assigned with one of the three Ising interactions. Without loss of generality, for each bond $\langle ij\rangle_\mu$, we fix the convention $i \in \{1\}$ that belongs to the odd sublattice and $j \in \{2\}$ the even sublattice. The periodic boundary conditions are imposed on both $\hat{x}$ and $\hat{y}$ directions. The system has $N = N_x N_y$ plaquettes and $3N$ bonds.

The ground state can be solved in a redundant Majorana fermion representation

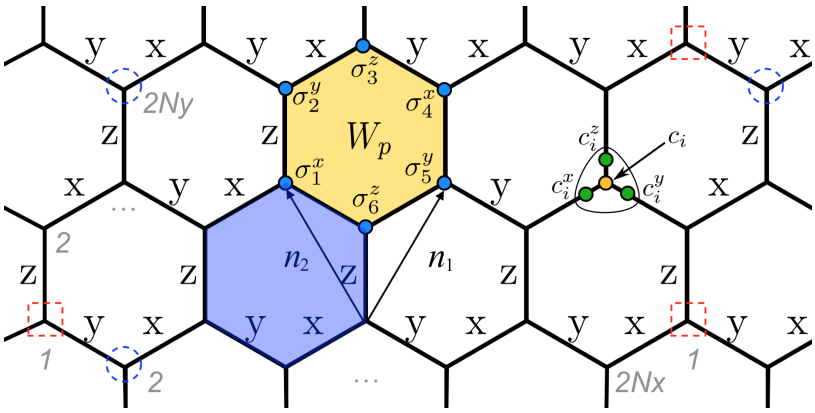

Figure 1.4: Geometry of Kitaev honeycomb lattice. Each spin operator σ_i^μ is mapped to three gauge (c_i^μ) and one matter (c_i) Majorana fermions. We impose periodic boundary conditions on $\hat{x}$ and $\hat{y}$ directions with a total number of plaquettes $N = N_x N_y$. Dashed red rectangles (blue circles) on the boundaries denote equivalent sites that belong to the odd (even) sublattice. Adapted from Ref. [16] and Ref. [130].

[18, 55]. Let us denote the two-dimensional physical spin space as $\mathfrak{L}$. A fermionic parton construction

$$\sigma_j^\mu = i c_j c_j^\mu \tag{1.89}$$

would map each spin onto four Majorana fermions with the latter living in a four-dimensional Fock space $\mathfrak{F}$. Implementing anti-commutation relations for Majorana fermions $\{c_i, c_j\} = 2\delta_{ij}$ and $\{c_i^\mu, c_j^\nu\} = 2\delta_{ij}\delta_{\mu\nu}$, the SU(2) Lie algebra of spin operators $[\sigma_i^\mu, \sigma_j^\nu] = 2i\epsilon^{\mu\nu\rho}\sigma^\rho\delta_{ij}$ is respected if and only if

$$D_j = c_j c_j^x c_j^y c_j^z \equiv 1. \tag{1.90}$$

Apparently, $(D_j)^2 = 1$ and $[D_j, \mathcal{H}] = 0$. The D_j operator can only take the value of ± 1. It then defines a projector from the enlarged Fock space $\mathfrak{F}$ to the physical space $\mathfrak{L}$

$$\mathcal{P} = \prod_j \frac{1 + D_j}{2}. \tag{1.91}$$

By the mapping (1.89), the Hamiltonian turns into

$$\mathcal{H} = i \sum_{\langle ij \rangle_\mu} J_\mu c_i c_j \cdot \hat{u}_{\langle ij \rangle_\mu}, \qquad \hat{u}_{\langle ij \rangle_\mu} = i c_i^\mu c_j^\mu. \tag{1.92}$$

To clarify different degrees of freedom, it is convenient to introduce two types of complex bond fermions: one chosen on each z-bond and the other covering all three bonds

$$\psi_{\langle ij\rangle_z} = \frac{1}{2}(c_i + ic_j), \qquad \chi_{\langle ij\rangle_\mu} = \frac{1}{2}(c_i^\mu - ic_j^\mu). \tag{1.93}$$

Similar to the case of the p-wave superconducting chain (1.61), both of them are constructed from a pair of Majorana fermions. The difference lies in the fact that at low temperatures, the energy spectrum of the model is purely determined by the matter fermion $\psi_{\langle ij\rangle_z}$. Gauge fermions $\chi_{\langle ij\rangle_\mu}$ remain in the ground state as a reflection of the static $\mathcal{Z}_2$ gauge field.

Now, one can proceed to fix the gauge structure by identifying all non-dynamical observables [130]. First, it is easy to notice $(\hat{u}_{\langle ij\rangle_\mu})^2 = 1$ and $[\hat{u}_{\langle ij\rangle_\mu}, \mathcal{H}] = 0$. Operators $\hat{u}_{\langle ij\rangle_\mu} = 1 - 2\chi^\dagger_{\langle ij\rangle_\mu}\chi_{\langle ij\rangle\mu}$ thus take the value $+1$ or -1 corresponding to the vacuum or excited state of gauge fermions. Then based on them, a set of loop operators $\{W_L | L = p, x, y\}$ that commute with the Hamiltonian

$$W_L = \prod_{\langle ij\rangle_\mu \in L} \sigma_i^\mu \sigma_j^\mu = \pm 1 \tag{1.94}$$

can be constructed

$$\begin{aligned} W_p &= \sigma_1^x\sigma_2^y\sigma_3^z\sigma_4^x\sigma_5^y\sigma_6^z = \prod_{\langle ij\rangle_\mu \in p} \hat{u}_{\langle ij\rangle_\mu}, \\ W_x &= -\sigma_1^z\sigma_2^z\cdots\sigma_{2N_x}^z, \quad W_y = -\sigma_2^y\sigma_3^y\sigma_4^x\sigma_5^x\cdots\sigma_{2Ny-2}^y\sigma_{2N_y-1}^y\sigma_{2N_y}^x\sigma_1^x. \end{aligned} \tag{1.95}$$

Here, subscripts $L = p, x, y$ denote the loops that encircle hexagon plaquettes and two edges along $\hat{x}$ and $\hat{y}$ directions (see Fig. 1.4). On one hand, taking into account the global constraint $\prod_p W_p = 1$, in total $\{W_L\}$ contributes to $(N+1)$ flux degrees of freedom. The rest $(2N-1)$ flux degrees of freedom that belong to gauge fermions χ are compensated by gauge transformations D_j. Since $c_i^\mu = \chi_{\langle ij\rangle_\mu} + \chi^\dagger_{\langle ij\rangle_\mu}$ for $i \in \{1\}$ and $c_j^\mu = i(\chi_{\langle ij\rangle_\mu} - \chi^\dagger_{\langle ij\rangle_\mu})$ for $j \in \{2\}$, each D_j operator changes the occupation number of three associated gauge fermions or equivalently the sign of $u_{\langle ij\rangle_\mu}$'s. Consequently, the

flux states of three neighbouring plaquettes are flipped by D_j from W_p to $-W_p$. It should be noted that the global gauge transformation $D = \prod_j D_j$ flips every plaquette twice and leaves the flux pattern of the lattice unaffected. Therefore, one extra flux degree of freedom should be subtracted from $2N$ D_j operators. On the other hand, if one goes back to the physical space $\mathfrak{L}$ hosting $2N$ spins, after the projection (1.91) all D_j's are frozen to $+1$. It means apart from $(N+1)$ independent loop operators W_L, the remaining $(N-1)$ spin degrees of freedom are restored exclusively by bond matter fermions ψ. One missing constraint on ψ can be found in the following argument:[10] for any physical state in $\mathfrak{L}$, the global gauge transformation satisfies $D = (-1)^{N_\psi + N_\chi} \equiv 1$. In other words, the total number of matter and gauge fermions $(N_\psi + N_\chi)$ should always be even.

The advantage of the Majorana representation (1.89) is revealed in the ground state configuration of the flux sector that is frozen to the 0-flux:

$$W_p = \prod_{\langle ij \rangle_\mu \in p} \hat{u}_{\langle ij \rangle_\mu} = 1, \quad \forall p. \tag{1.96}$$

And we call an excited plaquette ($W_p = -1$) the π-flux. The conservation of the loop operators can be proven by Lieb's theorem using translational invariance [131]. If one views the variables $u_{\langle ij \rangle_\mu} = \pm 1$ as a $\mathcal{Z}_2$ gauge field, it is natural to interpret W_p as the magnetic flux on a plaquette p. Lieb's theorem then states that for a half-filled band of electrons that hop on a bipartite lattice in dimension d with periodicity on at least $(d-1)$ directions, the magnetic flux pattern for the minimal ground state energy is fixed. The optimal configuration should be 0-flux per planar cell containing 2 (mod 4) sites (*e.g.* the hexagonal lattice) and π-flux per planar cell containing 0 (mod 4) sites (*e.g.* the square and cubic lattices). For the Kitaev honeycomb model, the vortex-free configuration (1.96) can also be verified by performing a perturbation theory in the deep gapped phases (1.104) or by numerical computation of the energy spectrum on

[10] By definition (1.93), $(-1)^{N_\psi} = \prod_{i \in \{1\}} (1 - 2\psi^\dagger_{\langle ij \rangle_z} \psi_{\langle ij \rangle_z}) = \prod_{\langle ij \rangle_z} (-ic_i c_j)$ and $(-1)^{N_\chi} = \prod_{\langle ij \rangle_\mu} (ic_i^\mu c_j^\mu)$.

a finite-size lattice [11] for the gapless phase [18]. Later in Section 4.1, we will apply Lieb's theorem to solve the phase diagram of a generalized Kitaev square ladder where a π-flux phase is stablized in the ground state.

After identifying conserved loop variables W_p, we are now left with combined $(N+1)$ degrees of freedom in the matter sector ψ and the remaining flux sectors $W_{x,y}$. A convenient way to fulfill 0-flux per plaquette is to set

$$\hat{u}_{\langle ij\rangle_\mu} = u_{\langle ij\rangle_\mu} = 1, \quad \forall i \in \{1\}, \quad \mu = x, y, z. \tag{1.97}$$

This artificial gauge choice respects translational symmetry and allows us to perform Fourier transform of the quadratic Hamiltonian (1.92) in terms of matter Majorana fermions c. One arrives at

$$\mathcal{H} = \frac{1}{2}\sum_k \begin{pmatrix} c_{1,-k}, & c_{2,-k} \end{pmatrix} \begin{pmatrix} 0 & if(\vec{k}) \\ -if^*(\vec{k}) & 0 \end{pmatrix} \begin{pmatrix} c_{1,k} \\ c_{2,k} \end{pmatrix}, \tag{1.98}$$

with the function $f(\vec{k}) = 2(J_x e^{-i\vec{k}\cdot\vec{n}_1} + J_y e^{-i\vec{k}\cdot\vec{n}_2} + J_z)$. Equivalently, through the mapping (1.93) one can go to the representation of bond matter fermions $\psi_{\langle ij\rangle_z}$. From now on, we neglect the subscript $\langle ij\rangle_z$ in the matter sector. In the complex bond fermion basis,

$$\mathcal{H} = \frac{1}{2}\sum_k \Psi_k^\dagger H(k) \Psi_k, \quad \Psi_k = \begin{pmatrix} \psi_k \\ \psi_{-k}^\dagger \end{pmatrix}, \tag{1.99}$$

the BdG Hamiltonian takes the form

$$H(k) = \vec{h}(k)\cdot\vec{\tau} = \mathrm{Re}\, f(\vec{k})\cdot\tau^z + \mathrm{Im}\, f(\vec{k})\cdot\tau^y. \tag{1.100}$$

As is shown in Fig. 1.4, two unit vectors are chosen in coordinates of the xy-plane: $\vec{n}_1 = (1/2, \sqrt{3}/2), \vec{n}_2 = (-1/2, \sqrt{3}/2)$. In the absence of a magnetic field, the Hamiltonian respects time reversal and particle-hole symmetries: $\mathcal{T} = \mathcal{K}$, $\mathcal{P} = \tau^x\mathcal{K}$. From

[11] It is found in Ref.[18] that on a torus with $J_x = J_y = J_z = 1/3$, the vortex-free pattern produces a ground state energy $E_0 = -1.5746$ per unit cell. Adding an isolated vortex increases the energy by an amount $E_{\mathrm{vortex}} = 0.1536$.

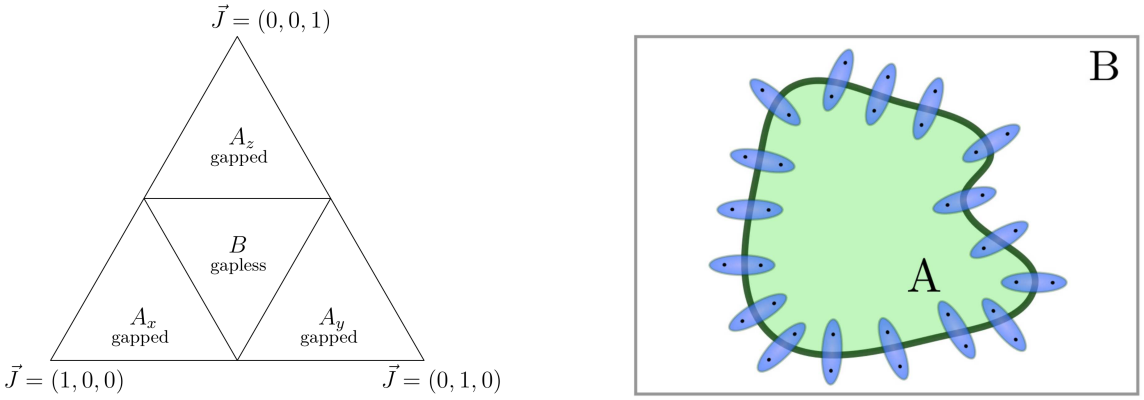

Figure 1.5: (a) Phase diagram of the Kitaev honeycomb model [55] with ferromagnetic Ising couplings $\vec{J} = (J_x, J_y, J_z)$. Unless pointed out explicitly, throughout the text we assume $\sum_\mu J_\mu = 1$. (b) Bipartition of the honeycomb lattice into subregions A and B [16]. An area law scaling of entanglement entropy in subsystem A persists in all phases, mainly influenced by the domain wall contribution. The topological entanglement entropy, a universal negative correction, comes from entangled gauge flux pairs across the domain wall.

the energy spectrum $E_\pm(k) = \pm|f(\vec{k})|$, one finds a gapless spin liquid B phase in the following parameter regime

$$|J_\mu| \leq |J_\nu| + |J_\rho|, \tag{1.101}$$

where (μ, ν, ρ) involve all permutations of (x, y, z). Otherwise, the phases become gapped with a tendency to form dimers in alignment with the largest Ising coupling. On the phase diagram drawn in Fig. 1.5a, they are denoted as A_x, A_y, A_z. In particular, for these gapped spin liquid phases, there are four degenerate ground states living on the base manifold $T^2 = \mathrm{BZ}^2 \times \mathcal{M}^0$. It agrees with two types of topologically distinct loops on a torus. In principle, one can also diagonalize the Hamiltonian directly in real space. In that case, the fourfold degeneracy is manifested in the flux sector $W_{x,y} = \pm 1$.

We go on to elucidate the spin liquid nature of the ground state in all phases. Formally, the wave function of QSLs can not be disentangled to a product state under a finite set of local unitary transformations. To put it another way, there is

long-range entanglement between two quantum spins [17]. One explicit approach to quantify this property is to study the entanglement entropy. In Fig. 1.5b, a generic quantum system is decomposed into two parts $A \cup B$. The entanglement in subsystem A can be measured by the von Neumann entropy [132]

$$\mathcal{S}_A = -\mathrm{Tr}\rho_A \ln \rho_A, \tag{1.102}$$

where $\rho_A = \mathrm{Tr}_B \rho$ represents the reduced density matrix of subregion A. For the Kitaev honeycomb model, it has been found that the entanglement entropy consists of two pieces arising from the gauge field (G) and the matter fermion sector (F) [133]: $\mathcal{S}_A = \mathcal{S}_G + \mathcal{S}_F$. Different contributions read

$$\mathcal{S}_G = (L-1)\ln 2, \quad \mathcal{S}_F = \alpha_{\mathcal{S}} L + \mathcal{O}(1). \tag{1.103}$$

Now we take the thermodynamic limit $L \to \infty$, in the matter part $\mathcal{O}(1) \to 0$ and only the area law growth survives. For the $\mathcal{Z}_2$ gauge field, however, it further produces a universal negative topological correction $\mathcal{S}_{\mathrm{top}} = -\ln 2$. It is nothing but a direct consequence of the long-range entanglement [16]. If the ground state can be reduced to a disentangled product state, the area law contribution would completely vanish. The entanglement entropy then becomes negative due to $\mathcal{S}_{\mathrm{top}}$. It is in contradiction to the definition of entanglement entropy (1.102): $\mathcal{S}_A \geq 0$ with $\rho_A \in]0, 1]$.

1.3.2 Abelian anyons in the gapped phases

Next, we can explore the excitations above the ground state configuration. The emergent quasi-particles behave as Abelian and non-Abelian anyons in the gapped and gapless phases [18]. Anyons are particles defined in (2+1)-dimensional quantum systems with non-trivial mutual statistics [15, 134]. Suppose we move one particle counterclockwise around the other, the total wave function would pick up a phase from the winding of the trajectory: $\psi(r_1, r_2) \to e^{2i\theta}\psi(r_1, r_2)$. In one or higher dimensions [135, 136], the phase becomes topologically trivial: $e^{2i\theta} = 1$. In two dimensions,

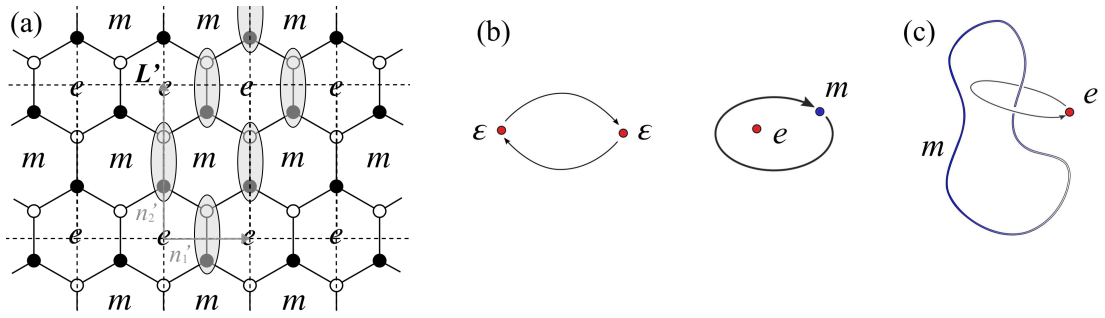

Figure 1.6: (a) Dimers on the strong z-links form an effective spin lattice $\mathcal{L}'$ (dashed lines). After spin rotations (1.106) that break the translational symmetry, the effective Hamiltonian is mapped to a two-dimensional toric code. In the original honeycomb lattice $\mathcal{L}$, excited vortices behave as e- and m-type of anyons and are assigned to the hexagon plaquettes in even and odd rows. Adapted from Ref. [18]. (b) Illustration of statistics of Abelian anyons in the toric code: self-exchange of two fermions ϵ and double exchange of two bosons e and m. Both processes bring a π-phase shift in the wave function. (c) In three dimensions, the excitation of magnetic particles m becomes a closed loop. Adapted from Ref. [16].

however, it can take an arbitrary value. When $\theta = 0$ or π, the particles carry the statistics of bosons or fermions; otherwise, one obtains anyons with exchange phase 2θ [134]. Distinct topological classes of the trajectories among N particles are described by braid group $\mathcal{B}_N$. The multiplication of group elements can be commutative or not, referring to the Abelian or non-Abelian nature.

Let us first illustrate the Abelian anyonic excitations in gapped phases. For simplicity, we look at the deep A_z phase with ferromagnetic Ising couplings $J_z \gg (J_x, J_y) \geq 0$. At $J_x = J_y = 0$, the ground state becomes decoupled dimers covering all z-bonds. It is then convenient to map the dimer configuration onto an effective spin space: $\Upsilon|mm\rangle_{\langle ij\rangle_z} = |m\rangle_{\langle ij\rangle_z}$ with $m = \uparrow, \downarrow$. Depicted in Fig. 1.6a, the effective spins reside on the bonds of a dual rectangular lattice $\mathcal{L}'$ expanded by unit vectors $\vec{n}'_1 = \vec{n}_1 - \vec{n}_2$ and $\vec{n}'_2 = \vec{n}_1 + \vec{n}_2$. When $(J_x, J_y) > 0$, the dimers start to resonate with each other. These weak Ising couplings can be treated as small perturbations. In the physical spin space, it leads to an effective Hamiltonian [18] that consists of loop operators

(1.95):

$$\mathcal{H}_{\text{eff}}^{(4)} = -\frac{(J_x J_y)^2}{16 J_z^3} \sum_p W_p. \tag{1.104}$$

Indeed, to minimize the energy a vortex-free phase is favored: $W_p = 1, \forall p$. It is consistent with Lieb's theorem. Interestingly, after the projection to the effective spins

$$W_p' = \Upsilon W_p \Upsilon^{-1} = \sigma^y_{\text{left}(p)} \sigma^y_{\text{right}(p)} \sigma^z_{\text{up}(p)} \sigma^z_{\text{down}(p)}, \tag{1.105}$$

one recovers the two-dimensional toric code [137]

$$\mathcal{H}_{\text{eff}}' = -K_{\text{eff}} \sum_{p \in \mathcal{L}} U W_p' U^{-1} = -K_{\text{eff}} \left[\sum_{s \in \mathcal{L}'} A_s + \sum_{p \in \mathcal{L}'} B_p \right], \tag{1.106}$$

with $K_{\text{eff}} = (J_x J_y)^2/(16 J_z^3) > 0$. Here, U stands for a set of successive spin rotations[12] that helps realize the effective operators in the toric code:

$$A_s = \prod_{i \in s} \sigma_i^x, \qquad B_p = \prod_{i \in p} \sigma_i^z. \tag{1.107}$$

In the dual lattice $\mathcal{L}'$ shown in Fig. 1.6a, A_s acts on four effective spins surrounding the vertex s and B_p selects its spin components on the bonds of the rectangular plaquette p. The ground state of the effective Hamiltonian (1.106) favors $A_s = B_p = +1$. Excitations that flip the signs of A_s's and B_p's are called electric charges (e) and magnetic vortices (m) respectively. They are bosons and live on the even and odd rows of the hexagonal plaquettes that belong to the original lattice $\mathcal{L}$ (see Fig. 1.6a). On account of the global flux constraint $\prod_{p \in \text{odd}} W_p \cdot \prod_{p' \in \text{even}} W_{p'} = 1$, the total number of the excitations $(N_e + N_m)$ should be even. Meanwhile, another global constraint $D = (-1)^{N_\psi + N_\chi} = 1$ translates into $\prod_{p \in \text{odd/even}} W_p = \prod_{\langle ij \rangle_z} \sigma_i^z \sigma_j^z$.[13] These global

[12] It is easy to check a natural choice of U in our setting would be $U = \prod_{j \in \perp} R_1(j) \cdot \prod_{j \in \parallel} R_2(j) R_3(j)$. Along the vertical direction ($\perp$) of the plaquette $p \in \mathcal{L}'$ (or the up and down sides), for each spin we perform a rotation $R_1(j) = e^{i\pi\sigma_j^z/4}$. Switching to the remaining horizontal direction ($\parallel$, or the left and right sides), two rotations $R_2(j) = e^{-i\pi\sigma_j^x/4}$ and $R_3(j) = e^{-i\pi\sigma_j^y/4}$ are combined onto each spin. In this way, U explicitly breaks the translational symmetry.

[13] One notices $\prod_{p \in \text{odd}} W_p = \prod_{p \in \text{even}} W_p = (-1)^{N_\chi^x + N_\chi^y}$ and $\prod_{\langle ij \rangle_z} \sigma_i^z \sigma_j^z = \prod_{\langle ij \rangle_z} (i c_i^z c_j^z)(-i c_i c_j) = (-1)^{N_\chi^z + N_\psi}$.

constraints ensure that anyonic excitations of e- and m-type are robust against local perturbations [130].

Then, we can address the braiding rule between these quasiparticles. It is revealed in the double exchange process drawn in Fig. 1.6b (right): moving one m-particle around one e-particle acquires a negative sign in the wave function. Suppose we put a pair of e and m particles on the neighboring plaquettes, denoted by the yellow and blue hexagons in Fig. 1.4. To move m-particle (blue) upward, one starts with the local operation $\sigma_1^x = ic_1c_1^x$ that reverses the signs of loop operators in two neighboring plaquettes sharing the x-link. A trajectory of m-particle encircling e-particle can be completed by operations $\sigma_6^z\sigma_5^y\sigma_4^x\sigma_3^z\sigma_2^y\sigma_1^x$, which is nothing but the loop operator W_p associated with e-particle (yellow). As $W_p = -1$, the sign change in the wave function is recovered. In addition, two anyons can be combined to form a different type of anyon through the fusion channels [15]: $\phi_\mu \times \phi_\nu = N_{\mu\nu}^\rho \phi_\rho$. Non-Abelian anyons hold multiple fusion channels, whereas for the Abelian anyons in the toric code there is only one fusion channel. It follows [18]

$$e \times m = \epsilon, \quad e \times e = m \times m = \epsilon \times \epsilon = 1. \tag{1.108}$$

Here, 1 stands for the vacuum state and ϵ represents a new composite particle from the combination of e and m. It is easy to check ϵ becomes fermionic under self-exchange depicted in Fig. 1.6b (left). Seeing as $4K_{\text{eff}} \ll 2J_z$ in the honeycomb model, the reverse process could happen upon thermalization: $\epsilon \to e + m$. Excited fermions in the superselection sector ϵ may decay into em-pairs with the help of a zero-temperature bath. It provides one potential approach to implementing the Abelian anyons [18]. Finally, it might be useful to compare with higher-dimensional analogues, for instance, the 3D toric code [16]. On a cubic lattice, A_s acts on the six bonds connected by the vertex s and B_p keeps the same form (1.107) involving plaquettes in all three planes (xy, yz, zx). In this setting, while e-particle remains pointlike, m-particle turns into a closed loop. As shown in Fig. 1.6c, the braiding

between them still accumulates a π-phase shift.

1.3.3 Non-Abelian anyons in the B phase with a magnetic field

Excitations of vortices in the B spin liquid phase, however, are not well defined due to the gapless spectrum of Majorana fermions. Intuitively, by analogy to the 2D Haldane model [21], one can open the fermion gap by introducing a time reversal symmetry breaking term. Starting from the gauge sector (1.97) initially chosen for the gapless spectrum, we would like to derive an effective Hamiltonian for the matter sector with the gauge field unchanged under small perturbations. We call the excitation of the gauge sector a *vison* of which the energy scale is assumed to be much larger than that of a matter Majorana fermion: $\Delta_v \gg \Delta_f$. In the Majorana representation, it requires a little more attention to fix the gauge of the $\mathcal{T}$ operator. We would like to show that the following transformation rule suffices [18]

$$\mathcal{T} c_j \mathcal{T}^{-1} = (-1)^j \cdot c_j, \quad \mathcal{T} c_j^\mu \mathcal{T}^{-1} = (-1)^j \cdot c_j^\mu, \tag{1.109}$$

where $(-1)^j = -/+$ for $j \in \{1\}/\{2\}$ that belongs to the odd/even sublattices. First, it allows a physical spin-1/2 to change its sign under $\mathcal{T}$:

$$\mathcal{T} \sigma_j^\mu \mathcal{T}^{-1} = \mathcal{T}(i c_j c_j^\mu)\mathcal{T}^{-1} = -\sigma_j^\mu. \tag{1.110}$$

Then for the vortex-free gauge sector, the six-spin loop operator W_p and variables $u_{\langle ij\rangle_\mu} = -ic_i^\mu c_j^\mu = +1$ are all $\mathcal{T}$-invariant. It implies that the spectral gap in the matter sector will not be opened by any perturbation that respects time reversal symmetry. In fact, the effective term that can induce a gap should come from the diagonal part in Hamiltonian (1.98): ic_ic_j where i and j belong to the same bipartite lattice. Indeed, it breaks time reversal symmetry with our convention (1.109): $\mathcal{T} ic_ic_j\mathcal{T}^{-1} = -ic_ic_j$.

In the phase diagram of Fig. 1.5a, we now look at the most simple case for the B phase: $J_x = J_y = J_z = J$. The effective interactions can be derived from an arbitrary

external magnetic field

$$\mathcal{V} = \sum_j h_\mu \sigma_j^\mu, \tag{1.111}$$

with $|h_\mu| \ll J, \mu = x, y, z$. Obviously, $\mathcal{H}_{\text{eff}}^{(1)} = 0$. The pair of π fluxes it creates is prohibited by the background of frozen $\mathcal{Z}_2$ vortices [138]. The surviving second order term $\mathcal{H}_{\text{eff}}^{(2)} \sim \sum_{\langle ij\rangle_\mu} -(h_\mu^2/J)\sigma_i^\mu \sigma_j^\mu$ is $\mathcal{T}$-invariant, leaving the spectrum gapless.[14] The leading order effective interaction comes from the $\mathcal{T}$-breaking cubic terms

$$\mathcal{H}_{\text{eff}}^{(3)} = -\kappa \sum_{\langle\langle ik\rangle\rangle} \sigma_i^\mu \sigma_j^\nu \sigma_k^\rho, \tag{1.112}$$

where $\kappa \sim h_x h_y h_z / J^2$ and $\langle\langle ik\rangle\rangle$ describes next-nearest neighbors i and k connected by site j. The orientations of spins σ_i^μ and σ_k^ρ follow the directions of Ising couplings on bonds $\langle ij\rangle_\mu$ and $\langle jk\rangle_\rho$. And the third spin σ_j^ν satisfies $\nu \neq \mu \neq \rho$. It can be checked that all intermediate π fluxes are annihilated under $\mathcal{H}_{\text{eff}}^{(3)}$ and the gauge sector remains vortex-free. In the Majorana picture, the effective interaction (1.112) enters into the BdG form (1.100) as

$$H(k) = \text{Re}\, f(\vec{k}) \cdot \tau^z + \text{Im}\, f(\vec{k}) \cdot \tau^y + g(\vec{k}) \cdot \tau^x, \tag{1.113}$$

with the function $g(\vec{k}) = -4\kappa(\sin(\vec{k}\cdot\vec{n}_1) + \sin[\vec{k}\cdot(\vec{n}_2 - \vec{n}_1)] - \sin(\vec{k}\cdot\vec{n}_2))$. Since $\mathcal{T}[g(\vec{k})\cdot\tau^x]\mathcal{T}^{-1} = -g(-\vec{k})\cdot\tau^x$, the time reversal symmetry is broken. The perturbed Hamiltonian falls into class D same as the spinless $p+ip$ superconductor in Section 1.2.3. The $\mathbb{Z}$-classified bulk topology is captured by the first Chern number (1.78). Taking into account $|\kappa| \ll J$, one can reach the defect Hamiltonian by performing an expansion around two original Dirac points $\pm\vec{k}^* = \mp(4\pi/3, 0)$,

$$H(k,r)|_{\pm\vec{k}^*} = \vec{R}(k,r)\cdot\vec{\tau} = -\sqrt{3}Jk_y\cdot\tau^y \pm \sqrt{3}Jk_x\cdot\tau^z \pm 6\sqrt{3}\kappa(r)\cdot\tau^x. \tag{1.114}$$

Here, the range of the small momentum is defined as $\delta k = (k_x, k_y) = \vec{k} - (\pm\vec{k}^*)$ and $|\delta k| \in \Omega(0,1)$. Clearly, the topologically distinct phases are characterized by the sign

[14] The Ising couplings in the energy spectrum $E_\pm(k) = \pm|f(\vec{k})|$ are slightly modified by the perturbation: $J_\mu \to J_\mu + \alpha h_\mu^2/|J|$. Under such smooth deformation of the topological Hamiltonian, the gapless Dirac points are protected.

of the mass term $m\Gamma_0(r) = \pm 6\sqrt{3}\kappa(r) \cdot \tau^x$. After a rotation of basis $(\tau^x, \tau^y, \tau^z) \to (\tau'^z, \tau'^x, \tau'^y)$, not surprisingly the defect Hamiltonian shares a similar form with that of the $p + ip$ superconductor (1.77):

$$H'(k,r)|_{\pm\vec{k}^*} = \vec{R}'(k,r) \cdot \vec{\tau'} = \pm\sqrt{3}\left[6\kappa(r) \cdot \tau'^z + J(k_x \cdot \tau'^y \mp k_y \cdot \tau'^x)\right]. \tag{1.115}$$

In the same manner, one can count the Chern number of the bulk $\kappa(r) = \kappa$ straightforwardly [15]

$$\mathrm{Ch}_1 = \mathrm{sgn}(\kappa) = \pm 1. \tag{1.116}$$

In three gapped Abelian phases, the first Chern number remains zero.

From the bulk-boundary correspondence, we proceed to study the topological line defect in Table 1.5, namely, the gapless chiral Majorana edge mode. In contrast to the gapless chiral Dirac mode in integer quantum Hall (QH) fluids [22, 139–141], the neutral particle cannot form an electric current at zero temperature. Yet at low temperatures, the Majorana mode carries an anomalous energy current. It leads to a quantized thermal Hall response [18, 142–144]. By analogy to the quantum Hall effect (QHE) [19], we put the honeycomb lattice on the xy plane and analyse the transverse thermal conductivity. Along the horizontal x direction, the forward propagating matter fermion mode ψ_k induces an energy current with positive momentum k and positive energy $\epsilon(k)$. The corresponding back propagating mode ψ_{-k} then gives an equal contribution to the current implied by the particle-hole symmetry: $\epsilon(k) = -\epsilon(-k)$. On the vertical y direction, the net energy current dI_x is driven by a transverse temperature difference dT_y. The ratio of them defines the thermal Hall

[15] One should add contributions from two Dirac points. In the neighborhood of $(\pm\vec{k}^*)$, the mapping from a torus to a sphere is described by unit vector $\vec{n}(k) = \vec{R}'(k)/R'$. For $0 < \kappa \ll J$, when $|\delta k|$ increases from 0 to 1, the mapping $\vec{n}(k)$ around $+\vec{k}^*$ $(-\vec{k}^*)$ goes from the north (south) pole to the equator, sweeping the upper (lower) hemisphere once. In total, one gets $\mathrm{Ch}_1 = +1$. Similarly, $\mathrm{Ch}_1 = -1$ for $\kappa < 0$.

conductivity [16]

$$\kappa_{xy} = \frac{dI_x}{dT_y} = c_- \partial_T \cdot \left[2 \int_{k>0} \frac{dk}{2\pi} \, \frac{1}{2} \epsilon(k) \langle \psi_k^\dagger \psi_k \rangle v(k) \right] = \frac{\pi}{6} c_- T, \tag{1.117}$$

where the group velocity reads $v(k) = \partial\epsilon(k)/\partial k$ and the density operator obeys the Fermi-Dirac distribution $n(k) = \langle \psi_k^\dagger \psi_k \rangle = [1 + e^{(\epsilon-\mu)/T}]^{-1}$. Here, c_- is a quantized constant that describes the chiral central charge (or the net chirality) of our system

$$c_- = \frac{1}{2}(\#\text{ of forward Majoranas} - \#\text{ of backward Majoranas}) = \frac{1}{2}\mathrm{Ch}_1. \tag{1.118}$$

The factor $1/2$ comes from the decomposition of one complex matter fermion into two real Majorana fermions (1.93). By the bulk-edge correspondence, on broader grounds c_- is related to the $\mathbb{Z}$-analytical index that characterizes the topological line defect [69]

$$c_- = \frac{1}{2}\mathrm{Ch}_{d-1}[H(k,r)] \in \frac{1}{2}\mathbb{Z}. \tag{1.119}$$

It should be noted that for the Kitaev honeycomb model in two dimensions, the chiral central charge $c_- = \pm 1/2$ is relatively hard to be associated with normal bulk observables, for instance two-spin correlators [18]. In Sec. 3.2, however, we show that when reduced to one dimension, this half-integer value can be probed in bipartite valence bond fluctuations [145] via a four-spin measurement.

Going back to the defect Hamiltonian (1.114), a finite bulk gap is guaranteed in the B phase

$$\Delta E(k)|_{\pm\vec{k}^*} = 2|\vec{R}(k,r)| = 2\sqrt{3(J^2k^2 + 36\kappa^2)}. \tag{1.120}$$

The associated correlation length can be estimated from the complex solution of $\Delta E(k_0) = 0$: $\xi = |\operatorname{Im} k_0|^{-1} \sim |J^3/(h_x h_y h_z)|$. Over a distance larger than ξ, one expects excitations in the bulk [18]. Each excited vortex associated with vorticity $l = 1$ can be viewed as a topological point defect characterized by a $\mathbb{Z}_2^{(1)}$-analytical

[16] We have set $\hbar$ (Planck's constant/2π) $= k_\mathrm{B}$ (Boltzmann constant) $= 1$.

index. Belonging to the same topological class as the spinless $p+ip$ superconductor, the index theorem (3.14) derived in Sec. 1.2.3 reveals that

$$\mathrm{ind}_{\mathbb{Z}_2}^{(1)} = \mathrm{Ch}_1 \times l \mod 2 = 1. \tag{1.121}$$

Each vortex carries an unpaired MZM. We denote such vortex as the superselection sector σ, along with the other two sectors 1 (vacuum) and ϵ (an excited fermion). Together they constitute three different types of non-Abelian anyons or Ising anyons [15]. Contrary to the Abelian anyons in the gapped phases (3.4), their fusion rules host multiple channels

$$\sigma \times \sigma = 1 + \epsilon, \quad \sigma \times \epsilon = \sigma, \quad \epsilon \times \epsilon = 1. \tag{1.122}$$

A full description of the non-Abelian braiding statistics involves the knowledge of the F matrices (the unitary transformation between two bases or equivalently associativity relations) and the $R_\rho^{\mu\nu}$ matrices (the phase acquired under the exchange of two particles μ, ν that fuse to a third particle ρ). More details about the algebraic structures can be found in Ref. [18].

1.3.4 One-dimensional analogue

In this section, we reduce the dimensionality of Kitaev spin liquids to one, as depicted in Fig. 1.7 (top) and address the quantum chain or wire model [146, 147]. The phase diagram corresponds to the bottom line in Fig. 1.5a with $J_z = 0, J_x = J_1 > 0, J_y = J_2 > 0$. After a mapping to Majorana fermions, the matter sector has a similar topological structure as a p-wave superconducting chain. However, the edge modes now differ and become two spin-1/2 complex fermions.

The lattice Hamiltonian of the Kitaev spin chain takes the form

$$\mathcal{H} = \sum_{j=2m-1} -J_1 \sigma_j^x \sigma_{j+1}^x - J_2 \sigma_{j+1}^y \sigma_{j+2}^y. \tag{1.123}$$

With this convention, the sum runs over odd sites only, such that $1 \leq m \leq M$ is an integer and M denotes the total number of unit cells. Applying the Jordan-

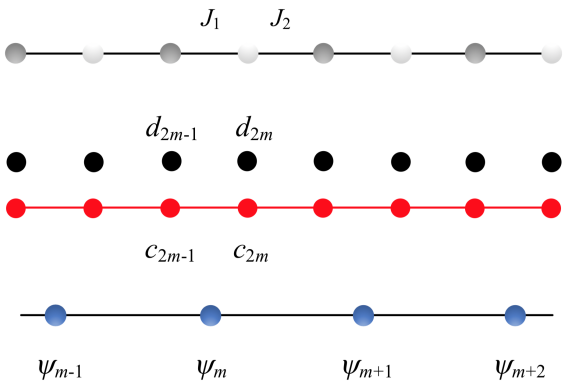

Figure 1.7: (Top) Kitaev spin-1/2 chain with alternating ferromagnetic Ising couplings $XYXY\cdots$, the strengths of which are described by parameters J_1 for x direction and J_2 for y direction. (Middle) Alternative representation of Majorana fermions from the mapping (1.126). (Bottom) Dual lattice of complex bond fermions by the construction (1.129).

Wigner transformation, one can map quantum spins-1/2 that satisfy Lie algebra $[\sigma_j^x, \sigma_j^y] = 2i\sigma_j^z$ onto spinless fermionic operators:

$$\begin{aligned} \sigma_j^+ &= a_j^\dagger \cdot \prod_{i<j}(-\sigma_i^z), \\ \sigma_j^- &= a_j \cdot \prod_{i<j}(-\sigma_i^z), \\ \sigma_j^z &= 2a_j^\dagger a_j - 1. \end{aligned} \tag{1.124}$$

At each site, σ_j^z takes the value of occupancy 1 for $|\uparrow_j\rangle_z$ and 0 for $|\downarrow_j\rangle_z$. The Hamiltonian (1.123) then reads

$$\mathcal{H} = \sum_{j=2m-1} -J_1(a_j^\dagger - a_j)(a_{j+1}^\dagger + a_{j+1}) + J_2(a_{j+1}^\dagger + a_{j+1})(a_{j+2}^\dagger - a_{j+2}). \tag{1.125}$$

At this stage, a direct Fourier transform of the spinless Hamiltonian does not work. By analogy to the Kitaev honeycomb model, one can employ $\mathcal{Z}_2$ symmetry and remove the degeneracy of the ground state by moving to the Majorana representation:

$$\begin{aligned} c_j &= i(a_j^\dagger - a_j), \quad d_j = a_j^\dagger + a_j, \quad j = 2m-1; \\ c_j &= a_j^\dagger + a_j, \quad d_j = i(a_j^\dagger - a_j), \quad j = 2m. \end{aligned} \tag{1.126}$$

Correspondingly,

$$\mathcal{H} = i \sum_{j=2m-1} (J_1 c_j c_{j+1} - J_2 c_{j+1} c_{j+2}). \tag{1.127}$$

The key point is that in this basis all the d Majorana fermions decouple from the chain shown in Fig. 1.7 (middle), and encode the double-degeneracy of the (spin) ground state on a given bond of nearest neighbors. A d Majorana fermion contributes to a $(\ln 2)/2$ entropy by analogy to the two-channel Kondo model [148, 149]. Going to 1D k-space of the c matter Majorana fermions, we obtain the Bloch form (1.98) with the complex function

$$f(k) = 2(J_1 + J_2 e^{-2ik}). \tag{1.128}$$

The lattice spacing l has been set to unity 1. To solve the energy spectrum, it is again convenient to introduce complex bond fermions that live on x-bonds:

$$\psi_m = \frac{1}{2}\left(c_{2m-1} + ic_{2m}\right). \tag{1.129}$$

Shown in Fig. 1.7 (bottom), ψ form a dual lattice with site index $m = 1, \ldots, M$. In the basis $\Psi^\dagger = (\psi_k^\dagger, \psi_{-k})$, the BdG Hamiltonian $H(k)$ of the Kitaev spin chain then shares the same form as that of the honeycomb model (see Eq. (1.99) and Eq. (1.100)) with two eigenvalues

$$E_k^\pm = \pm 2\sqrt{J_1^2 + J_2^2 + 2J_1 J_2 \cos(2k)}. \tag{1.130}$$

A gap is revealed if $J_1 \neq J_2$. Otherwise, when $J_1 = J_2$ the gap closes at $k_F = \pi/2$ and the chain on the dual lattice results in a critical gapless theory of free fermions with central charge $c = 1$.

To uncover the edge modes in the topological phase, we can re-express the Hamiltonian (1.127) in terms of bond fermions on the dual lattice

$$\mathcal{H} = \sum_{m=1}^{M} -J_1\left(1 - 2\psi_m^\dagger \psi_m\right) + J_2\left(\psi_m^\dagger \psi_{m+1} + \psi_m^\dagger \psi_{m+1}^\dagger + h.c.\right). \tag{1.131}$$

Bond fermions behave as a p-wave superconducting chain (1.57) and one identifies immediately

$$\mu = -2J_1, \quad t = -J_2, \quad \Delta = J_2. \tag{1.132}$$

In the topological regime $J_1 < J_2$ (or $|\mu| < |2t|$), there are two MZMs γ_1, γ_{2M} localized at the ends of the dual lattice. Especially, when $J_1 = 0$ they become c_1 and c_{2M}. Yet in the presence of free d gauge Majorana fermions in the original spin space (see Fig. 1.7, middle), these MZMs can not be separated from the bulk. Together $\{\gamma_1, d_1\}$, $\{\gamma_{2M}, d_{2M}\}$ recombine and form one quantum spin-1/2 on each end. From this perspective, one foresees the challenges of probing chiral Majorana edge state and bulk anyons in the Kitaev honeycomb model. Interaction effects within and between the gauge and matter sectors need to be taken into account. Promising approaches are reviewed in Section 1.4.2.

The exact solution of the Kitaev spin chain allows us to derive an analytical expression of bipartite valence bond fluctuations in Section 3.2 and probe central charge $c = 1$ at the quantum critical point. Furthermore, in Section 4.1 we apply the Jordan-Wigner string to a Kitaev spin ladder and obtain a new phase diagram. The generalized ladder model can be viewed as coupling two Kitaev spin chains via alternating ZZ' Ising exchanges on the rungs.

1.4 Applications

In this section, we review some recent experimental and theoretical developments in the search of Majorana fermions in condensed matter systems. Various concepts and techniques find origins in quantum Hall physics [15]. While the exact solutions of the Kitaev superconducting wire and Kitaev spin liquids navigate future research to the discovery of novel topological quantum materials [150], the engineered systems with artificial gauge fields in cold-atoms and quantum circuits have also become promising candidates for the simulation of non-Abelian topological phases. Alongside the physical realization, we also discuss briefly about braiding statistics and potential applications in quantum computation.

1.4.1 Motivation from quantum Hall physics

It has been known from the 80s and 90s that systems exhibiting the fractional quantum Hall effect [151, 152] host anyons as emergent quasiparticles. When a 2D electron gas (2DEG) is subject to a strong magnetic field B, a gap is opened between a degenerate ground state and excited states. While the longitudinal conductivity vanishes, the Hall conductivity becomes quantized: $\sigma_{xy} = \nu e^2/h$. Here, the filling factor $\nu = n\Phi_0/B$ associated with the electron density n and the flux quantum $\Phi_0 = hc/e$, can be an integer or a fraction. Remarkably, quasiparticle excitations from a fractional quantum Hall state carry fractional charges and behave as anyons. The direct observation of the Abelian anyonic braiding statistics [153] is reported for the $\nu = 1/3$ Laughlin state [24] using an electronic Fabry-Perot interferometer [154]. In the experiment, a 2DEG in a GaAs/AlGaAs heterostructure gives rise to localized quasiparticles with fractional charge $e/3$ in the bulk. A current is then inserted and carried by the chiral edge state of the material at $\nu = 1/3$. Under the influence of backscattering with quantum point contacts (QPC), a closed loop can be completed by backscattered quasiparticles effectuating the braiding process depicted in Fig. 1.6b (right). It leads to a jump in the Aharonov-Bohm phase $2\Delta\theta = 2\pi \times (0.31 \pm 0.04)$, in agreement with the theoretical prediction for the Abelian anyon $\theta = \pi/3$. This statistical angle has also been verified in anyon collision experiments through the measurement of current correlations [155].

Another interesting filling factor occurs at $\nu = 5/2$ and supports non-Abelian anyonic excitations with fractional charge $e/4$ [13]. The trial Moore-Read Pfaffian wave function, exact ground state of a repulsive three-body interaction, can be viewed as the quantum Hall analogue of the $p+ip$ superconductor [14, 156]. At low temperatures, in the GaAs/AlGaAs heterostructure at $\nu = 5/2$, one then realizes a BCS state formed by composite fermions. Although such a state is found to be fragile and the temperature required extremely low ~ 20 mK [15], a half-integer value of the thermal Hall

conductance [157] has been observed: $\kappa_{xy} = (2.5)\kappa_0 T$ with $\kappa_0 = \pi^2 k_B^2/(3h)$[17], thus revealing the non-Abelian nature. Other platforms that exhibit even-denominator fractional quantum Hall states and potentially host Majorana quasiparticles include the superfluid phase of low-temperature He^3 reached at high pressure [14] and more recently the bilayer graphene [158].

Alternative probes of the fractional charges of anyons come from dynamical processes, for instance, the measurement of the photo-assisted shot noise (PASN) [159–161]. At the QPC, a reflected $\nu = 2/5$ inner chiral edge state gives rise to anyons with charge q. When the contacts are irradiated by microwaves, a singularity can be identified in PASN at the frequency f_J that follows a Josephson relation $f_J = qV/h$. Here, V denotes the DC voltage. Depending on whether the inner chiral edge state is fully or weakly reflected, emergent anyons carrying fractional charges $q = e/3$ and $q = e/5$ have been observed [162]. The real-time Ramsey interferometry can also be applied to a Hall sample with a QPC: the fractional charge of the associated edge states is revealed in the interference pattern of the current noise brought by the tunneling of particles (either fractional quasiparticles or electrons) during two distinct short pulses [163]. Once the QPC is placed at the middle of the Hall sample with a weak link[18], bipartite charge fluctuations in time can be read from the current noise as well, and from them one is able to reconstruct the real-space entanglement spectrum together with the Rényi entropies [164].

1.4.2 Topological quantum materials

In the last decade, there has been a rapid development in the experimental realization of MZMs [76, 165, 166] based on the theoretical models of 1D and 2D topological superconductors in Sec. 1.2.2 and Sec. 1.2.3.

On one hand, the Kitaev p-wave superconducting chain can be engineered from a variety of heterostructures: for instance, 1D semi-conducting nanowires [167–169],

[17] $\kappa_0 = \pi/6$ under the same convention as Eq. (1.117) in the Kitaev honeycomb model.
[18] It refers to a strong gate voltage that only allows the weak tunneling of electrons.

edges of 2D topological insulators [170] or 3D topological insulator nanowires [171] on the surface of conventional s-wave superconductors. Proximity effects induce effective p-wave superconducting pairings in the quasi-one-dimensional bulk. The transition from spin-1/2 electrons to spinless fermions is achieved with the help of spin-orbit couplings and the introduction of time-reversal symmetry breaking terms.

On the other hand, to engineer the spinless $p + ip$ chiral superconductors, same principles can be applied to the topological insulator-superconductor heterostructures [172–174] while taking into account additional complexity arising from hybridization at the interface with the parent s-wave superconductor [175, 176]. One can also replace the topological insulator with semiconductor-based devices [177, 178], or more conventionally, may resort to material realizations in doped topological insulators [179], iron-based superconductors [180] and transition metal dichalcogenides (MX_2) [181, 182]. Among the latter, many are nodal topological superconductors with strong Rashba spin-orbit coupling (SOC) (e.g., $NbSe_2$, TaS_2). Driven by an in-plane magnetic field, six pairs of nodal points connected by Majorana flat bands are predicted along Γ-M lines of the Brillouin zone [183]. These nodal points are protected by chiral symmetry against local disorder. The hidden mechanism of the formation of Majorana flat bands is similar to that of a $p + ip$ superconductor [184]. RG analysis further shows that $NbSe_2$ favours a chiral superconducting phase with Chern number 6 when both Rashba SOC and spin-triplet interactions are sufficiently large [185]. It is relevant to point out that the crystal structure of MX_2, two hexagonal chalcogen layers sandwiching transition metal atoms, provides the unique opportunity to form superconductor-normal junctions between the layers, and make Majorana fermions engineering more feasible [150].

Meanwhile, the coupled-wire construction [28–30] shows a promising alternative path towards the $p+ip$ superconductivity [186, 187], which is one of the main focuses of Chapter 2. There, the orbital magnetic field effects are introduced to help engineer the ip pairing channel in weakly coupled ladders. Alternatively, one can also consider

two arrays of semi-conducting quantum wires each coated on one side with a thin s-wave superconducting layer. Stacking them with a twisted angle $\pi/2$ is found to support a fully gapped chiral $p+ip$ superconducting phase with vortex defects hosting MZMs [188]. In fact, the aforementioned routes can be combined in full-shell nanowire systems (with a semiconductor at the core surrounded by a superconducting shell) [189]: the MZMs located at the ends of a wire are shown to be stabilized by the flux-induced winding of the superconducting phase.

Once MZMs are synthesized, we are able to explore non-Abelian braiding statistics [15, 190]. A simple physical picture [178, 191] can be grasped through a $p+ip$ superconductor with four vortices, each carrying an unpaired Majorana mode. Artificially, we construct two complex fermions ψ_1 and ψ_2 from the Majorana pairs: $\psi_1 = (\gamma_1 + i\gamma_2)/2$, $\psi_2 = (\gamma_3 + i\gamma_4)/2$. Starting from the initial state $|n_1, n_2\rangle$ with the number operator $n_j = \psi_j^\dagger \psi_j$, one can perform a braiding that results in a clockwise exchange of two Majorana fermions γ_i and γ_j: $\gamma_i \to -\gamma_j, \gamma_j \to \gamma_i$. Here, the extra minus sign agrees with fermion statistics. It is equivalent to build a unitary operator $U_{ij} = (1 + \gamma_i\gamma_j)/\sqrt{2}$ such that $U_{ij}\gamma_{i/j}U_{ij}^{-1} = \mp\gamma_{j/i}$. Depending on the order of exchanges, the final state of the vortices differs. The total wave function may acquire a phase shift $U_{12}|n_1, n_2\rangle = e^{i\pi(1-2n_1)/4}|n_1, n_2\rangle$ or go under rotation $U_{23}|n_1, n_2\rangle = [|n_1, n_2\rangle + ie^{i\pi n_1}|1 - n_1, 1 - n_2\rangle]/\sqrt{2}$. Although such features of non-Abelian statistics from MZMs are not rich enough [15], with sufficient implementations more realistic Majorana surface codes [10, 11, 192] are proposed and partially pave the way for universal quantum computation.

The Kitaev honeycomb model in Sec. 1.3 is another exciting future candidate platform towards fault-tolerant quantum computation [18, 55]. Efforts have been focused on the search of related quantum materials that embody the physics of frustrated magnets [17, 50, 127–129, 193–198]. The most fruitful one comes from the material α-$RuCl_3$ with potentially dominant FM Kitaev couplings shown by ab-initio and spin-wave studies [199–201]. Significant experimental progress on α-$RuCl_3$ has been made

in recent measurements of Raman [202] and neutron [203] scatterings, nuclear magnetic resonance [204], and thermal transport [205–207]. The observation of the half-integer thermal Hall effect from transverse thermal conductivity $\kappa_{xy} = (0.5) \times (\pi T/6)$ (1.117) remains intriguing due to small Hall angles ($\kappa_{xy}/\kappa_{xx} \sim 10^{-3}$) [207]. It can be partially explained by taking into account the couplings to phonons [208, 209] and the effects of disorder from site dilution [210]. Besides, materials in this category favor a magnetic ordering at low temperatures owing to Heisenberg interactions [193]. Numerical simulations [211, 212] also reveal that when introducing an external magnetic field, AFM symmetric-anisotropic Γ-interactions may drive the system into an intermediate Kitaev spin liquid phase. Naturally, to better distinguish the topologically non-trivial phases, novel protocols are to be designed from theoretical perspectives. Notable developments have been made in the computation of dynamical spin correlations [213–218] as well as the entanglement entropy [133, 216]. In Chapter 3, we propose a relevant entanglement probe based on valence bond fluctuations [145]. In addition, one may consider the α-$RuCl_3$/graphene heterostructures [219, 220]. Due to charge transfer, the α-$RuCl_3$ monolayer becomes electron doped and the Kitaev interactions are found to be enhanced by strain from ab-initio calculations [221] . Experimental signatures further show anomalous quantum oscillations of the bilayer structure at low temperatures [220]. This phenomenon can be captured by an effective Kitaev-Kondo model [222], and might be interpreted as an indirect evidence of fractionalized excitations in Kitaev spin liquids since the formerly excited neutral Majorana quasiparticles now acquire charge through hybridisation with the graphene Dirac band.

When 2D Kitaev materials approximately enter the spin liquid regime, one addresses a more challenging question of braiding Ising non-Abelian anyons. A recent proposal [223] introduces superconducting circuits at the interface between a Kitaev material and a $\nu = 1$ integer quantum Hall system such that an injected electron along the $\nu = 1$ edge is converted to an emergent chiral Majorana boundary mode

in the spin liquid, arising from the effect of fermion condensation due to strong interface interactions. It offers a counterpart of traditional transport probes designed for fractional quantum Hall states. By analogy to the Fabry-Perot interferometer, for instance, adding a constriction to the Kitaev material leads to non-trivial braidings between the incident emergent Majorana edge mode and bulk quasiparticles (1.122) of type $(1, \sigma, \epsilon)$, and in turn leaves out distinct signatures in electrical conductances. Three types of bulk excitations can also be detected by a variation, the time-domain anyon interferometry [224] that exploits rich dynamics coming from time-dependent couplings of the chiral Majorana edge state to two ancillary spins.

1.4.3 Engineered systems with artificial gauge fields

With the rapid development of artificial gauge fields in quantum simulation [225, 226], more flexibility and tunability can be achieved by realizing Kitaev spin liquids in engineered systems, such as ultracold atoms [227–229] and quantum circuits [230, 231].

In 3D optical lattices comprising cold atoms, a honeycomb lattice on the x-y plane can be formed after the suppression of spin exchanges along the vertical z direction via potential barriers [232–234]. Three in-plane spin-dependent trapping potentials from collisions of atoms during the second-order tunneling processes then help stabilize the anisotropic nearest-neighbour Ising interactions [227]. Based on this experimental scheme, the creation and braiding of non-Abelian anyons can be carried out in principle [229]. Meanwhile, larger Kitaev couplings are possible with polar molecules trapped in stacked triangular lattices under combined effects of microwave excitation, dipole-dipole interaction and spin-rotation exchanges [228].

For the cQED architectures, starting from new phase diagram of a two-leg Kitaev spin ladder [147], in Chapter 4 we present a driven superconducting box circuit as building blocks towards the simulation of Kitaev spin liquids and exotic many-body Majorana states. One can also build a Cooper-pair box that resembles a spin-1/2

out of MZMs from an array of three superconducting nanowires when the charging energy becomes strong [231]. Extended to two dimensions, such boxes are shown to be useful for the construction of the Kitaev model on a decorated honeycomb lattice [56], of which the underlying chiral spin liquid phase ($\mathrm{Ch}_1 = \pm 1$) is expected to bear similar non-Abelian anyonic vortex excitations.

In the end, it is worthwhile to mention that to ensure universal quantum computation, a non-Abelian topological phase supporting Fibonacci anyons is required [15]. It can be found in the Levin-Wen honeycomb model [235, 236] where all spins-1/2 sit on the links of the lattice and are afflicted to a set of generalized toric code operators (1.107): A_s acting on three spins adjacent to vertex s and B_p on twelve spins surrounding hexagonal plaquette p. Similar to the Kitaev honeycomb model, it is exactly solvable via string-net condensation and shares the advantage that the topological regime of interest resides deep in the phase diagram, far away from neighbouring broken symmetry phases. Quantum circuits can be constructed accordingly for the non-Abelian Fibonacci code [237].

Chapter 2

Coupled wires construction from spinless fermions

In this chapter, we study a multi-wires system in the low-energy subspace, where each wire is described by a topological p-wave superconductor [72]. We address the interplay between intrawire and interwire tunneling and superconducting pairing terms, including orbital magnetic field effects. Such orbital magnetic field effects have been realized in coupled nanowires [238] through the application of a magnetic field perpendicular to the plane of the wires. Similar efforts are underway in cold-atom systems [226, 239, 240], where quantum Hall phases have been observed in ladder geometries [241, 242]. The possibility of engineering fractional quantum Hall phases in these ladders has stimulated a vigorous research activity, focused on both bosonic and fermionic systems [68, 243–248]. Orbital magnetic field effects have also started to attract some theoretical interest in the case of two coupled Kitaev chains [31, 249]. Here, we present new phenomena in hybrid systems made of two asymmetric wires, and then we build two-dimensional topological models with chiral edge modes from coupled-ladder systems in the presence of magnetic fields.

We start by studying the bonding-antibonding band representation of two coupled wires, which allows us to access the strong-tunneling limit [63, 250] between the wires. Afterwards, we introduce hybrid (spinless) systems coupling a chain of free fermions with a Kitaev chain and study the effect of Andreev processes. An Andreev process

allows the transfer of a Cooper pair from a superconducting system into a normal metal (here the other wire). Such a process leads to superconducting correlations in the normal wire. In the case of spin-1/2 fermions, Andreev processes have already been shown to influence the properties of cuprate superconductors near the Mott insulating regime [251]. They also give rise to a fractional quantum Hall phase at filling factor $\nu = 1/2$ in the case of hybrid spin-1/2 wire systems [68].

In the later part of this work, we apply the wire construction method [29, 30] to engineer, in coupled-ladder geometries, an $ip_x + p_y$ superconductor with spinless fermions [14] as well as a fractional quantum Hall state at $\nu = 1/2$ [68, 244] for spin-1/2 fermions [68]. The $p + ip$ superconducting proposal could be implemented, *e.g.* with two different Peierls phases acting on the intrawire and interwire hopping terms [226, 239]. It has been recently shown that one can also realize a topological $(p_x \pm ip_y)$ superconductor on the honeycomb lattice with Rashba spin-orbit interaction, as a result of the interplay of geometric phase and electron correlation [252].

The organization of the chapter is as follows. In Sec. 2.1, we introduce the model with the different flux situations to be studied. In Sec. 2.2, we introduce magnetic flux effects and analyse the case of hybrid systems, with one wire being a topological p-wave superconductor and the other wire a free fermion model or a Luttinger liquid, taking into account the physics of Andreev processes [253]. In Sec. 2.3, we first show how magnetic field effects can turn the one-dimensional topological superconductor into a two-dimensional topological $p + ip$ superconductor by coupling the ladders to the same (s-wave) superconducting reservoir [70]. We then discuss a realization of a $\nu = 1/2$ Laughlin phase in coupled (hybrid) ladders comprising spin-1/2 fermions, in the presence of a uniform magnetic field.

2.1 Model and definitions

We begin by illustrating the building block of our coupled wire construction: a flux-assisted two-leg ladder system of spinless fermions, captured by the Hamiltonian (see

Fig. 2.1a)

$$\mathcal{H} = \mathcal{H}_{\parallel} + \mathcal{H}_{\perp} + \mathcal{H}_{\Delta} + \mathcal{H}_{\Delta_0}, \tag{2.1}$$

which includes tunneling terms along and between the wires

$$\begin{aligned}
\mathcal{H}_{\parallel} &= -\sum_{j}\sum_{\alpha=1,2}[\mu c_{\alpha}^{\dagger}(j)c_{\alpha}(j) + te^{-i\zeta a/2}c_1^{\dagger}(j)c_1(j+1) + te^{i\zeta a/2}c_2^{\dagger}(j)c_2(j+1) + \text{H.c.}], \\
\mathcal{H}_{\perp} &= -\sum_{j} t_{\perp}e^{i\chi x_j}c_1^{\dagger}(j)c_2(j) + \text{H.c.},
\end{aligned} \tag{2.2}$$

as well as pairing interactions induced by the proximity to the superconducting (superfluid) reservoir

$$\begin{aligned}
\mathcal{H}_{\Delta} &= \sum_{\alpha=1,2}\sum_{j}\Delta_{\alpha}c_{\alpha}^{\dagger}(j)c_{\alpha}^{\dagger}(j+1) + \text{H.c.}, \\
\mathcal{H}_{\Delta_0} &= \sum_{j}\Delta_0 c_1^{\dagger}(j)c_2^{\dagger}(j) + \text{H.c.}.
\end{aligned} \tag{2.3}$$

We denote the lattice spacings of the wires as a and a' for the horizontal x and vertical y directions. For a square ladder, $a' = a$. The positions of the sites along each wire are denoted as $x_j = ja$, where $j = 1, ..., M$. The total length of one wire becomes $L = Ma$. The operator $c_{\alpha}^{\dagger}(j)$ creates a spinless fermion on site j of the wire α. Here, μ stands for the global chemical potential. For symmetric and decoupled (or weakly-coupled) wires, this condition will then ensure that the Fermi wave vectors in the two wires satisfy $k_F^1 = k_F^2$, but we will also address cases (when specified hereafter) with asymmetric wires where $k_F^1 \neq k_F^2$. The intrawire and interwire pairing amplitudes are denoted $\Delta_{1,2}$ and Δ_0, respectively. Here, the phase associated with the pairing terms is fixed by the properties of the superconducting (superfluid) reservoir. In Sec. 2.3.1, we will also include a diagonal term $\Delta_0(c_1^{\dagger}(j)c_2^{\dagger}(j+1) + c_2^{\dagger}(j)c_1^{\dagger}(j+1) + \text{H.c.})$, which will play an important role for the realization of the $p + ip$ superconducting phase.

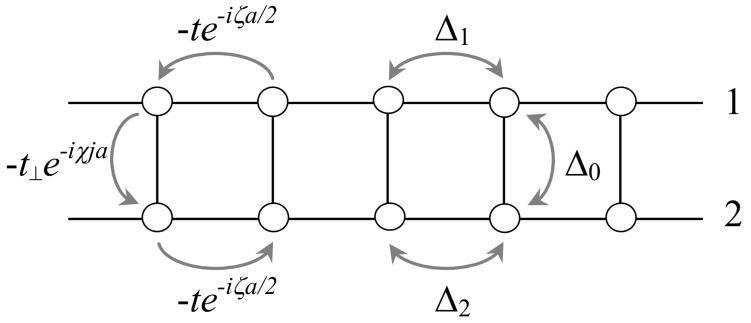

(a)

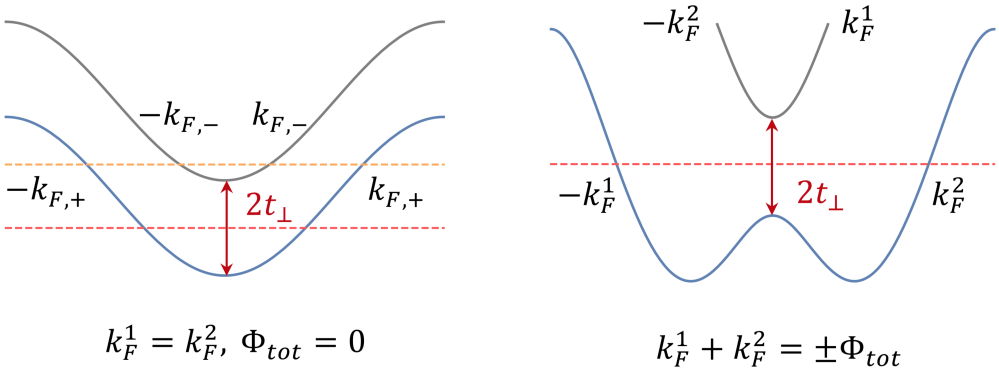

(b) (c)

Figure 2.1: (a) Two-leg ladder lattice comprising spinless fermions; we introduce the different flux situations discussed in the article through χ and ζ such that the total flux per plaquette is $\Phi_{\text{tot}} = (\chi - \zeta)$ assuming $a = a' = 1$. (b) Band structure in the absence of magnetic field and superconductivity. The blue and grey curves correspond to the bonding (+) and antibonding (−) bands [63]. A gap of the order of $2t_\perp$ is opened by the interwire tunneling term. Varying the chemical potential, the dashed lines denote the Fermi levels which host different numbers of gapless Fermi points. (c) Band structure with flux insertion and opening of a gap in the crossing region between the two bands. The lowest bonding band now mixes fermionic states with different chiralities (corresponding to left movers in the first wire with a wavevector $-k_F^1$ and to right movers in the second wire with a wavevector $+k_F^2$).

Even though we do not write the Coulomb interaction in the Hamiltonian, we shall comment hereafter on the stability of the physics towards interaction effects. The stability of the topological superconducting phases and the possibility to realize correlated and Mott phases in the presence of Coulomb interactions or nearest-neighbor interactions have been discussed, for instance, for the Kitaev chain in Refs. [254, 255] and for two coupled wires (when $t_\perp = 0$) in Ref. [31].

Below, for simplicity we assume that t and $t_\perp$ are real. The orbital effects of magnetic fields are included by multiplying t and $t_\perp$ by phase factors $e^{\pm i\zeta a/2}$ and $e^{\pm i\chi x_j}$, respectively (see Fig. 2.1a). The effect of the magnetic field on the superconducting order parameter can be safely neglected when the 3D reservoir (*e.g.* s-wave superconductor) is sufficiently large. We define the Peierls phases for a unit charge $q = 1$ and we set $\hbar = 1$. Furthermore, we introduce the quantity

$$\Phi_{\text{tot}} = \chi - \zeta. \tag{2.4}$$

This quantity has the dimension of a wave vector. The flux per plaquette or square unit cell is defined as $(\chi - \zeta)a$. Therefore, Φ_{tot} can also be seen as the total flux in a unit cell or plaquette with $a = a' = 1$. [1]

When $\chi \neq 0$ and $\zeta = 0$, this situation will correspond to the case of a uniform magnetic field $B_z = \chi/a'$ applied along z direction and a vector potential gauge $A_y = +x_j\chi/a'$ along y. In that case, one can also perform a gauge transformation to absorb the effect of the induced fluxes (or phases) onto a boost of the wave vector k for each wire, resulting in Fig. 2.1c.

When χ and ζ are both non-zero, this situation will allow us to engineer the $p+ip$ superconductor in Sec. 2.3.1. In Fig. 2.1a, this corresponds to a vector potential specified by the components $A_x = -(-1)^{y_j/a'}\frac{\zeta}{2}$ and $A_y = x_j\chi/a'$, with $y_j = 0$ for the lower wire and $y_j = a'$ for the upper wire. This choice of vector potential corresponds

[1] In reality, this requirement can be loosened: for instance, on a double quantum-wire sample, the quantum tunnelling with orbital magnetic field effects occurs when the interwire distance a' reaches $10 - 40\,\mu\text{m}$ [238].

to a magnetic field perpendicular to the plane of the wires,

$$B_z = \partial_x A_y - \partial_y A_x = \frac{\chi}{a'} - \frac{\zeta\pi}{2a'}\sin(\pi y/a'), \tag{2.5}$$

and reproduces a net flux $\Phi_{\rm tot} = \chi - \zeta$ in a square unit cell. Formally, to regularize properly the function A_x and ensure that $\partial A_x/\partial y$ is real (as it should be), we can use the form $A_x = -1/2(e^{i\pi y/a'} + e^{-i\pi y/a'})\frac{\zeta}{2}$ which reproduces $A_x = -(-1)^{y/a'}\frac{\zeta}{2}$ for $y = y_j$ and produces the second term $-\zeta\pi/(2a')\sin(\pi y/a')$ in the magnetic field in Eq. (2.5). To realize the $p + ip$ superconductor in coupled-ladder geometries (see Sec. 2.3.1), we require that the vector potentials and the magnetic field(s) are indeed periodic if we change $y \to y + 2a'$. In addition, the magnetic field B_z must be staggered if we change $y \to y + a'$, therefore we will also assume in Sec. 2.3.1 that χ takes a staggered (periodic) step-like form $\{\chi; -\chi\}$ associated to two successive square cells in the y direction.

The particular situation in which $\chi = \zeta = \pi/a$, of interest here, admits two physical interpretations in the absence of the superconducting pairing. On the one hand, the system is equivalent to a model of two wires with imaginary hopping terms $\pm it$ or band dispersions $\mp 2t\sin(ka)$ in Fig. 2.1c, with an alternating transverse hopping term $t_\perp(-1)^j$. On the other hand, because the total net flux is zero in a given unit (square) cell, the band structure of the two-wire system is also analogous to the one in Fig. 2.1b after gauge transformation, with a uniform transverse hopping term $t_\perp$ [2].

Below, we introduce four cases of interest, which will be addressed throughout this chapter.

In the first case, we consider that orbital magnetic fields are vanishing, $\zeta = \chi = 0$. The band structure of two wires is characterized by the bonding (+) and antibonding

[2]The "local" gauge transformation on the fermionic operators takes the form $c_1(j) \to e^{i\chi x_j/2}c_1(j)$ and $c_2(j) \to e^{-i\chi x_j/2}c_2(j)$ in Eq. (2.2). This situation also corresponds to the case where $A_x = 0$ and $A_y = \chi x/a' - \zeta\pi/(2a')\sin(\pi y/a')x$. We check that transporting one particle from the upper to the lower wire (vertically) produces a (zero) phase $\int_0^{a'=a} A_y dy = 0$ accompanying the transverse hopping term $t_\perp$ when $\zeta = \chi$.

(-) fermion operators [250]

$$c_{\pm}(j) = \frac{1}{\sqrt{2}} \left[c_1(j) \pm c_2(j) \right]. \tag{2.6}$$

If we neglect the superconducting terms Δ_i, the non-interacting part can be diagonalized as

$$\mathcal{H}_0 = \mathcal{H}_{\parallel} + \mathcal{H}_{\perp} = \sum_{\lambda=\pm} \sum_{k} \xi_{k,\lambda} c_{\lambda}^{\dagger}(k) c_{\lambda}(k), \tag{2.7}$$

with an energy dispersion

$$\xi_{k,\pm} = -2t \cos(ka) \mp t_{\perp} - \mu. \tag{2.8}$$

In Eq. (2.7), we have used the Fourier transform $c_{\alpha}(j) = (1/\sqrt{M}) \sum_k e^{ikx_j} c_{\alpha}(k)$, with $k = 2\pi n/(Ma)$ and $n = -M/2, -M/2+1, \ldots, 0, \ldots, M/2-1$ (if we assume M even). The energy spectrum of the two bands is shown in Fig. 2.1b. The Fermi wave vectors for the bonding and antibonding bands are $k_{F,\pm} = (1/a) \arccos[(\pm t_{\perp} + \mu)/(-2t)]$. We will include the effect of pairing terms at the Fermi points of this band structure, which is justified if the pairing amplitudes satisfy $\Delta_i \ll (t, t_{\perp})$ with $i = 0, 1, 2$. In Sec. 2.2, we will use a complementary approach in the wire basis addressing the weak-coupling limit. If we turn on the pairing interactions in this strong-tunneling limit, one can envision phase transitions towards SPT phases with 4 and 2 Majorana zero-energy modes (MZM) by shifting the chemical potential [249]. It can be viewed as a Lifshitz transition, *i.e.* induced by a change of the Fermi surface topology or by a change of the number of Fermi points from 4 to 2. The associated Van Hove singularity in the density of states can be observed, for instance, through local compressibility measurements. Our collaborators V. Perrin, A. Petrescu and I. Garate have tested numerically the stability of the Majorana fermions and the structure of induced pairing terms at low-energy in the strong-coupling region [187].

The second case of interest corresponds to $\zeta = 0$ and $\chi \neq 0$. In Sec. 2.2, we further set $\Delta_2 = \Delta_0 = 0$ which implies a hybrid system composed of a Kitaev superconducting

wire and a free fermion wire. The phase associated to the vertical tunneling terms can be absorbed through the local transformation

$$c_1(j) = e^{i\chi x_j/2}\tilde{c}_1(j), \quad c_2(j) = e^{-i\chi x_j/2}\tilde{c}_2(j). \tag{2.9}$$

The effect of the flux insertion $\Phi_{\text{tot}} = \chi$ is then equivalent to a shift (boost) of the momentum of the two energy bands:

$$\begin{aligned} \xi_{k,\tilde{1}} &= -2t\cos[(k+\chi/2)a] - \mu, \\ \xi_{k,\tilde{2}} &= -2t\cos[(k-\chi/2)a] - \mu. \end{aligned} \tag{2.10}$$

Within these definitions, the two bands cross when $\xi_{k,\tilde{1}} = \xi_{k,\tilde{2}}$, meaning at the wave vector $k = k_0 = 0$ in the new basis associated to Fig. 2.1c, which then makes the effect of a uniform interwire hopping term relevant in this region. In fact, in the strong-coupling limit, $t_\perp$ is only relevant at the band crossing point k_0, resulting in [238]

$$\begin{aligned} \mathcal{H}_\perp &= -t_\perp \sum_k \tilde{c}_1^\dagger(k)\tilde{c}_2(k) + h.c. \\ &\simeq -t_\perp(\tilde{c}_+^\dagger(k_0)\tilde{c}_+(k_0) - \tilde{c}_-^\dagger(k_0)\tilde{c}_-(k_0)), \end{aligned} \tag{2.11}$$

which then splits the energies of the bonding and antibonding bands at the crossing point $k_0 = 0$ accordingly. In the original frame, this corresponds to have $k_F^1 + k_F^2 = \pm\Phi_{\text{tot}}$ at the crossing point such that a gap $2t_\perp$ can be opened, as shown in Fig. 2.1c. When the Fermi level is between the upper and lower bands, the two gapless modes form an edge state falling into the category of an Abelian quantum Hall phase provided that $\Delta_i \ll t_\perp$.

In the weak-coupling limit, on the other hand, we find a superconducting topological phase at flux $\Phi_{\text{tot}} = \pi$. When adjusting the densities of the wires such that $(k_F^1 + k_F^2) = \pi/a$, Andreev processes between the two wires stabilise superconductivity in the two wires similarly to the case of zero magnetic flux. The system shows 4 Majorana fermions via proximity effect. At π flux, in the strong-tunneling limit,

the lowest (bonding) band which now mixes the two wire states at the Fermi points can be fully filled and can therefore open a gap in the single-particle spectrum when the upper band is empty. This situation, which is analogous to a band insulator, gives rise to a charge density wave in the wire basis associated to long-range order with one particle on each rung. We show below that this charge density wave state forms phase-coherent particle-hole pairs along the wires which then survive even if the transverse hopping term $t_\perp$ becomes comparable (slightly larger) to the pairing channel amplitudes.

The third case is $\zeta = \chi = \pi/a$, our starting point towards implementing a $p + ip$ superconductor in coupled-ladder geometries via the Δ_0 (interwire) pairing channel. Due to the $\pm it$ hopping terms in the two wires, the time-reversal symmetry and the chiral symmetry are not present, but particle-hole symmetry is preserved. The transverse hopping term $t_\perp(-1)^j$ now becomes real, and this will then ensure the stability of Majorana modes at zero energy even if $t_\perp \neq 0$. In Sec. 2.3.1, we perform the local gauge transformation to map the band structure onto the one of Fig. 2.1b, similar to the one in the absence of magnetic fields, and then we show how the interwire pairing term Δ_0 can give rise to a purely imaginary ip_x channel for the bonding fermions in a two-leg ladder architecture. Coupling pairs of wires or ladders together, then we realize a p_y channel through the same superconducting (s-wave) reservoir, assuming that the B_z magnetic field in Eq. (2.5) is uniform in the x direction and staggered in the y direction (which implies that χ generates a step function changing of sign on each successive plaquette in y direction).

The fourth case is analogous to the second $\zeta = 0, \chi \neq 0$ with spinful fermions. In Ref. [68], Karyn and A. Petrescu have shown the possibility to realize a fractional quantum Hall phase at filling factor $\nu = 1/2$ in hybrid systems. In Sec. 2.3.2, we generalize the analysis in coupled-ladder geometries with a uniform magnetic field showing how the chiral edge mode becomes more protected towards backscattering effects (when the bulk becomes larger).

The last two cases place us on track to search for topological phases in quasi-one-dimensional systems by coupling flux-assisted two-leg ladders through vertical tunnelings. This is the subject of the analysis performed in Sec. 2.3.

2.2 Hybrid two-leg ladder: Andreev mechanism

In this section, we consider a hybrid system consisting of one Kitaev superconducting wire and a wire of free fermions. In Fig. 2.2a, we depict the situation corresponding to the second case discussed in Sec. 2.1. The model is described by

$$\mathcal{H}_{\text{hybrid}} = \mathcal{H}(\zeta = 0, \chi \neq 0, \Delta_2 = \Delta_0 = 0, \Delta_1 = \Delta). \tag{2.12}$$

The precise goals below are as follows: first, we study the evolution of the topological superconducting phases in the presence of a gap anisotropy and study the weak-coupling limit. In addition, we study possible quantum phase transitions under a uniform magnetic flux. The schematic phase diagram is plotted in Fig. 2.2b and Fig. 2.2c for different flux conditions. When $\pm\chi a = \pi$, in the weak coupling limit p-wave superconductivity is induced in the free fermion wire. Deviating slightly from the $\pm\chi a = \pi$ situation, we analyze the Meissner and Majorana currents in the bulk and at the boundaries, respectively. We also address Abelian quantum Hall phases for particular relations between magnetic flux and densities in the wires and describe properties of the charge density wave state in real space when the bonding band is fully filled, occuring at $\pm\chi a = \pi$ in the strong-tunneling limit.

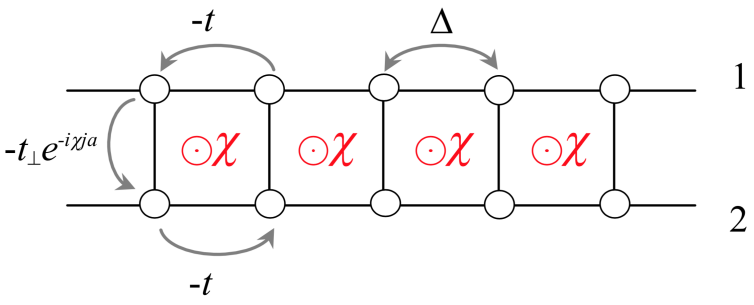

(a)

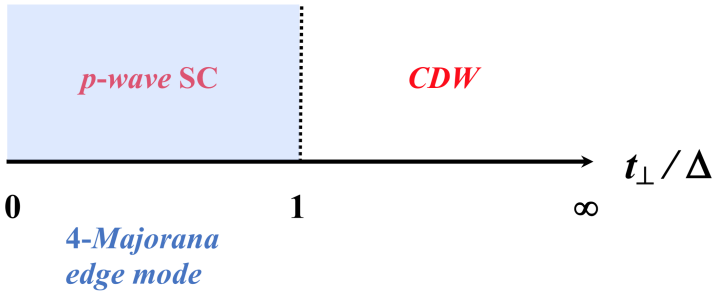

$$\left(k_F^1 + k_F^2\right)a = \pm\chi a = \pi$$

(b)

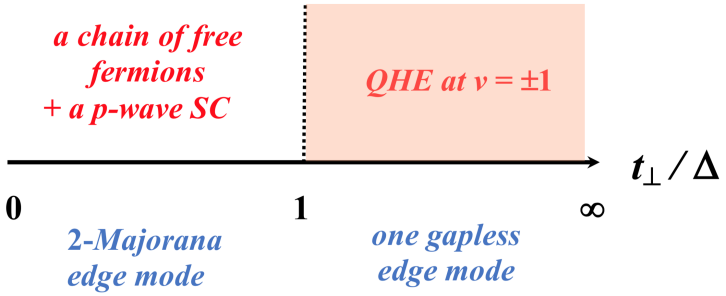

$$\left(k_F^1 + k_F^2\right)a = \pm\chi a \neq \pi$$

(c)

Figure 2.2: (a) Hybrid system comprising a topological superconducting Kitaev p-wave chain and a chain of free fermions. (b) and (c) Phase diagrams for $K = 1$ and for densities in the wires such that $(k_F^1 + k_F^2)a = \pm\chi a = \pi$ and $(k_F^1 + k_F^2)a = \pm\chi a \neq \pi$. For the superconducting phase in blue, the condition on k_F^i ensures the occurrence of 4 MZM until the charge density wave transition. The dashed lines refer to quantum phase transitions.

To acquire a physical understanding of the system's properties in real space (such as induced currents) when applying a magnetic field and to generalize the results when $t_\perp \ll \Delta$, we now switch to the bosonization picture or Luttinger liquid description [34, 35, 256, 257] in the wire basis. This allows us to include higher-order processes in the tunnel-coupling description. The approach below specifically addresses the limit $t \gg t_\perp \gg \Delta$, such that we can apply the continuum limit in the x direction parallel to the wires. Assuming the continuum limit $\psi_\alpha(x) = c_\alpha(j)/\sqrt{a}$ with $x = x_j = ja$, a fermionic operator can be written in terms of bosonic fields ϕ_α and θ_α:

$$\begin{aligned} \psi_\alpha(x) &= \psi_R^\alpha(x) + \psi_L^\alpha(x), \\ \psi_r^\alpha(x) &= \frac{U_r^\alpha}{\sqrt{2\pi a}} e^{irk_F^\alpha x} e^{-i[r\phi_\alpha(x) - \theta_\alpha(x)]}. \end{aligned} \tag{2.13}$$

The index $r = +1(-1)$ is taken for $r = R(L)$, *i.e.* for the right (left) moving particle. Formally, $\alpha = 1, 2$ or $+, -$ can embody the wire or band basis. In this section, we switch to the bonding and anti-bonding basis (2.6). The Klein factors U_r^α enforce the Fermi statistics and satisfy the relations: $U_{r,\alpha}^\dagger = U_{r,\alpha}$, $\{U_{R,\alpha}, U_{L,\alpha}\} = 0$. For convenience, it is sufficient to set $U_{R,\alpha}U_{L,\alpha} = i$ and all others to unity $U_{r,\alpha}U_{r',\alpha'} = 1$. The bosonic fields satisfy the commutation relation

$$[\phi_\alpha(x), \theta_\beta(x')] = i\frac{\pi}{2}\delta_{\alpha\beta}\mathrm{Sign}(x' - x). \tag{2.14}$$

In the bosonization picture (2.13), the kinetic term along the wires in $\mathcal{H}_{\mathrm{hybrid}}$ takes the form

$$\begin{aligned} \mathcal{H}_\parallel &= \mathcal{H}_0^+ + \mathcal{H}_0^-, \\ \mathcal{H}_0^\pm &= \frac{v^\pm}{2\pi}\int dx \left[K^\pm(\nabla\theta^\pm)^2 + \frac{1}{K^\pm}(\nabla\phi^\pm)^2\right], \end{aligned} \tag{2.15}$$

with the rotated fields $\theta^\pm = (\theta_1 \pm \theta_2)/\sqrt{2}$ and $\phi^\pm = (\phi_1 \pm \phi_2)/\sqrt{2}$. These modes can be understood as symmetric and anti-symmetric superpositions of bosonic fields in the wire basis. The sound velocities and Luttinger liquid parameters satisfy $v^\pm K^\pm = vK = v_F$, where the Fermi velocity takes the form $v_F = 2ta\sin(k_F a)$ if we linearize

the band structure of each wire close to each Fermi point, and in this formula k_F refers either to k_F^1 or k_F^2. For simplicity, we assume that the two wires have (almost) the same velocity. If we neglect the effect of the Coulomb interaction or nearest-neighbor interaction parallel to the chain $V_\parallel$, then formally $K = 1$. If we take into account this interaction, then this would adiabatically renormalize K to a value smaller than 1, according to $v^\pm/K^\pm = v/K \approx v + 2V_\parallel a/\pi$. Below, we assume that $K \to 1$, for simplicity.

The interwire hopping term takes the form

$$\mathcal{H}_\perp = -\frac{2t_\perp}{\pi a}\int dx \cos(\sqrt{2}\theta^- - \chi x)[\cos((k_F^1 + k_F^2)x - \sqrt{2}\phi^+) + \cos[(k_F^1 - k_F^2)x - \sqrt{2}\phi^-)]. \tag{2.16}$$

The conservation of the total number of particles in the system at $t_\perp = 0$ and $t_\perp \neq 0$ implies the equality $k_F^1 + k_F^2 = k_{F,+} + k_{F,-}$ in accordance with Luttinger's theorem. The pairing term in wire 1 takes the form

$$\mathcal{H}_\Delta = -\frac{2\Delta}{\pi a}\int dx \sin(k_F^1 a)\cos(2\theta_1). \tag{2.17}$$

Furthermore, we choose densities in the wires $k_F^i \neq \pi/(2a)$, such that intrawire insulating transitions do not occur, since they have been well studied [31, 254, 255]. Still, we will show below that a charge density wave transition can occur in the system, giving rise to an analogue of the rung-Mott insulator for which the total charge ϕ^+ and the superfluid phase difference θ^- are pinned [258]. The physics is adiabatically linked to the half-filled situation where the lowest band is fully occupied and the upper band is empty, implying $k_{F,-} = 0$ and $k_{F,+} = \pi/a$ when $t_\perp > 2t$. In the wire basis, the half-filled condition at $t_\perp = 0$ refers accordingly to $(k_F^1 + k_F^2) = \pi/a$.

It should be noted here that in principle the effect of Coulomb interactions between the wires [31] could give rise to an additional term proportional to $V_\perp \int dx \cos[2(\phi_1 - \phi_2)(x) - 2(k_F^1 - k_F^2)x]$ in the wire basis. To be able to describe the topological superconducting proximity effect induced by $t_\perp$, we assume below that $k_F^1 \neq k_F^2$ such

that the $V_\perp$ term averages to zero. Since $V_\perp$ is already a four-fermion operator, higher-order contributions will likewise not be relevant.

Let us start with the case without flux insertion, $\chi = 0$. For general situations where $k_F^1 \neq k_F^2$, all the terms in Eq. (2.16) oscillate rapidly and average to zero. This implies that one must include higher-order effects in $t_\perp$ in the weak-coupling regime [68, 251, 253]. Appendix B presents a perturbative approach developed to build the possible non-oscillating terms to higher order in $t_\perp$.

In the weak-coupling limit $t_\perp \ll \Delta \ll t$, to show the emergence of 4 MZM as soon as $t_\perp \neq 0$, we expand the partition function to second order and identify the effective Hamiltonian

$$\begin{aligned}\mathcal{H}_\perp^{(2)} &= -\frac{2t_\perp^2}{\pi a \Delta}\int dx \cos(2\sqrt{2}\theta^-) \\ &= -\frac{2\bar{\Delta}_2}{\pi a}\int dx \cos(2\theta_2). \end{aligned} \tag{2.18}$$

This corresponds to an Andreev process where a Cooper pair is transported from wire 1 to wire 2. For the second equality, we use the fact that at energies smaller than Δ, the charge field of wire 1 is pinned to a classical value $\langle\cos(2\theta_1)\rangle \sim 1$ implying $\theta_1 \sim 0$, due to the strong pairing $\mathcal{H}_\Delta$ term (4.57). Classically, to minimize energy (at zero temperature) the superfluid phase θ_1 will be pinned at one minimum of the (periodic) cosine potential $-\cos(2\theta_1)$. Each minimum $\theta_1 = 2n\pi$ with $n \in \mathbb{Z}$ is equivalent and thus we can assume that the phase is pinned at $\theta_1 \sim 0$, neglecting instanton effects from one minimum to another. We then observe an effective induced superconducting gap in the second wire: $\bar{\Delta}_2 \sim t_\perp^2/\Delta$. Therefore in the weak tunneling region, the superconducting phase shows 4 MZM for a large range of chemical potentials, roughly when $-2t < \mu < 2t$.

Formally, minima of the form $\theta_1 = (2n+1)\pi$ are also allowed and correspond to a twist of π in the definition of the fermionic operator in Eq. (2.13). In the Kitaev model for the wire 1, this π phase shift is equivalent to the $\mathbb{Z}_2$ symmetry $c_1 \to -c_1$ in the BCS Hamiltonian. A redefinition of the global phase by π of the fermionic operator

associated with the wire 1 also corresponds to change $t_\perp \to -t_\perp$ and $\Delta_0 \to -\Delta_0$ in Eq. (2.1). This corresponds to the transformation $c_1 \leftrightarrow c_2$ in the Hamiltonian. In the band picture, this π-phase shift simply inverts the bonding and anti-bonding bands. It is however important to recognize that the intra- and interwire pairing terms would have a π-phase shift of difference, which seems difficult to realize with a unique (three-dimensional) superfluid reservoir.

In the regime $t \gg t_\perp \gg \Delta$, one can also generate a similar term

$$\mathcal{H}_\perp^{(2)} = -\frac{2t_\perp^2}{\pi a \Lambda} \int dx \cos(2\sqrt{2}\theta^-). \tag{2.19}$$

The energy cutoff Λ depends on the short time and short distance considered in the virtual processes (see more details in Appendix B). The original pairing term in wire 1 can be estimated as $\langle \cos(2\theta_1) \rangle \sim \Delta/\Lambda$, when evaluating the effect of the pairing term at low energy perturbatively in Δ. More precisely, we calculate $\langle \cos(2\theta_1(x)) \rangle = \mathrm{Tr}[e^{-\beta H} \cos(2\theta_1(x))]$ to first order in Δ leading to $\langle \cos(2\theta_1(x)) \rangle \sim \Delta \int_{1/\Lambda}^{\beta \to +\infty} d\tau \langle \cos(2\theta_1(x,\tau)) \cos(2\theta_1(x,0)) \rangle$, where τ represents the imaginary time and $\langle ... \rangle$ means an average on the quadratic Luttinger theory of the correlation function at the position x. Remembering that $\langle \cos(2\theta_1(x,\tau)) \cos(2\theta_1(x,0)) \rangle \sim (\Lambda\tau)^{-2}$, we check that $\langle \cos(2\theta_1) \rangle \sim \Delta/\Lambda$. The $\mathcal{H}_\perp^{(2)}$ term then gives a contribution in $\sim (t_\perp^2/\Lambda) \langle \cos(2\theta_1) \rangle \int dx \cos(2\theta_2)$. Starting from a Gaussian Luttinger theory, we have the equality $\langle e^{2i\theta_1(x)} \rangle = \langle e^{-2i\theta_1(x)} \rangle = e^{-2\langle \theta_1^2(x) \rangle}$, implying that only the product of cosine functions contributes. A gap is induced in wire 2 and its amplitude now evolves as $\bar{\Delta}_2 \sim t_\perp^2 \Delta/\Lambda^2 \sim \Delta$. This argument can also be checked applying the arguments in the bonding-antibonding representation in Sec. 2.1. The term Δ_1 in the band basis gives a term such as $\Delta_1 \sin(k_F^1 a)(c_+^\dagger(k)c_+^\dagger(-k) + c_-^\dagger(k)c_-^\dagger(k))$, which induces a contribution $\Delta_1 \sin(k_F^1 a) c_2^\dagger(k) c_2^\dagger(-k)$ with $\Delta_1 = \Delta$. This confirms the preceding argument that the induced superconducting gap in wire 2 becomes equal to the superconducting gap in wire 1 in the strong-coupling limit. Bosonization arguments apply as long as the energy spectrum is linear, implying that k_F^1 is not too close to zero and therefore

that $\sin(k_F^1 a) \sim 1$, which then validates the equivalence with Eq. (2.19). If we consider the regime close to the bottom of a band, then one must rely on the band basis arguments showing that the induced gap in wire 2 is $\Delta \sin(k_F^1 a)$.

To identify the number of Majorana fermions in this regime, we resort to the band-structure arguments of the preceding section. The proximity effect gives rise to 4 MZM, 2 MZM or 0 MZM depending on the value of μ. Our collaborators V. Perrin, A. Petrescu and I. Garate have checked numerically that when approaching the bottom of the lowest band, close to the strong-paired phase transition, the proximity effect becomes fragile as $\Delta \sin(k_F^1 a)$ becomes very small [187].

2.2.1 At π flux

For non-zero values of the magnetic field with $\chi \neq 0$, one must adjust the densities or the Fermi wave-vectors in the two wires in Eq. (2.16) to produce a proximity effect, *e.g.* to make the tunneling term $t_\perp$ or higher-order contributions relevant. Here, we study the situation with π-flux per plaquette. We assume that $(k_F^1 + k_F^2)a = \pi$ such that the following commensuration relation is satisfied

$$a\left[(k_F^1 + k_F^2) \mp \chi\right] = 0 \mod 2\pi, \tag{2.20}$$

with $\chi a = \pm\pi$. This corresponds to a half-filled ladder with one particle per rung. The interwire hopping term (2.16) becomes

$$\mathcal{H}_\perp = -\frac{2t_\perp}{\pi a} \int dx \cos(\sqrt{2}\theta^-) \cos(\sqrt{2}\phi^+), \tag{2.21}$$

modulo an oscillatory term. In the strong-coupling limit, both modes θ^- and ϕ^+ are pinned to the classical values: $\theta^- \sim 0$, $\phi^+ \sim 0$. The pinning of the mode ϕ^+ suppresses fluctuations in the total density (or total charge) on a given rung. The system shows $a(k_F^1 + k_F^2)/\pi = 1$ particle and 1 hole per rung. Adding a particle or a hole at a given rung costs an energy, and the system shows a long-range charge order associated to the channel ϕ^+. Each rung is equivalent with one another, leading to a uniform charge density wave order with an effective wave vector $q = (k_F^1 + k_F^2 \mp \chi) = 0$.

Essentially, when $t_\perp \gg \Delta$ and more precisely $t_\perp > 2t$, in the bonding and antibonding representation of Fig. 2.1c, the lowest band becomes filled and adding one more particle in the antibonding band costs an energy of the order of $t_\perp$. The bosonization argument above suggests that this conclusion remains in fact correct even when $t_\perp < t$, but with $t_\perp \geq \Delta$, due to renormalization group arguments. Indeed, $t_\perp$ is a relevant perturbation associated to the kinetic terms $\mathcal{H}_0^{\pm}$, and therefore will grow under the renormalization scheme to values larger than t. More precisely, defining the dimensionless quantities $\tilde{\Delta} = \Delta/\Lambda^*$ and $\tilde{t}_\perp = t_\perp/\Lambda^*$ with Λ^* being the high-energy cutoff (which can be taken to be larger than t since the total bandwidth for a given wire is $4t$), the invariance of the partition function to second-order in $\tilde{t}_\perp \ll 1$ and $\tilde{\Delta} \ll 1$ leads to the following two equations:

$$\begin{aligned} \frac{d\tilde{t}_\perp}{dl} &= \left(2 - \frac{K_+}{2} - \frac{1}{2K_-}\right)\tilde{t}_\perp, \\ \frac{d\tilde{\Delta}}{dl} &= \left(2 - \frac{1}{2K_+} - \frac{1}{2K_-}\right)\tilde{\Delta}, \end{aligned} \tag{2.22}$$

where $l = -\log(\Lambda^*/E)$ and E corresponds to the energy scale of interest. This renormalization procedure is detailed in Appendix C. It can also be seen as an integration of modes at short distances with typical lengths between $\hbar v/\Lambda^* \sim a$ (with $\hbar = 1$) and $\mathcal{L} = \hbar v/E$, corresponding to an integration of blocks in real space and a redefinition of the lattice spacing as $\mathcal{L}$. For free fermions, setting $K_+ = K_- = 1$, we check that both $\tilde{t}_\perp$ and $\tilde{\Delta}$ flow to strong couplings. If we assume free fermions ($K_+ = K_- = 1$) or weakly-interacting fermions ($K_+ < 1$, $K_- < 1$) and if we consider the limit where $t_\perp \gg \Delta$, then we confirm that the term $\tilde{t}_\perp$ will flow to strong coupling faster than the term $\tilde{\Delta}$. In this case, the low-energy physics will be strongly associated with the properties of Eq. (2.21) and the ground state is a charge density wave.

For free fermions, our results are also in agreement with a filled lowest bonding band. Excitations above the charge gap corresponding to transferring a particle in the anti-bonding band then are accompanied with a phase change of π associated to the fermion operator c_2 (from Eq. (2.6)), which is equivalent to $\theta_1 - \theta_2 + \chi a = \pm\pi$

in the presence of the magnetic field. Another manner to understand the pinning of the phase θ^- is through the condition that at each site j (or each wave-vector k) the charge density wave formation implies $\langle\tilde{c}_1^\dagger\tilde{c}_1\rangle + \langle\tilde{c}_2^\dagger\tilde{c}_2\rangle = 1$ or $k_F^1 + k_F^2 = \pi/a = k_{F,+} + k_{F,-}$. If we consider the strong-coupling fixed point of the renormalization group arguments then this corresponds to a situation with a large $\tilde{t}_\perp \sim 1$ and with a fully occupied lowest band, *i.e.* with $k_{F,+} = \pi/a$ and $k_{F,-} = 0$. From the equality $\langle\tilde{c}_+^\dagger\tilde{c}_+\rangle = 1 = \frac{1}{2}(\langle\tilde{c}_1^\dagger\tilde{c}_1\rangle + \langle\tilde{c}_2^\dagger\tilde{c}_2\rangle) + \frac{1}{2}(\langle\tilde{c}_1^\dagger\tilde{c}_2\rangle + \langle\tilde{c}_2^\dagger\tilde{c}_1\rangle)$, we then infer $\langle\tilde{c}_1^\dagger\tilde{c}_2\rangle + \langle\tilde{c}_2^\dagger\tilde{c}_1\rangle = 1$ on each rung of the ladder system. In the continuum limit, phase coherence takes place between a particle $(\psi_R^1)^\dagger$ and a hole ψ_L^2 . This constraint is naturally fulfilled through the pinning conditions of ϕ^+ and θ^- in $\mathcal{H}_\perp$. Here, θ^- can be seen as the phase associated to the bosonic particle-hole pair wavefunction, and there is then a global phase coherence for the particle-hole pairs.

We also observe that the $\pm\pi$ magnetic flux suppresses the effect of the superconducting term Δ_1 when $t_\perp \gg \Delta$, since at low energy $\cos(2\theta_1) = \cos(\sqrt{2}(\theta^+ + \theta^-))$ and $\langle e^{i\sqrt{2}\theta^+}\rangle \sim 0$ due to the pinning of the dual mode ϕ^+, and the quantum uncertainty principle resulting from commutation rules between ϕ^+ and θ^+.

In the wire or chain representation, the system is analogous to the rung-Mott insulator [258, 259] of the ladder system. In the rung-Mott state of hard-core bosons, the Josephson effect produced the pinning of the phase θ^-. We name the phase found here Charge Density Wave (CDW) in the phase diagram of Fig. 2.2b associated to the long-range correlations of the field ϕ^+ in the wire basis. This state of matter is driven here by the $t_\perp$ term (rather than the interaction term), and is also related to a filled band insulator when $t_\perp \sim 2t$.

For the weak coupling regime $t_\perp \leq \Delta$, $\tilde{\Delta}$ now flows first to the strong-coupling regime assuming moderate repulsive interactions ($K_+, K_- > 1/2$); therefore, we have $\theta_1 \sim 0$ and its dual mode ϕ_1 becomes fast oscillating inside $\cos(\sqrt{2}\phi^+) = \cos(\phi_1 + \phi_2)$. $\mathcal{H}_\perp$ is then irrelevant to the first order. To the second order in perturbation, however, we still find an effective term reminiscent of an Andreev process between wires where

a Cooper pair is transported from wire 1 to wire 2, then triggering a superconducting gap in the free fermion wire (see Fig. 2.3 and more details in Appendix B)

$$\begin{aligned}\mathcal{H}_{\perp}^{(2)} &= -\frac{2t_{\perp}^2}{\pi a\Delta}\int dx\cos(2\sqrt{2}\theta^- - 2\chi x)\\ &= -\frac{2t_{\perp}^2}{\pi a\Delta}\int dx\cos(2\theta_2).\end{aligned} \tag{2.23}$$

In the last equality, we regard $2\chi x$ as multiples of 2π and θ_1 is pinned to zero for large Δ. Similar to the 0-flux case, the induced gap takes the form $\bar{\Delta}_2 = t_{\perp}^2/\Delta$. To minimize classically the energy in $\mathcal{H}_{\perp}^{(2)}$, we obtain the pinning condition

$$\langle\cos(2\sqrt{2}\theta^- - 2\chi x)\rangle = 1. \tag{2.24}$$

This phase is referred to as the p-wave SC phase in the phase diagram of Fig. 2.2b. Here, the phase reveals 4 MZM until the occurrence of the CDW order transition. Together, the conditions $k_F^1 + k_F^2 = \pi/a$ and $\chi = \pi$ imply that the chemical potential will take a value where the 4 MZM phase occurs. At the transition between the CDW and the 4 MZM topological phase, the modes ϕ^+ and θ^+ should become gapless, since in the CDW phase the system tends to favor the pinning of the mode ϕ^+ and in the superconducting phase, both θ_1 and θ_2 are pinned, implying consequently that both θ^- and θ^+ are pinned. Hence, a Luttinger liquid is expected in the vicinity of the transition line (dashed line in Fig. 2.2b) separating the CDW and the 4 MZM phases.

Below, we study the Meissner and Majorana currents that originate when $a\chi$ deviates slightly from $\pm\pi$. It is interesting to comment that the argument below would also be applicable for the 4 MZM topological superconducting phase close to the zero flux situation. We define and measure the Meissner-Majorana current at the edge by a small disturbance in fluxes $\Delta\chi$, as in Fig. 2.3. From Eq. (2.24), we obtain

$$\widetilde{\chi} = \chi + \Delta\chi, \quad \langle\nabla\theta^-(x)\rangle = \Delta\chi/\sqrt{2}. \tag{2.25}$$

It is relevant to observe that $\Delta\chi$ acting on the θ^- mode in Eq. (2.15) plays a similar role as a chemical potential $-\tilde{\mu}\nabla\theta^-(x)$ on a band insulator with $\tilde{\mu} = \Delta\chi v^- K^-/(\sqrt{2}\pi)$.

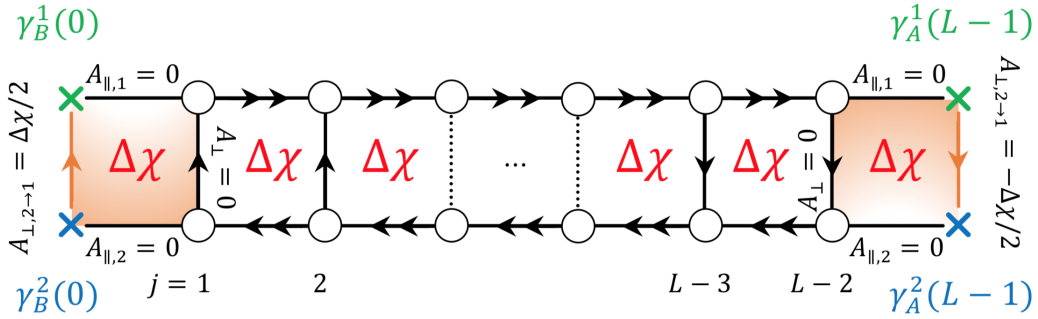

Figure 2.3: Weakly coupled hybrid wires in the presence of a uniform magnetic field with $\Phi_{\rm tot} = \chi a = \pm\pi$. The condition $k_F^1 + k_F^2 \mp \chi = 0$ allows us to make Andreev terms flowing to strong couplings close to $\Phi_{\rm tot} = \mp\pi$, similarly as the situation at zero net flux. A Meissner current formed by the Cooper pairs and proportional to $\Delta\chi$ is formed within each plaquette under a small flux deviation from $\Phi_{\rm tot} = \chi a = \pm\pi$, and the bulk transverse current effectively averages to zero as described through the vertical dashed lines. The induced parallel flow screens the effect of the perturbation $\Delta\chi$. The conservation of the Meissner current close to the boundaries is ensured through Andreev processes shown at rungs $(1,2)$ and $(L-3, L-2)$ which have flown to the strong-coupling limit. In addition, at the sites 0 and $L-1$, similar to the Josephson junction with Majorana fermions [76, 172, 262], the presence of gapless Majorana modes allows for a (perturbative) current proportional to $t_\perp$. We then find a Majorana current in orange satisfying the property $\langle j_{M,2\to1}(0)\rangle = -\langle j_{M,2\to1}(L-1)\rangle$, where 2 and 1 refer to the wire indices. The choice of vector potentials at the first and last rungs are fixed such that the Peierls phase for an electron or Majorana fermion is half of that of a Cooper pair.

Therefore, the topological proximity effect takes place as long as $|\tilde{\mu}| < \bar{\Delta}_2$. For $|\tilde{\mu}| = \bar{\Delta}_2$, by analogy to the commensurate-incommensurate transition [260], the pinning of θ^- should be suppressed, and the system effectively behaves as if there is a chain of free fermions and a topological superconducting wire with 2MZM in Fig. 2.2c. Next, we develop a linear-response analysis in $\Delta\chi$ for the ladder system along the lines of Ref. [261]. In particular, we address the Majorana particle current at the boundaries of the system with 4 MZM, building an analogy with the topological Josephson junction [172, 262].

To evaluate the Meissner and Majorana currents, we employ the Heisenberg equation of motion for the density operator $d(n_1 - n_2)/dt = i[\mathcal{H}_{\rm hybrid}, n_1 - n_2]$ with $\hbar = 1$ and with $n_1(x) - n_2(x) = -\sqrt{2}\partial_x\phi_-/\pi$ (modulo a global background charge). Inte-

grating the continuity equation $\int dx[\partial(n_1 - n_2)/\partial t + \nabla \cdot \mathbf{j}(x)] = 0$, then we identify the parallel (intrawire) current (density) $j_\parallel$ and the interwire (vertical) current $j_\perp$ associated respectively to $\mathcal{H}_0^-$ and $\mathcal{H}_\perp$.

The perpendicular current associated with a unit charge $q = 1$ takes the form:

$$j_\perp(x) = -\frac{4t_\perp}{\pi} \sin(\sqrt{2}\theta^-) \cos(\sqrt{2}\phi^+). \tag{2.26}$$

If we apply the pinning condition found above $\langle\theta^-(x)\rangle = \Delta\chi x/\sqrt{2}$, we observe that the vertical current which was formally zero when $\Delta\chi = 0$ now gives an oscillatory response with the space variable x in the continuum limit. We check that $\int dx\langle j_\perp(x)\rangle = 0$, as an indication that circulating Meissner currents still take place if we assume a small deviation from π flux. Below, we assume that the left and right boundaries of the sample are located at $x = 0$ and $x = L - 1$ as in Fig. 2.3. Since we have fixed $a' = a = 1$, the variable $L - 1$ here will also denote the position of the last site.

To evaluate the parallel current from Eq. (2.15), it is important to mention that the charge operator has been defined as $n_1(x) - n_2(x) = -\sqrt{2}\partial_x\phi_-/\pi$ for a unit charge $q = 1$. To define the current associated to Cooper pairs, we shall then multiply this operator by $q = 2$, which then results in:

$$j_\parallel(x) = -\frac{2\sqrt{2}vK}{\pi}\nabla\theta^-(x). \tag{2.27}$$

In the bulk, a Meissner current with charge $q = 2$ is then formed. From Eq. (2.25), we obtain:

$$\langle j_\parallel(x)\rangle = -\frac{2\sqrt{2}vK}{\pi}\langle\nabla\theta^-(x)\rangle = -\frac{2vK\Delta\chi}{\pi}, \tag{2.28}$$

which screens the effect of the magnetic flux variation; see Fig. 2.3. The continuity of the bulk Meissner current $\langle j_\parallel\rangle = -2vK\Delta\chi/\pi$ close to the two boundaries in the vertical direction (at sites $j = 1, 2$ and sites $j = L-3, L-2$ formally) is ensured by the Andreev processes, which have flowed to the strong-coupling limit. Once $\Delta\chi a \neq 0$,

in addition to the normal Meissner current formed by the bulk Cooper pairs, the hopping term at the two edges also induces an edge Majorana fermion current. The Majorana responses at sites 0 and $L-1$ will be proportional to the perturbation $t_\perp$.

Based on the analysis of Sec. 1.2.2, we introduce the four MZM operators according to the convention in Eq. (1.61):$\{\gamma_B^1(0), \gamma_B^2(0), \gamma_A^1(L-1), \gamma_A^2(L-1)\}$. To describe the effect of $\Delta\chi$ symmetrically on the Majorana fermions in the first and last (orange) unit cells in Fig. 2.3, we define a vector potential of the form $A_\perp(0) = A_{\perp,2\to1} = (\Delta\chi a)/(2a')$ at the first rung (and effectively zero vector potentials in the other segments of the first cell) associated to a unit charge $q = 1$; the symbol $2 \to 1$ means going from (lower) wire 2 to (upper) wire 1. The associated Peierls phase at $j = 0$ for the Majorana fermions then takes the form $A_\perp(0)a' = \Delta\chi a/2$. In the last unit cell, we may define $A_\perp(L-1) = A_{\perp,2\to1} = -A_\perp(0)$ (and effectively zero vector potentials in the other segments of the last cell). In this geometry of parallel wires, the operator $c_1^\dagger c_2$ then turns into $\gamma_B^1(0)\gamma_B^2(0)/4$, which results in

$$\begin{aligned}\mathcal{H}_\perp(0) &= \frac{t_\perp}{2}\sin\left(\frac{\Delta\chi a}{2}\right) i\gamma_B^1(0)\gamma_B^2(0) \\ &\approx \frac{t_\perp a}{4}\Delta\chi i\gamma_B^1(0)\gamma_B^2(0).\end{aligned} \tag{2.29}$$

When $\Delta\chi a = 0$, $\mathcal{H}_\perp(0)$ is zero, reflecting that the phase with 4-Majorana edge modes is protected against a π-flux since the hopping term $t_\perp e^{i\chi x_j} = t_\perp(-1)^j$ becomes real and the presence of time-reversal symmetry indicates that in this case $t_\perp$ should not hybridize the MZM.

At the left boundary of the system, the Majorana current is denoted as $\langle j_M(0)\rangle = \langle j_{M,2\to1}(0)\rangle$ and is defined as $\langle j_M(0)\rangle = \partial\langle\mathcal{H}_\perp(0)\rangle/\partial(aA_{\perp,2\to1}(0)) = 2\partial\langle\mathcal{H}_\perp(0)\rangle/\partial(a\Delta\chi)$, which results in:

$$\langle j_M(0)\rangle = (t_\perp/2)\langle i\gamma_B^1(0)\gamma_B^2(0)\rangle. \tag{2.30}$$

In the π-flux configuration, $[i\gamma_B^1(0)\gamma_B^2(0), \mathcal{H}_{\text{hybrid}}] = 0$, the parity operator $i\gamma_B^1(0)\gamma_B^2(0)$ associated to these two MZM is equally likely to take an expectation value ±1. Then,

$\langle i\gamma_B^1(0)\gamma_B^2(0)\rangle = 0$ on average and accordingly $\langle j_M(0)\rangle$. As soon as one switches on $\Delta\chi a = 0^+$, to minimize the energy, the parity operator $\langle i\gamma_B^1(0)\gamma_B^2(0)\rangle$ is locked to -1, producing a response $\langle j_M(0)\rangle = (t_\perp/2)$. Here, the Majorana current satisfies $\langle j_M(0)\rangle = -\langle j_M(L-1)\rangle$ where $j_M(L-1) = j_{M,2\to1}$. This relation can be derived from the boundary term

$$\mathcal{H}_\perp(L-1) \approx -\frac{t_\perp a}{4}\Delta\chi i\gamma_A^1(L-1)\gamma_A^2(L-1). \tag{2.31}$$

By symmetry between the two wires' boundaries, we have the relations $\gamma_A^1(L-1) \leftrightarrow \gamma_B^2(0)$ and $\gamma_A^2(L-1) \leftrightarrow \gamma_B^1(0)$, ensuring that $\langle\mathcal{H}_\perp(0)\rangle = \langle\mathcal{H}_\perp(L-1)\rangle$. The identification $\langle j_M(0)\rangle = -\langle j_M(L-1)\rangle$ comes from the vector potential $A_{\perp,2\to1}(L-1) = -A_{\perp,2\to1}(0) = -(\Delta\chi a)/2a'$, as shown in Fig. 2.3. When writing Eq. (2.31), we have assumed that $t_\perp(-1)^j$ takes the same values at $j = 0$ and $j = L-1$ implying that $L-1$ is even; an odd value of $L-1$ would lead to the same physical result and would just flip the value of $\langle i\gamma_A^2(L-1)\gamma_A^1(L-1)\rangle$ at the boundary to satisfy $\langle\mathcal{H}_\perp(0)\rangle = \langle\mathcal{H}_\perp(L-1)\rangle$. This shows that the physics remains the same independently of the relative parity between the two pairs of Majorana fermions at the boundaries.

If we change $\Delta\chi \to -\Delta\chi$, all the currents should flip their signs. The energy conservation of $\langle\mathcal{H}_\perp\rangle$ is related to a flip of the parity operator formed by the two Majorana fermions at one boundary. There is then a jump of size $t_\perp$ associated with the edge MZM current when changing the sign of $\Delta\chi$ close to π-flux per plaquette. This situation is therefore very similar to a Josephson junction with a resonant level which can be realized with a double-dot charge qubit and which shows a similar 'jump' in the superconducting Josephson response for a π phase shift [263]. The resonant level here is formed at π flux per plaquette through the two values of the expectation value of the parity operator $i\gamma_B^1(0)\gamma_B^2(0) = \pm1$ at the boundary. Fig. 2.3 illustrates the formation of the composite Meissner-Majorana current. It enables us to detect the 4-Majorana edge mode through the measurement of the vertical current at the two boundaries. Physically, to measure the Majorana current, one can resort

to a setting similar to the one suggested in Ref. [264], where an analogy between Majorana fermions and a resonant level was also addressed.

2.2.2 At arbitrary flux

We can also consider, in general, any configuration allowed by Eq. (3.34):

$$a\left[(k_F^1 + k_F^2) - m\chi\right] = 0 \mod 2\pi, \tag{2.32}$$

with m odd and $\chi a \neq \pm\pi$. Adjusting the densities in the two wires, one can then reach quantum Hall plateaux for specific values of the magnetic field. As before, one can safely drop out fast oscillating terms, such as $\propto \int dx \cos(\cdots \mp 2\chi x)$ in $\mathcal{H}_\perp$ (2.16), and reach for $m = 1$

$$\mathcal{H}_\perp = -\frac{t_\perp}{\pi a}\int dx \cos[\sqrt{2}(\theta^- - m\phi^+)]. \tag{2.33}$$

In the strong-coupling limit, $t_\perp \gg \Delta$, the form of the interwire hopping term $\mathcal{H}_\perp$ (2.33) satisfies the classification of a $\nu = 1/m$ Laughlin state (with m odd) and integer quantum Hall effect when $\nu = 1$ [28, 29]. We show below that in that case the intrawire pairing term Δ flows to zero according to renormalization group arguments. In the case of $m = 1$, the quantum Hall phase can be achieved for free fermions, as experimentally confirmed in ultra-cold atoms [241], and we check that the hopping term is relevant in that case for $K = 1$ under the renormalization group procedure. Long-range Coulomb forces resulting in $K \ll 1/2$ can also stabilize the fractional quantum Hall state at $\nu = 1/3$ by making the tunneling term in Eq. (2.33) relevant for $m = 3$, as numerically observed [245, 246]. In that case, one must include higher harmonics contributions to the definition of the fermion operator in Eq. (2.13) to obtain Eq. (2.33) for the same density-flux constraint as in Eq. (2.32) [245].

The relevance of the hopping term $t_\perp$ here pins the mode $(\theta^- - m\phi^+)$ to zero, which can be interpreted as a (bulk) gapped mode by analogy to a two-dimensional system. A ladder system is described by four bosonic fields, which implies that two modes are

still gapless. The latter describe the two chiral edge modes of the ladder system. To properly describe the system and the edge states, it is convenient to introduce four chiral fields [68, 244]

$$\phi_r^\alpha = \frac{\theta_\alpha}{m} + r\phi_\alpha, \tag{2.34}$$

with $\alpha = 1, 2$ representing the wire index and now $r = +1/-1$ denoting the left/right moving particles in agreement with Eq. (2.13). The chiral bosonic fields satisfy the commutation relation

$$[\phi_r^\alpha(x), \phi_p^\beta(x')] = ir\frac{\pi}{m}\delta_{rp}\delta_{\alpha\beta}\text{Sign}(x' - x). \tag{2.35}$$

New modes can be constructed from ϕ_r^α which capture the properties of the gapped bulk states (θ, ϕ)

$$\begin{cases} \phi = (-\phi_{-1}^1 + \phi_{+1}^2)/2, \\ \theta = (\phi_{-1}^1 + \phi_{+1}^2)/2, \end{cases} \tag{2.36}$$

and gapless edge states (θ', ϕ')

$$\begin{cases} \phi' = (-\phi_{-1}^2 + \phi_{+1}^1)/2, \\ \theta' = (\phi_{-1}^2 + \phi_{+1}^1)/2. \end{cases} \tag{2.37}$$

The commutation relation reads:

$$[\phi(x), m\theta(x')] = i(\pi/2)\text{Sign}(x' - x), \tag{2.38}$$

and the same for the gapless modes (ϕ', θ'). The bulk gapped mode is now related to the field ϕ. When $t_\perp \gg \Delta$, correspondingly, the bulk mode ϕ is pinned to a classical value since

$$\mathcal{H}_\perp = -\frac{t_\perp}{\pi a}\int dx \cos(2m\phi). \tag{2.39}$$

A gap is opened in the bulk as previously shown in Fig. 2.1c. In Appendix D and Eq. (D.11), we check that the two gapless modes which produce a chiral Luttinger theory are $L(x) = \phi_{+1}^1(x) = \theta'(x) + \phi'(x)$ and $R(x) = \phi_{-1}^2(x) = \theta'(x) - \phi'(x)$. Starting

from free fermions and $K = 1$, the edge Luttinger parameters are $K^e = 1$, $v^e = v$. We thus realize an Abelian quantum Hall phase at filling factor $\nu = 1/m = 1$ in the presence of an arbitrary uniform flux. If we change the direction of the magnetic field, which is equivalent to change $m \to -m$ in Eq. (2.32), we obtain similar results by inverting the left and right-moving particles' definitions in Eq. (2.34).

The two gapless modes are, furthermore, protected against a small intrawire pairing. Indeed, we can rewrite $\mathcal{H}_\Delta$ as

$$\mathcal{H}_\Delta = -\frac{\Delta}{\pi a}\int dx e^{i[2m\theta+\sqrt{2}(\theta^- + m\phi^-)]} + \text{H.c.}. \tag{2.40}$$

Since ϕ is pinned to a classical value minimizing the cosine potential term, then the dual mode θ oscillates rapidly: $\langle e^{i\theta(x)}e^{-i\theta(0)}\rangle \propto e^{-x/\xi}$ with a correlation length ξ proportional to $1/t_\perp$. Therefore, $\mathcal{H}_\Delta$ flows to zero for large $t_\perp$. For the observables, the integer Laughlin state is revealed in the edge current. A direct calculation of the parallel and perpendicular currents defined in Sec. 2.2.1 for a unit charge $q = 1$ leads to

$$\begin{aligned}\langle j_\perp(x)\rangle &= -\frac{2t_\perp}{\pi}\langle \sin(2m\phi)\rangle = 0,\\ \langle j_\parallel(x)\rangle &= -\frac{\sqrt{2}vK}{\pi}\langle \nabla\theta^-(x)\rangle.\end{aligned} \tag{2.41}$$

Choosing an alternative gauge for the magnetic vector potential

$$A_\perp = 0, \qquad \oint \vec{A}\cdot d\vec{l} = \left(A^1_\parallel - A^2_\parallel\right)a = \chi a, \tag{2.42}$$

we rewrite the quadratic contribution to the action for the $-$ bosonic field, as

$$S[\phi^-,\theta^-] = \frac{v}{2\pi}\int dx d\tau \left[\frac{1}{K}\left(\nabla\phi^-\right)^2 + K\left(\nabla\theta^- + A^-_\parallel\right)^2\right], \tag{2.43}$$

where $A^-_\parallel = (A^1_\parallel - A^2_\parallel)/\sqrt{2}$. To extremize the action $\partial S/\partial\theta^- = 0$, it requires $\langle\nabla\theta^-(x)\rangle = -A^-_\parallel$. The edge current of the integer Laughlin state for a unit charge $q = 1$ and for free electrons $K = 1$ hence becomes

$$\langle j_\parallel(x)\rangle = \frac{vK\chi}{\pi}. \tag{2.44}$$

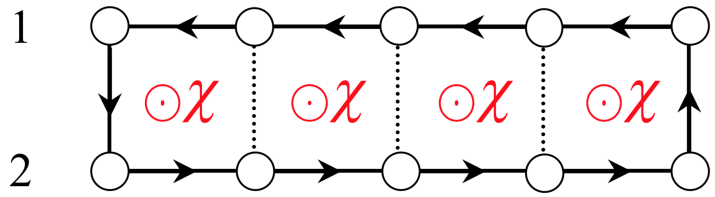

Figure 2.4: Edge current for a unit charge $q = 1$ in the Abelian quantum Hall state ($\nu = 1$) when $t_\perp \gg \Delta$. An arbitrary uniform magnetic flux is applied on each plaquette.

It follows the same direction as the vector potential produced by the magnetic flux (shown in Fig. 2.4).

In the presence of Coulomb interactions, as shown in Appendix D, backscattering effects occur for $K \neq 1$ when integrating out the bulk (gapped) mode on the two-leg ladder system, and as a result the charge at the edges will be adiabatically deformed [68, 238, 244]. In contrast, the bulk polarization in a Thouless pump geometry [265] is stable under Coulomb interactions as shown in Appendix E, reflecting the Zak phase, and measuring ν. Similar arguments apply to the Laughlin phase $\nu = 1/3$ stabilized with long-range Coulomb interactions [245, 246]. The charge at the edges in these ladder systems could be measured accurately [162, 238, 244, 266–268].

The quantum Hall phase at $\nu = 1$ occurs when $t_\perp \geq \Delta$. In the weak-coupling limit $t_\perp \leq \Delta$, for an arbitrary flux, both the first order (2.33) and the second order (2.23) contributions of $t_\perp$ are irrelevant from renormalization group arguments since the superfluid mode θ_1 is now pinned. In Appendix B, we find that the most relevant term is

$$\begin{aligned} \mathcal{H}_\perp^{(4)} &= -\frac{t_\perp^4}{3\pi a \Delta^3} \int dx \cos[2(\theta_2(x+2a) - \theta_2(x)) + 4\chi a], \\ &\propto e^{4i\chi a} c_2^\dagger(x-a) c_2^\dagger(x) c_2(x+a) c_2(x+2a) + H.c.. \end{aligned} \tag{2.45}$$

The constraint on the phases

$$\theta_2(x+2a) - \theta_2(x) = -2\chi a, \tag{2.46}$$

helps to form a local current formed by the Cooper pairs within three adjacent pla-

quettes and using Eq. (2.28), this leads to

$$\langle j_{\parallel}(x)\rangle_{\text{plaquette}} = -\frac{2vK\chi}{\pi}. \tag{2.47}$$

Deviating from the π-flux substantially in the weak-coupling region, an arbitrary flux breaks the time reversal symmetry $\mathcal{T}$ and destabilizes the proximity effect. Consequently, there is no induced superconducting gap in the free fermion wire. Still, two Majorana edge modes persist in the original Kitaev superconducting wire. The protection against orbital magnetic effects in this weak-coupling region could be useful for applications in quantum computation and engineering of Majorana fermions with magnetic fluxes [269].

Fig. 2.2b and Fig. 2.2c show the phase diagrams for the cases of π flux per plaquette at half filling and arbitrary fluxes, when adjusting the densities in the wires such that the proximity effect can effectively takes place. In the strong-coupling limit, on the other hand, one is able to distinguish the CDW and Abelian quantum Hall states from the responses of Thouless pump [265]. We refer the reader to Appendix E, where a proposal for the measurement is raised and the stability of the bulk polarization under Coulomb interactions is also discussed.

2.3 Weakly coupled ladders

In this section, we present two proposals to realize two-dimensional topological phases using multiple coupled wires or coupled ladders, corresponding to the third and fourth cases of Sec. 2.1.

First, we design a $p+ip$ superconductor [14] starting from the bonding-antibonding band representation of a pair of wires — "ladder geometry" — and generalizing the analysis to coupled ladder systems. The advantage of fabricating weakly coupled ladder systems compared to symmetrically coupled wires is that one can control the range of the p-wave superconducting channel in both directions, namely x and y, when projecting a pair of wires or the ladder system onto the lowest bonding band.

Here, a pair of wires with appropriate Peierls phases ζ and χ will generate an ip_x superconducting channel, and coupling weakly the ladders together will provide the p_y channel. If we would consider instead only strongly coupled wires or symmetrically coupled wires, then the projection onto the lowest band would result in long-range pairing terms in the direction perpendicular to the wires, through the tunneling term $t_\perp$. However, the effective two-dimensional model projected onto the lowest band basis would be of the same class as a topological p_x superconductor (with two Fermi points). Other proposals coupling quantum wires have suggested the possible engineering of ip channels through bath or reservoir engineering [30, 270–272] by analogy to the two-dimensional case [14]. It is also important to mention that for spins-1/2 fermions, similar ladder constructions allow us to reproduce d-wave superconductivity, D-Mott and pseudogap physics, relevant to cuprate superconductors [63, 273, 274].

Second, we address the case of coupled spinful or spin-1/2 ladder systems. We start by giving a brief review of the previous result obtained by Karyn and A. Petrescu [68] on the two-leg ladder, where a Cooper pair Laughlin state is formed at filling $\nu = 1/2$. In the presence of a uniform magnetic field and long-range repulsive interactions, we then show explicitly how the coupled wire system can form a single bulk fluid with chiral modes at the edges now carrying a charge in agreement with the two-dimensional bulk-edge correspondence [25].

2.3.1 A spinless $p + ip$ superconductor

In the first subsection, we present our proposal to engineer the $p+ip$ superconductor in coupled ladder geometries, referring to the third case of study in Sec. 2.1. Depicted in Fig. 2.5 (left), our building block is a blue ladder comprising two strongly-coupled wires labeled by $\alpha = 2l - 1, 2l$ where l is an integer. The flux attachment which will be responsible for the ip_x channel is shown in Fig. 2.5 (right top).

First, we re-analyze a block, say with $\alpha = 1, 2$, for the case with $\zeta = \chi$. The kinetic

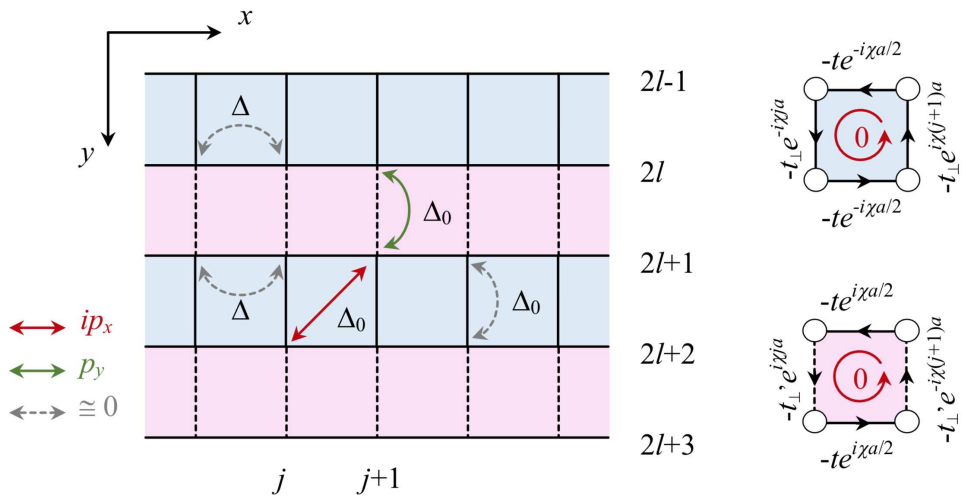

Figure 2.5: (Left) Coupled ladder construction for a $p+ip$ superconductor. A building block is formed in blue with two strongly-coupled wires. The blue ladders then couple together via the pink regions. While the pairing terms denoted by grey arrows (both intra- and interwire) are suppressed in the strong coupling limit, the pairings denoted by red and green arrows (interwire only) are responsible for the ip_x and p_y channels; (Right) Flux attachment in each square plaquette with $\zeta a = \chi a = \pi$. In each square unit cell, the total net flux is zero. Peierls phases take opposite values within two successive plaquettes in y direction for the same hopping process.

part of the Hamiltonian is described by $\mathcal{H}_{\parallel}$ and $\mathcal{H}_{\perp}$ in Eq. (2.2) with

$$\zeta = \chi, \quad \Phi_{\text{total}} = 0. \tag{2.48}$$

As discussed in Sec. 2.1, we assume here that the vector potentials related to ζ and χ are engineered, for instance, in ultra-cold atom systems. In solid-state nanowires, this can also be realized through a space-dependent magnetic field $B_z = \chi/a' - \zeta\pi/(2a')\sin(\pi y/a')$. Since the total flux per plaquette is zero, we can rewrite the band structure as the one of Fig. 2.1b, in the absence of magnetic flux, performing a proper gauge transformation similar to Eq. (2.9). The pairing terms will be modified accordingly, then providing the required physics, namely an ip_x channel, after fixing the value of $\chi = \zeta = \pi/a$. Coupling weakly the ladders together, we realize a p_y channel. There are two key properties to this proposal. First, the magnetic field B_z will be staggered in y direction implying that χ also takes opposite values in two successive plaquettes in y direction with the requirement that $\Phi_{\text{tot}} = 0$ in all

plaquettes. Here, χ represents a periodic staggered step-like function in y direction. Therefore, induced Zeeman effects at the position of the wires will be small and controllable through another magnetic field B_x along x direction (which is important to induce the proximitized p-wave pairing potentials [275]). Second, the choice $\chi = \zeta = \pi/a$ leads to imaginary hopping terms $\pm it$ along the wires, which break chiral symmetry and time-reversal symmetry while preserving particle-hole symmetry. This then allows for a wire-construction of a topological phase of class D, *e.g.* a two-dimensional $p + ip$ superconductor [70]. The transverse hopping term of the form $t_\perp(-1)^j$ is real, therefore ensuring that Majorana modes can occur at zero energy. Below, we provide two physical understandings of the results when using equivalent low-energy theories related to Fig. 2.1b and Fig. 2.1c.

Performing the gauge transformation (2.9),

$$c_1(j) = e^{i\chi x_j/2}\widetilde{c}_1(j), \quad c_2(j) = e^{-i\chi x_j/2}\widetilde{c}_2(j), \tag{2.49}$$

we can define the new basis for the bonding (+) and anti-bonding (−) fermions

$$\widetilde{c}_\pm(j) = [\widetilde{c}_1(j) \pm \widetilde{c}_2(j)]/\sqrt{2}. \tag{2.50}$$

The two-band model in Eq. (2.7) and Eq. (2.8) is recovered with the band structure shown in Fig. 2.1b. A gap of scale $(2t_\perp)$ is opened between "+/−" bands. Below, we fix the chemical potential μ such that the + band becomes partially filled and the − band remains empty. We then project a pair of wires, the blue ladder system, onto the lowest bonding band pair basis:

$$\mathcal{H}_{0,+} = -\sum_{k_x}[2t\cos(k_x a) + t_\perp + \mu]\widetilde{c}_+^\dagger(k_x)\widetilde{c}_+(k_x). \tag{2.51}$$

In the strong coupling limit $t_\perp \gg \Delta_i$, the phase ζ is important to suppress the intrawire pairing. The intrawire pairing term $\Delta_1 = \Delta_2 = \Delta$ becomes

$$\mathcal{H}_\Delta = i\Delta\sum_{k_x}\sin(k_x a)\cos(\zeta/2a)\widetilde{c}_+^\dagger(k_x)\widetilde{c}_+^\dagger(-k_x) + \text{H.c.}. \tag{2.52}$$

Below, we set $\chi = \zeta = \pi a$, such that this contribution becomes zero. The interwire contribution Δ_0 involving a given rung also vanishes between nearest (N) neighbors when projecting onto the lowest band:

$$\begin{aligned} 0 = \mathcal{H}_{\Delta_0,\mathrm{N}} &= \Delta_0 \sum_j c_1^\dagger(j) c_2^\dagger(j) + \mathrm{H.c.} \\ &= \frac{\Delta_0}{4} \sum_{k_x} \{\widetilde{c}_+^\dagger(k_x), \widetilde{c}_+^\dagger(-k_x)\} + \mathrm{H.c.}, \end{aligned} \tag{2.53}$$

but survives between next-nearest (NN) neighbors

$$\begin{aligned} \mathcal{H}_{\Delta_0,\mathrm{NN}} &= \Delta_0 \sum_j c_1^\dagger(j) c_2^\dagger(j+1) + \mathrm{H.c.} \\ &= \widetilde{\Delta} \sum_{k_x} i \sin(k_x a) \widetilde{c}_+^\dagger(k_x) \widetilde{c}_+^\dagger(-k_x) + \mathrm{H.c.}, \end{aligned} \tag{2.54}$$

with $\widetilde{\Delta} = (\Delta_0 e^{i\chi a/2})/2$. Adding a term $\Delta_0 \sum_j c_2^\dagger(j) c_1^\dagger(j+1) + \mathrm{H.c.}$ would result in an identical contribution in the bonding band basis. In the equations above, we have ignored all irrelevant terms involving the " $-$ " band. Once we fix the flux value

$$\chi a = \pi, \quad \widetilde{\Delta} = i\Delta_0/2, \tag{2.55}$$

we engineer a purely imaginary ip_x channel for the bonding fermions in each blue building block $\alpha = 2l-1, 2l$. The pair of strongly-coupled wires then effectively behaves as a topological ip_x superconductor with two Majorana zero modes, one at each boundary.

Now, we couple the blue building blocks or ladders along the y direction by the tunneling amplitude $t'_\perp$ (corresponding to the pink blocks in Fig. 2.5, left) with a reversed flux unit $\chi \to -\chi$ depicted in Fig. 2.5 (right bottom). The magnetic field $B_z = \chi/a' - \zeta\pi/(2a')\sin(\pi y/a')$ then becomes staggered in the y direction. To realize the $ip_x + p_y$ superconductor (or $p_x \pm ip_y$ superconductor modulo gauge redefinitions), the magnetic field B_z must be uniform in the x direction but staggered in the y direction.

Formally, this construction is correct as long as $t'_\perp \ll t_\perp$, such that the bonding-antibonding band representation of a two-coupled wire model remains valid. Through a pink region, we obtain the Hamiltonian:

$$\begin{aligned}\mathcal{H}'_\perp &= -t'_\perp \sum_{l=1}^{M'/2} e^{-i\chi x} c^\dagger_{2l}(x) c_{2l+1}(x) + \text{H.c.},\\ \mathcal{H}'_{\Delta_0,\text{N}} &= \Delta_0 \sum_{l=1}^{M'/2} c^\dagger_{2l}(x) c^\dagger_{2l+1}(x) + \text{H.c.}\end{aligned} \tag{2.56}$$

For the coupled wire system, the gauge transformation (2.49) can be generalized as

$$c_{2l-1}(j) = e^{i\chi x_j/2}\widetilde{c}_{2l-1}(j), \quad c_{2l}(j) = e^{-i\chi x_j/2}\widetilde{c}_{2l}(j), \tag{2.57}$$

which leads to

$$\begin{aligned}\mathcal{H}'_\perp &= -t'_\perp \sum_{k_y} \cos(k_y a')\widetilde{c}^\dagger_+(k_y)\widetilde{c}_+(k_y),\\ \mathcal{H}'_{\Delta_0,\text{N}} &= \frac{\Delta_0}{2}\sum_{k_y} i\sin(k_y a')\widetilde{c}^\dagger_+(k_y)\widetilde{c}^\dagger_+(-k_y) + \text{H.c.}.\end{aligned} \tag{2.58}$$

Thus we can implement a purely real p_y channel for the bonding fermions, assuming that $t'_\perp \ll (t_\perp, t)$. The relative phase between the ip_x and p_y channel is locked through the gauge transformation (2.57).

Next, we define two-dimensional fermion operators $\widetilde{c}_+(\mathbf{k}) = \widetilde{c}_+(k_x, k_y)$. The goal is to study the phase diagram and edge state properties associated with the system. To that end, it is convenient to switch to the Majorana fermion representation,

$$\widetilde{c}_+(\mathbf{k}) = \frac{1}{2}\left(\gamma_1(\mathbf{k}) + i\gamma_2(\mathbf{k})\right). \tag{2.59}$$

Similar to Ref. [30], for simplicity we set the lattice spacing $a = a' = 1$ and we concentrate on the regime with low densities around $\mathbf{k} \simeq (0,0)$, where we have

$$\begin{aligned}\mathcal{H}_+ &\simeq \mathcal{H}_{0,+} + \mathcal{H}_{\Delta_0,\text{NN}} + \mathcal{H}'_\perp + \mathcal{H}'_{\Delta_0,\text{N}}\\ &= -\frac{1}{4}\sum_{\mathbf{k}} \gamma^T(-\mathbf{k})\mathcal{H}_+(\mathbf{k})\gamma(\mathbf{k}),\end{aligned} \tag{2.60}$$

with $\gamma^T(-\mathbf{k}) = (\gamma_1(-\mathbf{k}), \gamma_2(-\mathbf{k}))$ and

$$\mathcal{H}_+(k) = uk_x\tau^z + [\epsilon_0 + \frac{k_x^2}{2m} + T_2\cos(k_y)]\tau^y + R_2\sin(k_y)\tau^x. \tag{2.61}$$

Here τ^i $(i = x, y, z)$ denote Pauli matrices and effective parameters are given by $u = \Delta_0$, $m = 1/(2t)$. The three parameters locating the phase transitions read

$$\epsilon_0 = -2t - t_\perp - \mu, \quad T_2 = -t'_\perp, \quad R_2 = -\Delta_0. \tag{2.62}$$

The phase diagram of $\mathcal{H}_+$ (2.61) is carefully studied in Ref. [30], and we adjust the discussion for the Majorana zero modes at a boundary to our situation. By tuning μ, ϵ_0 goes from a large negative value to a large positive value (with respect to $\pm|T_2|$), and this produces two phase transitions from an anisotropic topological superconducting phase to the trivial strong paired state through the occurrence of an intermediate topological two-dimensional Moore-Read Particle-Hole phase [13].

A large (positive) $\epsilon_0 \gg |T_2|$ value hinders the occurrence of MZM from energetics point of view in the trivial strong-paired phase. The chemical potential is located below the bottom of the lowest band. When $\epsilon_0 = +t'_\perp = +|T_2|$, we enter into the intermediate topological phase. The energy spectrum becomes gapless in the two-dimensional sense with the lowest energy eigenvalue $-\Delta_0\sqrt{k_x^2 + k_y^2}$ close to $k_x = k_y = 0$. A two-dimensional gapless Majorana mode flows around the sample, as a chiral edge mode. The physics is then related to the neutral sector of a Moore-Read Particle-Hole Pfaffian phase [13] with an effective $p_x - ip_y$ channel for $R_2 < 0$. By changing the sign of $\chi = \zeta$ by $-\pi$, we flip the sign of R_2, and the intermediate region now becomes the Pfaffian phase [13]. Changing the sign of R_2 will change the velocity (direction) of propagation of the Majorana mode. In fact, as long as $|\epsilon_0| \leq |T_2|$ [30], the system stabilizes one gapless chiral Majorana fermion. Increasing the chemical potential further, this results in (very) negative values of $\epsilon_0 \leq -|T_2|$ and therefore low-energy modes move away from $k_x = k_y = 0$. Modes in the y direction associated to the $R_2\sin(k_y)\tau^x$ term now cost a finite energy and the system

becomes anisotropic. This parameter regime is adiabatically linked to N decoupled ip_x topological superconductors with $2N$ MZM. In our geometry, the $2N$ gapless Majorana modes should be protected against *real* Δ_0 and $t'_\perp$ terms in Eq. (2.58), meaning that the Majorana fermions of each chain should remain decoupled from those in other chains.

For completeness, we provide an alternative understanding of the emergence of a purely ip_x channel using the band structure of Fig. 2.1c. As mentioned in Sec. 2.1, the $\zeta a = \pm\pi$ phase on the two wires produces equivalently purely imaginary hopping terms $\pm it$ for the two wires, then modifying the band structure of free fermions as $\mp 2t \sin(k_x a)$. When $t_\perp = 0$, these two bands cross at $k_x = k_0 = 0$ with the indices 1 and 2 in Fig. 2.1c switched. Furthermore, in Eq. (2.2), the perpendicular tunneling term $t_\perp$ becomes modified as $t_\perp(-1)^j$. By Fourier transform, we then conclude that for this situation, the tunneling term $t_\perp$ does not open a gap at the crossing point, *i.e.* at $k_0 = 0$. If we also Fourier transform the Δ_0 channel in Eq. (2.54) including the effect of the phases $\zeta a = \pm\pi$ for the two wires, then the wave-vectors (of the two wires) in Fig. 2.1c are modified as $k_x \to k_x \pm \zeta/2$, and around the crossing point $k_0 = 0$, the Δ_0 NN-neighbor channel can indeed produce a term, as:

$$\frac{\Delta_0}{M} \sum_j \sum_{k_x, k'_x} \widetilde{c}_1^\dagger(k'_x) \widetilde{c}_2^\dagger(k_x) e^{i(k_x + k'_x)ja} e^{ik'_x a} e^{i\frac{a\zeta}{2}} + \text{H.c.}. \tag{2.63}$$

When $k_x = -k'_x = 0$, the pairing term vanishes. Then, we confirm that the induced gap at the Fermi energy takes the form $\widetilde{\Delta} = (\Delta_0 e^{i\zeta a/2})/2$ with here $\zeta = \chi = \pi/a$. We also check that the N-neighbor Δ_0 channel vanishes in the low-energy subspace due to anti-commutation rules between fermionic operators $\Delta_0 \widetilde{c}_1^\dagger(0) \widetilde{c}_2^\dagger(0) + \text{H.c} \approx 0$. To proceed and understand the correspondence with Eq. (2.61), we remind that the mapping onto Fig. 2.1c is applicable as long as one assumes to be close to the band crossing point. Taking into account the momentum boost $k \to k \pm \zeta/2$ with $\zeta = \pi/a$, this corresponds to the case where each wire is half-filled. In the corresponding Fig. 2.1b this implies that the lowest band is now close to the full filling, which

corresponds to change $-2t \to +2t$ for the lowest bonding band compared to the case studied before where the (lowest) band is almost empty. One must therefore re-adapt in the arguments that ϵ_0 now becomes $+2t - \mu - t_\perp$; when the lowest band is filled then this means that $k_{F,+} = \pi/a$. Then, to make the correspondence with Eq. (2.61) complete, one can then re-identify the fermionic operators $\widetilde{c}_1(k)$ and $\widetilde{c}_2(k)$ close to the crossing point k_0 with the left-moving and right-moving branches of the lowest band operator $\widetilde{c}_+(k)$. From Fig. 2.1, one can then apply the same arguments as in Eq. (2.61), modulo the fact that one re-defines $\epsilon_0 = 2t - t_\perp - \mu$.

When fixing the total flux per plaquette $\Phi_{\rm tot} = \chi - \zeta = 0$ and changing (decreasing) adiabatically the value of $\chi = \zeta$ from π/a, *i.e.* decreasing slightly the value of the magnetic field B_z, we observe that the transformation (2.57) remains applicable. Then, this produces additional real channels to the ip_x superconducting channel coming from Eq. (2.52) and Eq. (2.54), resulting in a $i(p_x - ip'_x)$ channel, whereas the p_y channel remains identical. A superconducting channel of the form $(p_x - ip'_x)$ (defined modulo the gobal phase $\pi/2$) should then slightly move progressively the $2N$ Majorana fermions in the anisotropic phase away from zero energy. On the other hand, the two-dimensional chiral gapless edge mode seems to survive in the Moore-Read phase. More precisely, entering this phase from the strong-paired phase which means that $\epsilon_0 = +t'_\perp = +|T_2|$, the lowest energy eigenvalue turns slightly into $-(u^2k_x^2 + (R_2k_y + vk_x)^2)^{1/2}$, where v is proportional to $\delta\chi\Delta_0$ and $\delta\chi = \pi/a - \chi$ (with $a = 1$). Therefore, when fixing either $k_x \neq 0, k_y = 0$ or $k_x = 0, k_y \neq 0$, the energy spectrum still allows for a linear gapless Majorana mode.

It is instructive to briefly address the limiting case where $B_z = 0$. In that case, all the channels p_x and p_y are real. In the low-energy description of Eq. (2.61) we have $u = 0$ and the last term R_2 describes all the superconducting terms $\tilde{\Delta}\sin k_y + \tilde{\tilde{\Delta}}\sin k_x$, where $\tilde{\Delta} = -\Delta_0$, and now $\tilde{\tilde{\Delta}}$ takes into account all the intra-ladder pairing terms $\tilde{\tilde{\Delta}} \sim -\Delta$. Assuming that $\tilde{\Delta} \sim \tilde{\tilde{\Delta}}$, we can redefine the R_2 contribution as $2\tilde{\Delta}\sin((k_x + k_y)/2)\cos((k_y - k_x)/2)$. The superconducting pairing term can be then re-written in

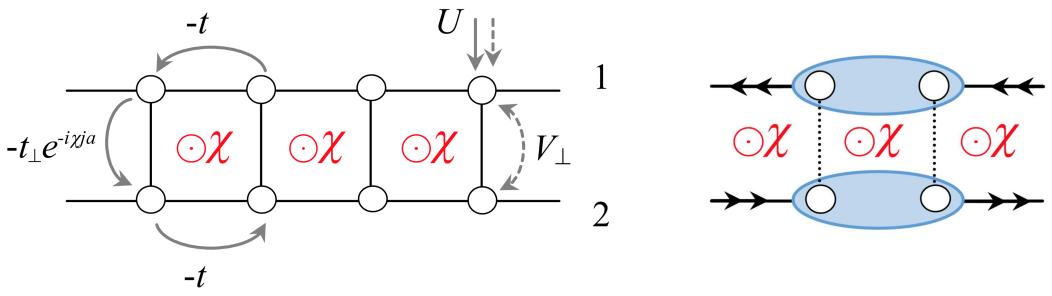

(a) (b)

Figure 2.6: (a) Weakly coupled spinful (spin-1/2) wires with a flux configuration $\Phi_{\text{tot}} = \chi a = (k_F^1 + k_F^2)a$. The dashed arrows represent the interactions between fermions with different spins; (b) Formation of Cooper pair Laughlin state at $\nu = 1/2$, where the chiral edge currents move in opposite direction compared to those in the Meissner effect.

terms of the wave-vectors $k' = (k_x + k_y)/2$ and $k'' = (k_y - k_x)/2$, which implies that in that case gapless excitations defined around $k' = 0$ will correspond to nodal quasiparticles in the bulk propagating between a $+$ and $-$ p-wave lobe, associated with zeroes of the superconducting term.

2.3.2 Generalization to spinful fermions

With arbitrary fluxes discussed in Sec. 2.2.2, another interesting comparison can be made with the case of spinful or spin-1/2 fermions. Karyn and A. Petrescu have previously shown in Ref. [68], for a spin-1/2 system, that the attractive Hubbard interaction and the long-range repulsive interwire interaction help stabilize a ladder generalization of a Cooper pair Laughlin state at $\nu = 1/2$. The attractive channel allows us to realize a Luther-Emery model [276] with Cooper pairs or bosons, and the long-range repulsive interaction then realizes the hard-core boson regime. An essential difference with the spinless situation is that here we take into account the spin-charge separation phenomenon of the Luttinger liquid. Therefore, as for a Luther-Emery liquid, the Cooper pairs are realized through a gap in the spin channel in the two wires. The two charge fields are still free in the wires, allowing more tunability to realize a Laughlin state at $\nu = 1/2$ of hard-core bosons from the charge sector.

The filling factor $\nu = 1/2$ reflecting the charges of quasiparticles in the bulk can be accessed through Thouless pump measurements. The main difference with the Meissner effect is that the edge current now flows in opposite direction, as shown in Fig. 2.6b compared to Fig. 2.3. Below, we first briefly review the main results and then we will extend the building block to coupled-ladder systems referring then to the fourth case of study in Sec. 2.1.

The key ingredients of the spinful ladder can be found in Fig. 2.6a. Four parts enter into the Hamiltonian

$$\mathcal{H}_{\text{spinful}} = \mathcal{H}_{\parallel} + \mathcal{H}_{\perp} + \mathcal{U} + \mathcal{V}. \tag{2.64}$$

The intra- and interwire hopping terms $\mathcal{H}_{\parallel}$ and $\mathcal{H}_{\perp}$ keep the form of the spinless case with the addition of the spin flavor $s =\uparrow,\downarrow$: $c_{\alpha}(j) \to c_{\alpha,s}(j)$. The flux configuration also satisfies $\zeta = 0$ and the constraint (2.32) for an arbitrary value of χ. For the interactions, we take into account the Hubbard and interwire Coulomb repulsion:

$$\begin{aligned} \mathcal{U} &= \sum_{j} \sum_{\alpha=1,2} U_{\alpha} n_{\alpha,\uparrow}(j) n_{\alpha,\downarrow}(j), \\ \mathcal{V} &= V_{\perp} \sum_{j} \sum_{s,s'=\uparrow,\downarrow} n_{1,s}(j) n_{2,s'}(j), \end{aligned} \tag{2.65}$$

where $n_{\alpha,s}(j) = c^{\dagger}_{\alpha,s}(j) c_{\alpha,s}(j)$ denotes the particle number operator. For simplicity, we consider two identical wires sharing the same attractive Hubbard interaction $U = U_1 = U_2 < 0$ and a repulsive long-range interaction $V_{\perp} > 0$ is added between the wires. We consider the weak-coupling regime $t_{\perp} \ll (|U|, |V_{\perp}|)$, where $\mathcal{H}_{\perp}$ acts as a small perturbation.

Applying bosonization techniques [34, 256], we introduce the spin (σ) and charge (ρ) degrees of freedom through the transformation

$$\begin{aligned} \phi_{\sigma}(x) &= \frac{1}{\sqrt{2}} (\phi_{\uparrow}(x) - \phi_{\downarrow}(x)), \\ \phi_{\rho}(x) &= \frac{1}{\sqrt{2}} (\phi_{\uparrow}(x) + \phi_{\downarrow}(x)), \end{aligned} \tag{2.66}$$

and the same for the dual modes $\theta_{\sigma,\rho}$. The Hamiltonian then takes the form:

$$\begin{aligned}
\mathcal{H}_{\text{spinful}} &= \mathcal{H}_\sigma + \mathcal{H}_\rho + \mathcal{H}_\perp, \\
\mathcal{H}_\rho &= \mathcal{H}^+_{0,\rho} + \mathcal{H}^-_{0,\rho}, \\
\mathcal{H}_\sigma &= \sum_{\alpha=1,2} \mathcal{H}^\alpha_{0,\sigma} + \frac{U}{2\pi^2 a}\int dx \cos(2\sqrt{2}\phi^\alpha_\sigma), \\
\mathcal{H}_\perp &= -\frac{t_\perp}{2\pi a}\int dx \sum_{s=\pm1}\sum_{r,r'=\pm1} e^{i\chi a} e^{ir'(k^1_F + rk^2_F)x} \\
&\quad \times e^{-ir'(\phi^r_\rho + r'\theta^-_\rho + s(\phi^r_\sigma + r'\theta^-_\sigma))} + \text{H.c.}.
\end{aligned} \tag{2.67}$$

Here, $\mathcal{H}^\pm_{0,\rho}$ and $\mathcal{H}^\alpha_{0,\sigma}$ with $\alpha = 1, 2$ take the Luttinger form. The Luttinger parameters are defined as $K_\sigma = K^1_\sigma = K^2_\sigma = (1+u)^{-1/2}$, $K^\pm_\rho = (1 - u \pm v_\perp)^{-1/2}$, where $u = |U|a/(\pi v)$, $v_\perp = 2V_\perp a/(\pi v)$. In the spin part, the attractive Hubbard interaction $\mathcal{U}$ plays the same role as the pairing term $\mathcal{H}_\Delta$ for the spinless particles, resulting in the pinning conditions for the spin modes (modulo $\pi/\sqrt{2}$):

$$\phi_\sigma = \phi^1_\sigma = \phi^2_\sigma \sim 0. \tag{2.68}$$

The Cooper pairs formed along each wire are protected by a spin gap Δ_σ which grows exponentially fast at small U and then $\Delta_\sigma \propto |U|$ for strong interactions.

Below, we assume the flux condition $2(k^1_F + k^2_F) \pm 2\chi = 0$ following Ref. [68]. For the energy scales smaller than Δ_σ, the dual mode $\theta^-_\sigma = (\theta^1_\sigma - \theta^2_\sigma)/\sqrt{2}$, meanwhile, oscillates rapidly in $\mathcal{H}_\perp$ making the coupling term $t_\perp$ irrelevant to first order in perturbation theory. The second order term gives the charge contribution

$$\mathcal{H}^{(2)}_\perp = -\frac{t^2_\perp}{\Delta_\sigma \pi a}\int dx \cos[2(\theta^-_\rho \pm \phi^+_\rho)]. \tag{2.69}$$

To study the motion of Cooper pairs, we notice that the corresponding creation operator satisfies $(\psi^\alpha_{-r,\uparrow}\psi^\alpha_{r,\downarrow})^\dagger \sim e^{-ir\sqrt{2}\theta^\alpha_\rho}$. This implies a canonical transformation for Cooper pairs on each wire:

$$\begin{aligned}
\Theta^\alpha_\rho = \sqrt{2}\theta^\alpha_\rho, \quad \Phi^\alpha_\rho = \phi^\alpha_\rho/\sqrt{2}, \\
\mathcal{H}^{(2)}_\perp = -\frac{t^2_\perp}{\Delta_\sigma \pi a}\int dx \cos[\sqrt{2}(\Theta^-_\rho \pm 2\Phi^+_\rho)].
\end{aligned} \tag{2.70}$$

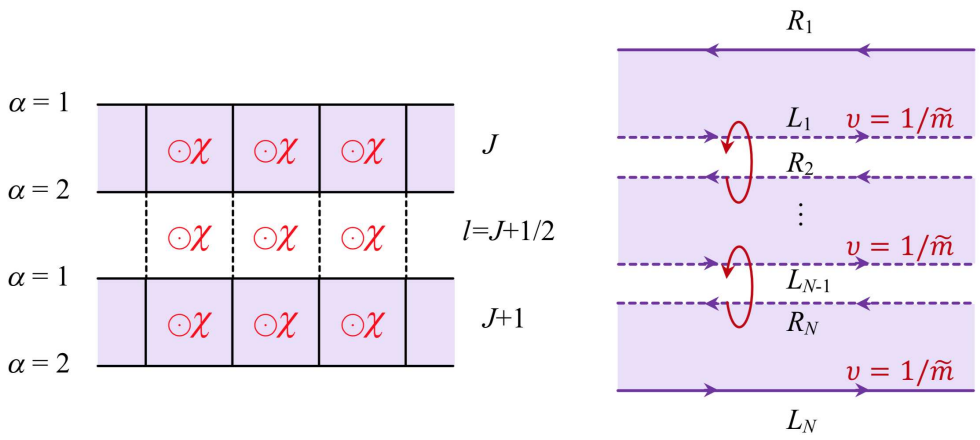

Figure 2.7: (Left) Coupled spinful ladders with uniform flux attachment; the variable J represents the ladder label and $l = J + 1/2$ in the middle of two successive ladders will represent the modes formed by coupling ladders together. (Right) Formation of a two-dimensional quantum Hall system with the filling factor $\nu = 1/\widetilde{m} = 1/2$. The two chiral edge states L_1 and R_N are now diagonal in the K-matrix structure producing an SPT phase of Class A [277].

By analogy with spinless fermions [see Eq. (2.33)], a fractional Cooper pair Laughlin state is observed at $\nu = 1/(2m) = \pm 1/2$ on the spinful ladder, as shown in Fig. 2.6b.

In the end, we comment that a relatively strong long-range repulsive interwire interaction $V_\perp$ plays a vital role in driving the system towards a fractional quantum Hall state [68].

Next, we continue to address the coupled spinful ladders based on the building block. A two-dimensional fractional quantum Hall state at $\nu = 1/2$ can be built from the Cooper pair Laughlin states formed on each ladder.

The general building block for the construction is shown in Fig. 2.7. Under the flux constraint (2.32), the coupling on the rungs of the J-th ladder gives a Sine-Gordon term (2.70) in the charge sector

$$\mathcal{H}_\perp^J = -\widetilde{v} \int dx \cos(\sqrt{2}\theta_J^- - \widetilde{m}\sqrt{2}\phi_J^+), \tag{2.71}$$

where we introduce the charge fields as $\theta_J^- = \Theta_{\rho,J}^-$, $\phi_J^+ = \Phi_{\rho,J}^+$ with $\widetilde{v} = t_\perp^2/(\Delta_\sigma \pi a)$ and $\widetilde{m} = 2m = \pm 2$. By analogy with the spinless case, one can build an edge theory on each ladder in the new basis of Eqs. (2.34)-(2.37) with the substitution $m \to \widetilde{m}$.

Accordingly, the bulk modes (θ^J, ϕ^J) generate a term

$$\mathcal{H}_\perp^J = -\widetilde{v} \int dx \cos(2\widetilde{m}\phi^J), \tag{2.72}$$

then pinning each mode ϕ^J and producing a gap. The two edge modes on the J-th ladder are identified as the chiral fields (see Fig. 2.7, right)

$$\begin{cases} L_J = \phi_{+1}^{1,J} = \theta'^J + \phi'^J, \\ R_J = \phi_{-1}^{2,J} = \theta'^J - \phi'^J, \end{cases} \tag{2.73}$$

with $\phi_r^{\alpha,J} = \theta^{\alpha,J}/\widetilde{m} + r\phi^{\alpha,J}$ and $\alpha = 1, 2$ representing the wire index inside each ladder. In Fig. 2.7 (right), each ladder behaves as a small quantum Hall system which gives rise to two low-energy chiral edge modes L_J and R_J. Neighboring chiral edge modes belonging to two successive ladders can then be coupled through an additional $t'_\perp$ term at low energy, smaller than the typical energy scale $\tilde{\Delta}$ at which the term $\tilde{v}$ has flown to strong couplings in each ladder. Here, $\tilde{\Delta}$ can be estimated as $\Lambda_c(\tilde{v}/v)^{1/(2-2|\tilde{m}|K)}$ with $\Lambda_c \sim \Delta_\sigma$. As mentioned in the case of two-leg spinful ladder, we require the introduction of long-range Coulomb forces (such that $2|\tilde{m}|K < 2$) to stabilize the relevance of this energy scale. To couple the left-moving mode L_{J+1} of the ladder $J+1$ with the right-moving mode R_J of the ladder J, this requires momentum conservation during the tunnel process, and therefore this requires to apply a magnetic field $\chi' = +\chi$ in the region centered at the position $J + 1/2$.

It is then possible to couple two edge modes between ladders taking into account the effect of an additional intra-ladder magnetic flux $\chi' = \chi$ by analogy to the two-dimensional quantum Hall effect, as depicted in Fig. 2.7 (left). Between the J-th and $(J+1)$-th ladders, the flux constraint then follows

$$a\left[(k_F^1 + k_F^2) - m\chi'\right] = 0 \mod 2\pi. \tag{2.74}$$

Through a recombination of the fields as in Fig. 2.7,

$$\begin{cases} \tilde{\phi}_{J+1/2} = (-R_J + L_{J+1})/2, \\ \tilde{\theta}_{J+1/2} = (R_J + L_{J+1})/2, \end{cases} \tag{2.75}$$

for $t'_\perp \ll t_\perp$, the bulk and edge Hamiltonians take the form

$$\mathcal{H}^{\text{bulk}} = \tilde{\mathcal{H}}^0[\tilde{\theta}, \tilde{\phi}] - \sum_{l=J+1/2} \int dx \tilde{v}' \cos(2\tilde{m}\tilde{\phi}_l), \tag{2.76}$$

$$\mathcal{H}^{\text{edge}} = \frac{v^e}{8\pi} \int dx \left[A_{RR} (\nabla R_N)^2 + A_{LL} (\nabla L_1)^2 \right]. \tag{2.77}$$

The tunnel process $\tilde{v}' = {t'_\perp}^2/(\tilde{\Delta}\pi a)$ represents the backscattering process of fractional charges $m(2e)$ from one left-moving chiral edge to another right-moving edge. The bulk quadratic Hamiltonian $\tilde{\mathcal{H}}^0$ has the coupled form in $\tilde{\theta}$ and $\tilde{\phi}$

$$\begin{aligned} \tilde{\mathcal{H}}^0[\tilde{\theta}, \tilde{\varphi}] =& \frac{v^e}{8\pi} \sum_{l=J+1/2} \int dx (A_{RR} + A_{LL}) [(\nabla \tilde{\theta}_l)^2 + (\nabla \tilde{\phi}_l)^2] \\ &+ A_{RL} (\nabla \tilde{\theta}_{l-1} + \nabla \tilde{\phi}_{l-1})(\nabla \tilde{\theta}_l - \nabla \tilde{\phi}_l), \end{aligned} \tag{2.78}$$

with the non-zero backscattering term $A_{RL} = 2\tilde{m}^2 K^e - 2/K^e$ and the velocity v_e similar to the one introduced in Appendix D. We also identify $A_{RR} = A_{LL} = \tilde{m}^2 K^e + 1/K^e$ and the new fields satisfy

$$[\tilde{\phi}_l(x), \partial_{x'} \tilde{\theta}_{l'}(x')] = i(\pi/m)\delta_{l,l'}\delta_{x,x'}. \tag{2.79}$$

By analogy with the arguments of two-leg spinful ladder, once the long-range repulsive interactions are present between the ladders, $\tilde{v}'$ in $\mathcal{H}^{\text{bulk}}$ becomes relevant. This leads to a gapped bulk, corresponding to the pinning of the phases $\tilde{\phi}_{l=J+1/2} \sim 0$.

Since $L_J = \tilde{\theta}_{l-1} + \tilde{\phi}_{l-1}$, $R_J = \tilde{\theta}_l - \tilde{\phi}_l$, two edge modes R_N and L_1 no longer entangle with the bulk. The coupled wire system now forms a single bulk $\nu = 1/2$ fluid in Fig. 2.7 (right). Since the edge mode theory for these modes is a chiral Luttinger model with $A_{RL} = 0$, the properties of the charge at these edges only depend on the value of K_e. If we set $A_{LR} = 0$ at an edge with the condition that $\tilde{m} = \pm 2$, then we check from Eq. (2.78) that the fractional charge $K_e = 1/2$ is now in agreement with the bulk-edge correspondence. This phase which shows a perfectly diagonal structure for the edges can be thought as an SPT phase of Class A in terms of the K-matrix structure [277].

Similar arguments could be applied for the reconstruction of the Abelian $\nu = 1$ and $\nu = 1/3$ quantum Hall states with wires and coupled ladder systems.

Chapter 3

Valence bond fluctuations in Kitaev spin models

In this chapter, we propose valence bond fluctuations as a probe of entanglement properties in the ground state of the Kitaev spin model [18].

A valence bond (VB) [38] here corresponds to the spin-spin pairing between two nearest neighbor electrons. Our first insight comes from the system of SU(2)-symmetric quantum spins with resonating valence bonds (RVB) where we find the bond fluctuations can be related to valence bond entropy of Einstein-Podolsky-Rosen (EPR) pairs or Bell pairs [278]. Extending to the Kitaev spin liquids discussed in Sec. 1.3, in the three gapped phases, the valence bonds between nearest neighbors form a crystalline or dimer order [18]. Approaching the transition(s) to the gapless intermediate phase, these bonds now resonate giving rise to gapless critical fluctuations, which in principle encode information on quantum phase transitions and entanglement properties. Our calculations indeed reveal an identical scaling between valence bond fluctuations and entanglement entropy in one-dimensional chain and two-dimensional honeycomb lattice. These mathematical findings are compared with numerical calculations from our collaborator K. Plekhanov, *e.g.* through the Density Matrix Renormalization Group (DMRG). In one dimension, the gapless phase is reduced to a quantum critical point [146], which then develops into a plane for ladder systems [147]. In two dimensions, in the absence of a magnetic field, the long-range valence bond corre-

lations in space [279] share a similar scaling as the dynamical spin structure factor [213]. We include also the effects of a uniform magnetic field in the perturbative regime, and discuss relevant consequences from the excitations of flux pairs [215] and from the formation of U(1) gapless spin liquids once three Ising couplings become anti-ferromagnetic (AFM) [280]. In the end, to make a closer link with quantum materials, we give a comparison of valence bond fluctuations in the Néel state favored by strong AFM Heisenberg exchanges. Our mathematical development of the lattice summations are consistent with finite-size scaling results performed by K. Plekhanov.

3.1 Fluctuations as an entanglement probe

First, we begin with a brief review on the relation between bipartite fluctuations and entanglement entropy in many-body Hamiltonians characterized by different symmetries [164, 281–283]. In Sec. 3.1.1, we define the general fluctuations on a bipartite lattice, which from the information theory, provide a lower bound for the mutual information related to entropy. We then remind in Sec. 3.1.2, an exact expression for the entropy as a series expansion of even cumulants (with particle number or spin fluctuations the leading order) for the U(1) charge conserved systems [281] and an inequality between the two quantities emerging among the SU(2) quantum spins described by resonating valence bonds.

Generalizing these works to Kitaev spin liquids coupled to a gapped $\mathcal{Z}_2$ gauge field represents our central motivation of this chapter. The difficulty lies in finding the right observable encoding the long-range correlation of matter Majorana fermions in the gapless phase, hence the entanglement properties. Fortunately, by analogy to the RVB states in the three gapped phases, in Sec. 3.1.3 we verify that the valence bond fluctuations represent non-vanishing lower bound for the entropy.

3.1.1 Generalities

We decompose a generic quantum system into two parts $A \cup B$. For the subsystem A, the entanglement is measured by the von Neumann entropy [132]

$$\mathcal{S}_A = -\mathrm{Tr}\rho_A \ln \rho_A, \tag{3.1}$$

where $\rho_A = \mathrm{Tr}_B \rho$ represents the reduced density matrix of sub-system A. Once given two density matrices ρ and ρ', the distance between two states can be probed by the relative entropy

$$\mathcal{S}(\rho, \rho') = \mathrm{Tr}\left[\rho(\log \rho - \log \rho')\right], \tag{3.2}$$

with a norm bound [284]

$$\mathcal{S}(\rho, \rho') \geq \frac{1}{2} ||\rho - \rho'||^2 . \tag{3.3}$$

Here the norm stands for $||\rho|| = \mathrm{Tr}\sqrt{\rho^\dagger \rho}$ and we have assumed that $\mathrm{Tr}\rho = \mathrm{Tr}\rho' = 1$. Making an analogy with vectors, one may also write $S(\rho, \rho') = S(\rho \parallel \rho')$. For instance, for diagonal (density) matrices, each eigenvalue may refer to a coordinate along one direction. On the other hand, to evaluate the fluctuations, we introduce two measurements

$$\mathcal{F}_A = \left\langle \left(\sum_{i \in A} Q_i \right)^2 \right\rangle_c , \tag{3.4}$$

$$\mathcal{F}_{AB} = \left| \sum_{i \in A} \sum_{j \in B} \langle Q_i Q_j \rangle_c \right| . \tag{3.5}$$

Here, Q is a chosen operator for targeted systems: charge, particle number, one spin or two spins on a valence bond and $\langle Q_i Q_j \rangle_c = \langle Q_i Q_j \rangle - \langle Q_i \rangle \langle Q_j \rangle$ denotes the reduced correlation function. It is easy to notice while $\mathcal{F}_A$ measures the fluctuations in subsystem A, $\mathcal{F}_{AB}$ covers the correlations between A and B. There is an equality between the two quantities:

$$\mathcal{F}_{AB} = \frac{1}{2} \left| \mathcal{F}_A + \mathcal{F}_B - \mathcal{F}_{A \cup B} \right| . \tag{3.6}$$

An important finding so far established is to relate $\mathcal{F}_{AB}$ with $\mathcal{S}_A$ by mutual information [285]

$$I(A,B) = \mathcal{S}_A + \mathcal{S}_B - \mathcal{S}_{A\cup B}. \tag{3.7}$$

From the definition of relative entropy (3.2), the mutual information has an alternative expression

$$I(A,B) = \mathcal{S}(\rho_{A\cup B}, \rho_A \otimes \rho_B). \tag{3.8}$$

Choosing any operator of the matrix form $Q = Q_A \otimes Q_B$ with Q_A the bounded operator in region A and applying the Schwarz inequality $||\rho|| \geq \mathrm{Tr}(\rho Q)/\,||Q||$ to the norm bound (3.3), one obtains [286]

$$I(A,B) \geq \frac{\left(\langle Q_A Q_B\rangle - \langle Q_A\rangle\langle Q_B\rangle\right)^2}{2\,||Q_A||^2\,||Q_B||^2}. \tag{3.9}$$

The numerator recovers $\mathcal{F}_{AB}$. Correspondingly, for $\mathcal{F}_{AB} \neq 0$, we arrive at

$$\frac{I(A,B)}{\mathcal{F}_{AB}} \geq \mathrm{cst}. \tag{3.10}$$

Although the lower bound between the bipartite fluctuations and the mutual information is universal, it remains ambiguous what is the form of operator Q one should choose for a given many-body system such that the fluctuations measured are non-vanishing. A second inquiry would be: under which circumstances we could reach the equality of (3.10) such that the fluctuations share the same scaling as the original entropy.

3.1.2 Exact relations and inequalities

In this subsection, we give two known examples where one can relate entanglement entropy directly to charge or spin fluctuations: first, noninteracting fermions with conserved U(1) charge; second, SU(2) quantum spins with EPR pairs. We further show for the SU(2)-symmetric RVB state, the bond correlator is also a good option for operator Q.

(a) Noninteracting fermions with conserved U(1) charge

Let us consider a system of non-interacting fermions with conserved total charge, or more precisely total number of particles: $\hat{N}_{\rm tot}|\psi\rangle = N_{\rm tot}|\psi\rangle$. At zero temperature, the ground state $|\psi\rangle$ of the total system becomes pure. Basic properties of the entanglement entropy then follow

- *symmetric*: $\mathcal{S}_A = \mathcal{S}_B$;
- *subadditive*: $\mathcal{S}_A + \mathcal{S}_B \geq \mathcal{S}_{A\cup B} = 0$.

Without any calculation, one can already see the similarities between charge fluctuations and the entropy. If we take $\hat{Q}_A = \hat{N}_A$ in $\mathcal{F}_A$ (3.4), where $\hat{N}_A$ represents the number of particles in sub-region A, as a result of total charge conservation $\hat{N}_A - N_A = -(\hat{N}_B - N_B)$, the fluctuations also inherit the symmetric and sub-additive characteristics

$$\mathcal{F}_A = \mathcal{F}_B, \qquad \mathcal{F}_A + \mathcal{F}_B = 2\mathcal{F}_A \geq 0. \tag{3.11}$$

In fact, one can relate the two quantities more rigorously by the cumulant expansion of entropy [281]

$$\mathcal{S}_A = \lim_{K\to\infty} \sum_{n=1}^{\lfloor (K+1)/2 \rfloor} \alpha_{2n}(K) C_{2n}. \tag{3.12}$$

Here, the coefficients are all positive and related to the unsigned Stirling number of the first kind: $\alpha_n(K) = 2\sum_{k=n-1}^{K} S_1(k, n-1)/(k!k)$. The cumulants C_n are given by the generating function $\chi(\lambda) = \langle e^{i\lambda \hat{N}_A}\rangle$ according to

$$C_n = (-i\partial_\lambda)^n \ln \chi(\lambda)|_{\lambda=0}\,. \tag{3.13}$$

By definition, one verifies $\mathcal{F}_A = C_2$. For a Gaussian process, one can truncate the serie with $K = 1$, but for non-Gaussian models one needs to check carefully the convergence of the series with the appropriate number of cumulants [281]. As a comparison, if we

consider a Bell pair or an EPR pair, then this generally requires around 10 cumulants to reproduce the $\ln 2$ entropy. Although the equivalence of entropy and a complete set of even cumulants (3.12) is unique to the systems with a mapping to non-interacting fermions, the general relation between entropy and fluctuations (3.14) can be further extended to the interacting one-dimensional (1D) critical systems that conserve total charge, and can be described by a Gaussian model through conformal field theory (CFT) or bosonization. In those cases, $\mathcal{S}_A$ can also be truncated by a $K = 1$ upper-bound. Thus one gets

$$\frac{\mathcal{S}_A}{\mathcal{F}_A} \simeq \text{cst}. \tag{3.14}$$

The constant proves to encode rich information, for instance [281]

$$\text{cst} \cdot \frac{3}{\pi^2} = \begin{cases} K, & \text{Luttinger liquids;} \\ c/g, & \text{U(1) CFTs,} \end{cases} \tag{3.15}$$

where similarly to Refs. [281, 287], we also introduce the letter K for the Luttinger parameter and c represents the central charge in conformal field theory (CFT). Parameter $g = \pi v \kappa$ consists of the velocity v and compressibility $\kappa = \partial n / \partial \mu$.

(b) SU(2) quantum spins with EPR pairs

Intuitively, one may wonder what will happen when the system breaks U(1) charge conservation and when the system becomes higher dimensional, such as two-dimensional. Next, we give an example of the SU(2)-symmetric valence bond state [281]. Indeed, a direct correspondence in terms of inequality similar to relation (3.14), subsists if we replace $\mathcal{F}_A$ with $\mathcal{F}_{AB}$, by analogy to mutual information (3.10). Furthermore, we would like to extend the result of Ref. [281] and show how the two-spin fluctuations and valence bond fluctuations capture different features of the entanglement entropy. Here, by "two-spin fluctuations", we refer to fluctuations associated to spin-spin correlation functions. From Eq. (3.5), two-spin (TS) fluctuations and valence

bond fluctuations between two subregions read:

$$\begin{aligned} \mathcal{F}^{\mathrm{TS}} &= \mathcal{F}_{AB}(Q_{i,\alpha} = \sigma^z_{i,\alpha}), \\ \mathcal{F}^{\mathrm{VB}} &= \mathcal{F}_{AB}(Q_i = \sigma^z_{i,1}\sigma^z_{i,2}). \end{aligned} \tag{3.16}$$

In this work, our aim is to show that the valence bond fluctuations are essential since they provide relevant information both for SU(2) and $\mathcal{Z}_2$ quantum spin liquids.

We consider the two-dimensional Heisenberg antiferromagnetic (HAF) model where arise two competing phases: a Néel state and a gapped VB state. In either configuration, the valence-bond entropy has proven to exhibit distinct behaviors [278]:

$$\mathcal{S}^{\mathrm{VB}}_{\mathrm{2D\ HAF}} \sim \begin{cases} ax \ln x + bx & (\text{Néel}) \\ b'x & (\text{VB}) \end{cases}. \tag{3.17}$$

Here x denotes the length of the boundary between two subsystems. This measure can also accurately detect quantum phase transitions between Néel and RVB spin phases in quasi-one dimensional ladder systems [288]. For the moment, we focus on the fluctuations of the gapped VB state and will address the comparison with a Néel state later in Sec. 3.5.

Suppose our system comprises N sites on even and odd sublattices. Dimer coverings between different sublattices sharing the form

$$|\frown\rangle_{\overline{(i,1)(j,2)}} = \frac{1}{\sqrt{2}}(|\uparrow_{i,1}\rangle|\downarrow_{j,2}\rangle - |\downarrow_{i,1}\rangle|\uparrow_{j,2}\rangle), \tag{3.18}$$

minimize the energy from the antiferromagnetic Heisenberg interactions. The subscript (i,α) describes the site on i-th unit cell of the $\{\alpha = 1,2\}$ sublattice. A singlet state $|\Phi_0\rangle$ can then be represented as a complex superposition of all possible dimer or pairing configurations

$$\begin{aligned} |\Phi_0\rangle &= \sum_p \lambda_p |\varphi_p\rangle, \\ |\varphi_p\rangle &= \prod_{\overline{(i,1)(j,2)} \in p} |\frown\rangle_{\overline{(i,1)(j,2)}}. \end{aligned} \tag{3.19}$$

For a given global pairing distribution p, the product state goes over all local internal dimers $\overline{(i,1)(j,2)}$.

The corresponding VB entanglement entropy (3.17) is defined as [278]

$$\mathcal{S}^{\mathrm{VB}}(\Phi_0) = \frac{\sum_p \lambda_p \mathcal{S}^{\mathrm{VB}}(\varphi_p)}{\sum_p \lambda_p}. \tag{3.20}$$

Formally, acting on the singlet state $|\Phi_0\rangle$, the fluctuations and the VB entropy can be obtained from the decomposition (3.19)

$$\begin{aligned} \mathcal{F}^{\mathrm{TS/VB}}(\Phi_0) &= \sum_p \sum_{p'} \lambda_p^* \lambda_{p'} \mathcal{F}^{\mathrm{TS/VB}}(\varphi_p, \varphi_{p'}), \\ \mathcal{S}^{\mathrm{VB}}(\Phi_0) &= (\ln 2) \cdot \frac{\sum_p \lambda_p \mathcal{F}^{\mathrm{TS}}(\varphi_p, \varphi_p)}{\sum_p \lambda_p}. \end{aligned} \tag{3.21}$$

Eq. (3.21) indicates in general there is no simple correspondence between $\mathcal{F}^{\mathrm{TS/VB}}$ and $\mathcal{S}^{\mathrm{VB}}$. Yet, we may try to simplify (3.21) as

$$\mathcal{F}^{\mathrm{TS/VB}}(\Phi_0) := \sum_p |\lambda_p|^2 \mathcal{F}^{\mathrm{TS/VB}}(\varphi_p, \varphi_p). \tag{3.22}$$

For $\mathcal{F}^{\mathrm{TS}}$, the relation (3.22) is exact owing to the sublattice symmetry of two-spin correlation functions. For $\mathcal{F}^{\mathrm{VB}}$, it is a redefinition in the sense one counts the bond fluctuations inside each pairing pattern with probability $|\lambda_p|^2$ and at the same time, ignores the contributions from the overlaps of different pairing patterns. This redefinition is crucial for $\mathcal{F}^{\mathrm{VB}}$ to resemble the behavior of the VB entanglement entropy.

On one hand, if the gapped VB state is composed of N-site singlets carrying equal weights ($\lambda_p = \lambda$), we can show the following inequality reminiscent of the lower bound for mutual information (3.10)

$$\begin{aligned} \mathcal{S}^{\mathrm{VB}} &\propto \ln 2 \cdot n, \\ \frac{\mathcal{S}^{\mathrm{VB}}}{\mathcal{F}^{\mathrm{TS}} + \mathcal{F}^{\mathrm{VB}}} &\geq \ln 2. \end{aligned} \tag{3.23}$$

Here n denotes the number of singlets that the boundary crosses. Both relations above take the equality " $=$ " if the maximum resonating range $N \leq 4$. As $N \to \infty$, the system approaches the gapless critical point.

On the other hand, as soon as the singlet bonds decay exponentially with distance ($\lambda_p \sim e^{-r/\xi}$),

$$\mathcal{F}^{\mathrm{TS/VB}}_{\text{2D HAF}} = b^{\mathrm{TS/VB}} \cdot x + \mathcal{O}(x). \tag{3.24}$$

A similar area law scaling is revealed in two types of fluctuations alongside the VB entanglement entropy (3.17).

3.1.3 Generalization to Kitaev $\mathcal{Z}_2$ spin liquids

Valence bond states in SU(2) spin systems and Kitaev $\mathcal{Z}_2$ spin liquids may be distinguishable from the form of correlation functions. For the former, the two-spin correlator follows an exponential decay in the gapped phase; for the latter, however, the static correlation between two spins becomes exactly zero beyond nearest neighbors [138].

In fact, the Kitaev honeycomb model is solved in the Majorana representation with one spin operator mapped onto the product of one matter and one gauge Majorana fermions [18]. Once acting on the ground state embedded with a static $\mathcal{Z}_2$ gauge field, the gauge Majorana fermion creates a pair of fluxes in two adjacent hexagons. It renders two-spin fluctuations irrelevant, if given an arbitrary boundary (not assigned on the same Ising links)

$$\mathcal{F}^{\mathrm{TS}}_{\mathrm{Kitaev},\mathcal{Z}_2} = 0. \tag{3.25}$$

One should resort to the bond-bond operator [146]. Since the excitation of a flux pair is annihilated simultaneously by the other spin on the same bond, valence bond fluctuations always give a relevant lower bound regardless of the boundary position

$$\frac{\mathcal{S}_F}{\mathcal{F}^{\mathrm{VB}}_{\mathrm{Kitaev},\mathcal{Z}_2}} \geq \mathrm{cst}. \tag{3.26}$$

In the equation above, we have rescaled the mutual information by Fermi entropy according to the area law of entanglement entropy [133].

Another observation comes consistently from the SU(2)-invariant Kitaev spin liquids [289]: there, the two-spin operator can be expressed solely in terms of matter Majorana fermions (preserving the gauge structure) and its correlation becomes non-vanishing. Similar to the Heisenberg anti-ferromagnet (3.24), the spin and bond fluctuations obey a linear growth in the gapped region

$$\mathcal{F}^{\mathrm{TS/VB}}_{\text{Kitaev, SU(2)}} = b^{\mathrm{TS/VB}} \cdot x + \mathcal{O}(x). \tag{3.27}$$

We then conclude that both two-spin and valence bond fluctuations are appropriate as relevant probes of the entanglement entropy for the SU(2) spin systems, whereas for the Kitaev $\mathcal{Z}_2$ spin liquids only the valence bond fluctuations play a substantial role.

Below, we address valence bond fluctuations both for one-dimensional and two-dimensional Kitaev spin models. In Secs. 3.2 and 3.3, we prove how valence bond fluctuations (3.26) develop the same scaling as the entanglement entropy both for the one-dimensional chain and the honeycomb lattice.

3.2 Model on the chain

We start from the Kitaev spin chain depicted in Fig. 3.1a. In Section 1.3.4, it has been shown that the model (1.123) is exactly solvable via Jordan-Wigner transformation and a mapping to Majorana fermions. And the complex bond fermions (1.129) share a similar topological structure as a p-wave superconducting chain (1.131). In particular, from its energy spectrum (1.130) we check that the gap closes at $k_F = \pi/2$ when $J_1 = J_2$ and that the chain on the dual lattice encodes a critical gapless theory of free fermions with central charge $c = 1$. Here, we find its counterpart in the original spin basis through the observable "valence bond correlator".

3.2.1 Valence bond correlator

Using definitions in Secs. 1.3.4 and 3.1.1, we introduce the bond-bond correlation functions $I(i,j) = \langle Q_i Q_j \rangle_c$, with

$$Q_j = \sigma^x_{j,1}\sigma^x_{j,2} = -ic_{j,1}c_{j,2}. \tag{3.28}$$

It is important to underline that in Fig. 3.1a, we have chosen the strong bonds associated to the J_1 coupling, referring to the x spin Pauli operator in Q_j.

As before, the site index (j,α) represents the j-th unit cell of the sublattice $\alpha = \{1,2\}$. In the dual lattice, Q_j relates to the density of bond fermions $\psi^\dagger_j\psi_j$. At the gapless point, we get from Wick's theorem

$$I(i,j) = I(|i-j|) = \frac{1}{\pi^2}\frac{1}{|i-j|^2 - 1/4}, \tag{3.29}$$

for $i \neq j$. As a comparison, the usual two-spin correlator in the Majorana representation turns into

$$\langle \sigma^z_i \sigma^z_j \rangle = (-1)^{i+j+1} \langle c_i d_i c_j d_j \rangle . \tag{3.30}$$

Decoupled d Majorana fermions lead to $\langle c_i d_j \rangle = \langle d_i d_j \rangle = 0$. Applying Wick's theorem, $\langle \sigma^z_i \sigma^z_j \rangle$ vanishes in all phases beyond nearest neighbors, and the same for $\langle \sigma^x_i \sigma^x_j \rangle$ and $\langle \sigma^y_i \sigma^y_j \rangle$ which involve Jordan-Wigner strings formed by the pairings of c and d Majorana fermions. Once the distance of two sites goes beyond the nearest neighbour $|i-j| > 1$, one verifies

$$\langle \sigma^a_i \sigma^a_j \rangle = 0, \quad a = x, y, z. \tag{3.31}$$

Like the Kitaev honeycomb model, in its one-dimensional chain analogue, again the two-spin operator does not encode the long-range correlation of the gapless Majorana fermions.

Now deviating from the gapless point, from the bond-fermion model and from the Ising symmetry of the spin chain, we predict that the correlation length ξ of the bond

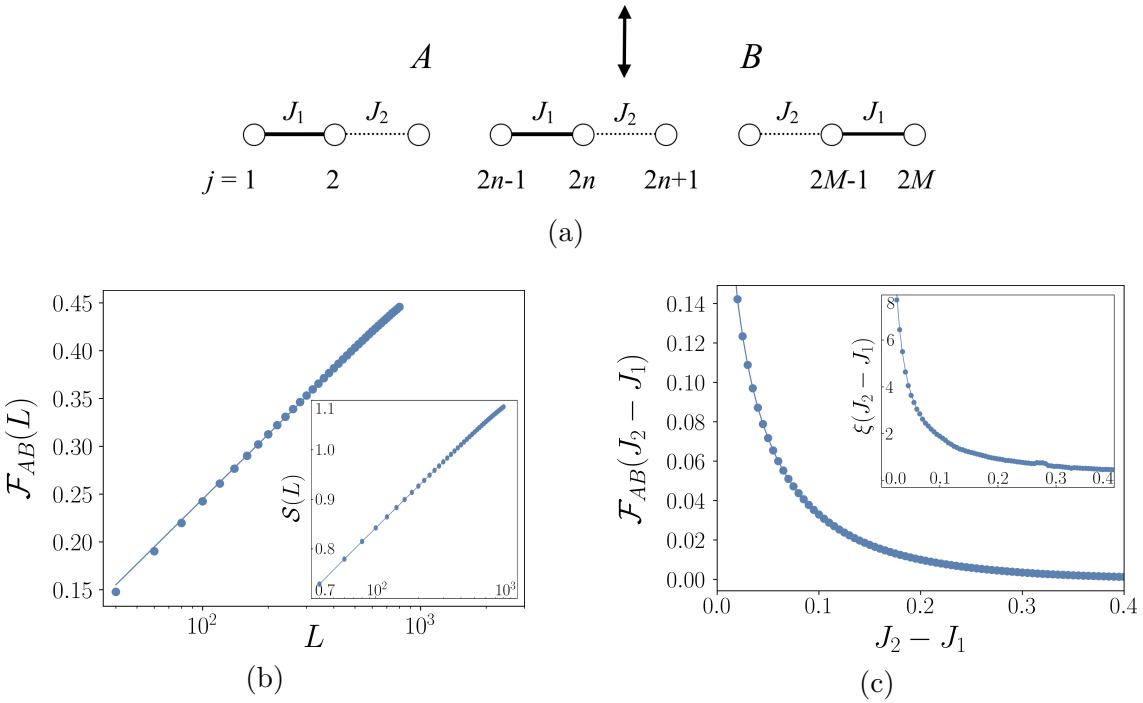

Figure 3.1: (a) Bipartition of the Kitaev spin chain into subparts A and B. (b) DMRG results for bipartite fluctuations as a function of the subsystem length $l_A = L$ at the critical point: $\mathcal{F}_{AB} = \alpha \ln L + \mathcal{O}(1)$ with $\alpha = 0.95/\pi^2$. The entanglement entropy is shown in the inset: $\mathcal{S} = (c/6) \ln L + \mathcal{O}(1)$ with central charge $c = 0.49$. (c) Bipartite fluctuations as a function of $\Delta = |J_2 - J_1|$ (here, $(J_1, J_2) < 0$ such that the strong bonds occur on the x-link). The inset shows the correlation length $\xi = 0.20 \times \Delta^{-\nu}$ with $\nu = 0.94$. For the gapped phase, we set $L_{\text{total}} = 1000$.

operator is proportional to the inverse of the gap $\Delta = |J_2 - J_1|$,

$$\xi \propto \Delta^{-\nu}, \quad \nu = 1. \tag{3.32}$$

The valence bond correlations share the behavior

$$I(i,j) = \begin{cases} c_1 |i-j|^{-2}, & |i-j| \leq \xi; \\ c_2 e^{-|i-j|/\xi}, & \text{otherwise.} \end{cases} \tag{3.33}$$

Our collaborator K. Plekhanov performs numerical calculations based on DMRG which verify these predictions with the associated critical exponent $\nu = 0.94 \sim 1$ in the inset of Fig. 3.1c.

3.2.2 Results on fluctuations

Below, we focus on $\mathcal{F}_{AB}$, which defines the fluctuations between two subsystems (3.5) associated to bond-bond correlations (3.28). Here the valence bond fluctuations $\mathcal{F}_{AB}$ also appear as the effective non-vanishing lower bound for mutual information (3.10).

Fig. 3.1a depicts the bipartition we choose for the spin chain with subsystem lengths $l_A = l_B = L_{\text{total}}/2 = L$. A direct lattice summation in Appendix F leads to

$$\mathcal{F}_{AB} = \begin{cases} (1/\pi^2) \ln l_A + (1/\pi^2) (\gamma + \ln 2 - 1/2) , J_1 = J_2; \\ c_1 \ln \xi + c_2 e^{-1} (2\xi^2 - \xi) + \mathcal{O}(1) , \quad |J_1| > |J_2|. \end{cases} \tag{3.34}$$

with $\gamma \simeq 0.57721$ the Euler constant. On the contrary, $\mathcal{F}_A$ always contains a higher order scaling linear in l_A.

Our findings (3.34) are confirmed by DMRG simulations from K. Plekhanov. At the gapless point $J_1 = J_2$ shown in Fig. 3.1b, in $\mathcal{F}_{AB}$ a logarithmic scaling is observed with respect to the length of subregion A: $\mathcal{F}_{AB} \propto \ln l_A$. Roughly, one can identify this term by taking the 1D integral of the bond correlation $I(i, j)$ in Eq. (3.29). Moreover, the pre-factor α/π^2 is recovered with $\alpha = 0.95$. Here, the fact that α reproduces central charge $c = 1$ of the dual lattice, is in agreement with the free bond fermion representation [290]. Fig. 3.1c further probes the gapped region. When $|J_1| \gg |J_2|$, $\mathcal{F}_{AB}$ goes to zero reflecting the crystallization of the dimers. Slowly closing the gap Δ, near the phase transition point, $|c_1| \gg |c_2|$, the logarithmic behavior $\propto \ln \xi$ dominates in $\mathcal{F}_{AB}$.

It is interesting to go beyond the lower bound and reveal the relation between $\mathcal{F}_{AB}$ and the original entanglement entropy. Deep in the gapped phase driven by $|J_1| \gg |J_2|$, eigenstates are formed on strong x-links. $\mathcal{S}_A$ vanishes accordingly when the boundary is set on the weak y-link (see Fig. 3.1a). By increasing $|J_2|$, long-range entanglement emerges among the dimers, which is accompanied by a logarithmic growth in entropy associated to the correlation length

$$\mathcal{S}_A \propto \ln \xi. \tag{3.35}$$

The same response is observed in valence bond fluctuations $\mathcal{F}_{AB}$ of the gapped region.

Meanwhile, the entropy reaches its maximum when the gap closes at $J_1 = J_2$. Suppose the critical chain is finite with open boundaries, the entropy is proven to show the universal behaviour [148, 291]:

$$\mathcal{S}_A = \frac{c}{6} \ln l_A + 2g + s_1, \tag{3.36}$$

where g counts the boundary entropy and s_1 stands for a non-universal constant. In inset of Fig. 3.1b, from DMRG, the central charge extracted from the entropy (3.36) reads: $c = 0.49 \sim 1/2$. It can be understood from the fact that after the Jordan-Wigner transformation, half of the spin degrees of freedom are disentangled from the Hamiltonian (1.88) by decoupling all d-Majorana fermions.

At the gapless point, both $\mathcal{F}_{AB}$ and $\mathcal{S}_A$ then share a logarithmic growth with subsystem size typical of (critical) conformal field theories in one dimension. Related to this finding, we would like to address the following comment: to evaluate the valence bond fluctuations we diagonalize the spectrum in momentum space in the ψ basis, whereas the entanglement entropy reflects the real space degrees of freedom on the original lattice. This justifies why in our calculations the central charge $c = 1$ is revealed in the valence bond fluctuations, whereas the central charge $c = 1/2$ is observed in the entanglement entropy.

We establish that in both the gapped and gapless phases of one-dimensional Kitaev spin liquids, there is an identical scaling rule between the valence bond fluctuations and the entanglement entropy

$$\mathcal{F}_{AB} \sim \mathcal{S}_A. \tag{3.37}$$

3.3 Model on the honeycomb lattice

As discussed briefly in Sec. 3.1.3 and as will be described below, on the two-dimensional honeycomb lattice, due to the protection of 0-flux configurations in the ground state,

the two-spin correlator also vanishes beyond nearest neighbors in all phases [138]. The valence bond correlator, however, preserves flux pairs in neighboring plaquettes and supports gapless fermion excitations. Although Ref. [279] finds numerically that it exhibits a power-law decay in the gapless phase and an exponential decay in gapped phases, the valence bond correlator itself does not locate precisely the phase transition (see Fig. 3.2a). It motivates us to develop an approach of evaluating its global fluctuations on a bipartite lattice. The enhanced features in fluctuations come intrinsically from the spatial dependence and anisotropy of the local bond correlator.

We demonstrate below that the valence bond fluctuations and the entanglement entropy allow us to locate quite accurately the phases and quantum phase transitions in the two-dimensional Kitaev honeycomb model [18].

3.3.1 Valence bond correlator

For the honeycomb lattice, as previously reviewed in Sec. 1.3, we start from the Hamiltonian $\mathcal{H} = -\sum_{\langle ij\rangle_\mu} J_\mu \sigma_i^\mu \sigma_j^\mu$, under the perturbation $\mathcal{V} = -\sum_j h_\mu \sigma_j^\mu$ of a uniform magnetic field along [111] direction. When $|h_\mu| \ll |J_\mu|$, the cubic term (1.112) in perturbation theory breaks time-reversal symmetry, and the effective Hamiltonian can be simplified to Eq. (1.113) in the momentum space. Below, we study the effect of $\kappa \sim h_x h_y h_z/(J_\mu J_\rho)$ in the perturbative regime where $\kappa \ll J_x + J_y + J_z$.

We choose to measure the valence bond correlator onto the z-links, as compared to the x-links used for the one-dimensional chain in Sec. 3.2:

$$Q_i = \sigma_{i,1}^z \sigma_{i,2}^z = -ic_{i,1}c_{i,2}u_{\langle i_1 i_2\rangle_z} := -ic_{i,1}c_{i,2}. \tag{3.38}$$

Since any physical observable is independent of a specific gauge [138], in the last equality, we can adapt our gauge choice for the gauge Majorana fermions. One thus sees the bond correlator probes the matter Majorana fermions without disturbing the gauge part.

On the contrary, as pointed out in Sec. 1.3, a single spin operator $\sigma_{j,1}^z = ic_{j,1}c_{j,1}^z$

influences the gauge structure [138]. From the construction of the bond gauge fermion $\chi = (c^z_{j,1} - ic^z_{j,2})/2$, we find that the number operator $N_\chi = \chi^\dagger\chi = (1 - u_{\langle j_1 j_2\rangle_z})/2$ takes the value 1 and 0 depending on the gauge choice of $u_{\langle j_1 j_2\rangle_z} = \pm 1$. In either gauge, $\sigma^z_{j,1} = ic_{j,1}(\chi^\dagger + \chi)$ changes the occupation number of the bond gauge fermion χ. It is equivalent to flip the linking number $u_{\langle j_1 j_2\rangle_z}$ to $-u_{\langle j_1 j_2\rangle_z}$ and excite one π-flux pair in two neighbouring plaquettes. Therefore, the two-spin correlation is totally suppressed by the static $\mathcal{Z}_2$ gauge background beyond nearest neighbours (the latter case goes back to the measurement on a single bond).

Next, we focus on the local structure of the non-vanishing valence bond correlation. From Wick's theorem, one obtains a compact form from the spectrum (1.113)

$$I(i,j) = -\sum_{\vec{k},\vec{q}} \frac{e^{i(\vec{k}+\vec{q})\cdot(\vec{r}_j - \vec{r}_i)}[g(\vec{k})g(\vec{q}) + f(\vec{k})^* f(\vec{q})]}{N^2\sqrt{(\xi^2_{\vec{k}} + |\Delta_{\vec{k}}|^2)(\xi^2_{\vec{q}} + |\Delta_{\vec{q}}|^2)}}, \tag{3.39}$$

with N the total number of lattice unit cells. And two auxiliary parameters read

$$\xi_{\vec{k}} = \mathfrak{Re} f(\vec{k}), \quad \Delta_{\vec{k}} = -g(\vec{k}) + i\mathfrak{Im} f(\vec{k}). \tag{3.40}$$

in terms of the $f(\vec{k})$ and $g(\vec{k})$ functions

$$\begin{aligned} f(\vec{k}) &= 2(J_x e^{-i\vec{k}\cdot\vec{n}_1} + J_y e^{-i\vec{k}\cdot\vec{n}_2} + J_z), \\ g(\vec{k}) &= -4\kappa[\sin(\vec{k}\cdot\vec{n}_1) + \sin(\vec{k}\cdot(\vec{n}_2 - \vec{n}_1) - \sin(\vec{k}\cdot\vec{n}_2)]. \end{aligned} \tag{3.41}$$

(a) Zero field

In the absence of magnetic field $\kappa = 0$, $I(i,j)$ has no singularities in the three gapped Abelian phases, therefore this results in an exponential decay of $I(i,j)$. In the intermediate gapless semi-metal phase, singularities appear at two Dirac points $\pm\vec{k}^*$.

We first look at the behavior of bond correlations in the gapless region. A detailed analysis of the asymptotic behavior of $I(i,j)$ at long distances can be found in Appendix G. Performing an expansion around the two Dirac points similar to the $p_x + ip_y$ superconductor [292], we recover a power-law decay [279]

$$I(i,j) = \frac{\widetilde{c}_1}{r^4}, \tag{3.42}$$

and establish that the $\widetilde{c}_1$ coefficient depends on the cutoff function $t(\Lambda)$ and on the anisotropic function $Y(\vec{r})$. More precisely,

$$\widetilde{c}_1 = t^2(\Lambda) \cdot Y(\vec{r}),$$
$$Y(\vec{r}) = \cos^2(\vec{k}^* \cdot \vec{r}) - \cos^2(\theta^*). \tag{3.43}$$

Here, θ^* is the angle between the vectors $\vec{r} = \vec{r}_i - \vec{r}_j$ and $\vec{k}^*$. The space variable r refers to $|\vec{r}_i - \vec{r}_j|$.

We can start from the simplest case by making the directions of $\vec{r}$ and $\vec{k}^*$ perpendicular to each other: $\vec{r}_\perp = \vec{r}_j - \vec{r}_i = (j-i)(\vec{n}_1 + \vec{n}_2)$. The spatial oscillations disappear in the bond correlator with $Y(\vec{r}_\perp) = 1$. Checked via a finite-size scaling method by K. Plekhanov, our analytic expression becomes consistent with the numerical fitting results of Ref. [279]. Shown in Fig. 3.2a, it supports a smooth curve of $I(i,j)$ revealing the r^{-4} scaling in the gapless region ($J_z < 0.5$).

We can derive a more precise analysis. At the gapless point $J_x = J_y = J_z = 1/3$, in Appendix G we obtain the expression for the cutoff function

$$t(\Lambda) = \frac{\sqrt{3}}{2\pi} \int_0^\Lambda J_1(k) k dk, \tag{3.44}$$

where inside the integral $J_1(k)$ denotes the Bessel function of the first kind. Here, the cutoff $\Lambda = \xi r$ can be further approximated by setting the radius of the momentum integration $\xi = 1$ and taking $r \simeq r_{\max}$ to be the total system size $L = 100$. Analytically, we obtain $\log|I(i,j)| = c_1 - \alpha \log|i-j|$ with $c_1 = \log(\widetilde{c}_1/9)|_{\Lambda=100} = -4.63$, $\alpha = 4$. Here, "log" is equivalent to the natural logarithm with the base e. It recovers well the numerical fitting result (see Fig. 3.2a): $c_1 = -4.60, \alpha = 4.06$.

It is important to stress that Ref. [279] has not pointed out the role of the anisotropic Y-function. Once shifted to other directions $Y(\vec{r}) \neq$ cst, $c_1 = \log(|\cos^2(\vec{k}^* \cdot \vec{r}) - \cos^2(\theta^*)|) - 4.63$. Accordingly, as verified by Fig. 3.2b and Fig. 3.2b, the sampling points of $\log|I(i,j)|$ along the non-perpenticular direction oscillate rapidly. We also emphasize here the forms of $\tilde{c}_1$ and the anisotropic Y-function in Eq. (3.43) remain

true for the whole gapless region. Later, we will study these anisotropic effects on the bipartite fluctuations in relation with Fig. 3.4.

For the gapped phase, on the other hand, from numerics $I(i,j)$ follows an exponential decay with a fast decreasing correlation length shown in Fig. 3.2a (a). Meanwhile, in Fig. 3.2b, one observes less anisotropy effects in the gapped region.

It may be relevant to mention that once the gapless intermediate phase is subject to a magnetic field along the $\hat{z}$ direction, an identical power-law behavior (including the same angular dependence) emerges in the dynamical correlation function [213]:

$$\begin{aligned} g(t,\vec{r}) &= \langle \sigma_r^z(t)\sigma_0^z(0)\rangle - \langle \sigma_0^z(0)\rangle^2 \\ &\simeq \frac{64h_z^2}{\pi^2 h_0^2}\frac{r^2(\cos^2(\vec{k}^*\cdot\vec{r}) - \cos^2(\theta^*)) - 3(Jt)^2\cos^2(\vec{k}^*\cdot\vec{r})}{(r^2-3(Jt)^2)^3} \end{aligned} \tag{3.45}$$

where h_z is the strength of the magnetic field and the parameter h_0 can be estimated as $h_0 \sim J$. We find at long distances and at a finite time,

$$t \ll r \to \infty, \quad \frac{g(t,\vec{r})}{I(\vec{r},\kappa=0)} \propto \text{cst.} \tag{3.46}$$

Both observables are proportional to the density-density correlation function of the bond fermions (1.93): $\psi_r = \psi_{\langle ij\rangle_z} = \frac{1}{2}(c_i + ic_j)$.

(b) Small finite field

We further study the effects of a small uniform magnetic field on the bond correlation in the intermediate phase. For simplicity, we take $J_x = J_y = J_z = J = 1/3$.

When $0 < \kappa \ll J$, a gap opens and the valence bond correlator in Fig. 3.2e now reveals an exponential decay, similar to three gapped spin liquid phases. Yet its sign changes from positive to negative when increasing the strength of the magnetic field (see Fig. 3.2d. Consequently, in Fig. 3.2f we observe an enhancement in the amplitude of bond correlation functions once the magnetic field is sufficiently large.

We find that this sign change originates from the competition between the Ising interactions and the external magnetic field. For $\kappa \neq 0$, the valence bond correlator

(3.39) can be expressed in an alternative form: $I(i,j) = F(\vec{r})^2 - G(\vec{r})^2$ with

$$F(\vec{r}) = \frac{1}{N}\sum_k e^{i\vec{k}\cdot\vec{r}}\frac{f(k)^*}{\sqrt{\xi_k^2 + |\Delta_k|^2}},$$
$$G(\vec{r}) = \frac{1}{N}\sum_k e^{i\vec{k}\cdot\vec{r}}\frac{g(k)}{\sqrt{\xi_k^2 + |\Delta_k|^2}}. \tag{3.47}$$

While the Ising interactions give a positive contribution to the bond correlators, the external magnetic field gives a negative one.

Changing the strength of the external magnetic field κ, it is verified that

$$\text{Sign}\left(\frac{\partial I(i,j)}{\partial \kappa}\right) = \text{Sign}(-\kappa), \tag{3.48}$$

as $\partial_\kappa I(i,j) = 2[\partial_\kappa F(\vec{r})\cdot F(\vec{r}) - \partial_\kappa G(\vec{r})\cdot G(\vec{r})]$ and

$$\frac{\partial F(\vec{r})}{\partial \kappa} = -\frac{1}{N}\sum_k e^{i\vec{k}\cdot\vec{r}}\frac{f(k)^* g(k)^2}{\kappa(\xi_k^2 + |\Delta_k|^2)^{3/2}},$$
$$\frac{\partial G(\vec{r})}{\partial \kappa} = \frac{1}{N}\sum_k e^{i\vec{k}\cdot\vec{r}}\frac{g(k)|f(k)|^2}{\kappa(\xi_k^2 + |\Delta_k|^2)^{3/2}}. \tag{3.49}$$

When $\kappa > 0$, the derivative of $I(i,j)$ is always negative.

The monotonically decreasing bond correlation function is expected to cross zero around the point where the strengths of the Ising interactions and the magnetic field are comparable. We can roughly estimate the crossover point by starting from a relatively small κ parameter. In this circumstance, $I(i,j)$ is still governed by an expansion $|\delta\vec{k}| \in \Omega(0,1)$ around two original Dirac points $\pm\vec{k}^*$. The denominator in Eq. (3.47) turns out to be

$$E_k = \sqrt{\xi_k^2 + |\Delta_k|^2} = 3\sqrt{3}|\kappa|\sqrt{1 + (\lambda k)^2}. \tag{3.50}$$

When the parameter $\lambda = J/(6\kappa) > 1$, $\kappa < \kappa_c = 0.055$, the $F(\vec{r})^2$ term arising from the Ising interactions is dominant and $I(i,j)$ rau2016ps a positive sign. Otherwise $\lambda \ll 1$, $\kappa \gg \kappa_c$, then the $-G(\vec{r})^2$ term from the external magnetic field grows steadily and has the tendency to drive $I(i,j)$ negative. In accordance with the numerical calculations shown in Fig. 3.2d and Fig. 3.2d, for different distances, all crossover points where $I(i,j)$ changes sign are located at $\kappa > \kappa_c$.

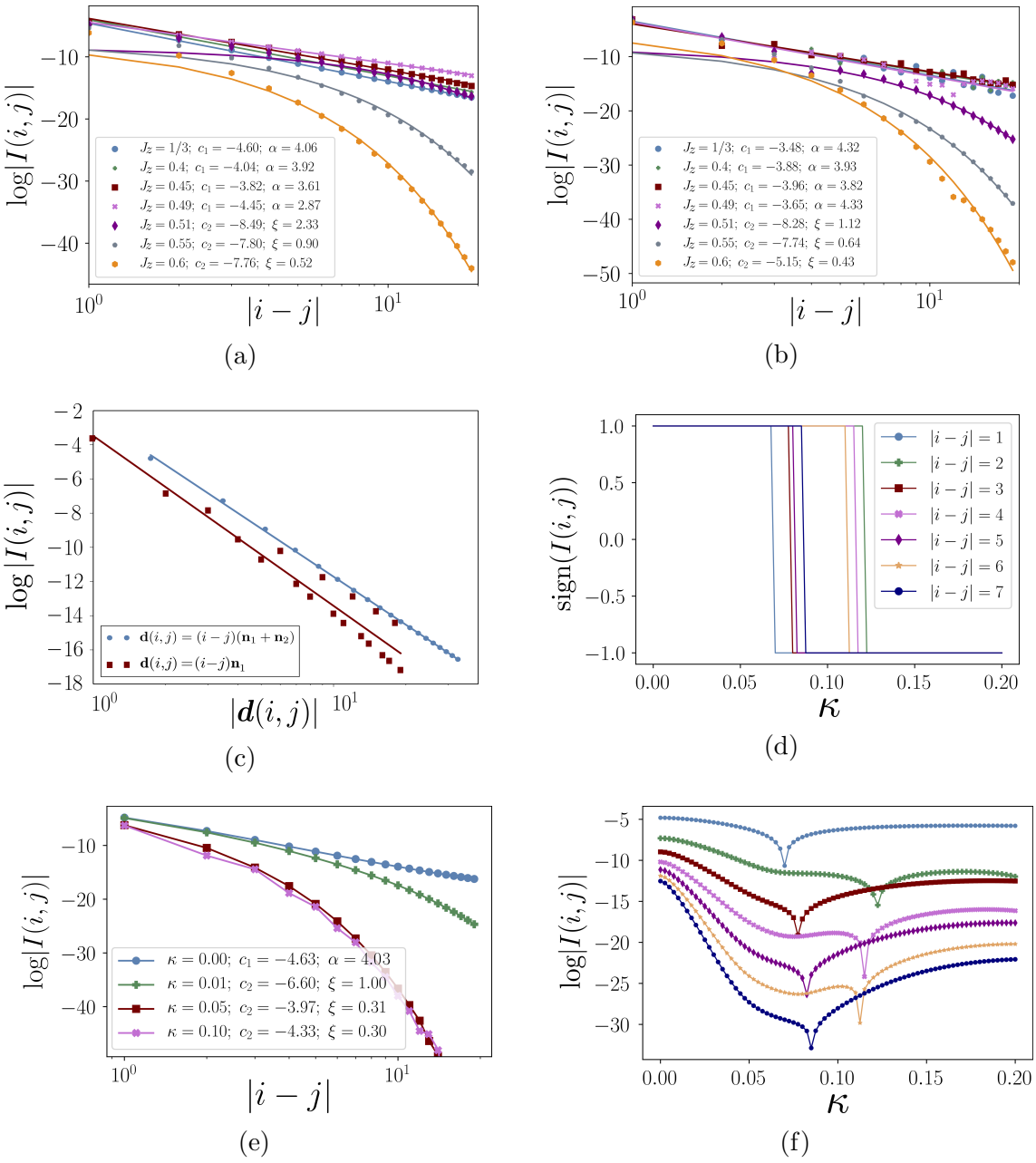

Figure 3.2: (a), (b) and (c): valence bond correlation functions for different phases in the pure Kitaev honeycomb model. The coupling constants are chosen according to $J_x = J_y, \sum_a J_a = 1$ and we take the total system size as $N = L \times L = 100 \times 100$. While the gapped phase ($J_z > 0.5$) exhibits an exponential decay in bond correlators: $\log|I(i,j)| = c_2 - |i-j|/\xi$, the gapless intermediate phase ($J_z \leq 0.5$) supports a power-law decay: $\log|I(i,j)| = c_1 - \alpha \log|i-j|$. The relative vector is set along the direction $\mathbf{d}(i,j) = \vec{r}_i - \vec{r}_j$: (a) $\mathbf{d}(i,j) = (i-j)(\vec{n}_1 + \vec{n}_2) = (0, \sqrt{3}(i-j))$; (b) $\mathbf{d}(i,j) = (i-j)\vec{n}_1 = ((i-j)/2, \sqrt{3}(i-j)/2)$. (c) Anisotropy effects in the gapless phase ($J_x = J_y = J_z = 1/3$). Valence bond correlator for the intermediate phase in the presence of a uniform magnetic field [111]: (d) Sign change; (e) Exponential decay for the finite field; (f) Absolute amplitude with varied magnetic strengths. Here we present the case $J_x = J_y = J_z = 1/3$. The direction of the relative vector is chosen on $\mathbf{d}(i,j) = (i-j)(\vec{n}_1 + \vec{n}_2)$.

3.3.2 Results on fluctuations

(a) Area law

Next, to gain some intuition on the behavior of bipartite fluctuations, in Appendix H we perform analytically the lattice summation by assuming an isotropic form of $I(i,j)$, namely with $Y(\vec{r}) = 1$.

Given a bipartition on the honeycomb lattice represented in Fig. 3.3a, we first derive a general scaling form for fluctuations within an arbitrary region $\Omega = l_x \times l_y$

$$I(r) \propto \frac{1}{r^\alpha}, \quad \mathcal{F}_\Omega \propto \begin{cases} L^4, & \alpha = 0; \\ L^3, & \alpha = 1; \\ L^2, & \alpha \geq 2, \end{cases} \tag{3.51}$$

with l_x and l_y of the same order as L.

For the Kitaev honeycomb model, from Sec. 3.3.1 we see the valence bond correlator reveals a power law decay ($\alpha = 4$) in the gapless phase and an exponential decay ($\alpha \to \infty$) in the gapped phases. Therefore, in all phases $\mathcal{F}_A$ shows the volume law: $\mathcal{F}_A \propto L^2 = \mathcal{V}$. As usual, we can extract $\mathcal{F}_{AB}$ from the equality (3.6): $|\mathcal{F}_{A\cup B} - \mathcal{F}_A - \mathcal{F}_B|/2$. With a subsystem size $A = B = (L/2) \times L$, it is noticeable that the volume term vanishes after the subtraction, leading to an area law in $\mathcal{F}_{AB} \propto L = \mathcal{A}$, where $\mathcal{A}$ refers then to an area.

Meanwhile, under the Y-isotropic form assumption, we establish in Appendix H the linear scaling factor of valence bond fluctuations in different phases:

$$\mathcal{F}_{AB} = \alpha_{\mathcal{F}} L + \mathcal{O}(\ln L). \tag{3.52}$$

In the gapless phase, we obtain $\alpha_{\mathcal{F}} = 3.84\tilde{c}_1$ where $\tilde{c}_1$ denotes the constant coefficient in the bond correlator (3.42) for a given set of J_a's. In a gapped phase, we obtain $\alpha_{\mathcal{F}} \propto \xi^3$ with ξ the correlation length. This approach then implies that with a rapidly growing correlation length, $\alpha_{\mathcal{F}}$ must reach a maximum when undergoing a quantum phase transition from a gapped phase into the gapless intermediate regime (see Fig. 3.4a).

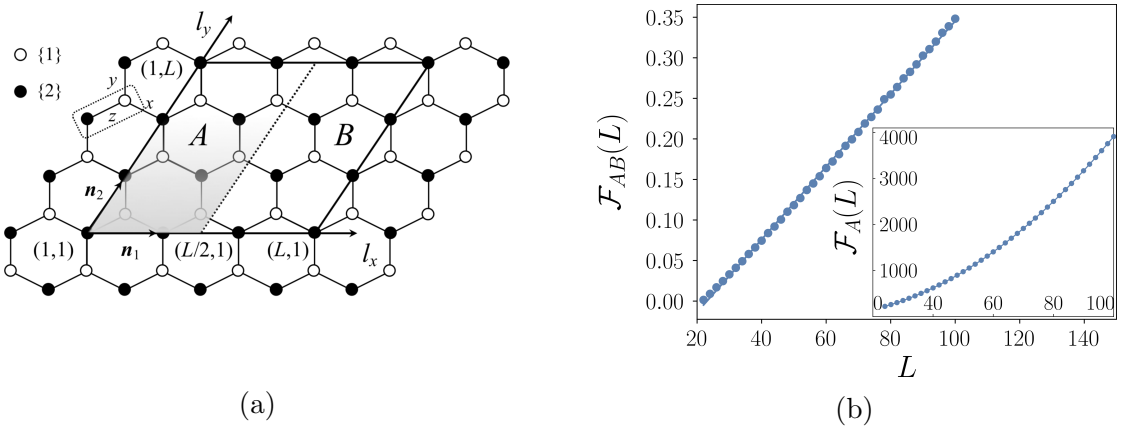

(a) (b)

Figure 3.3: (a) Bipartition into two subsystems A and B. The parallelogram is formed with unit vectors: $\vec{n}_1 = (1/2, \sqrt{3}/2)$, $\vec{n}_2 = (-1/2, \sqrt{3}/2)$. The bond observable is chosen on each z-link (dashed box); (b) Scaling of $\mathcal{F}_{AB} = \alpha_{\mathcal{F}} L + \mathcal{O}(\ln L)$ in the gapless intermediate phase $J_x = J_y = J_z$. We obtain numerically $\alpha_{\mathcal{F}} = 0.00449$. The inset shows the scaling of $\mathcal{F}_A = \alpha L^2 + \beta L + \mathcal{O}(\ln L)$ with $\alpha = 0.391, \beta = 0.0129$..

Numerically, we check these results by the method of finite-size scaling which starts from the anisotropic form (3.39) of the function $I(i, j)$. The exact anisotropic numerical calculations agree well with our previous Y-isotropic form approximation. In Fig. 3.3b, we recover the linear scaling of $\mathcal{F}_{AB}$ in the gapless phase ($J_x = J_y = J_z$). The inset shows the scaling of $\mathcal{F}_A$, where the leading-order L^2 term (0.391) is dominated by the on-site bond fluctuations (0.362, from Eq. (H.13)). Since these on-site contributions are later subtracted, $\mathcal{F}_{AB}$ contains more information about the entanglement properties.

(b) Peak structure in linear scaling factor

Shown in Fig. 3.4a, we continue our study by extracting numerically the linear scaling factor of valence bond fluctuations from different regimes of the phase diagram. A peak structure centered at the quantum phase transition line is observed. While the gapped region can be understood from the simultaneous evolution with the correlation length ($\alpha_{\mathcal{F}} \propto \xi^3$), we check that the anisotropy effects in the Y-function are responsible for the decrease of $\alpha_{\mathcal{F}}$ when the system goes deeper into the gapless phase.

It is noted that after the double summation in $\mathcal{F}_{AB}$ (3.5), the bond fluctuations around the boundary (or domain wall) between two subsystems become the major contribution. Therefore, we can focus on the short-range behavior of the anisotropic factor $Y(\vec{r})$ in the bond correlator (3.43) along the direction perpendicular to the boundary. Illustrated by Fig. 3.4b, at short distances, $Y(\vec{r})$ reaches the maximum value when J_z evolves to the phase transition line. Consequently, the amplitude of the linear scaling $\alpha_{\mathcal{F}}$ in $\mathcal{F}_{AB}$ would drop when we decrease J_z in the gapless phase.

Fig. 3.4c also includes the development of the linear scaling factor $\alpha_{\mathcal{F}}$ with different magnetic strengths. The signature of the peak structure in $\alpha_{\mathcal{F}}$ across the phase transition line is robust against small fields ($\kappa \leq 0.10$). By increasing κ, the gap is enlarged. The anisotropic effects of the $Y(\vec{r})$ function originally dominant in the gapless region become reduced significantly, thus making the cusp of α_F more smooth. Stronger magnetic field effects are discussed qualitatively in Sec. 3.4.

(c) Relation to Fermion entropy

Now, we address the behavior of the entanglement entropy in the Kitaev model. As pointed out in Ref. [133], the total entanglement entropy of the Kitaev honeycomb model consists of two pieces: the gauge field part $\mathcal{S}_G = (L-1)\ln 2$ and the fermionic contribution

$$\mathcal{S}_F = \alpha_{\mathcal{S}} L + \mathcal{O}(1). \tag{3.53}$$

Since the measurement of valence bond fluctuations preserves the $\mathcal{Z}_2$ gauge field structure, $\mathcal{F}_{AB}$ probes the entanglement properties of the fermion sector. Fortunately, $\mathcal{S}_F$ is responsible for all the essential differences between the Abelian and non-Abelian phases.

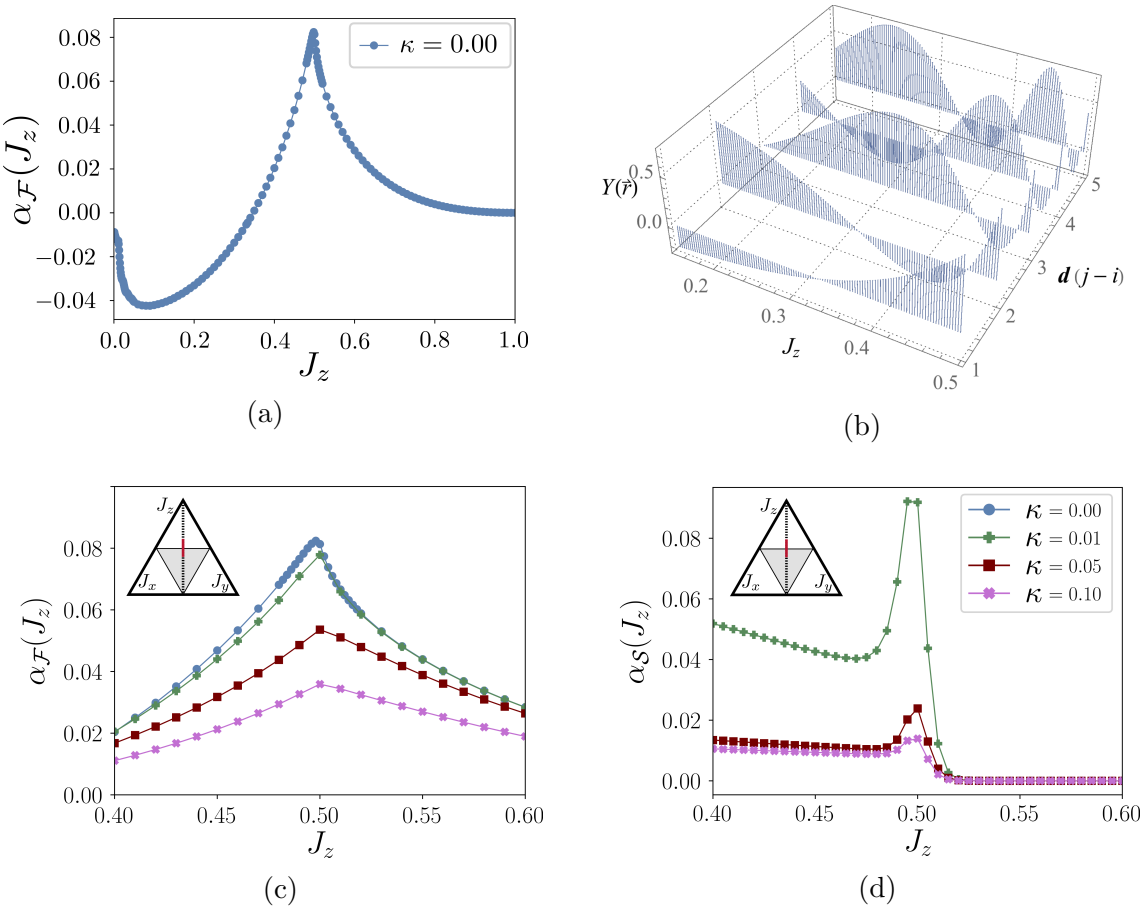

Figure 3.4: (a) Prefactor $\alpha_{\mathcal{F}}$ of the linear term in the bipartite fluctuations $\mathcal{F}_{AB}$ for the gapless intermediate phase ($J_z \leq 0.5$) and the gapped phase with bonds polarized in the z direction ($J_z > 0.5$) of the Kitaev honeycomb model. (b) Anisotropic function $Y(\vec{r})$ in the gapless phase. The relative vector is set along the direction of $\vec{n}_1$ (perpendicular to the boundary between subsystems A and B): $\vec{r} = \vec{r}_j - \vec{r}_i = \mathbf{d}(j-i) = (j-i)\vec{n}_1$. Effects of a small uniform magnetic field on the linear scaling factors of valence bond fluctuations and the Fermi entropy : (c) Prefactor $\alpha_{\mathcal{F}}$ in $\mathcal{F}_{AB}$; (d) Prefactor $\alpha_{\mathcal{S}}$ in $\mathcal{S}_F$. In four plots, the conventions for coupling constants $J_x = J_y$ and $J_x + J_y + J_z = 1$ are adopted. And the magnetic field strength κ varies in the range $[0.00, 0.10]$. The calculation of $\mathcal{F}_{AB}$ is performed on a finite lattice cluster $\Omega = A \cup B = L \times L$ with the total length L varying from 30 to 100. For the finite-size scaling of $\mathcal{S}_F$, on the other hand, the length of the zigzag boundary across x-links is taken as $L = N_x \in [40, 100]$.

We then extract the linear factor $\alpha_{\mathcal{S}}$ from $\mathcal{S}_F$ following the methods of Refs. [133, 293]. It is found that in a small magnetic field $\kappa = 0.01$, the linear scaling factor $\alpha_{\mathcal{S}}$ shares the same response as $\alpha_{\mathcal{F}}$ across the phase transition line shown in Fig. 3.4d. On top of that, once the magnetic field strength is increased, the peak structure of $\alpha_{\mathcal{S}}$ in Fermi entropy disappears slightly more quickly than the one in bond fluctuations. In addition, it is relevant to observe that $\alpha_{\mathcal{S}}$ remains zero for $J_z > 0.5$. Another interesting observation is that as a function of J_z, the magnitudes of $\alpha_{\mathcal{F}}$ and $\alpha_{\mathcal{S}}$ vary approximately in the same range $[0, 0.10]$.

To summarize, in two dimensions, we also find that valence bond fluctuations and the entanglement entropy of the Fermi sector show the same area law scaling in all phases:

$$\mathcal{F}_{AB} \sim S_F. \tag{3.54}$$

Moreover, their linear scaling factors act as signatures to characterize quantum phase transitions between the Abelian and non-Abelian phases in the Kitaev honeycomb model.

3.4 Influence of perturbations

In this section, we would like to make brief remarks about the effects of stronger magnetic fields on the gapless phase of the Kitaev honeycomb model. Two scenarios are presently discussed in the literature: one with excitations of flux pairs [204, 215], and the other with a transition to another type of gapless spin liquid with U(1) symmetry [280]. We will propose possible responses from the valence bond fluctuations respectively.

3.4.1 Perturbed Kitaev QSLs with gauge-flux pairs

For the Kitaev materials in a gapless spin liquid state, two types of gaps have been observed in the presence of a small tilted magnetic field [204]

$$\Delta = \Delta_v + \Delta_f. \tag{3.55}$$

Here, Δ_v denotes the gap from the creation of a pair of fluxes (or visons) and $\Delta_f \propto h_x h_y h_z$ refers to the one induced by one matter Majorana fermion excitation. Our previous analysis of Sec. 3.3 remains valid as long as $\Delta_v \gg \Delta_f$.

In Ref. [215], it was suggested that one can construct an exact perturbed ground state with even number of virtual fluxes by a unitary mapping U from the unperturbed state $|\varphi_0\rangle$: $|\varphi\rangle = U|\varphi_0\rangle$. The transformed spin operator takes the form [215]

$$U^\dagger \sigma_i^a U = iZc_i c_i^a + \cdots + f_{ijk}^a i c_j c_k + \cdots, \tag{3.56}$$

with $Z = 1, f = 0$ for the pure Kitaev model and $Z < 1, f \neq 0$ in the presence of perturbations. The nonzero f parameters open a Majorana fermion gap instantaneously.

One immediately notices for the valence bond operator $Q_i = \sigma_{i,1}^z \sigma_{i,2}^z$, that the leading order contribution turns into

$$U^\dagger Q_i U = Z^2(-ic_{i,1}c_{i,2}) + (\text{quartic terms}). \tag{3.57}$$

Concerning the gauge Majorana fermions c_i^a, we have used the gauge convention form $u_{\langle i_1 i_2\rangle_z} = +1$ and all others being zero, acting on the unperturbed state. The first term in the transformed bond operator (3.57) has a rescaling factor Z^2. It leads to a r^{-4} decay in valence bond correlation $I(i,j) = \langle Q_i Q_j\rangle_c$ within the distance shorter than the correlation length ($r < \xi$). The second part contains products of four matter Majorana fermions, which then result in much faster decays in bond correlations, for instance r^{-6} and r^{-8} over short distances.

Neglecting these higher order corrections arising from the f-decomposition and taking into account the general scaling rule on honeycomb lattice (3.51), we establish

that the valence bond fluctuations still show an area law

$$\mathcal{F}^{\mathrm{VB}}_{AB,\mathrm{perturbed}} = \alpha_{\mathcal{F},\mathrm{perturbed}} \cdot L + \mathcal{O}(\ln L), \tag{3.58}$$

The linear scaling factor is rescaled according to

$$\alpha_{\mathcal{F},\mathrm{perturbed}} \simeq Z^4 \alpha_{\mathcal{F},0}, \tag{3.59}$$

where $\alpha_{\mathcal{F},0}$ denotes the prefactor of the linear term reminiscent of the zero-flux Kitaev spin liquids. Based on Sec. 3.3.2, we thus find

$$\alpha_{\mathcal{F},0} \propto \xi_f^3 \propto \Delta_f^{-3}. \tag{3.60}$$

With excitations of flux pairs, the linear scaling factor now combines two pieces of information: the vison gap Δ_v determining the amplitude of Z^4 and the Majorana fermion gap Δ_f coming into play through $\alpha_{\mathcal{F},0}$.

It may be relevant to mention that the two-spin fluctuations become already nonzero in the perturbed limit. From Eq. (3.56), one gets contributions from the f-sector of Majorana fermions. Accompanied by an exponential decay in the spin-spin correlation, we obtain

$$\mathcal{F}^{\mathrm{TS}}_{AB,\mathrm{perturbed}} = \alpha^{\mathrm{TS}}_{\mathcal{F}} \cdot L + \mathcal{O}(\ln L), \tag{3.61}$$

where

$$\alpha^{\mathrm{TS}}_{\mathcal{F}} \propto (f^z)^2 \cdot \Delta_f^{-3}. \tag{3.62}$$

When $\Delta_v \gg \Delta_f$, no excitation of fluxes is allowed. When $f^z \to 0$, $\alpha^{\mathrm{TS}}_{\mathcal{F}} \to 0$, we check the result of vanishing two-spin fluctuations in the solvable limit (3.25).

3.4.2 Transition to U(1) gapless spin liquids

If one continues to increase the strength of the uniform magnetic field, from numerical simulations [280], while the Kitaev ferromagnet produces a trivial polarized phase

(PL), the Kitaev antiferromagnet might give rise to an intermediate phase supporting U(1) gapless spin liquids (GSL).

In the PL phase, there is no correlation between two subsystems and both the two-spin and valence bond fluctuations vanish

$$\mathcal{F}^{\mathrm{TS/VB}}_{AB,\mathrm{PL}} = 0. \tag{3.63}$$

For the GSL phase in the Kitaev antiferromagnet, one can assume a gapless spinon Fermi surface coupled to a U(1) gauge field. In an effective picture of complex Abrikosov fermions [280], a spin operator is mapped onto the product of fermions $2\vec{S} = f^{\dagger}_{\alpha}\vec{\sigma}_{\alpha\beta}f_{\beta}$, with spin index $\alpha, \beta = \uparrow, \downarrow$ and a U(1) symmetry $f^{\dagger}_{\alpha} \to e^{i\theta}f^{\dagger}_{\alpha}$. From this perspective, the spin and bond correlations follow power-law decays (r^{-4}, r^{-8} respectively) in the gapless phase. We predict that an "enhancement" might be observed in the prefactor of the area-law bipartitie fluctuations

$$\mathcal{F}^{\mathrm{TS/VB}}_{AB,\mathrm{GSL}} = \alpha^{\mathrm{TS/VB}}_{\mathcal{F},\mathrm{GSL}} \cdot L + \mathcal{O}(\ln L). \tag{3.64}$$

The existence of a similar peak structure in $\alpha_{\mathcal{F}}$ between the gapped Kitaev spin liquids and U(1) gapless spin liquids is possible and can be tested numerically in the future.

3.5 Comparison with the Néel phase

In this final section, a comparison with the Néel state supported by antiferromagnetic Heisenberg interactions will give us additional insights with regard to the application in quantum materials.

In the end, to make a closer link with quantum materials, it is perhaps useful to compare the obtained behavior of bond-bond correlation functions from the ones of the two-dimensional Heisenberg model, *i.e.*, of a Néel ordered phase subject to spin-wave excitations. When antiferromagnetic Heisenberg interactions are dominant, the modified spin-wave theory predicts that a staggered magnetic field is required to stabilize the Néel state at zero temperature for finite lattices [287, 294].

Performing a spin-wave analysis in Appendix I, then we find that the same valence bond correlation shows:

$$I(i,j) = c_0 + c_1 r^{-1} \tag{3.65}$$

with $c_0 = 0.131$ and $c_1 = 0.141$.

As a result, the bipartite fluctuations now follow a volume square law:

$$\mathcal{F}_{AB} \propto L^4, \tag{3.66}$$

arising from the non-vanishing long-range correlation of c_0. Measuring the precise leading order scalings then allows to probe the phase, Kitaev spin liquid versus Néel state, of a two-dimensional quantum material. We emphasize here that the entanglement entropy of the Néel state still reveals an area law [287], as in the Kitaev spin model. The violation of the lower bound (3.10) originates from the finite-size regularization procedure taken in the modified spin-wave theory.

Chapter 4

Quantum spin liquids in ladder models and Majorana box engineering in cQED

In this chapter, we design a Majorana box starting from a superconducting four-site circuit [58, 295, 296] with the goal to engineer quantum spin liquids and many-body Majorana states. Starting with four transmon qubits, we present a Nuclear Magnetic Resonance (NMR) double-period protocol to realize the box. We study the quantum dynamics in time to implement the required protocols and to detect the $\mathcal{Z}_2$ gauge fields through spin variables.

Within our framework, a lattice system can then be built by coupling a number of boxes, forming then coupled-ladder models in the same spirit as our coupled wire construction of the spinless $p + ip$ superconductor in Sec. 2.3.1. Coupled boxes in this chapter, however, could allow us to encode spin-1/2 degrees of freedom and re-build the Kitaev $\mathcal{Z}_2$ quantum spin model of the honeycomb lattice[18], in ladder systems [56, 146, 147, 297–299] with potential applications in the toric code [137] and other surface codes [300]. These models have stimulated the discovery of quantum materials [127, 194, 204, 301–303] as well as the design of ultra-cold atoms [227, 304] and other superconducting architectures [305–307]. It is important to mention other proposals of Majorana boxes related to topological superconducting wires [8, 10–12] and topological superconductors [9]. Realizing a pure four-body Majorana

fermion coupling also allows us to emulate the Sachdev-Ye-Kitaev (SYK) model [308–310] with coupled boxes as elaborated below. The SYK model, which involves a (long-range and disordered) coupling between four Majorana fermions, has attracted attention theoretically in high-energy [311–313] and low-energy physics [314–316] due to possible black-hole gravity holographic correspondence [310] and link to quantum chaos [317]. Only a few realizations of the SYK Majorana model have been discussed so far [314–316]. SYK spin models could also bring light on quantum glasses [309].

This chapter is organized as follows. In Sec. 4.1, we review the generalized phase diagram of the Kitaev square ladder in collaboration with A. Soret. In Sec. 4.2, we show how to engineer the Hamiltonian of a single plaquette from the same ladder geometry with superconducting circuits, as an introduction of our main algorithm. In Sec. 4.3, we give a short summary of numerical tests on the time-dependent Hamiltonian that is performed by our collaborator L. Henriet, including the detuning stability, dissipation effects, measurements of gauge fields and the presence of disorders. We address in Sec. 4.4 the constraints on the experimental parameters of our dynamical protocol. In Sec. 4.5, we discuss applications for an ensemble of coupled boxes, such as the realization of Kitaev spin models and the emergence of Néel (Ising-like) order for the gauge fields, probe of Majorana physics and quantum phase transitions through local measurements, as well as relations with Wen's toric code [318] and possible SYK loop models.

4.1 Phase diagram of a two-leg Kitaev spin ladder

We start with a review of our phase diagram for a generalized two-leg Kitaev spin ladder (see Fig. 4.1). On horizontal bonds, there are $XYXY$ alternating Ising interactions with coupling constants J_1 and J_2. For the vertical bonds, we allow $ZZ'ZZ'$ couplings with strengths J_3 and J_4. We note that the square type ladder has been addressed in several works [146, 297, 319]. In our framework, however, by setting $J_4 = 0$ and $J_3 \neq 0$ we realize a brickwall ladder geometry, which is reminiscent of the

honeycomb ribbons and has not been addressed so far, to the best of our knowledge. In the brickwall ladder, we show that the gapless B phase of Fig. 4.1c is reduced to a line.

In Fig. 4.1a, the two-leg ladder can be viewed as two spin chains coupled by the vertical Ising exchanges. Without loss of generality, we set l as the distance between two connected vertices (lattice spacing) and assume $2M$ sites on each chain. The sites are then labelled by two integers (j, α) with the site index $j = 1, 2, \ldots, 2M$ and the row index $\alpha \in \{1, 2\}$. The Hamiltonian of the system reads :

$$H = H_1 + H_2 + H_I, \tag{4.1}$$

where

$$\begin{aligned} H_1 &= \sum_{j=2m-1} J_1 \sigma^x_{j,1}\sigma^x_{j+1,1} + J_2 \sigma^y_{j+1,1}\sigma^y_{j+2,1} \\ H_2 &= \sum_{j=2m-1} J_1 \sigma^x_{j+1,2}\sigma^x_{j+2,2} + J_2 \sigma^y_{j,2}\sigma^y_{j+1,2} \\ H_I &= \sum_{j=2m-1} J_3 \sigma^z_{j,1}\sigma^z_{j,2} + J_4 \sigma^z_{j+1,1}\sigma^z_{j+1,2}, \end{aligned} \tag{4.2}$$

with $(J_1, J_2, J_3, J_4) < 0$ being the ferromagnetic coupling constants.

By analogy to the Kitaev spin chain in Sec. 1.3.4, we can write the Hamiltonian (4.1) in terms of fermionic operators, using the Jordan-Wigner transformation. One can show that the emergent Hamiltonian is independent of the chosen string path [147] (see Fig. 4.2 (right top) for different string configurations). Following an arbitrary string, we define

$$\begin{cases} \sigma^-_{j,\alpha} = a_{j,\alpha} e^{i\pi \sum_{\{i,\alpha\} \in string} a^\dagger_{i,\alpha} a_{i,\alpha}} \\ \sigma^+_{j,\alpha} = a^\dagger_{j,\alpha} e^{i\pi \sum_{\{i,\alpha\} \in string} a^\dagger_{i,\alpha} a_{i,\alpha}} \end{cases} \quad \alpha \in \{1, 2\}. \tag{4.3}$$

$$\begin{cases} \sigma^x_{j,\alpha} = \sigma^+_{j,\alpha} + \sigma^-_{j,\alpha} = (a^\dagger_{j,\alpha} + a_{j,\alpha}) e^{i\pi \sum_{i<j} a^\dagger_{i,\alpha} a_{i,\alpha}} \\ \sigma^y_{j,\alpha} = \frac{1}{i}(\sigma^+_{j,\alpha} - \sigma^-_{j,\alpha}) = i(a^\dagger_{j,\alpha} - a_{j,\alpha}) e^{i\pi \sum_{i<j} a^\dagger_{i,\alpha} a_{i,\alpha}}, \end{cases} \tag{4.4}$$

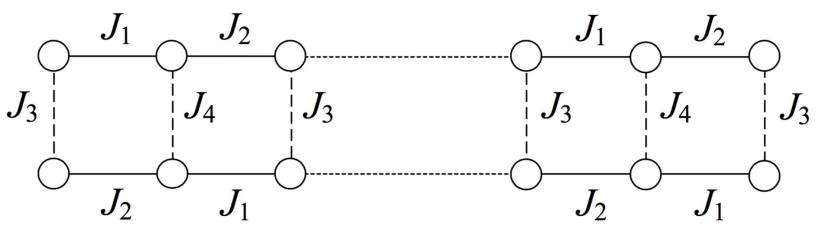

(a)

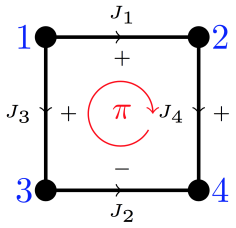

(b)

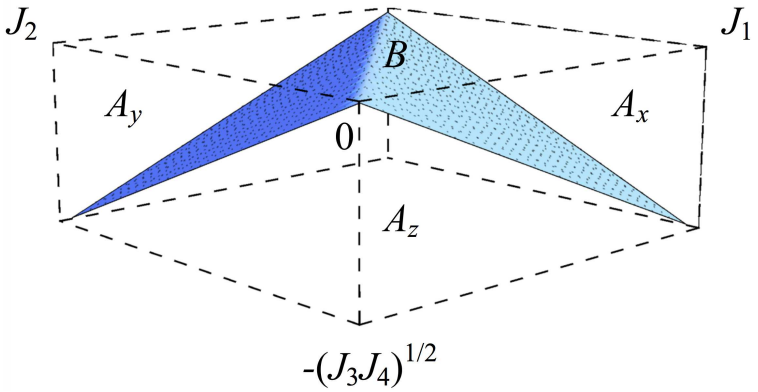

(c)

Figure 4.1: (a) Geometry of a square ladder: distinct ZZ' Ising couplings with strengths J_3 and J_4 are assigned alternatively on vertical bonds. (b) In ladder geometries, one can define $\mathcal{Z}_2$ gauge fields by analogy with the Kitaev honeycomb model [18]. By Lieb's theorem [131], the flux operator $\mathcal{P}_d = D_{1,3}D_{2,4}$ is fixed to $+1$ for $J_i < 0$, corresponding to a π-flux configuration. (c) Generalized phase diagram for the quantum ladder. The gapless B spin liquid phase is located on the plane where $J_3J_4 = (J_1 - J_2)^2$.

and introduce the Majorana fermion representation:

$$c_{j,\alpha} = \begin{cases} i(a^\dagger_{j,\alpha} - a_{j,\alpha}) \ , \ j+\alpha = 2m \\ a^\dagger_{j,\alpha} + a_{j,\alpha} \ , \ j+\alpha = 2m-1 \end{cases} \tag{4.5}$$

$$d_{j,\alpha} = \begin{cases} a^\dagger_{j,\alpha} + a_{j,\alpha} \ , \ j+\alpha = 2m \\ i(a^\dagger_{j,\alpha} - a_{j,\alpha}) \ , \ j+\alpha = 2m-1 \end{cases} \tag{4.6}$$

In this construction, the Hamiltonian takes the form :

$$\begin{aligned} H = -i \sum_{j=2m-1} [&J_1 c_{j,1}c_{j+1,1} - J_2 c_{j+1,1}c_{j+2,1} \\ &+ J_1 c_{j+1,2}c_{j+2,2} - J_2 c_{j,2}c_{j+1,2} \\ &+ J_3 D_{j,1}c_{j,1}c_{j,2} + J_4 D_{j+1,1}c_{j+1,1}c_{j+1,2}], \end{aligned} \tag{4.7}$$

where $D_{j,\alpha}$ depends only on the $d_{j,\alpha}$ operators on a vertical bond through $D_{j,\alpha} = (-i)d_{j,\alpha}d_{j,\alpha+1}$.

Here, $D_{j,\alpha}$ commutes with the Hamiltonian and can take classical values ± 1 as the gauge variables $\hat{u}_{\langle ij\rangle\mu}$ of the Kitaev honeycomb model [18]. To fix the gauges of $D_{j,\alpha}$, we can then make a precise connection with the approach by Kitaev in two dimensions, where the spin operators in the expanded space are decomposed in terms of Majorana fermions c_j^μ and c_j:

$$\sigma_j^\alpha = ic_j c_j^\mu \quad \mu \in \{x, y, z\}. \tag{4.8}$$

Defining $u_{j,k} = ic_j^\mu c_k^\mu$ such that $\sigma_j^\mu \sigma_k^\mu = -iu_{j,k}c_j c_k$, and the Hamiltonian acquires the general form :

$$H = \frac{-i}{2}\sum_{\langle j,k\rangle} J_{j,k}u_{j,k}c_j c_k, \tag{4.9}$$

where the sum is performed over nearest neighbors $\langle j, k\rangle$. Within this notation $\langle j, k\rangle$ gives a factor 2 when summing over j and k since $u_{j,k} = -u_{k,j}$.

Now, let us make an explicit connection with Hamiltonian (4.7) obtained from the Jordan-Wigner string. For convenience, in a unit cell of four sites, we label the individual sites by index $\lambda = 1, 2, 3, 4$ depicted by Fig. 4.1b. By analogy to the 2D case (1.95), the loop operator on this single square plaquette can be constructed as

$$W_p = u_{1,2}u_{2,4}u_{4,3}u_{3,1}, \tag{4.10}$$

in a counterclockwise direction. These four gauge variables can be identified in Eq. (4.7) straightforwardly: $u_{1,2} = u_{3,4} = +1$ and $u_{3,1} = -D_{1,3}$, $u_{2,4} = D_{2,4}$. It leads to $W_p = -D_{1,3}D_{2,4}$. From Lieb's theorem [131], when the Ising couplings share the same sign, in contrast to the 0-flux ground state of the hexagon plaquettes (with all W_p's fixed to $+1$), the square plaquettes select a π-flux configuration for the $\mathcal{Z}_2$ gauge field (with all W_p's fixed to -1). In the ground state, we then obtain conserved quantities in terms of the flux operator,

$$\mathcal{P}_d = D_{1,3}D_{2,4} = d_1 d_2 d_3 d_4 = +1. \tag{4.11}$$

Artificially, we can fix $D_{1,3} = D_{2,4} = +1$ in Hamiltonian (4.7). And we will see below that the energy spectrum (4.13) is invariant under the transformation $J_3 \to -J_3$ and $J_4 \to -J_4$. Moving to the momentum space by Fourier transform, the Hamiltonian can be diagonalized conveniently in the basis of matter Majorana fermions c:

$$H = -i \sum_k X^T \underbrace{\begin{pmatrix} 0 & \alpha & \beta & 0 \\ -\alpha^* & 0 & 0 & \gamma \\ -\beta^* & 0 & 0 & -\alpha^* \\ 0 & -\gamma^* & \alpha & 0 \end{pmatrix}}_{M} X \tag{4.12}$$

with $\alpha = J_1 e^{-ikl} + J_2 e^{ikl}$, $\beta = J_3 e^{-il}$, $\gamma = J_4 e^{-il}$ and $X^T = (c_{k,1}, c_{k,2}, c_{k,3}, c_{k,4})$.

The energy spectrum reads

$$\epsilon(k) = \pm \sqrt{\frac{A(k)}{2} \pm \frac{\sqrt{A(k)^2 - 4B(k)}}{2}}, \tag{4.13}$$

with

$$A(k) = 2\left(J_1^2 + J_2^2 + 2J_1 J_2 \cos(2kl) + \frac{J_3^2 + J_4^2}{2}\right)$$

and

$$B(k) = (J_1^2 + J_2^2 + 2J_1 J_2 \cos(2kl))^2 + 2J_3 J_4 (2J_1 J_2 + (J_1^2 + J_2^2)\cos(2kl)) + J_3^2 J_4^2.$$

We shall now study the phase diagram of the system. In a four-parameter space, (J_1, J_2, J_3, J_4), the spectrum is gapless if there exists a mode k such that $\epsilon(k) = 0$. It is important to notice that $\epsilon(k) = 0$ is equivalent to $B(k) = 0$. This equality results in the location of the gapless phase B in the phase diagram of Fig. 4.1c, for the generalized ladder with distinct J_3 and J_4 couplings. We also insist on the fact that the gapless B phase is reduced to two transition lines for the square ladder studied in Ref. [146] where $J_3 = J_4$, as we also reproduce.

The emergence of the gapless B phase in the generalized phase diagram of Fig. 4.1c can also be understood from a dual mapping, using the notations of Ref. [146]. The

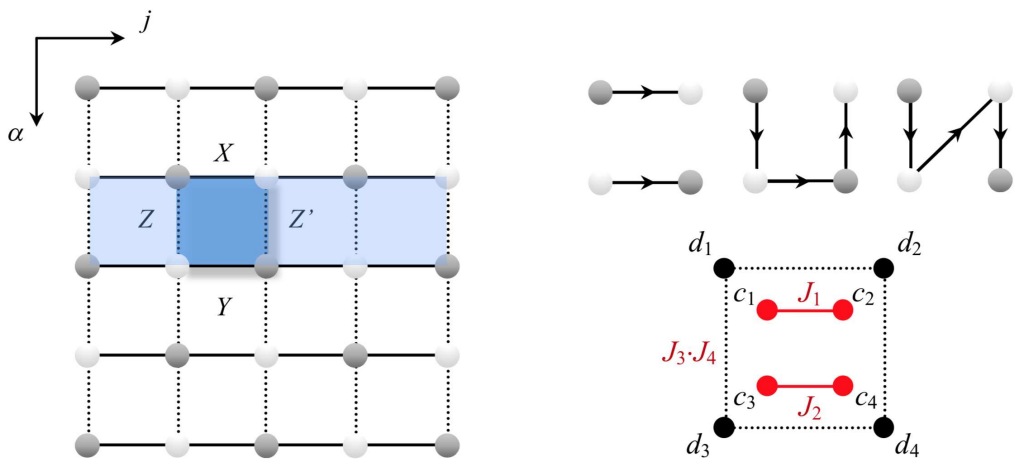

Figure 4.2: (Left) Two-dimensional lattice built from coupled boxes with $\mathcal{Z}_2$ symmetry: $XYXY$ alternating Ising couplings along horizontal bonds and $ZZ'ZZ'$ couplings on vertical bonds. (Right top) Different configurations of Jordan-Wigner strings for one unit cell. (Right bottom) Majorana representation: J_1, J_2, $J_3(J_4)$ denote respectively the X, Y and Z coupling constants. When $|J_1|, |J_2| \gg |J_3|, |J_4|$, c Majorana particles are gapped at high energies and the d Majorana fermions describe the state of gauge fields in each unit cell or square plaquette.

Hamiltonian can be indeed re-written as [320]

$$H = \sum_j J_1 \tau^x_{2j-2}\tau^x_{2j} - J_2 \tau^y_{2j-2}\tau^y_{2j} + J_3 \tau^z_{4j} + J_4 \tau^z_{4j+2}. \tag{4.14}$$

The fact that the odd sites do not enter in the mapping reflects the macroscopic degeneracies of the different phases. Using the change of variable $2j-2 \to j-1$ and $2j \to j$, then we obtain a spin-1/2 XY chain with alternating transverse fields. The Hamiltonian is solved exactly using the Jordan-Wigner transformation and one recovers a gapless spectrum when $J_3 J_4 = (J_1 - J_2)^2$ which corresponds to $B(k) = 0$.

4.2 Algorithm on an island

Before proceeding to the engineering side of the circuit network, it is useful to reinforce the notion of flux states arising from the ladder geometry of Sec. 4.1. On a general lattice of Fig. 4.2, a unit cell of four sites is depicted as the blue box. Lattice of this type holds a class of exactly solvable models for quantum spin liquids. By setting $Z' = 0$, the brick-wall lattice recovers the Kitaev honeycomb model. Multi-leg ladders

can then be addressed, as well as the passage from one to two dimensions, or higher-dimensional lattices.

For a square of four sites, in Sec. 4.1 we have derived the Hamiltonian in the Majorana presentation (4.7)

$$\begin{aligned}\mathcal{H}_K &= J_1\sigma_1^x\sigma_2^x + J_2\sigma_3^y\sigma_4^y + J_3\sigma_1^z\sigma_3^z + J_4\sigma_2^z\sigma_4^z \\ &= -iJ_1c_1c_2 + iJ_2c_3c_4 - iJ_3D_{1,3}c_1c_3 - iJ_4D_{2,4}c_2c_4\end{aligned} \tag{4.15}$$

with $D_{1,3} = -id_1d_3$ and $D_{2,4} = -id_2d_4$. In our cQED networks, the couplings J_1 and J_2 are ferromagnetic (or $J_1, J_2 < 0$), and the couplings J_3 and J_4 are adjustable couplings through the fluxes Φ_3 and Φ_4 in Fig. 4.3a. On a square unit cell, the associated flux operator has been defined as

$$\mathcal{P}_d = d_1d_2d_3d_4 = D_{1,3}D_{2,4}. \tag{4.16}$$

This flux operator acting on a unit square cell, and encoded with the d-Majorana $\mathcal{Z}_2$ variables, in our representation intervenes through the product of parity operators of two d-Majorana fermions forming the vertical bonds.

The limit of weak vertical bonds $|J_1|, |J_2| \gg |J_3|, |J_4|$ (see Fig. 4.2 Right bottom) is of particular interest to us. The c-Majorana fermions are gapped describing the formation of valence bonds in the spin language between sites 1 and 2, and 3 and 4, respectively. In addition, $-ic_1c_2 = +1$ and $ic_3c_4 = +1$ such that we can define the operator $\mathcal{P}_c = c_1c_2c_3c_4 = +1$. The d-Majorana particles will be coupled in a 4-body coupling, as in the SYK model. More precisely, the leading-order term in the perturbation theory gives $-J_3J_4/(|J_1| + |J_2|)\sigma_1^z\sigma_2^z\sigma_3^z\sigma_4^z = -J_3J_4/(|J_1| + |J_2|)\mathcal{P}_d\mathcal{P}_c$ with $\mathcal{P}_c = 1$. If $J_3J_4 > 0, \mathcal{P}_d = 1$ corresponds to the π-flux configuration in a square unit cell, in agreement with the Lieb's theorem [131]; otherwise $\mathcal{P}_d = -1$ relates to the 0 flux.

Below, we show how to detect the gauge fields, at the level of one box and a few boxes. It is also relevant to note that by assembling boxes, one can then build a spin

model, which turns out to be a quantum spin liquid with a π-flux ground state. A staggered flux order has also been suggested for high-T_c cuprates [321–323]. Recent efforts in quantum materials report the observation of orbital loop currents in Mott materials with spin-orbit coupling [324] by analogy with cuprates [325]. Here, we can tune parameters in the spin system and adjust the ground state to have such a π flux. The coupled-ladder geometry then presents some tunability.

4.2.1 Physics of a box

First, we introduce the physical structure of one box in Fig. 4.3. Within a cell of four sites shown in Fig. 4.3a, we denote the superconducting phases as $\hat{\varphi}_j$ ($j = 1, 4 \in \{A\}; j = 2, 3 \in \{B\}$). One box can be decomposed into three parts: the on-site transmon, the local NMR device and the inter-site couplings. Fig. 4.3b shows the internal structure of each site. We build a transmon qubit on the site j via sets of capacitances and Josephson junctions $\{C_{q,A}, E_{J_{q,A}}\}$ and $\{C_{q,B}, E_{J_{q,B}}\}$, of which the resonance (plasma) frequencies will be adjusted accordingly. The qubit Hamiltonian reads:

$$\mathcal{H}_{q,j} = \frac{C_{q,j}\phi_0^2}{2}\dot{\hat{\varphi}}_j^2 - E_{J_{q,j}} \cos \hat{\varphi}_j, \tag{4.17}$$

where $\phi_0 = \hbar/(2e)$ denotes the rescaled quantum of flux and $E_{J_{q,j}}$ represents the Josephson energy of the internal junction.

In Fig. 4.3c, we then connect each node j to an inductance L'_j and a capacitance C'_j followed by an AC source of voltage, generating a time-dependent NMR field

$$\mathcal{H}_{\mathrm{NMR},j} = E_{L',j}\left(\varphi'_j - \hat{\varphi}_j\right)^2 + \frac{C'\phi_0^2}{2}\left(\dot{\varphi}'_j - \dot{\hat{\varphi}}_j\right)^2 + E_{V_{AC},j}. \tag{4.18}$$

The main purpose of this field is to cancel the local magnetic field in the rotating frame, as we will show later. Time dependence of $\mathcal{H}_{\mathrm{NMR},j}$ is encoded in parameters φ'_j and $\dot{\varphi}'_j$ which satisfy the relations: $\phi_0\dot{\varphi}'_j = -V_{AC,j} = -V_{0,j}\sin(\omega_j t)$, $\varphi'_j = \int dt\ \dot{\varphi}'_j = V_{0,j}\cos(\omega_j t)/(\phi_0\omega_j)$. We choose to apply this NMR device because it preserves the

$\mathcal{Z}_2$ symmetry of the Hamiltonian. This protocol is then distinct from the protocol used in Ref. [58] for the 3-qubit system.

For the interaction part, as can be seen from 4.3a, horizontal bonds of the box are coupled by an inductance L and a capacitance C to engineer respectively X and Y couplings. The corresponding interaction Hamiltonians take the form

$$\mathcal{H}_L = E_L \left(\hat{\varphi}_2 - \hat{\varphi}_1\right)^2, \quad \mathcal{H}_C = \frac{C\phi_0^2}{2}\left(\dot{\hat{\varphi}}_4 - \dot{\hat{\varphi}}_3\right)^2 \tag{4.19}$$

with $E_L = \phi_0^2/(2L)$.

Realizing pure Z couplings on vertical bonds can be achieved through SQUIDs. The SQUIDs (with characteristic Josephson energies $E_{J,3}$ and $E_{J,4}$) are controlled via applied magnetic fields Φ_3 and Φ_4, and we add auxiliary inductances $\tilde{L}_3$ and $\tilde{L}_4$ to compensate additional X couplings from junctions. For instance, on the vertical bond $(1,3)$, the interaction energy of the SQUID has the form

$$\mathcal{H}_{S,3} = -E_{J,3}\cos\left(\hat{\varphi}_1 - \hat{\varphi}_3\right), \tag{4.20}$$

while the auxiliary inductance $\tilde{L}_3$ contributes to

$$\mathcal{H}_{\tilde{L},3} = E_{\tilde{L}}\left(\hat{\varphi}_1 - \hat{\varphi}_3\right)^2, \tag{4.21}$$

with $E_{\tilde{L}} = \phi_0^2/(2\tilde{L})$. We study perturbations arising from vertical bonds in Sec. 4.3.

The total Hamiltonian can now be written as

$$\mathcal{H} = \sum_{j=1}^{4} \mathcal{H}_{q,j} + \mathcal{H}_{\mathrm{NMR},j} + \mathcal{H}_L + \mathcal{H}_C + \mathcal{H}_S + \mathcal{H}_{\tilde{L}}. \tag{4.22}$$

4.2.2 Quantized Hamiltonian

We start from the quantization [296] of the transmon qubit Hamiltonian $\mathcal{H}_{q,j}$, which behaves as harmonic oscillators with anharmonicity from Josephson junctions. Expanding the nonlinear cosine potential in Eq. (4.17) to the fourth order and choosing the bosonic representation: $[\hat{\varphi}_j, \hat{\pi}_l] = i\hbar\delta_{j,l}, \hat{\varphi}_j = (b_j^\dagger + b_j)/\lambda_j, \dot{\hat{\varphi}}_j = (b_j^\dagger - b_j)(-e\lambda_j)/(i\phi_0 C_{q,j})$ with conjugate momentum $\hat{\pi}_j = \phi_0^2 C_{q,j}\dot{\hat{\varphi}}_j$, we reach

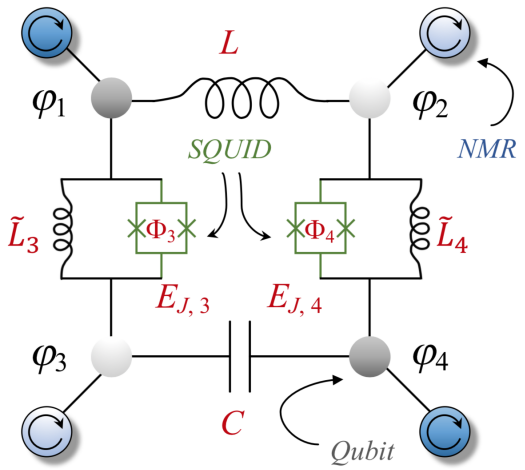

(a)

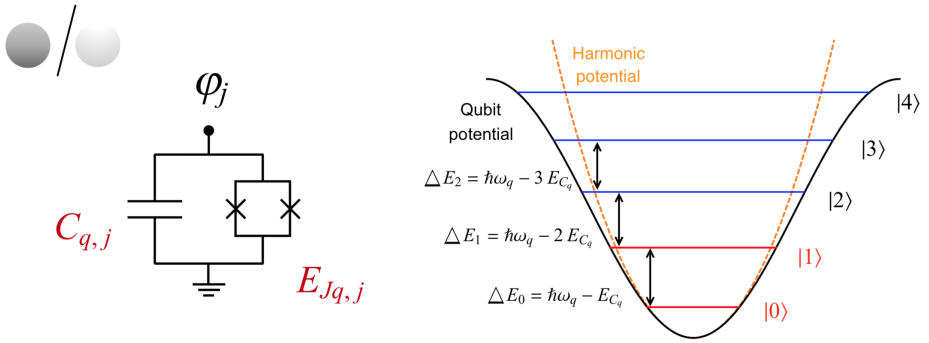

(b)

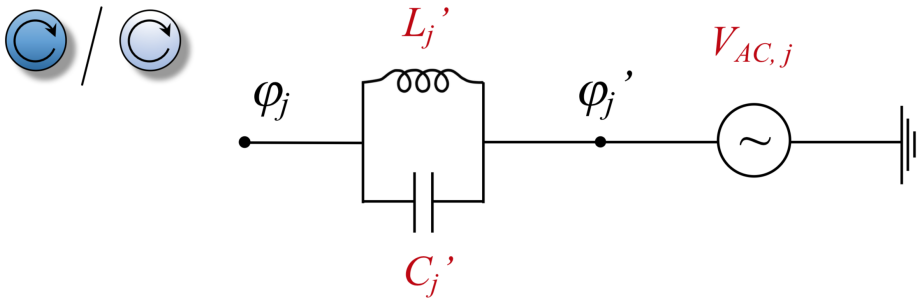

(c)

Figure 4.3: (a) We engineer X and Y Ising couplings through inductance L and capacitance C on horizontal bonds, Z couplings with SQUIDs and auxiliary inductances $\tilde{L}$ on vertical bonds; (b) (Left) Structure of on-site transmon qubits: composed of two Josephson junctions and a capacitance in parallel; (b) (Right) Spectrum of transmon qubits realized with the two lowest levels; (c) Structure of the generalized NMR device: producing a circularly polarized driven field. Different colors of qubits (grey and white) and NMR fields (dark blue and light blue) indicate two distinct sets of frequency patterns for sublattices A and B.

$$\mathcal{H}_{q,j} = -E_{J_{q,j}} + \hbar\omega_{q,j}\left(b_j^\dagger b_j + \frac{1}{2}\right) - \frac{E_{C_{q,j}}}{12}\left(b_j^\dagger + b_j\right)^4. \tag{4.23}$$

Here we assume the system in the large $\lambda_j = (E_{J_{q,j}}/(2E_{C_{q,j}}))^{1/4}$ limit. $E_{C_{q,j}} = e^2/(2C_{q,j})$ depicts the charging energy associated with the transfer of a single electron. $\omega_{q,j} = \sqrt{8E_{C_{q,j}}E_{J_{q,j}}}/\hbar$ is known as the Josephson plasma frequency ($\sim$ GHz corresponding to $T \sim 0.1$ K).

As shown in Fig. 4.3b (right), we denote the eigenstates of a pure harmonic oscillator as $|n_j\rangle$. Taking into account the leading-order correction from the quartic term in Eq. (4.23), the spectrum of a transmon is modified into $E_{n,j} = -E_{J_q,j} + \hbar\omega_{q,j}\left(n_j + 1/2\right) - E_{C_q,j}\left(6n_j^2 + 6n_j + 3\right)/12$. The gap is decreasing between two successive energy levels: $\Delta E_{n,j} = E_{n+1,j} - E_{n,j} = \hbar\omega_{q,j} - E_{C_q,j}\left(n_j + 1\right)$. If we restrict the state of each transmon j to the two lowest energy levels $|0\rangle_j$ the quantum vacuum and $|1\rangle_j$ the state with one excited quantum, a qubit will be formed. As transitions to higher levels are forbidden, b_j become hard-core bosons obeying $b_j^n = (b_j^\dagger)^n = 0$ for any $n \geq 2$. It allows an exact mapping to the spin-1/2 states for an individual site: $|0\rangle_j \leftrightarrow |\downarrow\rangle_j, |1\rangle_j \leftrightarrow |\uparrow\rangle_j, b_j^\dagger \leftrightarrow \sigma_j^+, b_j \leftrightarrow \sigma_j^-$ with $|\downarrow\rangle_j$ and $|\uparrow\rangle_j$ polarized along z direction. In the spin space,

$$\sigma_j^x = b_j^\dagger + b_j, \quad \sigma_j^y = \frac{1}{i}(b_j^\dagger - b_j), \quad \sigma_j^z = 2b_j^\dagger b_j - 1. \tag{4.24}$$

Eigenvalues of σ_j^z are well fixed to ± 1 since we restrict ourselves to the subspace where $b^\dagger b = 0$ or 1. Now, the effective Hamiltonian of a transmon qubit acts as a strong local magnetic field

$$\mathcal{H}_{q,j} \simeq \Delta E_{0,j} b_j^\dagger b_j = \epsilon_{q,j}\sigma_j^z, \tag{4.25}$$

where $\epsilon_{q,j} = \Delta E_{0,j}/2 = (\hbar\omega_{q,j} - E_{C_q,j})/2$ characterizes the transition energy from $|0\rangle_j$ to $|1\rangle_j$. In the absence of an AC driving source, the spin system would be polarized meaning that all the transmon systems would be in the quantum vacuum.

Through this quantization procedure, the NMR field is transformed into

$$\begin{aligned}\mathcal{H}_{\mathrm{NMR},j} = &-\frac{\hbar\omega_{L',j}}{2}\cos(\omega_j t)\sigma_j^x - \frac{\hbar\omega_{C',j}}{2}\sin(\omega_j t)\sigma_j^y \\ &+ (\epsilon_{L',j} + \epsilon_{C',j})\,\sigma_j^z,\end{aligned} \tag{4.26}$$

with the fast-oscillating terms $E_{L',j}(\varphi_j')^2$, $C'(\phi_0\dot{\varphi}_j')^2/2$ and $E_{V_{AC},j}$ dropped out. For simplicity, all coefficients are listed in Table 4.2. Furthermore, we impose

$$\omega_{L',j} = \omega_{C',j} = \omega_{1,j} \tag{4.27}$$

to generate a circularly polarized field. The stability in the presence of a small detuning from this condition will be discussed in Eq. (4.60).

On the horizontal bonds, the interaction Hamiltonians become

$$\begin{aligned}\mathcal{H}_L &= \epsilon_{L,A}\sigma_1^z + \epsilon_{L,B}\sigma_2^z + J_1\sigma_1^x\sigma_2^x, \\ \mathcal{H}_C &= \epsilon_{C,B}\sigma_3^z + \epsilon_{C,A}\sigma_4^z + J_2\sigma_3^y\sigma_4^y,\end{aligned} \tag{4.28}$$

where $J_1 < 0$ and $J_2 < 0$.

A more detailed analysis is needed for the vertical bonds. In the large λ_j limit, $\hat{\varphi}_j$ can be viewed as a small quantum variable. We are allowed to ignore higher order contributions of the cosine potential in Eq. (4.20). To the fourth order, $\mathcal{H}_{S,3} = -E_{J,3}(1 - (\hat{\varphi}_1 - \hat{\varphi}_3)^2/2! + (\hat{\varphi}_1 - \hat{\varphi}_3)^4/4! + \cdots)$. The quadratic terms give arise to an effective X coupling $\hat{\varphi}_1\hat{\varphi}_3 \sim \sigma_1^x\sigma_3^x$ and a magnetic field $\hat{\varphi}_1^2 \sim \sigma_1^z, \hat{\varphi}_3^2 \sim \sigma_3^z$. For the quartic contribution, the only effective term $\hat{\varphi}_1^2\hat{\varphi}_3^2$ produces a Z coupling $\sigma_1^z\sigma_3^z$. Thus,

$$\mathcal{H}_{S,3} = J_3\sigma_1^z\sigma_3^z + J_3^x\sigma_1^x\sigma_3^x + \epsilon_{J,1}\sigma_1^z + \epsilon_{J,3}\sigma_3^z, \tag{4.29}$$

where $J_3, J_3^x \propto -E_{J,3}$. Both the signs and amplitudes of vertical couplings can be adjusted by the flux Φ_3 inside the SQUID as $E_{J,3} \sim \cos(\Phi_3/(2\phi_0))$.

At the same time, the auxiliary inductance $\tilde{L}_3$ gives a negative X coupling

$$\mathcal{H}_{\tilde{L},3} = \tilde{J}_3^x\sigma_1^x\sigma_3^x + \epsilon_{\tilde{L},A}\sigma_1^z + \epsilon_{\tilde{L},B}\sigma_3^z. \tag{4.30}$$

We can then reduce the vertical X couplings to zero:

$$J_3^x + \tilde{J}_3^x = 0, \tag{4.31}$$

with the phase $\Phi_3/(2\phi_0) \in [\pi/2 + 2n\pi, 3\pi/2 + 2n\pi[\,, n \in \mathbb{Z}$ for a positive J_3^x. It is the same case with bond $(2, 4)$.

Combined with the local σ_j^z field of the transmon qubit, the total effective Hamiltonian of the box becomes

$$\begin{aligned} \mathcal{H} &= \mathcal{H}_K + \mathcal{H}_C(t), \\ \mathcal{H}_K &= J_1^x \sigma_1^x \sigma_2^x + J_2 \sigma_3^y \sigma_4^y + J_3 \sigma_1^z \sigma_3^z + J_4 \sigma_2^z \sigma_4^z, \\ \mathcal{H}_C(t) &= \sum_j \frac{\hbar\omega_{0,j}}{2} \sigma_j^z - \frac{\hbar\omega_{1,j}}{2} \left(\cos(\omega_j t)\, \sigma_j^x + \sin(\omega_j t)\, \sigma_j^y\right). \end{aligned} \tag{4.32}$$

The time-dependent Hamiltonian $\mathcal{H}_C(t)$ here is distinct from the capacitive Hamiltonian $\mathcal{H}_C$ introduced above in the intermediate steps of the reasoning. Generally, $\hbar\omega_{0,j}/2 = \epsilon_j = \epsilon_{q,j} + \epsilon_{L',j} + \epsilon_{C',j} + \epsilon_{L,j} + \epsilon_{C,j} + \epsilon_{J,j} + \epsilon_{\tilde{L},j}$. The main contribution to $\omega_{0,j}$ arises from the qubit transition energy $\epsilon_{q,j}$. Other minor terms may vary depending on the geometries (e.g. isolated boxes or infinite lattices) and the dynamic processes (e.g. changing the sign of J_4 couplings). But we can always form two different frequency patterns $\{\omega_{0,A}, \omega_{0,B}\}$ from the beginning and treat the potential deviations as small local detunings (as will be discussed in Sec. 4.3). Meanwhile, $\omega_{1,j}$ can be adjusted by parameters L_j', C_j' and $V_{AC,j}$ such that it is comparable to $\omega_{0,j}$.

4.2.3 Generalized NMR protocol

In this section, we illustrate the core idea of our algorithm. The aim is to find a unitary transformation $U(t) = \prod_j U_j(t) = \prod_j e^{iF_j(t)}$ from $\mathcal{H} = \mathcal{H}_K + \mathcal{H}_C$ to G such that in the new gauge, the local magnetic field σ_j^z in $\mathcal{H}_C$ vanishes and no additional spin couplings other than the Kitaev type emerge. We denote $\psi(t)$ and $\phi(t)$ as the eigenstates of $\mathcal{H}$ and G that are related by the transform $\phi(t) = U(t)\psi(t)$. Meanwhile, $\phi(t)$ satisfy the Schrödinger equation $G\phi(t) = i\partial_t\phi(t)$. It is easy to check that after

the gauge transformation, $G = G_C + U\mathcal{H}_K U^{-1}$ where $G_C = (i\partial_t U)\, U^{-1} + U\mathcal{H}_C U^{-1}$. Our requirements can be interpreted as

$$\begin{cases} G_C = 0, \\ G = U\mathcal{H}_K U^{-1} = \mathcal{H}'_K. \end{cases} \tag{4.33}$$

Here, $\mathcal{H}'_K$ takes a similar Kitaev form (4.15) with renormalized coupling constants J'_ν.

First, we introduce new variable $\tau_j = \omega_j t$ and present the derivation of some useful mathematical formulas for our dynamical protocol. Spin operators commute on different sites, so do $F_j(\tau_j)$. It enables us to suppress site index j for the moment, and focus on the single spin problem:

$$\begin{aligned} \mathcal{H}_C(\tau) &= \omega_0 S_z - \omega_1 \left(\cos\tau S_x + \sin\tau S_y\right), \\ G_C &= e^{iF}\mathcal{H}_C e^{-iF} + i\omega \left(\partial_\tau e^{iF}\right) e^{-iF}. \end{aligned} \tag{4.34}$$

Applying the Baker-Campbell-Hausdorff formula,

$$\begin{aligned} e^{iF}\mathcal{H}_C e^{-iF} &= \mathcal{H}_C + i\left[F, \mathcal{H}_C\right] + \frac{i^2}{2!}\left[F, \left[F, \mathcal{H}_C\right]\right] \\ &\quad + \frac{i^3}{3!}\left[F, \left[F, \left[F, \mathcal{H}_C\right]\right]\right] + \cdots, \\ \left(\partial_\tau e^{iF}\right) e^{-iF} &= \partial_\tau \left(\sum_{n=0}^{\infty} \frac{(iF)^n}{n!}\right) e^{-iF} \\ &= i\partial_\tau F + \frac{i^2}{2!}\left[F, \partial_\tau F\right] + \frac{i^3}{3!}\left[F, \left[F, \partial_\tau F\right]\right] + \cdots. \end{aligned} \tag{4.35}$$

$F(\tau)$ can be taken as a linear function of S_i $(i = x, y, z)$:

$$F(\tau) = l(\tau)S_x + m(\tau)S_y + n(\tau)S_z. \tag{4.36}$$

Due to the closed SU(2) algebra for spin-1/2: $[S_i, S_j] = i\epsilon_{ijk}S_k$, G_C is also linear in S_i. Moreover, an arbitrary linear function $Q\left(S_i\right)$ satisfy

$$\left[F, \left[F, \left[F, Q\right]\right]\right] = \alpha^2 \left[F, Q\right], \quad \alpha^2 = l^2 + m^2 + n^2. \tag{4.37}$$

It allows to group the infinite series in G_C (4.35) into a finite form

$$\begin{aligned} G_C &= \mathcal{H}_C + \frac{\sin\alpha}{\alpha} i\left[F, \mathcal{H}_C\right] + \frac{\cos\alpha - 1}{\alpha^2}\left[F, \left[F, \mathcal{H}_C\right]\right] \\ &\quad + \hbar\omega \left(-\partial_\tau F + \frac{\cos\alpha - 1}{\alpha^2} i\left[F, \partial_\tau F\right] - \frac{\sin\alpha - \alpha}{\alpha^3}\left[F, \left[F, \partial_\tau F\right]\right]\right). \end{aligned} \tag{4.38}$$

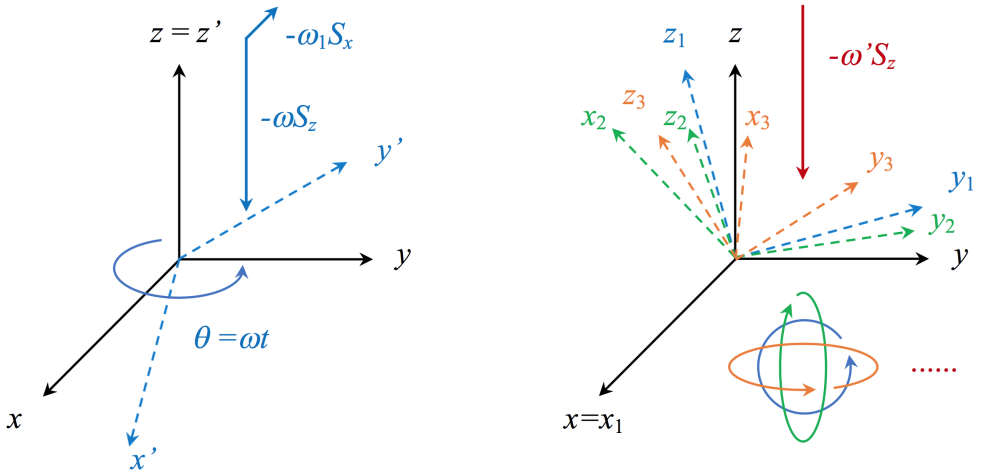

Figure 4.4: Sketch of different rotating frames. (a): In the normal NMR protocol. Two magnetic fields are generated along x and z axes. The field $(-\omega_1 S_x)$ hinders the formation of the spin liquid phases. (b): In our generalized NMR protocol assisted by the AC driving device. First three rotations in $U = e^{iF(\tau)} = U_x^{(1)} U_y^{(1)} U_z^{(1)} \cdots$ are drawn here with $U_x^{(1)}$ in colour blue, $U_y^{(1)}$ in green and $U_z^{(1)}$ in orange. The infinite series of rotations in U result in an effective magnetic field $(-\omega' S_z)$ with vanishing components in x and y directions.

In the same manner, a single local spin operator S_i takes the following expression in the rotating frame

$$e^{iF} S_i e^{-iF} = S_i + \frac{\sin\alpha}{\alpha} i\,[F, S_i] + \frac{\cos\alpha - 1}{\alpha^2}\,[F, [F, S_i]]\,. \tag{4.39}$$

In order to find a suitable form of $F(\tau)$ that fulfils our two requirements (4.33), we try with the normal NMR protocol ($\sim \mathcal{O}(\omega)$):

$$F(\tau) = \tau S_z, \qquad U = e^{i\tau S_z}. \tag{4.40}$$

It is equivalent to setting a rotating frame around z axis with a time-dependent angle $\theta = \tau = \omega t$ shown in Fig. 4.4a. Plugging $F(\tau)$ into the expression of G_C (4.38), we get two local magnetic fields along z and x directions:

$$G_C = (\omega_0 - \omega)\, S_z - \omega_1 S_x. \tag{4.41}$$

Although the original S_z field can be compensated by tuning $\omega = \omega_0$, the new S_x field will always remain. It removes the macroscopic degeneracies of the spin liquid

ground states in the gapped phases. For instance, in the A_x phase of our Majorana box (4.15) with $J_1 \ll J_{2,3,4} < 0$, the emergent magnetic field $-\omega_1 S_x$ ($\omega_1 > 0$) creates an energy gap $\Delta = 4\,|\omega_1|$ between two RVB states $|+_1+_2\rangle_x$ and $|-_1-_2\rangle_x$ for the upper horizontal bond. When coupling the boxes to form a 2D lattice $\mathcal{L}$ as depicted in Fig. 4.2 (left), the system then selects a single ground state $\prod_{i\in\mathcal{L}} |+_i\rangle_x$ with zero entanglement entropy. So the normal NMR protocol does not work for the simulation of Kitaev spin liquids.

When the driving frequency ω is large, an alternative unitary transformation can be built from the Floquet theory [326–329]. $F(\tau)$ is assumed to be of smaller order $\sim \mathcal{O}(\omega^{-1})$ compared with the NMR condition ($\sim \mathcal{O}(\omega)$, in Eq. (4.40)). It allows us to solve G_C perturbatively by expansions:

$$G_C = \sum_{n=0}^{\infty} \frac{1}{\omega^n} G_C^{(n)}, \qquad F(\tau) = \sum_{n=1}^{\infty} \frac{1}{\omega^n} F^{(n)}. \tag{4.42}$$

From (4.34) - (4.35), the leading order takes the form

$$\begin{aligned} G_C^{(0)} &= H_C - \partial_\tau F^{(1)}, \\ G_C^{(1)} &= i\left[F^{(1)}, H_C\right] - \partial_\tau F^{(2)} - \frac{i}{2}\left[F^{(1)}, \partial_\tau F^{(1)}\right]. \end{aligned} \tag{4.43}$$

The fact that $G_C^{(0)}$ and $G_C^{(1)}$ are both time-independent leads to

$$G_C = \left(\omega_0 - \frac{\omega_1^2}{2\omega} + \mathcal{O}(\omega^{-2})\right) S_z, \tag{4.44}$$

$$F(\tau) = \left(-\frac{\omega_1}{\omega} + \frac{\omega_0\omega_1}{\omega^2} + \mathcal{O}(\omega^{-3})\right)(\sin\tau S_x - \cos\tau S_y). \tag{4.45}$$

Here, the high-frequency Floquet protocol generates a magnetic field along z direction and can be viewed as infinitely successive rotations of the frame around x, y and z axes shown in Fig. 4.4b:

$$U = e^{iF(\tau)} = e^{ic_1(\tau)S_x} e^{ic_2(\tau)S_y} e^{ic_3(\tau)S_z} \cdots = U_x^{(1)} U_y^{(1)} U_z^{(1)} U_x^{(2)} U_y^{(2)} U_z^{(2)} \cdots .$$

In the perturbation series (4.44), we are able to adjust the frequency of the AC voltage ω such that $G_C = 0$. To the first order $\mathcal{O}(\omega^{-1})$, we find the requirement $\omega_1 = \sqrt{2\omega_0\omega}$.

Then ω_1 should be comparable to ω_0. From Table 4.2, it can be realized by tuning parameters L', C' and V_{AC}.

However, the Floquet approach is not applicable to small values of ω. Fortunately, we find an exact transformation in a similar form as the Floquet construction (4.45):

$$F(\tau) = \alpha \left[\sin(\tau) S_x - \cos(\tau) S_y\right]. \tag{4.46}$$

Here, the value of α is to be determined later. Moving to the basis of Pauli matrices, $F_j(\tau_j) = (\alpha_j/2)\left(\sin\tau_j\sigma_j^x - \cos\tau_j\sigma_j^y\right)$. From Eq. (4.38), we derive explicitly the expression of G_C:

$$\begin{aligned} G_C = \frac{\hbar}{2}\sum_{j=1}^{4} &\left(\omega_{0,j}\cos\alpha_j + \omega_{1,j}\sin\alpha_j - \omega_j\cos\alpha_j + \omega_j\right)\sigma_j^z \\ -&\left(\omega_{1,j}\cos\alpha_j - \omega_{0,j}\sin\alpha_j + \omega_j\sin\alpha_j\right)\left(\cos\tau_j\sigma_j^x + \sin\tau_j\sigma_j^y\right). \end{aligned} \tag{4.47}$$

The second time-dependent term vanishes as long as

$$\begin{aligned} \cos\alpha_j &= -(\omega_{0,j} - \omega_j)/\sqrt{\omega_{1,j}^2 + (\omega_{0,j} - \omega_j)^2}, \\ \tan\alpha_j &= \omega_{1,j}/(\omega_{0,j} - \omega_j). \end{aligned} \tag{4.48}$$

G_C then becomes a time-independent effective magnetic field polarized on z direction only:

$$G_C = \sum_j \frac{\hbar}{2}\left(\omega_j - \sqrt{w_{1,j}^2 + (\omega_{0,j} - \omega_j)^2}\right)\sigma_j^z. \tag{4.49}$$

If the frequencies of the AC voltages satisfy

$$\omega_j = \frac{\omega_{1,j}^2 + \omega_{0,j}^2}{2\omega_{0,j}}, \qquad G_C = 0. \tag{4.50}$$

Next, to meet our second requirement (4.33), we go on to analyze the remaining part $U\mathcal{H}_K U^{-1}$ in the effective Hamiltonian G. Constructed from spin operators, $U_j(t)$ commute between different sites. For the ν-link ($\nu = x, y, z$), $U\sigma_A^\nu\sigma_B^\nu U^{-1} = (U_A\sigma_A^\nu U_A^{-1})(U_B\sigma_B^\nu U_B^{-1})$. In the rotating frame, from Eq. (4.39) spin operators on site

j undergo the following gauge transformation:

$$\begin{aligned} U_j\sigma_j^x U_j^{-1} &= \left(1+\cos^2(\tau_j)(\cos\alpha_j-1)\right)\sigma_j^x \\ &\quad + \frac{\cos\alpha_j-1}{2}\sin(2\tau_j)\sigma_j^y - \sin\alpha_j\cos(\tau_j)\sigma_j^z, \\ U_j\sigma_j^y U_j^{-1} &= \left(1+\sin^2(\tau_j)(\cos\alpha_j-1)\right)\sigma_j^y \\ &\quad + \frac{\cos\alpha_j-1}{2}\sin(2\tau_j)\sigma_j^x - \sin\alpha_j\sin(\tau_j)\sigma_j^z, \\ U_j\sigma_j^z U_j^{-1} &= \cos\alpha_j\sigma_j^z + \sin\alpha_j\cos(\tau_j)\sigma_j^x + \sin\alpha_j\sin(\tau_j)\sigma_j^y. \end{aligned} \tag{4.51}$$

We denote $\langle f(t)\rangle_T$ as the time average $(1/T)\int_0^T f(t)dt$. Averaging over a long timescale

$$T = NT_A = T_B, \quad T_j = 2\pi/\omega_j, \quad N \geq 2, N \in \mathbb{Z}, \tag{4.52}$$

most of the time-dependent terms in the product $(U_A\sigma_A^\nu U_A^{-1})(U_B\sigma_B^\nu U_B^{-1})$ will vanish. However, terms such as $\left\langle\cos^2(\tau_{A/B})\right\rangle_T = \left\langle\sin^2(\tau_{A/B})\right\rangle_T = 1/2, \langle\cos^2(\tau_A)\cos^2(\tau_B)\rangle_T = \left\langle\sin^2(\tau_A)\sin^2(\tau_B)\right\rangle_T = 1/4$ survive. By imposing different frequency patterns ($N \neq 1$) for sublattices A and B, we ensure that only Kitaev couplings are non-vanishing after the rotation

$$\langle G\rangle_T = \left\langle U\mathcal{H}_K U^{-1}\right\rangle_T = \mathcal{H}'_K, \quad J'_\nu = r_\nu J_\nu. \tag{4.53}$$

The parameters r_ν ($\nu = x, y, z$) are listed in Table 4.1 for quick reference.

In the end, it is important to emphasize that compared with the normal NMR protocol (4.40) and the high-frequency Floquet approach (4.45), our generalized NMR protocol (4.46)-(4.50) fulfils the central requirements of the experimental scheme (4.33) for all values of driving frequencies $\{\omega_j\}$.

Table 4.1: Parameters for generalized NMR protocol

Parameter	Relation
α	$\arctan(2\omega_0\omega_1/(\omega_0^2-\omega_1^2))$
r_x, r_y	$\cos^2(\alpha_A/2)\cos^2(\alpha_B/2)$
r_z	$\cos\alpha_A\cos\alpha_B$
u	$\cos\alpha_A - 1$
v	$\cos\alpha_B - 1$
r_1	$u^2v^2/64 + (u^2v + uv^2 + u^2 + v^2)/8$ $+uv + u + v + 1$
r_2	$u^2v^2/64$
r_3	$u^2v^2/64 + (uv^2 + v^2)/8$
r_4	$u^2v^2/64 + (u^2v + u^2)/8$

4.2.4 Measuring flux states through multi-channels

Within a single box, we define four types of 'loop' operators in the rotating frame associated with Hamiltonian G (4.53):

$$\begin{aligned}
\mathcal{P}_c &= \sigma_1^x\sigma_2^x\sigma_3^y\sigma_4^y = c_1c_2c_3c_4,\\
\mathcal{P}_d &= \sigma_1^y\sigma_2^y\sigma_3^x\sigma_4^x = d_1d_2d_3d_4,\\
\mathcal{P}_e &= \sigma_1^y\sigma_2^x\sigma_3^y\sigma_4^x = -d_1c_2c_3d_4,\\
\mathcal{P}_f &= \sigma_1^x\sigma_2^y\sigma_3^x\sigma_4^y = -c_1d_2d_3c_4.
\end{aligned} \tag{4.54}$$

These operators will be important in the detection of $\mathcal{Z}_2$ gauge fluxes. In particular, in the limit of strong horizontal bonds, as mentioned in the beginning of this section (see argument below Eq. (4.15)) we predict $\mathcal{P}_c = c_1c_2c_3c_4 = +1$. In our Majorana representation, they become four-body Majorana couplings. Meanwhile, the flux operator $\mathcal{P}_d = +1$ corresponds to the π-flux configuration while $\mathcal{P}_d = -1$ relates to the 0 flux. The NMR protocol thus enables us to measure experimentally the flux states encoded in $\mathcal{Z}_2$ gauge fields. We denote $\langle U\mathcal{P}U^{-1}\rangle_T = \langle\langle\mathcal{P}\rangle\rangle$ as the time-

averaged measurement (over the large Floquet period) in the original spin space. From Eq. (4.51), the unitary transformation to the rotating frame entangles these four loop operators

$$\begin{pmatrix} \langle\langle \mathcal{P}_d \rangle\rangle \\ \langle\langle \mathcal{P}_c \rangle\rangle \\ \langle\langle \mathcal{P}_e \rangle\rangle \\ \langle\langle \mathcal{P}_f \rangle\rangle \end{pmatrix} = \begin{pmatrix} r_1 & r_2 & r_3 & r_4 \\ r_2 & r_1 & r_4 & r_3 \\ r_3 & r_4 & r_1 & r_2 \\ r_4 & r_3 & r_2 & r_1 \end{pmatrix} \begin{pmatrix} \mathcal{P}_d \\ \mathcal{P}_c \\ \mathcal{P}_e \\ \mathcal{P}_f \end{pmatrix}. \tag{4.55}$$

The coefficients read

$$\begin{aligned} r_1 &= \big\langle \big(1+\sin^2(\tau_A)u\big)\cdot\big(1+\sin^2(\tau_B)v\big)\cdot \\ &\qquad \big(1+\cos^2(\tau_B)v\big)\cdot\big(1+\cos^2(\tau_A)u\big)\big\rangle_T\,, \\ r_2 &= \frac{u^2v^2}{16}\big\langle \sin^2(2\tau_A)\sin^2(2\tau_B)\big\rangle_T\,, \\ r_3 &= \frac{v^2}{4}\big\langle \sin^2(2\tau_B)\cdot\big(1+\sin^2(\tau_A)u\big)\cdot\big(1+\cos^2(\tau_A)u\big)\big\rangle_T\,, \\ r_4 &= \frac{u^2}{4}\big\langle \sin^2(2\tau_A)\cdot\big(1+\sin^2(\tau_B)v\big)\cdot\big(1+\cos^2(\tau_B)v\big)\big\rangle_T\,, \end{aligned} \tag{4.56}$$

where $u=\cos\alpha_A-1, v=\cos\alpha_B-1$. The time-averaged values of r_i's are given in Table 4.1. In particular, the flux operator can be measured directly from the observables in the original frame by the inverse of the matrix (4.55). For instance,

$$\mathcal{P}_d = \frac{1}{\mathcal{D}}\left(\tilde{r}_1\langle\langle\mathcal{P}_d\rangle\rangle + \tilde{r}_2\langle\langle\mathcal{P}_c\rangle\rangle + \tilde{r}_3\langle\langle\mathcal{P}_e\rangle\rangle + \tilde{r}_4\langle\langle\mathcal{P}_f\rangle\rangle\right), \tag{4.57}$$

where $\mathcal{D}=\sum_{m=1}^4 r_m^4 - 2\sum_{m<m'} r_m^2 r_{m'}^2 + 8\prod_{m=1}^4 r_m$ and $\tilde{r}_m = r_m\left(r_m^2 - \sum_{m'\neq m} r_{m'}^2\right) + 2\prod_{m'\neq m} r_{m'}$. An expression can be obtained for $\mathcal{P}_c$ in the same manner.

4.3 Summary of numerical tests

In this section, we summarize the numerical tests performed by our collaborator L. Henriet, that are important for the understanding of the strengths and limitations of our algorithms.

Our protocol (valid to any order in $1/\omega_j$) is tested numerically by solving the time-dependent Hamiltonian with a diagonalization and the time-averaged observables

$\langle\langle\sigma_j^z\rangle\rangle$ and $\langle\langle\sigma_j^z\sigma_l^z\rangle\rangle$ are evaluated. The results are almost identical for different integer values $N = 3, 5, 7$ in the choice of the double frequencies (4.52). Here, $\langle\langle f\rangle\rangle = \langle\langle f\rangle(t)\rangle_T$ denotes the time averaged quantity $(1/T)\int_0^T \mathrm{Tr}(\rho(t)f)$ with $\rho(t)$ being the density matrix of the system and $T = 2\pi/\omega_{min}$ with $(\omega_{min} = \omega_B)$. Therefore, T corresponds to the larger Floquet period.

The calculation of spin observables averaged in time under the Hamiltonian $\mathcal{H}$ agrees with the calculation in the rotating frame with the Hamiltonian G. Fig. 4.5a shows results in the particular limit of strong vertical bonds with antiferromagnetic couplings $J_3 = J_4 \gg |J_1| = |J_2|$. $\langle\langle\sigma_j^z\rangle\rangle = 0$ since on each site a spin can be polarized in the $|+z\rangle$ and $|-z\rangle$ direction equally. We check that $\langle\langle\sigma_j^x\rangle\rangle$ and $\langle\langle\sigma_j^y\rangle\rangle$ are zero. In Fig. 4.5a, two-spin correlator $\langle\langle\sigma_1^z\sigma_3^z\rangle\rangle$ takes the anticipated value close to $-1 \times r_z = -0.11$ (due to the large J_3 coupling in the rotating frame). The flux variables through the 4-body spin operators can also be detected directly and agree with the mathematical predictions in Sec. 4.2.4. Fig. 4.5a shows in the regime of weak vertical bonds, $\mathcal{P}_c \sim \mathcal{P}_d \sim 1$. These two quantities are obtained from the measurement of four separate channels $\langle\langle\mathcal{P}_\xi\rangle\rangle$ $(\xi = c, d, e, f)$ based on formulas (4.54) and (4.55) and correspond to the precise engineering of the π-flux configuration.

Next, we address the effects of detuning. So far, we have three steps of fine tunings throughout our proposal:

(i) The cancellation of vertical X couplings;

(ii) The engineering of a circularly polarized NMR field in Hamiltonian (4.32);

(iii) The cancellation of local magnetic field in the rotation frame.

The prerequisite (i) is important for the realization of Kitaev Hamiltonians. We show later that such perturbations can be useful to produce local flux impurities, at a perturbation level. For (i), the condition for the parameters from Eq. (4.31) becomes

$$E_{\widetilde{L},m} = -E_{J,m}/2, \quad m = 3, 4. \tag{4.58}$$

This can be reached by tuning the phases Φ_3, Φ_4. We will discuss this point more carefully in the later part of section. For (ii), we impose $\omega_{1,j} = \omega_{L',j} = \omega_{C',j}$ in terms of parameters (see Table 4.2 in Sec. 4.4). We discuss below perturbation effects from that condition. Now for the algorithm (iii), we consider a small deviation in the frequency pattern $\omega_j \to \widetilde{\omega}_j = \omega_j + \delta\omega_j$. The Hamiltonian of the NMR field becomes

$$\begin{aligned}\mathcal{H}_{\rm NMR}(t) = &-\sum_{j=1}^{4} \frac{\hbar\omega_{1,j}}{2}(\cos(\widetilde{\omega}_j t)\sigma_j^x + \sin(\widetilde{\omega}_j t)\sigma_j^y) \\ &+\frac{\hbar\omega_{1,j}}{2}\frac{\delta\omega_j}{\omega_j}\cos(\widetilde{\omega}_j t)\sigma_j^x. \end{aligned} \tag{4.59}$$

The third term comes from the change in $\omega_{L',j}$ while $\omega_{C',j}$ remains unchanged in relation with Eq. (4.32). More details on the parameters of the box are given in Sec. 4.4. We can study the consequences of the detuned Hamiltonian (4.59) in the rotating frame. Firstly, the variable $\widetilde{\alpha}_j$ characterizing the unitary transformation has a small shift:

$$\begin{aligned}\cos\widetilde{\alpha}_j &\simeq \cos\alpha_j + \frac{\cos\alpha_j(1-\cos^2\alpha_j)}{1-\omega_{0,j}/\omega_j}\frac{\delta\omega_j}{\omega_j}, \\ \sin\widetilde{\alpha}_j &\simeq \sin\alpha_j - \frac{\cos^2\alpha_j}{1-\omega_{0,j}/\omega_j}\frac{\delta\omega_j}{\omega_j}. \end{aligned} \tag{4.60}$$

When $\delta\omega_j \ll \omega_j$, we can assume $\cos\widetilde{\alpha}_j \simeq \cos\alpha_j, \sin\widetilde{\alpha}_j \simeq \sin\alpha_j$. The effective Hamiltonian G_C in Eq. (4.49) takes the form accordingly

$$G_C \simeq \sum_j \frac{\hbar\omega_{0,j}}{2\omega_j}\delta\omega_j\sigma_j^z. \tag{4.61}$$

In our numerical simulation $\omega_0 \sim \omega$, G_C becomes sensitive under detuning. To analyze the consequence of the extra third term in the Hamiltonian (4.59), we go back to the general unitary transform (4.51) and after time average

$$\left\langle\left\langle \frac{\hbar\omega_{1,j}}{2}\frac{\delta\omega_j}{\omega_j}\cos(\widetilde{\omega}_j t)\sigma_j^x \right\rangle\right\rangle \simeq \frac{\hbar}{4}\left(\frac{2\omega_{0,j}}{\omega_j} - \frac{\omega_{0,j}^2}{\omega_j^2}\right)\delta\omega_j\sigma_j^z, \tag{4.62}$$

where we keep the initial large time period $T(\omega)$ unchanged and $\langle\cos^2(\widetilde{\omega}_j t)\rangle_T \simeq 1/2 + \mathcal{O}(\delta\omega_j)$. In the end, combining Eq. (4.61) and Eq. (4.62) we expect the detuning

$\omega_j + \delta\omega_j$ on each site would create a non-zero effective magnetic field:

$$\widetilde{\mathcal{H}}_z = \sum_j \frac{\omega_{0,j}}{\omega_j}\left(1 - \frac{\omega_{0,j}}{4\omega_j}\right)\hbar\delta\omega_j\sigma_j^z. \tag{4.63}$$

The pre-factor cannot be zero, otherwise $\omega_{1,j}^2 < 0$ by the relation (4.50): $2\omega_j\omega_{0,j} = \omega_{1,j}^2 + \omega_{0,j}^2$. The gapped phase is protected to the first order perturbation under $\widetilde{H}_z$. To second order $\mathcal{O}(\delta\omega/|J_1|)$, effective couplings $\sigma_1^z\sigma_2^z$ and $\sigma_3^z\sigma_4^z$ are generated but quite small. For the gapless phase (e.g. in the Kitaev honeycomb model), the magnetic field is polarized purely along z direction without a gap opening. The above effects are tested numerically by simultaneously detuning four sites or a single site. All physical observables (especially $\mathcal{P}_d$) are supposed to be stable via a small detuning. When $\delta\omega_j$ is comparable to ω_j, we could detect large fluctuations. Fig. 4.5b demonstrates the effect of detuning the driving frequency of the site 2 on the gauge-field four-body operator $\mathcal{P}_d$. Small errors of the order of 3% are gained for more than 14 time periods if the detuning is of the order of 5%.

It is also important to characterize the influence of losses and dephasing on the dynamical protocols. γ and Γ denote respectively the dephasing and loss rates of the qubit in the Lindblad-type master equation. Independent losses and dephasing are imposed on each site, with the same strength. As can be seen in Fig. 4.5c, the presence of losses and dephasing destroys the quantization of both $\mathcal{P}_d$ (yellow) and $\mathcal{P}_c$ (red) at the level of one box. When simulating the proper Hamiltonian in an experiment, one should therefore perform all measurements within a timescale τ_{mes} set by these characteristic rates, $\tau_{mes} \ll 1/\gamma, 1/\Gamma$. It is relevant to note the similar role γ and Γ in these measurements.

At the end of this section, we analyze the effects of non-zero vertical X couplings on single-box systems, arising from Josephson junctions. In the limit of strong horizontal bonds, the ground state is highly degenerate: $|\mathrm{GS}\rangle = |\alpha\alpha\rangle_{x,(1,2)} \otimes |\beta\beta\rangle_{y,(3,4)}, (\alpha,\beta) = \pm 1$. From perturbation theory, interactions on the vertical bonds contribute to $\mathcal{H}_{\mathrm{eff}}^{(2)} = -J_3J_4/(|J_1| + |J_2|)\,(\sigma_1^z\sigma_2^z\sigma_3^z\sigma_4^z)_{\mathrm{eff}} - J_3^xJ_4^x/|J_2|\,(\sigma_1^x\sigma_2^x\sigma_3^x\sigma_4^x)_{\mathrm{eff}}$. Strong J_1 links ensure

that $\langle \sigma_1^x \sigma_2^x \rangle = 1$. Thus,

$$\mathcal{H}^{(2)} = -\frac{J_3 J_4}{|J_1| + |J_2|} \langle \sigma_1^z \sigma_2^z \sigma_3^z \sigma_4^z \rangle - \frac{J_3^x J_4^x}{|J_2|} \langle \sigma_3^x \sigma_4^x \rangle . \tag{4.64}$$

In the Majorana basis,

$$\langle \sigma_1^z \sigma_2^z \sigma_3^z \sigma_4^z \rangle = \mathcal{P}_c \mathcal{P}_d = \mathcal{P}_d, \quad \langle \sigma_3^x \sigma_4^x \rangle = -i d_3 d_4, \tag{4.65}$$

where we have taken into account $\mathcal{P}_c = \langle \sigma_1^x \sigma_2^x \sigma_3^y \sigma_4^y \rangle = 1$. Once we add an additional inductance $\widetilde{L}_3$ between sites 1 and 3 and turn off the vertical X coupling such that $J_3^x + \widetilde{J}_3^x = 0$ (we have Φ_3 fixed and $J_3 > 0$), the contribution from J_4^x vanishes and we check that $\sigma_2^x \sigma_4^x$ becomes an irrelevant operator to any higher order in perturbation theory. The gapped phases of Kitaev type spin models are therefore fully protected against local J_4^x noises. This point is crucial to the flux engineering later in Sec. 4.5.2. Furthermore, we gain the flexibility of tuning the Φ_4 phase, which is useful to engineer local defects with 0 flux in a unit cell.

Suppose we deviate from the condition in Eq. (4.31), and study some effects of J_3^x and J_4^x. To second-order in $J_3^x J_4^x$, we then engineer a term in the Hamiltonian, which is equivalent to add a small inductance between the sites 3 and 4: $\delta \mathcal{H}_{\parallel} = \delta J_1 \sigma_3^x \sigma_4^x = -i \delta J_1 d_3 d_4$, where δJ_1 is proportional to $J_3^x J_4^x$. Tuning progressively the flux Φ_4 in time would change the sign of J_4^x from positive to negative. Then this allows us to locally change the flux in a square cell from π to 0 and have also a time control on the local gauge fields. Next we discuss this protocol in more detail. In this protocol, we flip the sign of the parity operator $-i d_3 d_4$ in time. The time-control on local fluxes is illustrated in Fig. 4.5d, where $\mathcal{P}_d$ is progressively changed from +1 to -1 while $\mathcal{P}_c$ remains roughly constant.

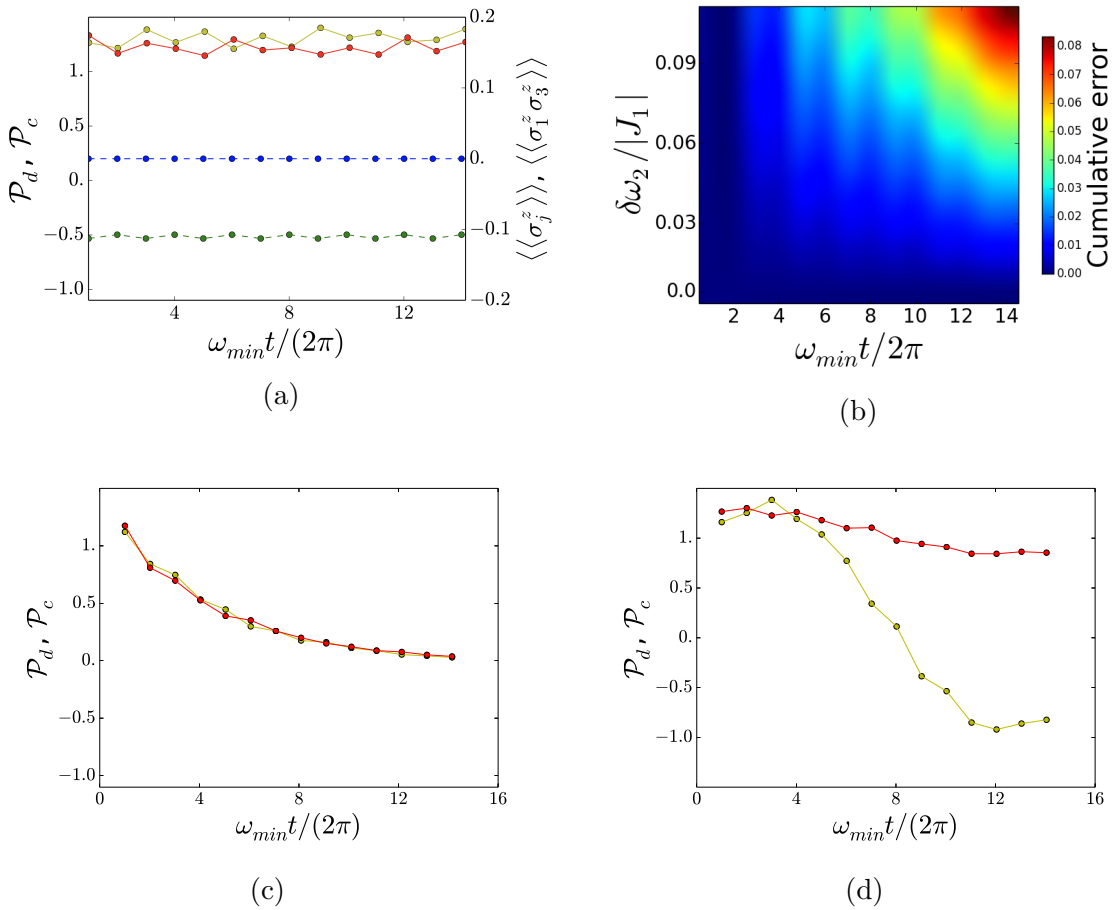

Figure 4.5: (a) Time evolution of $\langle\langle\sigma_j^z\rangle\rangle$ (blue) and $\langle\langle\sigma_1^z\sigma_3^z\rangle\rangle$ (green) (dashed lines); and of the fluxes $\mathcal{P}_d$ (yellow) and $\mathcal{P}_c$ (red) (solid lines) averaged over the longest period $2\pi/\omega_{min}$ with $\omega_{min} = \omega_A/N = \omega_B$ and $N = 3$. The NMR frequency pattern is selected on each site as $\omega_{1,j} = \sqrt{2}\omega_{0,j}$, $\omega_j = 3\omega_{0,j}/2$. These initial frequency conditions remain the same in plots (b)-(d). The top panel corresponds to weak vertical bonds $|J_1| = |J_2| = 0.4\hbar\omega_B$, $|J_3| = |J_4| = 0.045|J_1|$, while the bottom panel deals with the regime of strong vertical bonds $J_3/\epsilon_3 = J_4/\epsilon_4 = 0.8$. (b) Detuning effects in $\delta\omega_2$ of the driving frequency ω_2. Average error on $\mathcal{P}_d$ (averaged over time) induced by this detuning, as a function of both $\delta\omega_2$ and the adimensional time $\omega_{min}t/2\pi$. This plot corresponds to the weak vertical bonds configuration of (a). (c) Time evolution of the fluxes $\mathcal{P}_d$ (yellow) and $\mathcal{P}_c$ (red) in dissipative processes. Here, we have taken weak vertical bonds $|J_1| = |J_2| = 0.4\hbar\omega_B$, $|J_3| = |J_4| = 0.045|J_1|$. Losses and dephasing, with rates $\Gamma = 5\ 10^{-3}\omega_B$ and $\gamma = 5\ 10^{-3}\omega_B$, lead to a monotonous exponential decay of the fluxes $\mathcal{P}_d$ and $\mathcal{P}_c$ from their initial quantized value $+1$ to zero. (d) Time evolution of $\mathcal{P}_d$ (yellow) and $\mathcal{P}_c$ (red) under a parity flip. Here, weak vertical bonds are taken $|J_1| = |J_2| = 0.4\hbar\omega_B$, and $2|J_3| = |J_3^x| = 0.1|J_1|$. A sinusoidal variation of $2J_4 = J_4^x$ is applied between the range $\pm 0.1|J_1|$. An additional small field $h_y\sigma_3^y$ is implemented with $h_y = 0.08J_1$. These numerical plots are provided by our collaborator L. Henriet.

4.4 Comments on experimental parameters

Our dynamical protocols simulated numerically in Sec. 4.3 are designed to study spin observables and detect $\mathcal{Z}_2$ gauge fields. Therefore, it is important to analyze the constraints in terms of experimental parameters. For simplicity, here we suppress the site index j.

From Table 4.2, the limit of weak vertical bonds $|J_1|, J_2| \gg |J_3|, |J_4|$ requires $\lambda \gg 1 \gg s, s\lambda^2 \sim 1, E_L, E_C \gg E_{J,3}, E_{J,4}$. The main contribution to the magnetic field σ^z comes from the transition frequency of the qubit $\hbar\omega_q \gg E_L, E_C, E_J, E_{\tilde{L}}, E_{L'}, E_{C'}$. To cancel this local field, we engineer a circularly polarized field and impose $\omega_1 = \omega_{L'} = \omega_{C'}$ giving rise to $4E_{L'} = s'\lambda^2\hbar\omega$ with $\hbar\omega \gg E_{L'}, \lambda \gg 1 \gg s', 1 \gg s'\lambda^2$.

We further choose a particular combination of frequencies in numerics from Eq. (4.50): $\omega_1 = \sqrt{2}\omega_0$, $\omega = 3\omega_0/2$. It results in $V_0 = 3\sqrt{2}\phi_0\hbar\omega_0^2\lambda/(8E_{L'})$. Since $\omega_0 \gg E_{L'}, \lambda \gg 1$, both the amplitude V_0 and frequency ω of the AC driving device should be large. Additionally, it is also noted that inside the NMR, the plasma frequency ω_P is much smaller compared to ω: $\omega_P \sim 1/\sqrt{L'C'} \sim \sqrt{E_{L'}/C'} \ll \omega \sim \omega_0 \sim \omega_q \sim \sqrt{E_{J_q}/C_q}$, which leads to $E_{L'}/E_{J_q} \ll s' \ll 1$. It is consistent with our limit of large $\lambda \gg 1$.

4.5 Application with coupled-box ensembles

4.5.1 Quantum spin liquids, Majorana states, Probes

In the two-dimensional lattice of Fig. 4.2, once a box unit cell is built up one can construct more complex geometries with $J_4 \neq 0$ for square ladders [147], $J_4 = 0$ for brick-wall ladders [147] and their equivalents in two dimensions, the Kitaev honeycomb model [18]. In addition, the Kitaev spin chain can be mapped to the transverse field Ising model and the two-leg square ladders have the dual of the XY chain in alternating transverse fields [146, 147]. Spin-spin correlation functions could reveal the short-ranged entanglement in gapped phases [58]. Here, we discuss how the NMR device can be used to detect Majorana physics and quantum phase transitions in

Table 4.2: Parameters for box circuit

Parameter	Relation	Parameter	Relation
λ	$\left(E_{J_q}/(2E_{C_q})\right)^{1/4}$	J_1	$-2E_L/(\lambda_A\lambda_B)$
s	C/C_q	J_2	$-2E_C s_A s_B \lambda_A \lambda_B$
ω_q	$\sqrt{8E_{C_q}E_{J_q}}/\hbar$	J_3	$-E_{J,3}/(2\lambda_A\lambda_B)^2$
$\omega_{L'}$	$4E_{L'}V_0/(\hbar\phi_0\lambda\omega)$	J_4	$-E_{J,4}/(2\lambda_A\lambda_B)^2$
$\omega_{C'}$	$2V_0 e s'\lambda/\hbar$	J_3^x	$-E_{J,3}/(\lambda_A\lambda_B)$
ϵ_q	$\left(\hbar\omega_q - E_{C_q}\right)/2$	J_4^x	$-E_{J,4}/(\lambda_A\lambda_B)$
ϵ_L	E_L/λ^2	$\tilde{J}_3^x$	$-2E_{\tilde{L},3}/(\lambda_A\lambda_B)$
ϵ_C	$E_C(s\lambda)^2$	$\tilde{J}_4^x$	$-2E_{\tilde{L},4}/(\lambda_A\lambda_B)$
ϵ_J	$-E_{J,\perp}/(2\lambda^2)$	J'_ν	$r_\nu J_\nu$

* Notation of subscripts: A for sites $\{1,4\}$, B for sites $\{2,3\}$, $\nu = x,y,z$.

Kitaev spin models.

Let us assume the quantum phase transition with decoupled (zig-zag) chains in the two-dimensional honeycomb lattice model, $J_3 = J_4 = 0$. In Fig. 4.6a, the quantum phase transition occurs when $\delta J_2 = J_1$ for the upper chain. At the quantum phase transition, the Hamiltonian can be written in terms of Dirac fermions in the continuous limit by recombining c_{2m-1} and c_{2m} along the chain. The continuum model is a one-dimensional fermion Dirac model of $\psi(x)$ and $\psi^\dagger(x)$ operators and spin-spin correlation functions show power-law decay. Entanglement entropy measurements could be done to check the conformal field theory at the critical point [147, 330]. To probe the quantum critical fluctuations in the chain, one can weakly couple this chain to a spin-1/2 impurity $\vec{S}$ described by a transmon qubit, or another spinless fermion, that also reveals two Majorana fermions c and d, such that $S_z = icd$, $S_x = c$ and $S_y = d$. Adding a small coupling between this chain and the site (either capacitive or inductive depending on the coupling which involves the Majorana fermions c_1 and c_2 in the chain), then one can engineer a small coupling $i\alpha c c_1$, where $\alpha \ll J_1$. By

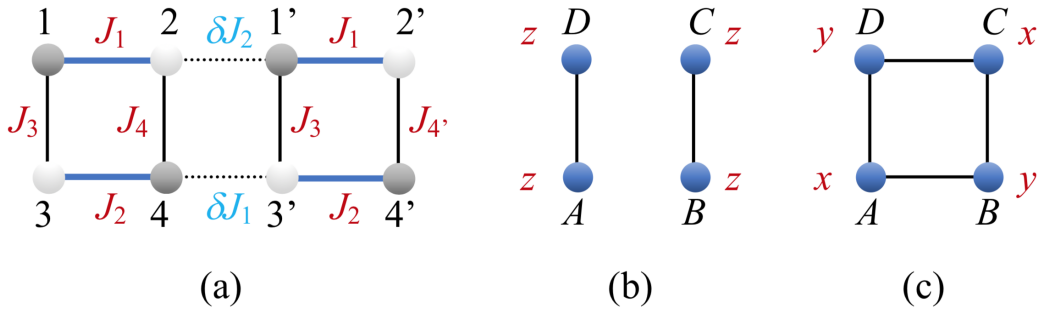

Figure 4.6: (a) Two coupled boxes in the limit of large J_1 and J_2; (b)-(c) Space of four effective spins formed by strong J_1 and J_2 links; While non-zero J_4 and $J_{4'}$ reproduce Ising couplings (b), suppressing J_4 and $J_{4'}$ would lead to a four-body Hamiltonian (c) related to Wen's toric code.

analogy to the two-channel Kondo model at the Emery-Kivelson line [331–333], we identify a coupling term $\propto i\alpha c(\psi(0)+\psi^\dagger(0))$. The fermion c will entangle with the chain and the Majorana fermion d will remain free. A signature of this free remnant Majorana fermion is a $(\ln 2)/2$ entropy as well as a logarithmic magnetic susceptibility $\chi_{imp} = \partial\langle S_z\rangle/\partial h \propto \ln h$, in contrast to a linear behavior for the one-channel Kondo model [331–333]. With the NMR device attached to the spin-1/2 impurity, one could control the field strength hS_z by detuning the on-site frequency ω from Eq. (4.63) and measure the logarithmic growth of the susceptibility reflecting the Majorana physics as well as quantum critical fluctuations in the chain. The gapped phases of the Kitaev model in ladder geometries also reveal edge mode excitations [147]. The NMR device could also probe in that case the susceptibility at low fields to detect these modes. These results do not probe non-Abelian statistics [13, 191], but still would give some response of Majorana fermions.

Boxes in the limit of strong vertical bonds could give rise to spin-1 quantum impurity physics [334].

4.5.2 $\mathcal{Z}_2$ gauge fields and Néel order of fluxes

Now we discuss a peculiar limit of coupled-box systems, where inside each box all c Majorana fermions are gapped due to the large J_1 and J_2 couplings (shown in Fig. 4.2

Right bottom). By coupling two boxes in the way of Fig. 4.6a with $J_3^x = 0$ and $J_3 > 0$, we are able to realize a Néel state of d-Majorana gauge fields.

One can perform the perturbation theory in the spin space. A system of two coupled boxes in Fig. 4.6a consists of the interaction terms:

$$\begin{aligned}
\mathcal{H}_0 &= J_1\left(\sigma_1^x\sigma_2^x + \sigma_{1'}^x\sigma_{2'}^x\right) + J_2\left(\sigma_3^x\sigma_4^x + \sigma_{3'}^x\sigma_{4'}^x\right), \\
V &= \delta\mathcal{H}_\perp + \delta\mathcal{H}_\parallel, \\
\delta\mathcal{H}_\perp &= J_3\left(\sigma_1^z\sigma_3^z + \sigma_{1'}^z\sigma_{3'}^z\right) + \left(J_4\sigma_2^z\sigma_4^z + J_{4'}\sigma_{2'}^z\sigma_{4'}^z\right), \\
\delta\mathcal{H}_\parallel &= \delta J_2\sigma_2^y\sigma_{1'}^y + \delta J_1\sigma_4^x\sigma_{3'}^x.
\end{aligned} \tag{4.66}$$

Here $(J_1, J_2) \ll -1, (\delta J_1, \delta J_2, J_3, J_3^x) \to (0^-, 0^-, 0^+, 0)$ and $J_4, J_{4'}$ can be controlled around $0^\pm$ by the phases $\Phi_4, \Phi_{4'}$. We notice in Sec. 4.3 when suppressing the vertical X couplings on J_3 bonds, $(J_4^x\sigma_2^x\sigma_4^x + J_{4'}^x\sigma_{2'}^x\sigma_{4'}^x)$ become irrelevant operators in any order of perturbation (see Eq. (4.64)), thus we have ignored them in $\delta\mathcal{H}_\perp$.

The ground state of $\mathcal{H}_0$ is constructed by four effective spins: $|\alpha\alpha\rangle_{x,(1,2)}\otimes|\beta\beta\rangle_{y,(3,4)}\otimes|\gamma\gamma\rangle_{x,(1',2')}\otimes|\delta\delta\rangle_{y,(3',4')}$ $(\alpha,\beta,\gamma,\delta = \pm 1)$. We introduce a map Υ: $\Upsilon|\alpha\rangle = |\alpha\alpha\rangle$ and find $\mathcal{H}_{\text{eff}}^{(0)} = 2(J_1 + J_2)$, $\mathcal{H}_{\text{eff}}^{(1)} = \Upsilon^\dagger V\Upsilon = 0$, $\mathcal{H}_{\text{eff}}^{(3)} = \Upsilon^\dagger V G_0' V G_0' V\Upsilon = 0$ where $G_0'(E) = ((E - \mathcal{H}_0)^{-1})'$. Non-zero contributions arise from the second and fourth orders

$$\begin{aligned}
\mathcal{H}_{\text{eff}}^{(2)} =& \Upsilon^\dagger V G_0' V\Upsilon = \text{cst} - \frac{J_3J_4}{|J_1| + |J_2|}\langle\sigma_1^z\sigma_2^z\sigma_3^z\sigma_4^z\rangle_{\text{eff}} - \frac{J_3J_{4'}}{|J_1| + |J_2|}\langle\sigma_{1'}^z\sigma_{2'}^z\sigma_{3'}^z\sigma_{4'}^z\rangle_{\text{eff}}, \\
\mathcal{H}_{\text{eff}}^{(4)} =& \Upsilon^\dagger V G_0' V G_0' V G_0' V\Upsilon \\
=& \text{cst} - \frac{1}{2(|J_1| + |J_2|)^3}\Big(J_3J_4(J_3^2 + J_{4'}^2)\langle\sigma_1^z\sigma_2^z\sigma_3^z\sigma_4^z\rangle_{\text{eff}} \\
&+ 2J_3^2J_4J_{4'}\langle\sigma_1^z\sigma_3^z\sigma_2^z\sigma_4^z\sigma_{1'}^z\sigma_{3'}^z\sigma_{2'}^z\sigma_{4'}^z\rangle_{\text{eff}} + J_3J_{4'}(J_3^2 + J_4^2)\langle\sigma_{1'}^z\sigma_{2'}^z\sigma_{3'}^z\sigma_{4'}^z\rangle_{\text{eff}}\Big) \\
&- \frac{\delta J_1\delta J_2}{2(|J_1| + |J_2|)^3}\Big(5J_3J_{4'}\langle\sigma_1^z\sigma_3^z\sigma_{2'}^z\sigma_{4'}^z\sigma_2^y\sigma_{1'}^y\sigma_4^x\sigma_{3'}^x\rangle_{\text{eff}} \\
&+ J_3J_4\langle\sigma_2^z\sigma_4^z\sigma_{1'}^z\sigma_{3'}^z\sigma_2^y\sigma_{1'}^y\sigma_4^x\sigma_{3'}^x\rangle_{\text{eff}} + J_3^2\langle\sigma_1^z\sigma_3^z\sigma_{1'}^z\sigma_{3'}^z\sigma_2^y\sigma_{1'}^y\sigma_4^x\sigma_{3'}^x\rangle_{\text{eff}} \\
&+ J_4J_{4'}\langle\sigma_2^z\sigma_4^z\sigma_{2'}^z\sigma_{4'}^z\sigma_2^y\sigma_{1'}^y\sigma_4^x\sigma_{3'}^x\rangle_{\text{eff}}\Big).
\end{aligned} \tag{4.67}$$

Moving to the Majorana representation, we find

$$\begin{aligned}\mathcal{H}_{\text{eff}}^{(2)} &= \text{cst} - \frac{J_3}{|J_1|+|J_2|}\left(J_4\mathcal{P}_1 + J_{4'}\mathcal{P}_3\right), \\ \mathcal{H}_{\text{eff}}^{(4)} &= \text{cst} - \frac{J_3}{2(|J_1|+|J_2|)^3}\left(2J_3J_4J_{4'}\mathcal{P}_1\mathcal{P}_3 + J_4(J_3^2+J_{4'}^2)\mathcal{P}_1 + J_{4'}(J_3^2+J_4^2)\mathcal{P}_3\right) \\ &\quad - \frac{\delta J_1 \delta J_2}{2(|J_1|+|J_2|)^3}\left(5J_3J_{4'}\mathcal{P}_{\widetilde{123}} + J_3J_4\mathcal{P}_2 + J_3^2\mathcal{P}_{\widetilde{12}} + J_4J_{4'}\mathcal{P}_{\widetilde{23}}\right),\end{aligned} \tag{4.68}$$

where $\mathcal{P}_\mu$ describes the four-body d-Majorana coupling on the vertices of box $\mu = 1, 2, 3$ (in Fig. 4.6a, $\mu = 2$ denotes an induced box in the middle). More precisely, $\mathcal{P}_1 = d_1d_2d_3d_4$, $\mathcal{P}_2 = d_2d_{1'}d_4d_{3'}$, $\mathcal{P}_3 = d_{1'}d_{2'}d_{3'}d_{4'}, \mathcal{P}_{\widetilde{12}} = \mathcal{P}_1\mathcal{P}_2 = d_1d_{1'}d_3d_{3'}$, $\mathcal{P}_{\widetilde{23}} = \mathcal{P}_2\mathcal{P}_3 = d_2d_{2'}d_4d_{4'}, \mathcal{P}_{\widetilde{123}} = \mathcal{P}_1\mathcal{P}_2\mathcal{P}_3 = d_1d_{2'}d_3d_{4'}$. To minimize the energy, fluxes within each box can be uniquely fixed by the signs of J_4 and $J_{4'}$. From the discussion of Sec. 4.3, we infer that when $J_3^x = 0$, non-zero J_4^x and $J_{4'}^x$ couplings are allowed and do not enter into effective terms in any order of perturbation. Thus, the flexibility on the signs of J_4 and $J_{4'}^x$ is virtually guaranteed. In Table 4.3, we list all possible orderings of three gauge fields for two coupled boxes.

In large networks, one could couple more boxes in the same way and build square ladders. When all products of J_3J_4 are kept positive, the emergent π-flux ground state leading to the Néel order of $\mathcal{Z}_2$ gauge fields is in agreement with Lieb's theorem. The Néel order could reveal a finite critical temperature in the case of long-range coupling between boxes, by analogy with the Ising model (see Sec. 4.5.4 below). By tuning the signs of J_4 one is able to create impurities of 0 fluxes in the static $\mathcal{Z}_2$ gauge fields: a pair of fluxes in the bulk or a single flux on the boundary. Another proposal to engineer many-body phases of fluxes in ladder systems has been done recently [68, 335]. Small ladder spin systems generally reveal rich dynamics due to Mott physics and gauge fields [336]. From Eq. (4.64) and Eq. (4.65), a small non-zero J_3^x on the vertical J_3-links would fix the parity of two Majorana pairs $-id_3d_4$ and $-id_{3'}d_{4'}$, and would then help in deciding between the two possible ordered ground states with 0 or π order.

Table 4.3: Ordering of gauge fields for two coupled boxes

$(\mathrm{sgn}[J_4], \mathrm{sgn}[J_{4'}])$	$(\mathcal{P}_1, \mathcal{P}_2, \mathcal{P}_3, \mathcal{P}_{\widetilde{12}}, \mathcal{P}_{\widetilde{23}}, \mathcal{P}_{\widetilde{123}})$	flux		
$(+,+)$	$(+1,+1,+1,+1,+1,+1)$	π	π	π
$(-,-)$	$(-1,-1,-1,+1,+1,+1)$	0	0	0
$(+,-)$	$(+1,+1,-1,+1,-1,-1)$	π	π	0
$(-,+)$	$(-1,-1,+1,+1,-1,-1)$	0	0	π

4.5.3 Towards Wen's toric code

Here we show how to implement Wen's two-dimensional toric code [318] with our coupled-box clusters. In Fig. 4.6a if we set $J_4 = J_{4'} = 0$, only one term remains in the perturbation (4.67):

$$\mathcal{H}_{\mathrm{eff}}^{(4)} = g \langle \sigma_1^z \sigma_3^z \sigma_{1'}^z \sigma_{3'}^z \sigma_2^y \sigma_{1'}^y \sigma_4^x \sigma_{3'}^x \rangle_{\mathrm{eff}} = g\hat{F}, \tag{4.69}$$

with $g = -\delta J_1 \delta J_2 J_3^2 / [2(|J_1| + |J_2|)^3] < 0$. Meanwhile, as J_4^x and $J_{4'}^x$ vanish together local J_3^x noises do not contribute to $H_{\mathrm{eff}}^{(4)}$. Recalling that $\Upsilon^\dagger$ maps each strong bond into one effective 1/2-spin (see Fig. 4.6c): $|\alpha\alpha\rangle_{x,(1,2)} \to |\alpha\rangle_{x,D}$, $|\beta\beta\rangle_{x,(1',2')} \to |\beta\rangle_{x,C}$, $|\gamma\gamma\rangle_{y,(3,4)} \to |\gamma\rangle_{y,A}$, $|\delta\delta\rangle_{y,(3',4')} \to |\delta\rangle_{y,B}$, in a loop of four effective spins we obtain,

$$\hat{F} = \langle \sigma_1^z \sigma_2^y \sigma_3^z \sigma_4^x \sigma_{1'}^x \sigma_{3'}^y \rangle_{\mathrm{eff}} = \tau_A^x \tau_B^y \tau_C^x \tau_D^y, \tag{4.70}$$

where $\tau^\nu (\nu = x, y, z)$ are spin operators acting on the effective space (see Fig. 4.6c). Based on this minimal cell with zero J_4 and $J_{4'}$, we can then build the two-dimensional lattices of coupled brick-wall ladders shown in Fig. 4.7a and reach the Hamiltonian of Wen's toric code in Fig. 4.7b:

$$\mathcal{H} = g \sum_i \hat{F}_i, \qquad \hat{F}_i = \tau_i^x \tau_{i+\hat{a}}^y \tau_{i+\hat{a}+\hat{b}}^x \tau_{i+\hat{b}}^y, \tag{4.71}$$

where $i = (i_a, i_b)$ denotes the square lattice sites. As each $\hat{F}_i$ commutes with each other, it is an exactly solvable model with the ground state configuration $F_i = +1, \forall i$ for $g < 0$.

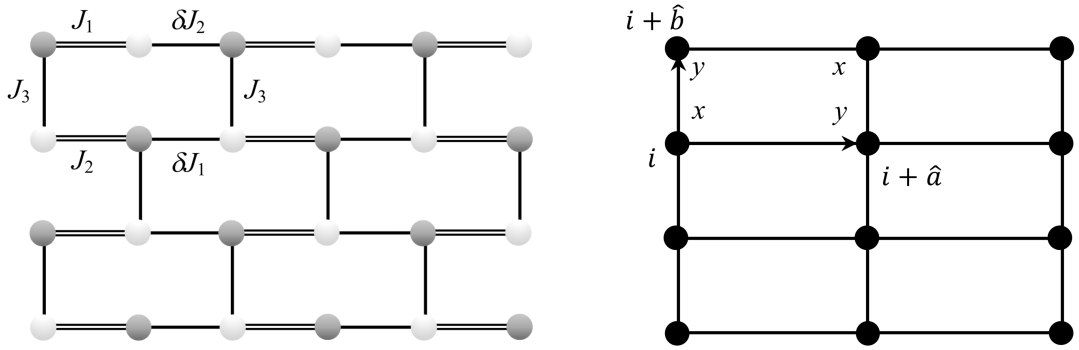

(a) (b)

Figure 4.7: (a) Brickwall ladders with coupling parameters $|J_1|, |J_2| \gg |\delta J_1|, |\delta J_2|, |J_3|$; (b) Wen's toric code manifested in effective spin space.

The excitations could be engineered in two ways. On one hand, in the effective spin space the local magnetic field σ_i^x or σ_i^y acting on the strong x or y bond (which could be achieved by an inductive or capacitive coupling to a small DC constant bias voltage as before) becomes the local operation $\hat{X}$ or $\hat{Y}$ which flips the spin on a single site. It creates a diagonal pair of excitations with two corresponding loop-qubit states changing from $+1$ to -1. On the other hand, picking up a single vertical bond labelled as $J_{3'}$ and changing its sign to $-J_{3'}$ via $\Phi_{3'}$ could introduce a neighboring pair of excitations (during the process the non-zero X coupling on this isolated vertical bond remains irrelevant). One can also relate Wen's toric code to Kitaev's toric code by moving spins from square lattice sites to the edges of a dual square lattice and performing unitary rotations.

4.5.4 SYK loop model and Random Ising models

For the original SYK model with quenched disorder, the Hamiltonian has the form:

$$\mathcal{H} = \frac{1}{4!} \sum_{i,j,k,l=1}^{N} J_{ijkl} d_i d_j d_k d_l, \tag{4.72}$$

where the couplings obey Gaussian distribution $P(J_{ijkl}) \sim \exp\left(-N^3 J_{ijkl}^2 / 12 J^2\right)$: $\overline{J_{ijkl}^2} = 3! J^2/N^3, \overline{J_{ijkl}} = 0$. The SYK model is found to be maximally chaotic and share the same Lyapunov exponent of a black hole in Einstein gravity [310].

By coupling two chains with strong x-links and y-links by weak z-links shown in Fig. 4.8a, we find two interesting limits to build up the effective Hamiltonian. We define $x = (|J_1|+|J_2|)^{-1}$ as a small number and therefore quantify the weak couplings through: $\{|J_3|, |J_4|\} = \mathcal{O}(x^s), \{|\delta J_1|, |\delta J_2|\} = \mathcal{O}(x^t), s, t \in \mathbb{N}^+$.

When $s \leq t$, we can restrict the system to the second-order perturbation in Eq. (4.68) and reach an effective Hamiltonian $\mathcal{O}(x^{2s+1})$:

$$\mathcal{H}_{\text{eff}}^{(2)} = \sum_{m,n=1}^{N} J_{mn} d_{(2m-1,1)} d_{(2m,1)} d_{(2n-1,2)} d_{(2n,2)}, \tag{4.73}$$

where subscript (j, α) denotes the site on the j-th column of Chain $\alpha = 1, 2$ and $J_{mn} = -J_3 J_{4,mn}/(|J_1| + |J_2|)$. The coupling constants J_{mn} are random variables with a Gaussian distribution ensured by the adjustability of $\Phi_{4,mn}$: $P(J_{mn}) \sim \exp(-NJ_{mn}^2/2J^2)$. $\left[id_{(2m-1,\alpha)}d_{(2m,\alpha)}, H_{\text{eff}}\right] = 0$ and $(id_{(2m-1,\alpha)}d_{(2m,\alpha)})^2 = 1$ imply that $id_{(2m-1,\alpha)}d_{(2m,\alpha)}$ is a good quantum number with the value ± 1. We arrive at the following map:

$$\mathcal{H}_{\text{eff}}^{(2)} = \sum_{m,n=1}^{N} J_{mn} \tau_{(m,1)}^z \tau_{(n,2)}^z, \tag{4.74}$$

where $\tau_{(m,\alpha)}^z = id_{(2m-1,\alpha)}d_{(2m,\alpha)}$. This gives rise to a one-dimensional Ising model (e.g. the zigzag path formed by orange loops and half of blue loops shown in Fig. 4.8b) with long-range random interactions (for example, green loops). Following the mapping to effective spin space as in Sec. 4.5.3, we can get the same result and take into account higher order corrections. Back to two coupled boxes in Fig. 4.6a, from Eq. (4.67) and Eq. (4.68)) we find $\mathcal{P}_1 = \langle \sigma_1^z \sigma_2^z \sigma_3^z \sigma_4^z \rangle_{\text{eff}} = \tau_D^z \tau_A^z, \mathcal{P}_3 = \langle \sigma_{1'}^z \sigma_{2'}^z \sigma_{3'}^z \sigma_{4'}^z \rangle_{\text{eff}} = \tau_C^z \tau_B^z$, which recovers the classical Ising couplings shown in Fig. 4.6b. Quantum corrections arise from the fourth-order perturbation with the terms: $\mathcal{P}_1\mathcal{P}_3 = \tau_A^z \tau_B^z \tau_C^z \tau_D^z, \mathcal{P}_{\widetilde{123}} = \tau_A^x \tau_B^x \tau_C^y \tau_D^y, \mathcal{P}_2 = \tau_A^y \tau_B^y \tau_C^x \tau_D^x, \mathcal{P}_{\widetilde{12}} = \tau_A^x \tau_B^y \tau_C^x \tau_D^y, \mathcal{P}_{\widetilde{23}} = \tau_A^y \tau_B^x \tau_C^y \tau_D^x$. Noises from non-zero X couplings on vertical bonds would produce a small magnetic field along z direction on sites A and B, as the effective interactions $\langle \sigma_3^x \sigma_4^x \rangle \sim \tau_A^z, \langle \sigma_{3'}^x \sigma_{4'}^x \rangle \sim \tau_B^z$.

When $s > t$, we can drop out the terms $\sim \mathcal{O}(x^{4s+3})$ in the fourth-order perturbation

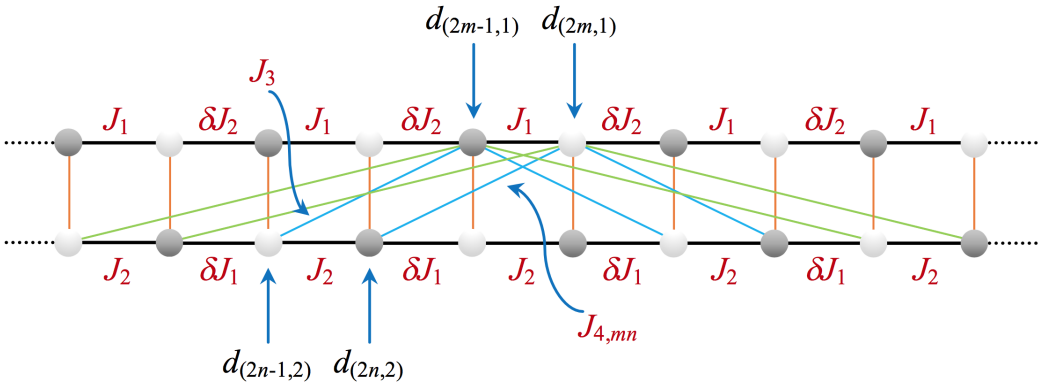

(a)

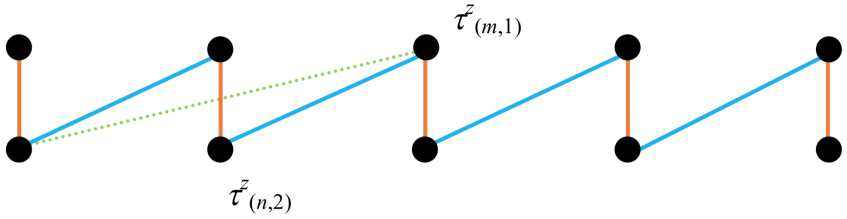

(b)

Figure 4.8: (a) Proposal to approximate the SYK model. The blue and green boxes describe longer-range couplings; (b) Mapping to the long-ranged Ising model.

of Eq. (4.68) and the effective Hamiltonian has the form $\mathcal{O}(x^{2s+2t+3})$:

$$\mathcal{H}^{(4)}_{\text{eff}} = \sum_{m,n=1}^{N} \sum_{l=1}^{4} J_{mnl} \mathcal{P}_d^{mnl}, \tag{4.75}$$

with coefficients $J_{mn1} = -\frac{\delta J_1 \delta J_2 J_3^2}{2(|J_1|+|J_2|)^3}$, $J_{mn2} = -\frac{5\delta J_1 \delta J_2 J_3 J_{4,(m+1)n}}{2(|J_1|+|J_2|)^3}$, $J_{mn3} = -\frac{\delta J_1 \delta J_2 J_3 J_{4,mn}}{2(|J_1|+|J_2|)^3}$, $J_{mn4} = -\frac{\delta J_1 \delta J_2 J_{4,mn} J_{4,(m+1)n}}{2(|J_1|+|J_2|)^3}$. Here $\mathcal{P}_d^{mnl}$ is the loop operator which denotes the 4-body couplings between d-Majoranas living on the vertices of "tilted" boxes: $\mathcal{P}_d^{mnl} = d_{(2m-1,1)} d_{(2m+l,1)} d_{(2n-1,2)} d_{(2n+l,2)} (l = 1, 2)$, $\mathcal{P}_d^{mn3} = d_{(2m,1)} d_{(2m+1,1)} d_{(2n,2)} d_{(2n+1,2)}$, $\mathcal{P}_d^{mn4} = d_{(2m,1)} d_{(2m+2,1)} d_{(2n,2)} d_{(2n+2,2)}$. This model could reveal glassy phases of the Ising model and quantum corrections could be controlled through effective fourth-order corrections, which can be studied in the future. An analogue of the Anderson-Edwards [337] order parameter could be measured as well as echo spin measurements [338]. Links with many-body localization phenomena could also occur [283].

Chapter 5

Conclusion and outlook

In this thesis, we have studied the effect of orbital magnetic fields on topological superconducting quantum wire systems. We have shown in Chapter 2, the occurrence of topological superconducting phases with two or four Majorana fermions per ladder as well as quantum Hall phases by tuning the magnetic flux and densities at the crossing points of the band structure. The adjustment of the chemical potential at the crossing region is a key ingredient to realize the appropriate low-energy physics. We have also studied Andreev processes and the induction of topological superconductivity in these quantum wire networks. Then, we have engineered a $p+ip$ topological superconducting state in weakly coupled ladder systems, projecting the low-energy physics on the (partially filled) lowest bonding band for each ladder, *i.e.*, or a pair of two-strongly-coupled wires. Chiral effects are introduced here through the application of a space-dependent magnetic field perpendicular to the plane of the wires. A natural question that arises in this context is the 2D generalization of our model to the strong coupling limit where two vertical couplings become equal ($t'_\perp = t_\perp$). Topological phase transitions might occur in intermediate coupling regimes. One can also include the diagonal hopping terms in each square plaquette and go beyond the one-band model of the $p+ip$ superconductor. For instance, a related recent proposal [339] has built the links with the extended Harper-Hofstadter model with total half-flux quanta per plaquette. In the presence of a small p_x pairing term, a robust chiral

superconducting phase with Chern number 2 has been found there. Our coupled-wires platform allows more flexibility on pairing channels, flux patterns and coupling strengths inside and between the ladders. It is expected to support an even richer phase diagram with diagonal hoppings. Meanwhile, we have also shown how the presence of superconductivity and preformed pairs can stabilize a two-dimensional $\nu = 1/2$ Laughlin quantum Hall phase in hybrid spin-1/2 systems, as a result of Andreev processes in the Luther-Emery description of a superconducting quantum wire. Similar fractional quantum Hall states can be constructed in bosonic coupled wires or quantum spin systems as well [29, 68, 244]. Besides, due to the analogy between p-wave superconductors, quantum Ising spin chains [340, 341] and $\mathcal{Z}_2$ Kitaev quantum spin liquids [18] (the links are revealed in Chapter 1 and Chapter 4 explicitly), one may anticipate further applicability of these findings in other interacting systems [342]. From the experimental perspective, we have illustrated a scheme to implement the orbital magnetic fields required in the coupled wire construction. It remains to test the feasibility of our proposal in realistic systems such as nanowires and cold atoms.

In Chapter 3, we have found a general relation between the valence bond fluctuations and the entanglement entropy of the Kitaev spin model in one and two dimensions. Valence bond fluctuations appear as a relevant tool to identify phases and phase transitions of Majorana magnetic quantum systems. One of the remaining challenges is the construction of similar observables to probe topological entanglement entropy, the universal negative constant arising from gauge Majorana fermions. Most likely, one has to resort to dynamical observables and consider vortex excitations above the ground state configurations under the influence of interactions [215]. Promising theoretical approaches include projected symmetry groups [343–347]. Application to three-dimensional systems [195, 348] can also be studied in the future.

In Chapter 4, we have suggested a superconducting toolbox starting from spin degrees of freedom (qubits) to study the formation of $\mathcal{Z}_2$ quantum spin liquids and

many-body Majorana states. The idea is motivated by the phase diagram of a generalized Kitaev square ladder where based on a Majorana fermion representation, we have predicted a plane of gapless (bulk) excitations, connecting three gapped spin liquid phases. Spin correlations can be measured with current technology [58, 330]. In lattices of multiple boxes, quantum spin liquid states are associated with a Néel order of gauge fields making analogies with Ising models. These Ising models can be disordered by engineering local fluxes and one could realize various glassy phases in relation with the SYK Majorana model. As for other practical applications, we have built relations with Wen's toric code in brickwall ladders. We also note another proposal to engineer four-body Ising interactions with Josephson junctions [349]. It is encouraging to see that the occurrence of orbital loop currents in Mott insulators [324, 325] has now been observed and realizing anistropic spin coupling constants in two dimensions and different spin phases is also possible in cold atoms [350]. With robust experimental platforms built, one may envision the braiding of Majorana fermions as the first step towards fault-tolerant quantum computation. In driven Floquet systems out of equilibrium, Majorana braiding with topological protection has been proposed theoretically for a single wire [351]. We can pursue operations alike in our coupled-box ensembles. In the meantime, we have tested the stability of our algorithm against local detuning, disorder and dissipation with the time-evolution of a four-site Majorana box. It is important to extend the current numerical results to a larger system size. There, the ground state properties of quantum spin liquids can be probed by time-averaged measurement of entanglement entropy [133, 216], as well as dynamical spin correlations (over a fixed longer time interval) [213–218].

In the following, we list other open questions related to the thesis that may require future exploration.

- We have shown via bosonization formalism that the emergent Majorana zero modes in two weakly coupled asymmetric wires are protected against weak

Coulomb interactions both inside and between the wires. In terms of moderate interactions, for a single Kitaev superconducting chain, the presence of a repulsive Coulomb interaction $V_{\parallel} \sum_j (2c_j^\dagger c_j - 1)(2c_{j+1}^\dagger c_{j+1} - 1)$ is shown to reduce the bulk gap [352], but at the same time broaden the window of the chemical potential that supports MZMs [353]. Further increasing the strength of the interaction [354] gives rise to an incommensurate CDW state ($V_{\parallel}/t > 1$) and finally a Mott insulating phase ($V_{\parallel} \gg t$). Similar phenomena [31] can be observed in two interacting Kitaev chains coupled by a repulsive Coulomb interaction $V_{\perp} \sum_j (2c_{j,1}^\dagger c_{j,1} - 1)(2c_{j+1,2}^\dagger c_{j+1,2} - 1)$: the intermediate phase that connects the topological regime with 4 MZMs and the Mott insulator becomes a gapless state that resembles double critical Ising (DCI) models. On the other hand, from DMRG calculations, moderate disorder can also help stabilize the topological order on a single superconducting wire [355]. In the future, the roles of strong Coulomb interactions and the local disorder on our two coupled wires and the multi-wire networks can be explored in more detail.

- Once we introduce spin-1/2 degrees of freedom to our coupled wire networks, it is promising to approximate 2D time-reversal-invariant topological superconductors [356] that support a Majorana Kramers pair at the boundary. By proximity effects, relevant proposal has been postulated successfully using a 2D semiconducting layer with large Rashba spin-orbit couplings on top of a nodeless $s_{\pm}$ wave iron-based superconductor [357].

- Encouraging progress has been made recently in the symmetry resolved entanglement spectroscopy [358–361]. One can resolve distinct contributions from the reduced density matrices of the subsystem, each associated with a possible value of the conserved quantity arising from the symmetry. Various techniques including the form factor bootstrap [362] and the generalized Fisher-Hartwig conjecture [363], are shown to be highly efficient to extract the subleading

terms in $\mathbb{Z}_2$-symmetry resolved von Neumann entropy $\mathcal{S}^{(\pm)}$, up to $\mathcal{O}(L^{-1})$. The $\mathbb{Z}_2$ Kitaev QSLs feature the fractionalization of a spin-1/2 into gauge and matter Majorana fermions at low energies. It is thus feasible to employ the same idea to the *hidden* symmetry in the matter fermion sector. In 1D, the bond fermions ψ behave as a p-wave superconducting chain on the dual lattice (1.131). The conserved quantity becomes the fermion number parity: $(-1)^Q = \pm 1$ with $Q = \sum_{m=1}^{M} \psi_m^\dagger \psi_m$. Translated back to the original spin space, $(-1)^Q = \prod_{m=1}^{M} (-ic_{2m-1}c_{2m}) = (-1)^M \sum_{j=1}^{2M} \sigma_j^x = \Delta_x$. The expectation value of the hidden string order parameter $\langle \Delta_x \rangle$ vanishes in the topologically non-trivial regime $J_1 < J_2$ [146]. It agrees with the degeneracy verified in the entanglement spectra of the even (+) and odd (−) parity sector [363]: $\lim_{M\to\infty} \mathcal{S}^{(+)} - \mathcal{S}^{(-)} = 0$. Both can be explained by the appearance of the spin-1/2 zero-energy modes at the edges of the entanglement Hamiltonian. For the Kitaev honeycomb model, similar hidden symmetries in the matter sector can be identified: *e.g.* $\Delta_{\nu,i} = \prod_{j\in\partial_i\mathcal{L},} \sigma_j^\nu$ with $\nu \in \{x, y, z\}$ and $i = h, v$ denoting the Ising coupling that covers one of the boundaries of the periodic lattice $\partial_i\mathcal{L}$ on the horizontal (h) and vertical (v) directions respectively[1]. Then it is possible to generalize related approaches to higher dimensions [364]. The subleading terms obtained in the symmetry-resolved entanglement entropy might lead to a better understanding of the topology of the two-dimensional integrable model.

- Doping the Kitaev-Heisenberg model has shown to give rise to topological superconductivity [347]. The motion of slow holes has also been studied systematically in the gapped phases of Kitaev honeycomb model [130]. It remains to see the occurrence of chiral superconductivity in the doped Kitaev ladder systems from the formation of resonating valence bond states.

- It might be challenging to study analytically the Kitaev honeycomb model be-

[1] In Fig. 1.4, one may choose $\Delta_{x(y),h} = \sum_{j\in\partial_h\mathcal{L}} \sigma_j^{x(y)}$, $\Delta_{z,v} = \sum_{j\in\partial_v\mathcal{L}} \sigma_j^z$.

yond the integrable limit [215], yet it may offer extra insights when one goes to lower dimension. For instance, the Kitaev-Gamma chain is shown to stablize an ermergent $SU(2)_1$ phase from the RG analysis [365]. Combining multiple numerical techniques (ED, finite-size and infinite DMRGs) [366], the phase diagram of the Kitaev-Gamma model is mapped out on the ladder geometry in the gapped spin liquid regime ($J_i = J, i = 1, \cdots, 4$). In an immediate uniform magnetic field, the flux per square plaquette changes from π to zero. There, a highly entangled chiral phase with staggered chirality and no magnetic ordering has been found and is speculated to be closely related to the 2D limit. In search for more exotic symmetry protected phases, we can start from the gapless spin liquid regime of our generalized ladder with $J_4 = 0$ (see the phase diagram in Fig. 4.1c). One may explore analytically the effects of a magnetic field, the formation of chiral Majorana fermion edge modes and the evolution of the vison gap in a hexagonal plaquette when the Kitaev and Gamma interactions are competing with each other.

- It is interesting to study the non-Hermitian analogues of Kitaev spin liquids [367] and extend the planar geometry to more exotic ones - for instance, doubled layers with twist angles [368]. From a broader perspective, originally postulated in particle physics, the topological models of Majorana fermions continue to carry strong links with high energy physics. Apart from the SYK model, emergent supersymmetry has also become a common feature of the Majorana-Hubbard model that can be built on various geometries [255, 369–374]. Potential experimental realizations of these models can be sought after in cQED and ultracold atoms.

Appendix A

Résumé en français

Au cours des dernières décennies, les fermions de Majorana ont ravivé l'intérêt pour le champ de la matière condensée en raison d'applications possibles dans l'information quantique en tant que qubits protégés [1–7] et codes de surface avec des variables $\mathcal{Z}_2$ [8–12]. D'une part, ils émergent en tant que modes fermioniques d'énergie nulle de Majorana (MZM) au niveau des défauts topologiques (par exemple, aux bords) dans une variété de systèmes topologiques avec une symétrie particule-trou. Ce sont des supraconducteurs à onde p, les analogues supraconducteurs des phases de Hall quantique [13–15]. D'autre part, les fermions de Majorana sont étroitement liés aux liquides de spin quantique $\mathcal{Z}_2$ [16, 17]. Le modèle de spin de Kitaev sur le réseau en nid d'abeille [18] représente une classe importante de modèles dans cette catégorie, et peut être résolu exactement dans une représentation de fermions de Majorana. Le modèle montre trois phases liquides de spin espacées et une phase intermédiaire qui peut être identifiée comme un semi-métal des fermions de Majorana.

La quête des phases topologiques a commencé par l'effet Hall quantique [19, 20], et puis a évolué vers des variantes sur le réseau en nid d'abeilles avec effectivement un flux magnétique nul dans une cellule unitaire [21]. Ces systèmes de Hall quantique sont caractérisés par un flux de charge robuste et unidirectionnel aux limites de l'échantillon [22, 23], ainsi que par l'émergence de charges fractionnaires dans le cas des états de Laughlin [24–27]. Récemment, une approche théorique pour étudier les

connexions entre les supraconducteurs topologiques et les phases de Hall quantique consiste à voir les systèmes bidimensionnels comme des réseaux de fils unidimensionnels couplés [28–30]. Cette approche dite de construction filaire a l'avantage de permettre d'étudier les effets d'interaction (comme le fractionnement) [31–33] qui vont au-delà de la théorie du champ moyen, via le paradigme liquide de Luttinger [34, 35].

La recherche de liquides de spin quantique dans le régime de Mott [36–41] est cependant restée un grand défi en relation avec la découverte de matériaux quantiques [42–50]. Les liquides de spin quantique présentent des propriétés topologiques et d'intrication intéressantes [51–54] qui sont utilisées pour des applications en information quantique [55]. Le modèle en nid d'abeilles de Kitaev [18] démontre l'importance des champs de jauge $\mathcal{Z}_2$ sur les propriétés de basse énergie. Il est également important de mentionner les constructions exactes de liquides de spin chiraux [56] et les états de liquide de spin dans les systèmes en échelle [57].

En partant des analogues de faible dimension, on peut envisager de simuler les liquides de spin de Kitaev à partir de la construction de boîtes Majorana à quatre sites dans des réseaux d'électrodynamique quantique de circuit (cQED). Notamment, un système de trois transmons a été réalisé récemment [58], avec des applications possibles dans les phases topologiques [59, 60]. Ces boîtes pourraient être utilisées dans des géométries variables allant des systèmes d'impuretés quantiques aux modèles d'échelle accordables et de plaquettes. Des ensembles de modèles de plaquettes carrées ont été réalisés dans des atomes ultrafroids [61] pour émuler un état liquide de spin Anderson Resonating Valence Bond [38, 62], et ont été montrés théoriquement comme étant liés à la superconductivité d'onde d (superfluidité) dans le modèle de Hubbard proche de l'état de Mott [63]. La conception de ces boîtes de Majorana répond à des questions difficiles concernant le choix des appariements. Des expériences dans des architectures supraconductrices cQED [64] et dans des atomes ultrafroids [65] rapportent des progrès dans l'ingénierie des interactions à quatre corps inspirées d'efforts théoriques

[66, 67].

Dans ces contextes, les objectifs de cette thèse sont de deux ordres: en premier, explorer les propriétés topologiques et d'enchevêtrement des fermions de Majorana dans les fils supraconducteurs topologiques et les liquides de spin de Kitaev; deuxièmement, concevoir des plates-formes physiques réalisables pour l'ingénierie quantique d'états Majorana à plusieurs corps.

Dans le chapitre 1, nous passons en revue une série de concepts topologiques de base à partir de la classification des phases topologiques pour les fermions non interactifs basée sur des symétries non spatiales, avec l'illustration de modeles centraux révélant des fermions de Majorana: des supraconducteurs d'onde p en $d = 1, 2$ et le modèle en nid d'abeille de Kitaev. Par correspondance, les modes de bord de Majorana sont protégés par l'écart de masse et leurs propriétés peuvent être dérivées d'invariants topologiques via le théorème d'indice. Un résumé des réalisations expérimentales potentielles de ces modèles topologiques de fermions de Majorana est donné à la fin de ce chapitre.

Dans le chapitre 2, nous présentons une étude théorique de l'interaction entre la supraconductivité topologique de l'onde p, les champs magnétiques orbitaux et les phases de Hall quantiques dans les systèmes à fils couplés. Nous analysons des systèmes hybrides constitués d'une chaîne Kitaev couplée à un liquide Luttinger. En accordant le champ magnétique et la densité des porteurs, nous identifions les phases de Hall quantique et d'onde de densité de charge, ainsi que les régimes dans lesquels la supraconductivité est induite dans la deuxième chaîne par effet de proximité. Cela nous permet d'envisager des systèmes bidimensionnels constitués d'échelles faiblement couplées. Nous parvenons à concevoir un supraconducteur $p + ip$ et à réaliser une généralisation de la phase de Hall quantique fractionnaire $\nu = 1/2$, à la suite des travaux précédents sur l'échelle tournante à deux pattes [68].

Au chapitre 3, nous introduisons les fluctuations des liaisons de valence pour caractériser les liquides de spin quantique et leurs propriétés d'enchevêtrement. En

appliquant des approches analytiques, nous trouvons une loi d'échelle identique entre les fluctuations des liaisons de valence et l'entropie d'intrication dans le modèle de spin de Kitaev à deux dimensions et dans les analogues de chaînes unidimensionnelles. Nous montrons également comment ces fluctuations de liaison de valence peuvent localiser, via le préfacteur de mise à l'échelle linéaire, les transitions de phase quantique entre les trois phases semi-métalliques Majorana espacées et sans lacunes dans le modèle en nid d'abeille. Nous étudions ensuite l'effet d'un champ magnétique uniforme selon la direction [111] ouvrant un intervalle dans la phase intermédiaire qui devient topologique. On obtient toujours un signal robuste pour caractériser les transitions vers les trois phases espacées. Des comparisons de notre travail analytique avec une etude DMRG sera effectuee.

Au chapitre 4, nous dérivons un diagramme de phase généralisé pour le système d'échelle carrée de Kitaev. Comme une réminiscence du modèle bidimensionnel, nous identifions trois phases liquides de spin espacées et une phase sans intervalle qui s'étend jusqu'à un plan. Sur la base des cellules unitaires de la géométrie de l'échelle, nous concevons une boîte supraconductrice avec quatre spins-1/2 (qubits). Au sein d'une boîte ou d'un îlot, nous introduisons un protocole de résonance magnétique nucléaire généralisé pour réaliser nos modèles. Les boîtes de couplage nous permettent de réaliser des liquides de spin Kitaev dans diverses géométries avec des applications dans le code torique. Nous montrons comment produire un état de flux Néel à la suite de l'état fondamental du flux π et abordons le rôle des flux d'impuretés locales conduisant à des modèles d'Ising aléatoires. Nous présentons une implémentation du modèle Sachdev-Ye-Kitaev Majorana dans des systèmes d'échelle couplés. Notre travail analytique sera ensuite comparé avec des simulations numériques sur les mesures temporelles moyennes, les correlations de spin et de flux, et l'effet de la dissipation.

Appendix B

Perturbative treatment of $\mathcal{H}_\perp$

Here, we give more detail on the derivations of the Andreev processes in Sec. 2.2. To find the relevant contribution from $t_\perp$, we can develop perturbation theory [68, 251, 253] for the hybrid wire Hamiltonian $\mathcal{H}_0 = \mathcal{H}_1 + \mathcal{H}_2 + \mathcal{H}_\Delta$ with a weak interwire coupling $V = \mathcal{H}_\perp$. Here, $\mathcal{H}_1 + \mathcal{H}_2$ refers to the quadratic part (Luttinger liquid contribution) of the Hamiltonian in each wire 1 and 2 respectively, the Hamiltonian density operator $V(x) = \mathcal{H}_\perp(x)$ reads,

$$\begin{aligned} V(x) = -\frac{t_\perp}{2\pi a} \Big\{ & \left[e^{i(\sqrt{2}\theta^-(x) - \chi x)} + e^{-i(\sqrt{2}\theta^-(x) - \chi x)} \right] \\ & \times \left[e^{i((k_F^1 + k_F^2)x - \sqrt{2}\phi^+(x))} + e^{-i((k_F^1 + k_F^2)x - \sqrt{2}\phi^+(x))} \right] \\ & + \left[e^{i(\sqrt{2}\theta^-(x) - \chi x)} + e^{-i(\sqrt{2}\theta^-(x) - \chi x)} \right] \\ & \times \left[e^{i((k_F^1 - k_F^2)x - \sqrt{2}\phi^-(x))} + e^{-i((k_F^1 - k_F^2)x - \sqrt{2}\phi^-(x))} \right] \Big\}. \end{aligned} \tag{B.1}$$

To the n-th leading order, the effective Hamiltonian reads

$$\mathcal{H}_{\text{eff}} = \mathcal{H}_0 + V^{(n)}. \tag{B.2}$$

For any observable A, the expectation value under $\mathcal{H}_{\text{eff}}$ takes the form

$$\langle A \rangle_{\mathcal{H}_0 + V} = \langle A \rangle_{\mathcal{H}_{\text{eff}}} + \mathcal{O}(V^n), \tag{B.3}$$

where

$$\begin{aligned}\langle A\rangle_{\mathcal{H}_0+V} &= \frac{\mathrm{Tr}\left[e^{-\int dxd\tau(\mathcal{H}_0+V)}A\right]}{\mathrm{Tr}\left[e^{-\int dxd\tau(\mathcal{H}_0+V)}\right]} \\ &= \left[\langle A\rangle_{\mathcal{H}_0}+\sum_{n=1}^{\infty}\frac{(-1)^n}{n!}\left\langle\left(\int V\right)^n A\right\rangle_{\mathcal{H}_0}\right] \\ &\times\left[1+\sum_{n=1}^{\infty}\frac{(-1)^n}{n!}\left\langle\left(\int V\right)^n\right\rangle_{\mathcal{H}_0}\right]^{-1} \end{aligned} \tag{B.4}$$

with the notation $\int V=\int dxd\tau V(x,\tau)$. As the mode θ_1 is pinned in Eq. (4.57), its dual field ϕ_1 oscillates rapidly and renders all terms involving ϕ^+ and ϕ^- irrelevant. Thus

$$\left(\int V\right)^n=0, \qquad n=\text{odd}. \tag{B.5}$$

We can keep the even order terms

$$\begin{aligned}\langle A\rangle_{\mathcal{H}_0+V} &= \langle A\rangle_{\mathcal{H}_0}+\sum_{k=2,4}\frac{1}{k!}\left\langle\left(\int V\right)^k A\right\rangle_{\mathcal{H}_0} \\ &-\frac{1}{k!}\left\langle\left(\int V\right)^k\right\rangle_{\mathcal{H}_0}\langle A\rangle_{\mathcal{H}_0}+\mathcal{O}\left[\left(\int V\right)^6\right]. \end{aligned} \tag{B.6}$$

B.1 Second order contribution to the π-flux

For the integral at the second order perturbation theory level, it is more convenient to switch to the relative and center-of-mass coordinates,

$$\begin{aligned} x&=(x_1+x_2)/2, \quad x'=x_1-x_2, \\ \tau&=(\tau_1+\tau_2)/2, \quad \tau'=\tau_1-\tau_2. \end{aligned} \tag{B.7}$$

Further, we introduce polar coordinates for the relative distances x' and τ',

$$d_{12}=\sqrt{(x')^2+v^2(\tau')^2}, \tag{B.8}$$

and consider the virtual processes

$$\begin{aligned} |x'|&=|x_1-x_2|\le\xi=v/\Delta, \\ |\tau'|&=|\tau_1-\tau_2|\le\Delta^{-1}. \end{aligned} \tag{B.9}$$

Then

$$\int dx'd\tau' = \int \frac{2\pi}{v} d_{12} d(d_{12}). \tag{B.10}$$

Correspondingly,

$$\begin{aligned}
&\int dx_1 d\tau_1 dx_2 d\tau_2 V(x_1,\tau_1)V(x_2,\tau_2) \\
\simeq &\frac{2\pi a}{v}(\xi - a)\int dx d\tau V(x,\tau)V(x+a,\tau) \\
\simeq &\frac{2\pi a}{\Delta}\int dx d\tau V^2(x,\tau) \\
= &\frac{4t_\perp^2}{\pi a \Delta}\int dx d\tau \Big[\cos(2\sqrt{2}\theta^- - 2\chi x) + \cos(2k_F^2 x - 2\phi_2) \\
&+ \cos(2\sqrt{2}\theta^- - 2\chi x)\cos(2k_F^2 x - 2\phi_2)\Big].
\end{aligned} \tag{B.11}$$

We have dropped out fast-oscillating terms which involve ϕ_1 fields together with other constant terms.

For the situation of two wires such that $k_F^2 \neq \pi/(2a)$, but with the π-flux gauge choice $\chi a = \pi$, we obtain

$$\left(\int V\right)^2 = \frac{4t_\perp^2}{\pi a \Delta}\int dx d\tau \cos(2\theta_2), \tag{B.12}$$

and in the last equality, θ_1 is pinned to zero and we regard $2\chi x$ as multiples of 2π.

On the other hand, when $\Delta \gg t_\perp$,

$$\begin{aligned}
\left\langle \left(\int V\right)^2 \right\rangle_{\mathcal{H}_0} &= \int dx_1 dx_2 d\tau_1 d\tau_2 \left\langle V(x_1,\tau_1)V(x_2,\tau_2)\right\rangle_{\mathcal{H}_0} \\
&= \left(\frac{2\pi}{v}\right)\int dx d\tau d_{12} d(d_{12}) R(d_{12}) e^{-d_{12}/\xi} \\
&\simeq \left(\frac{2\pi}{v}\right) a(\xi - a) R(a)\int dx d\tau \cdot 1 \\
&\simeq \left(\frac{2\pi a}{\Delta}\right) R(a)(L\beta) \sim 0,
\end{aligned} \tag{B.13}$$

where $R(r)$ denotes a power-law decreasing function. Therefore, the second order contribution reads

$$\mathcal{H}_\perp^{(2)} = -\frac{1}{2}\left(\int V\right)^2 = -\frac{2t_\perp^2}{\pi a \Delta}\int dx d\tau \cos(2\theta_2). \tag{B.14}$$

This reproduces Eq. (2.23) in Sec. 2.2, and the proximity effect since $\langle\cos(2\theta_2)\rangle$ now acquires a finite value, implying the pinning of the mode θ_2 in wire 2 and the opening of a superconducting gap due to the presence of Andreev processes, coupling wire 1 and 2.

B.2 Fourth-order contribution to the arbitrary flux

Away from half-filling, under our gauge choice (2.32) for the flux, the second order term vanishes

$$2\chi x = \pm 2(k_F^1 + k_F^2)x \neq \pm 2\pi n, \quad \left(\int V\right)^2 = 0. \tag{B.15}$$

Now if we go to the fourth order, in the same way as in Eq. (B.7) by changing the basis twice: (i) from (x_3, τ_3, x_4, τ_4) to ($\bar{x}$, $\bar{\tau}$, $\bar{x}'$, $\bar{\tau}'$); (ii) from (x, τ, $\bar{x}$, $\bar{\tau}$) to (X, η, X', η'), we reach

$$\begin{aligned}
\left(\int V\right)^4 &= \left(\frac{2\pi a}{\Delta}\right)^2 \int dx d\tau d\bar{a} d\bar{\tau} V^2(x,\tau) V^2(\bar{x},\bar{\tau}) \\
&\simeq \left(\frac{2\pi a}{\Delta}\right)^2 \frac{2\pi \cdot 2a}{v}(\xi - 2a) \int dX d\eta V^2(X,\eta) V^2(X+2a,\eta) \\
&\simeq \frac{8t_\perp^4}{\pi a \Delta^3} \int dx d\tau \cos\left[2\sqrt{2}(\theta^-(x) - \theta^-(x+2a)) + 4\chi a\right].
\end{aligned} \tag{B.16}$$

In the second equality, we notice the relative distance $|X'| = |x - \bar{x}| = |x_1 + x_2 - x_3 - x_4|/2 \in [2a, \xi]$. Meanwhile,

$$\begin{aligned}
&\left\langle \left(\int V\right)^4 \right\rangle_{\mathcal{H}_0} \\
&\simeq \left(\frac{2\pi a}{\Delta}\right)^2 \int dx d\tau d\bar{x} d\bar{\tau} \langle V^2(x,\tau) V^2(\bar{a},\bar{\tau})\rangle_{\mathcal{H}_0} \\
&= 2\left(\frac{2\pi a}{\Delta}\right)^3 R(2a)(L\beta) \sim 0.
\end{aligned} \tag{B.17}$$

Taken into account the pinned mode $\theta_1(x) \sim 0$, we find in the effective Hamiltonian $\mathcal{H}_{\text{eff}}$, that the leading-order contribution from $t_\perp$ becomes

$$\mathcal{H}_\perp^{(4)} = -\frac{t_\perp^4}{3\pi a \Delta^3} \int dx \cos[2(\theta_2(x+2a) - \theta_2(x)) + 4\chi a]. \tag{B.18}$$

Appendix C

Renormalization group analysis

In this section, we would like to derive the renormalization flow equations (2.22) in Sec. 2.2.1.

C.1 RG equations for a general interacting Hamiltonian

For simplicity, we start from a general form of interacting Hamiltonians [256]

$$\begin{aligned}\mathcal{H} &= \mathcal{H}_0 + \mathcal{H}', \\ \mathcal{H}_0 &= \frac{v}{2\pi}\int dx \left[K(\nabla\theta)^2 + \frac{1}{K}(\nabla\phi)^2\right], \\ \mathcal{H}' &= \frac{g}{a^2}\int dx \cos(m\sqrt{2}\theta),\end{aligned}$$

where g denotes the bare coupling strength and a - the lattice spacing. We take m as an arbitrary coefficient tailored to different perturbations. In the final flow equations we obtain, the same arguments from the θ field are valid for the ϕ field under an exchange: $K^{-1} \to K$.

The essence of the renormalization procedure is manifest in the fact - the low-energy properties of the system stay unaffected while changing the cutoff ($a \to a' = a + da$). To see the consequences, let us consider a physical observable, the correlation function

$$R(r_1 - r_2) = \langle e^{in\sqrt{2}\theta(r_1)} e^{-in\sqrt{2}\theta(r_2)} \rangle_{\mathcal{H}} = \langle A \rangle_{\mathcal{H}_0 + \mathcal{H}'}$$

with n an arbitrary coefficient. Based on our previous perturbation analysis, one finds a nonzero second-order contribution from $\mathcal{H}'$

$$R(r_1-r_2)=\langle A\rangle_{\mathcal{H}_0}+\frac{1}{2!}\left\langle\left(\int\mathcal{H}'\right)^2 A\right\rangle_{\mathcal{H}_0}-\frac{1}{2!}\left\langle\left(\int\mathcal{H}'\right)^2\right\rangle_{\mathcal{H}_0}\langle A\rangle_{\mathcal{H}_0}.$$

Changing variables from $\int=\int dxd\tau$ to $\int d^2r/v$ with $r=(x,y)$ and $y=v\tau$, we get

$$\begin{aligned}&R(r_1-r_2)\\&=\langle e^{in\sqrt{2}\theta(r_1)}e^{-in\sqrt{2}\theta(r_2)}\rangle_{\mathcal{H}_0}+\frac{1}{2}\left(\frac{g}{2a^2v}\right)^2\sum_{\epsilon_1,\epsilon_2=\pm}\int d^2r'd^2r''\Big[\langle e^{in\sqrt{2}\theta(r_1)}e^{-in\sqrt{2}\theta(r_2)}\\&\quad e^{i\epsilon_1 m\sqrt{2}\theta(r_1)}e^{-i\epsilon_2 m\sqrt{2}\theta(r_2)}\rangle_{\mathcal{H}_0}-\langle e^{in\sqrt{2}\theta(r_1)}e^{-in\sqrt{2}\theta(r_2)}\rangle_{\mathcal{H}_0}\langle e^{i\epsilon_1 m\sqrt{2}\theta(r_1)}e^{-i\epsilon_2 m\sqrt{2}\theta(r_2)}\rangle_{\mathcal{H}_0}\Big].\end{aligned}$$

Applying the Debye-Waller relation for the functional integral and the elemental correlations from bosonization [256],

$$\begin{aligned}&\langle T_\tau e^{\sum_j i(A_j\phi(r_j)+B_j\theta(r_j))}\rangle=e^{-\frac{1}{2}\langle T_\tau[\sum_j i(A_j\phi(r_j)+B_j\theta(r_j))]^2\rangle},\\&\langle[\phi(r)-\phi(0)]^2\rangle=KF_1(r),\quad\langle[\theta(r)-\theta(0)]^2\rangle=K^{-1}F_1(r),\quad\langle\phi(r)\theta(0)\rangle=\frac{1}{2}F_2(r),\end{aligned}$$

with

$$F_1(r)=\frac{1}{2}\log\left[\frac{x^2+(u|\tau|+a)^2}{a^2}\right],\quad F_2(r)=-i\mathrm{Arg}[y_a+ix],\quad y_a=v\tau+a\mathrm{Sign}(\tau),\tag{C.1}$$

one arrives at

$$\begin{aligned}R(r_1-r_2)=e^{-n^2K^{-1}F_1(r_1-r_2)}\Bigg[1+\frac{g^2}{8a^4v^2}\sum_{\epsilon_1=\pm}\int d^2r'd^2r''e^{-m^2K^{-1}F_1(r'-r'')}\\\left(e^{\epsilon_1 mnK^{-1}[F_1(r_1-r')-F_1(r_1-r'')-(r_1\to r_2)]}-1\right)\Bigg].\end{aligned}\tag{C.2}$$

In the equation above, it is easy to check the terms for $\epsilon_1=-\epsilon_2$ cancel with each other. From Eq. (C.1), inside the integral one can evaluate

$$e^{-m^2K^{-1}F_1(r'-r'')}=\left(\frac{a}{r'-r''}\right)^{m^2K^{-1}},$$

and notice the major contribution arises from small relative distance $r'-r''$. It is thus convenient to introduce new variables encoding the center of mass and relative

coordinates,

$$\begin{cases} R = (r' + r'')/2 \\ r = r' - r'' \end{cases}.$$

We proceed by taking into account

$$F_1(r_1 - r') - F_1(r_1 - r'') \simeq r \cdot \nabla_R F_1(r_1 - R), \qquad \text{for small } r.$$

Moreover, from the Taylor expansion of the exponential in Eq. (C.2), the first order term $\mathcal{O}(r)$ vanishes after the summation over $\epsilon_1 = \pm$. The second order term $\mathcal{O}(r^2)$ gives

$$R(r_1 - r_2) \simeq e^{-n^2K^{-1}F_1(r_1-r_2)} \left[1 + \frac{(gmn)^2}{8a^4(vK)^2} \int d^2R d^2r \sum_{i,j=x,y} e^{-m^2K^{-1}F_1(r)} r_i r_j \right.$$
$$\left. \nabla_{R_i}[F_1(r_1 - R_i) - F_1(r_2 - R_i)] \nabla_{R_j}[F_1(r_1 - R_j) - F_1(r_2 - R_j)] \right].$$

The rotation invariance in $r = (x, y)$ allows us to keep only the terms $i = j$. For $i \neq j$, a change of variable $x \to -x$ or $y \to -y$ would cancel the original contribution. Also, the general relation $\int d^2r\ r^2/2 = \int d^2r x^2 = \int d^2r y^2$ holds true when the integral acts on an arbitrary function $f(|r|)$. Therefore,

$$\begin{aligned} &R(r_1 - r_2) e^{n^2K^{-1}F_1(r_1-r_2)} \\ &= 1 - \frac{(gmn)^2}{16a^4(vK)^2} \int d^2R d^2r r^2 e^{-m^2K^{-1}F_1(r)} [F_1(r_1 - R) - F_1(r_2 - R)] \\ &\quad (\nabla_X^2 + \nabla_Y^2)[F_1(r_1 - R) - F_1(r_2 - R)]. \end{aligned}$$

Once $R \gg a$, $\nabla_R^2 F_1(R) = \nabla_R^2 \log(R/a) = 2\pi\delta(R)$. We obtain the expression of the correlation function

$$R(r_1 - r_2) = e^{-n^2K^{-1}F_1(r_1-r_2)} \left[1 + \frac{1}{2}\left(\frac{gmn\pi}{vK}\right)^2 F_1(r_1 - r_2) \int_\alpha^\infty \frac{dr}{r} \left(\frac{r}{a}\right)^{3-m^2K^{-1}}\right].$$

Restoring the exponential, we find the effective Luttinger parameter

$$\frac{1}{K_{\text{eff}}} = \frac{1}{K} - \frac{y^2}{2K^2} \int_a^\infty \frac{dr}{a} \left(\frac{r}{a}\right)^{3-m^2K^{-1}}, \tag{C.3}$$

where y denotes the rescaled coupling strength $y = mg\pi/v$.

Changing the cutoff from $a = a_0 e^l$ to $a' = a + da = a(1 + dl)$, the effective Luttinger parameter should keep the same form, namely

$$\frac{1}{K_{\text{eff}}(a')} = \frac{1}{K(a')} - \frac{y^2(a')}{2K^2(a')} \int_{a'}^{\infty} \frac{dr}{a'} \left(\frac{r}{a'}\right)^{3-m^2K^{-1}(a')}. \tag{C.4}$$

On the other hand, one can rewrite the integral inside $K_{\text{eff}}^{-1}(a)$ (C.3) as

$$\begin{aligned}\frac{1}{K_{\text{eff}}(a)} =& \frac{1}{K(a)} - \frac{y^2(a)}{2K^2(a)} \left[\int_a^{a+da} \frac{dr}{a} \left(\frac{r}{a}\right)^{3-m^2K^{-1}(a)} \right. \\ &\left. + \int_{a'}^{\infty} \frac{dr}{a'} \left(\frac{r}{a'}\right)^{3-m^2K^{-1}(a)} \left(\frac{a'}{a}\right)^{4-m^2K^{-1}(a)}\right].\end{aligned} \tag{C.5}$$

Comparing Eq. (C.4) and Eq. (C.5) and imposing

$$\frac{1}{K_{\text{eff}}(a)} = \frac{1}{K_{\text{eff}}(a')},$$

we identify the following renormalization flow equations for K and y in terms of new variable l:

$$\begin{aligned}\frac{d}{dl}\frac{1}{K(l)} &= -\frac{y^2(l)}{2K^2(l)}, \\ \frac{d}{dl}y(l) &\simeq \left(2 - \frac{m^2}{2K(l)}\right) y(l).\end{aligned} \tag{C.6}$$

While the first equation is exact for K, the second equation is only perturbative for y as we take the approximation $K(a) \simeq K(a')$ during the derivation. From Eq. (C.1), performing $K^{-1} \to K$ would give a flow equation for the ϕ field.

C.2 Scaling dimensions of $t_\perp$ and Δ

In the same manner, we can write down the renormalization equations for $t_\perp$ and Δ in hybrid wire systems in Sec. 2.2.1.

In the strong coupling limit $\Delta \leq t_\perp < t$, the inter-wire tunneling term $t_\perp$ enters into the effective Hamiltonian via a second-order process

$$\mathcal{H}_\perp = -\frac{g}{a^2} \int dx \cos(m\sqrt{2}\theta^-) \cos(m\sqrt{2}\phi^+),$$

where $g = 2t_\perp a/\pi$ and $m = 1$. In the non-interacting Hamiltonian $\mathcal{H}_0 = \mathcal{H}_0^+ + \mathcal{H}_0^-$,

$$\mathcal{H}_0^\pm = \frac{v_\pm}{2\pi}\int dx \left[K_\pm(\nabla\theta^\pm)^2 + \frac{1}{K_\pm}(\nabla\phi^\pm)^2\right],$$

(θ^+, ϕ^+) and (θ^-, ϕ^-) act as two pairs of decoupled and independent fields: $\langle\phi^+(r)\theta^-(0)\rangle = 0$. One can thus define a new correlation function,

$$R(r_1 - r_2) = \langle e^{in\sqrt{2}\phi^+(r_1)} e^{in\sqrt{2}\theta^-(r_1)} e^{-in\sqrt{2}\phi^+(r_2)} e^{-in\sqrt{2}\theta^-(r_2)}\rangle_{\mathcal{H}},$$

and safely drop out the correlators between two different rotated fields. Choosing the dimensionless quantities as usual

$$\tilde{t}_\perp = y = \frac{mg\pi}{v^\pm} = \frac{t_\perp}{\Lambda^*}, \quad \Lambda^* = \frac{v^\pm}{2a}, \tag{C.7}$$

we can directly apply the results of Eq. (C.6) and arrive at the flow equation for $\tilde{t}_\perp$:

$$\frac{d\tilde{t}_\perp}{dl} = \left(2 - \frac{K_+}{2} - \frac{1}{2K_-}\right)\tilde{t}_\perp. \tag{C.8}$$

Similarly, the pairing term

$$\mathcal{H}_\Delta = -\frac{2\Delta}{\pi a}\int dx \sin(k_F^1 a)\cos(2\theta_1) = -\frac{g}{a^2}\int dx \cos[m\sqrt{2}(\theta^+ + \theta^-)],$$

with $g = 2\Delta a \sin(k_F^1 a)/\pi$ and $m = 1$, corresponds to the flow equation

$$\frac{d\tilde{\Delta}}{dl} = \left(2 - \frac{1}{2K_+} - \frac{1}{2K_-}\right)\tilde{\Delta}, \tag{C.9}$$

with $\tilde{\Delta} = \Delta/\Lambda^*$. Here, $\Lambda^* = v^\pm/[2a\sin(k_F^1 a)]$ denotes the high-energy cutoff. For non-interacting fermions $K_\pm = K = 1, v_\pm K_\pm = (v_{F,1} + v_{F,2})K/2 = ta[\sin(k_F^1 a) + \sin(k_F^2 a)]$, $\Lambda^* \simeq t$. For interacting fermions $K_\pm < 1, v_\pm > v$, $\Lambda^* > t$.

The scaling dimensions of two terms read

$$\delta_{t_\perp} = \frac{K_+}{2} + \frac{1}{2K_-}, \quad \delta_\Delta = \frac{1}{2K_+} + \frac{1}{2K_-}.$$

Only if $\delta < 2$, the associated term can be relevant. In the non-interacting limit of free fermions we currently consider ($K_+ = K_- = 1$), the two channels have the same

scaling dimension $\delta_{t_\perp} = \delta_\Delta$. It renders that the transition of the superconducting phase and the charge density wave state takes place at $t_\perp/\Delta = 1$. In the weakly interacting case ($K_\pm < 1$), the transition point will be slightly shifted. We see that for the region where $t_\perp \geq \Delta$, $\tilde{t}_\perp$ will flow to the strong coupling faster than $\tilde{\Delta}$. The low-energy physics is still governed by $t_\perp$ and the system behaves as a CDW.

Appendix D

Edge theory at filling $\nu = 1$

Here, we study the effective edge theory in the quantum Hall phase found in Sec. 2.2.2, in the case of two wires or a two-leg ladder implying that the two edges are not fully separated from the bulk. We then perform an integration on the bulk (gapped) degrees of freedom to build the edge theory. The form of the interwire tunneling Hamiltonian $\mathcal{H}_\perp$ (2.33) satisfies the classification of the edge theory at the filling $\nu = 1/m$ [68, 244]. Below, we briefly review the construction approach.

The effective edge Hamiltonian can be built in the Luttinger liquid form

$$\mathcal{H} = \mathcal{H}_0^+ + \mathcal{H}_0^- + \mathcal{H}_\perp, \tag{D.1}$$

where $\mathcal{H}_0^\pm$ is given in Eq. (2.15) and $\mathcal{H}_\perp$ in Eq. (2.33). We are then able to integrate out the other bulk mode θ in the action

$$S[\theta^\pm, \phi^\pm] = \frac{1}{2\pi} \sum_{\alpha=\pm} \int dx d\tau \left[vK(\nabla\theta^\alpha)^2 + \frac{v}{K}(\nabla\phi^\alpha)^2 + 2i\partial_\tau \phi^\alpha \nabla\theta^\alpha \right]. \tag{D.2}$$

Changing the basis from $[\theta^+, \phi^+, \theta^-, \phi^-]$ to $[\theta, \phi, \theta', \phi']$ via Eqs. (2.34), (2.36) and (2.37), we get

$$\begin{aligned}
\sum_{\alpha=\pm} (\nabla\theta^\alpha)^2 =& \frac{m^2}{2} \left[(\nabla\theta)^2 + 2\nabla\theta'\nabla\theta + (\nabla\phi)^2 - 2\nabla\phi'\nabla\phi + (\nabla\theta')^2 + (\nabla\phi')^2 \right], \\
\sum_{\alpha=\pm} (\nabla\phi^\alpha)^2 =& \frac{1}{2} \left[(\nabla\theta)^2 - 2\nabla\theta'\nabla\theta + (\nabla\phi)^2 + 2\nabla\phi'\nabla\phi + (\nabla\theta')^2 + (\nabla\phi')^2 \right].
\end{aligned} \tag{D.3}$$

As the bulk mode ϕ is pinned, we can safely drop out all terms involving $\nabla\phi$. In the

total action (D.2), the bulk θ mode contributes to

$$S[\theta] = \int dx d\tau \frac{v}{2\pi} \left[G(\nabla\theta)^2 + F\nabla\theta'\nabla\theta \right] + \frac{i}{\pi}\partial_\tau\phi\nabla\theta, \tag{D.4}$$

with

$$G = \frac{1}{2}\left(m^2K + \frac{1}{K}\right), \quad F = m^2K - \frac{1}{K}. \tag{D.5}$$

We define a general Fourier transform with periodicity on $[0, L]$ (L-length of the wire),

$$f(r) = \frac{1}{\Omega}\sum_q f_q e^{iqr}, \tag{D.6}$$

where $\Omega = \beta L$, $\beta = 1/T$, $r = (x, v\tau)$, $q = (k, \omega_n/v)$ and $qr = kx - \omega_n\tau$. $\omega_n = 2\pi n/\beta (n \in \mathbb{N})$ denote the Matsubara frequencies for bosons. $S[\theta]$ can then be transformed into the momentum space

$$S[\theta] = \sum_q \left[\frac{ik\omega_n}{\pi}\phi_q\theta_q^*\right] + \frac{v}{2\pi}\sum_q k^2(G\theta_q^*\theta_q + F{\theta'_q}^*\theta_q). \tag{D.7}$$

Integrating out θ, we get the edge Hamiltonian

$$\mathcal{H}^e = \frac{v^e}{2\pi}\int dx \left[K^e(m\nabla\theta')^2 + \frac{1}{K^e}(\nabla\phi')^2\right], \tag{D.8}$$

with the Luttinger parameters

$$\begin{aligned} v^eK^e &= \frac{v}{m^2}\left(G - \frac{F^2}{4G}\right) = \frac{v}{2}\left[(K + \frac{1}{m^2K}) - \frac{(K - \frac{1}{m^2K})^2}{(K + \frac{1}{m^2K})}\right], \\ \frac{v^e}{K^e} &= vG = \frac{v}{2}\left(m^2K + \frac{1}{K}\right). \end{aligned} \tag{D.9}$$

Therefore, when $K = 1$ and $m = \pm 1$,

$$K^e = \frac{2}{m^2+1} = 1, \quad v^e = v. \tag{D.10}$$

In terms of edge chiral fields, $L(x) = \phi^1_{+1}(x) = \theta' + \phi'$, $R(x) = \phi^2_{-1}(x) = \theta' - \phi'$,

$$\mathcal{H}^e = \frac{v}{8\pi}\int dx \left[A_{RR}(\nabla R)^2 + A_{LL}(\nabla L)^2 + A_{RL}(\nabla R)(\nabla L)\right]. \tag{D.11}$$

The backscattering term vanishes: $A_{RL} = 2m^2K^e - 2/K^e = 0$ and $A_{RR} = A_{LL} = m^2K^e + 1/K^e$. In the end,

$$\mathcal{H}^e = \frac{v}{4\pi}\int dx \left[(\nabla R)^2 + (\nabla L)^2\right], \tag{D.12}$$

we reach a quantum Hall phase at $\nu = 1/m = \pm 1$ in the presence of an arbitrary uniform magnetic flux.

Appendix E

Thouless pump

E.1 Thin-torus geometry

One approach to probe the quantum Hall phase is the detection of the bulk polarization through the Thouless pump [243, 265]. We can now gap out the edge mode by mapping the two-wire system to a thin torus, shown in Fig. E.1. We add to the field operators two Aharonov-Bohm phases θ_x, θ_y along the torus with the periodicity $L_x = L$, $L_y = 2$. The torus Hamiltonian reads

$$\begin{aligned}\mathcal{H}(\theta_y) = &-t_\perp \sum_j \left[c_1^\dagger(j)c_2(j)e^{i(a\chi j+\theta_y/2)} + h.c.\right] \\ &-t'_\perp \sum_j \left[c_2^\dagger(j)c_1(j)e^{i(a\chi j+\theta_y/2)} + h.c.\right] \\ -t\sum_j &\left[c_1^\dagger(j)c_1(j+1)e^{-i\theta_x/L} + c_2^\dagger(j)c_2(j+1)e^{-i\theta_x/L} + h.c.\right] \\ &+\Delta\sum_j \left[c_1^\dagger(j)c_1^\dagger(j+1)e^{i\theta_x(2j+1)/L} + h.c.\right]. \end{aligned} \tag{E.1}$$

The condition $\theta_x = \theta_y = 0$ and $t'_\perp = 0$ gives back the original Hamiltonian. In the following analysis, for simplicity we take $t'_\perp = t_\perp$. In the bosonization picture, accordingly, the hopping term between two wires becomes

$$\begin{aligned}\mathcal{H}_\perp(\theta_y) = &-\frac{4t_\perp}{\pi a}\int dx \cos(\chi x + \theta_y/2)\cos(\sqrt{2}\theta^-) \\ &\times \cos[(k_F^1 + k_F^2)x - \sqrt{2}\phi^+]. \end{aligned} \tag{E.2}$$

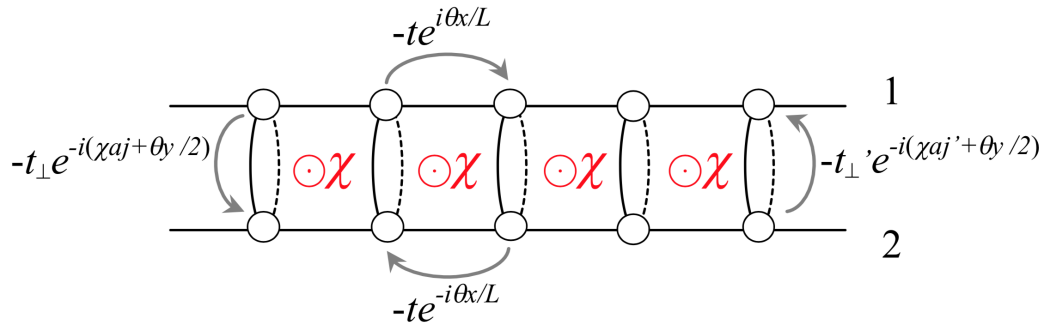

Figure E.1: Thin-torus lattice with $\theta_{x,y}$.

E.2 Bulk polarization

Under the gauge choice (2.32) for the arbitrary flux,

$$\mathcal{H}_\perp(\theta_y) = -\frac{2t_\perp}{\pi a}\int dx \cos(\sqrt{2}\theta^-)\cos(\theta_y/2 + m\sqrt{2}\phi^+), \tag{E.3}$$

with $m = \pm 1$. In this geometry, the two modes θ^- and ϕ^+ are pinned separately. Therefore, from Eq. (2.37), we obtain that the edge mode $\phi' = (\theta^-/m + \phi^+)/\sqrt{2}$ is indeed gapped out in this geometry. The variation of θ_y enters into the original bulk mode $\phi = (-\theta^-/m + \phi^+)/\sqrt{2} = -\theta_y/(4m)$. By changing θ_y periodically, one can probe the bulk polarization. During the process, one mode θ^- remains pinned and the magnetization current in the bulk stays fully suppressed: $\langle j_\parallel(x)\rangle \propto \langle \nabla\theta^-\rangle = 0$. For the other mode ϕ^+, when $\theta_y = 0$, $\phi^+ \sim 0$. A charge gap is formed in the total charge response and the system behaves as a charge density wave (CDW).

On an experimental setup [243], in order to induce a variation in θ_y, one can exert a constant force around the smaller perimeter $\hat{y}$ of the torus (see Fig. E.1) and adiabatically reach twisted boundary conditions: $F \propto \partial_t \theta_y$. When θ_y goes from 0 to 2π, one charge e is transported along the wires,

$$\int_0^L dx \Delta(n_1(x) + n_2(x)) = \frac{1}{m}\frac{\Delta\theta_y}{2\pi} = \frac{1}{m} = \nu = \pm 1. \tag{E.4}$$

It gives rise to a quantized Hall current perpendicular to the force

$$I_{\mathrm{H}} = e\nu\omega, \tag{E.5}$$

where ω denotes the frequency of variation. In Eq. (E.5), one identifies the filling factor with Chern number, which manifests the Zak phase on the thin-torus geometry

$$\begin{aligned}\nu &= -\int_0^{2\pi} d\theta_y \int_{\mathrm{BZ}} \frac{d\theta_x}{2\pi} \Omega_{\theta_x\theta_y} \\ &= \int_0^{2\pi} d\theta_y \partial\theta_y \int_{\mathrm{BZ}} \frac{d\theta_x}{2\pi} \mathcal{A}(\theta_x) \\ &= \int_0^{2\pi} \frac{d\theta_y}{2\pi} \partial\theta_y \varphi_{\mathrm{Zak}}(\theta_y). \end{aligned} \tag{E.6}$$

Here we use the fact that the Berry connection $\mathcal{A}(\theta_y)$ is periodic in θ_x. In the Berry curvature $\Omega_{\theta_x\theta_y} = \partial_{\theta_x}\mathcal{A}(\theta_y) - \partial_{\theta_y}\mathcal{A}(\theta_x)$, the first term thus vanishes.

Meanwhile, the Zak phase can also be interpreted through the electric polarization [375]. From macroscopic electrostatics, one relates the polarization density $P(\vec{r})$ to the charge density $\rho(\vec{r})$ through $\nabla \cdot P(\vec{r}) = -\rho(\vec{r})$. Combined with the continuity equation $\partial_t \rho(\vec{r}) + \nabla \cdot \vec{j}(\vec{r}) = 0$, we obtain

$$\nabla \cdot \left(\partial_t P(\vec{r}) - \vec{j}(\vec{r}) \right) = 0, \quad \Delta P = \int_0^T dt \vec{j}. \tag{E.7}$$

The second equation is valid up to a divergence-free part. It is given by the magnetic current in the bulk, which is identically zero due to the pinned mode θ^-. $\vec{j}$ represents the adiabatic current induced by the variation in external potentials [376] and is related to the total velocity by

$$\begin{aligned} \vec{j} &= e n_0 v(\vec{r}) = e \frac{1}{L} \sum_{\vec{r}} v(\vec{r}) = e \int_{\mathrm{BZ}} \frac{dq}{2\pi} v(q), \\ v(q) &= \frac{\partial \epsilon(q)}{\hbar \partial q} - \Omega_{qt}. \end{aligned} \tag{E.8}$$

For completness, in this formula, we have restored the Planck constant $\hbar$. One immediately sees, after the integration, the normal group velocity $\partial\epsilon(q)/(\hbar\partial q)$ vanishes. The anomalous velocity, on the other hand, comes from the Berry curvature $\Omega_{\mu\nu} = \frac{\partial}{\partial R^\mu}\mathcal{A}_\nu(R) - \frac{\partial}{\partial R^\nu}\mathcal{A}_\mu(R)$ in the parameter space $R = (q, t)$. Explicitly,

$$\Omega_{qt} = i \left[\left\langle \frac{\partial u}{\partial q} \middle| \frac{\partial u}{\partial t} \right\rangle - \left\langle \frac{\partial u}{\partial t} \middle| \frac{\partial u}{\partial q} \right\rangle \right], \tag{E.9}$$

with $|u(q,t)\rangle$ defined in the Bloch form of the instantaneous eigenstates $|\psi_q(x,t)\rangle = e^{iqx}|u(q,t)\rangle$. Now Ω_{qt} gives non-zero contribution to the difference of the polarization

$$\Delta P = -e\int_0^T dt \int_{\mathrm{BZ}} \frac{dq}{2\pi}\Omega_{qt}. \tag{E.10}$$

On the torus, in one period we can perform a change of variables from $dtdq$ to $d\theta_y d\theta_x$. It follows

$$\begin{aligned}\Delta P =& e\int_0^{2\pi} d\theta_y \partial_{\theta_y}\int_{\mathrm{BZ}} \frac{d\theta_x}{2\pi}\mathcal{A}(\theta_x)\\ =& \frac{e}{2\pi}[\varphi_{\mathrm{Zak}}(\theta_y=2\pi)-\varphi_{\mathrm{Zak}}(\theta_y=0)].\end{aligned} \tag{E.11}$$

Along the wires, we conclude $P = l_x e\varphi_{\mathrm{Zak}}/(2\pi)$ where l_x is the number of magnetic unit cells we measure on the $\vec{x}$ direction. Upon the time period T, when θ_y changes from 0 to 2π, the Zak phase in Eq. (E.6) goes continuously from 0 to $2\pi\nu$ and a quantized change in polarization density $P/e = l_x\nu = \pm l_x$ can be observed.

Another way to prove Eq. (E.11) is to re-express the anomalous velocity in Eq. (E.8) in two dimensions $\vec{\theta} = (\theta_x, \theta_y)$:

$$\vec{v}(\theta_x,\theta_y)_{\mathrm{anom.}} = -\frac{\partial\vec{\theta}}{\partial t}\times\left(\partial_{\vec{\theta}}\times\mathcal{A}(\theta_x,\theta_y)\right). \tag{E.12}$$

Applying $\mathbf{a}\times(\mathbf{b}\times\mathbf{c}) = \mathbf{b}(\mathbf{a}\cdot\mathbf{c}) - \mathbf{c}(\mathbf{a}\cdot\mathbf{b})$ and $\theta_y = 2\pi t/T$, the anomalous velocity along the x direction reads

$$v(\theta_x)_{\mathrm{anom.}} = -\frac{2\pi}{T}\left[\partial_{\theta_x}\mathcal{A}(\theta_y) - \partial_{\theta_y}\mathcal{A}(\theta_x)\right]. \tag{E.13}$$

Correspondingly, the difference in polarization

$$\Delta P = -\frac{e}{2\pi}\int_0^T dt\int_{\mathrm{BZ}} d\theta_x v(\theta_x)_{\mathrm{anom.}} \tag{E.14}$$

gives back Eq. (E.11) after a change of the variable from dt to $Td\theta_y/(2\pi)$.

E.3 Comparison with the π-flux and stability under Coulomb interactions

Switching to the π-flux configuration, the strong tunneling Hamiltonian (2.21) pins two modes together, θ^-, ϕ^+. The edge mode $\phi' = (\theta^-/m + \phi^+)/\sqrt{2}$ is now gapped

out from the beginning. The system turns into a charge density wave (CDW). If we perform the same Thouless pump measurement in the torus geometry (E.2)

$$\mathcal{H}_\perp(\theta_y) = -\frac{2t_\perp}{\pi a}\int dx \cos(\sqrt{2}\theta^-)[\cos(\theta_y/2+\sqrt{2}\phi^+)+\cos(\theta_y/2-\sqrt{2}\phi^+)]. \quad \text{(E.15)}$$

As soon as θ_y is varied by an external force, the responses in the ϕ^+ mode differ in signs and cancel with each other. No charge pumping would occur in the charge density wave state formed by the π-flux.

Here, we comment briefly on the effects of Coulomb interactions on the Thouless pump at filling factor $\nu = 1$, including both contributions parallel and perpendicular to the wires. The parameters in the Luttinger Hamiltonian are then modified as $v^\pm K^\pm = vK$, $v^\pm/K^\pm = v/K \pm (aV_\perp)/\pi$. During the charge pumping, however, the velocity of the parallel current remains unaffected:

$$\begin{aligned} \nabla\widetilde{j}_\parallel(x) &= -\partial_t[n_1(x)+n_2(x)], \\ \widetilde{j}_\parallel(x) &= -\frac{v^+K^+\sqrt{2}}{\pi}\nabla\theta^+(x) = -\frac{vK\sqrt{2}}{\pi}\nabla\theta^+(x). \end{aligned} \quad \text{(E.16)}$$

Under Coulomb interactions, we find the bulk is still stable in the Thouless pump measurement, and pumping effects are effectively described through Eq. (E.4).

Appendix F

Lattice summation on Kitaev spin chain

Here, we give a mathematical proof of Eq. (3.34).

For the critical Kitaev spin chain at the gapless point $J_1 = J_2$, we first evaluate the bipartite fluctuation within subregion A:

$$\mathcal{F}_A = \sum_{i,j\in A} I(i,j) = \sum_{i,j\in A} I(|i-j|). \tag{F.1}$$

The bond correlation depends only on the difference of two variables. One can thus convert the double sum into a single sum through

$$\sum_{i,j\in A} I(|i-j|) = I(0)l_A + 2\sum_{k=1}^{l_A}(l_A-k)I(k). \tag{F.2}$$

From the expression (3.29) of $I(k)$: $1/[\pi^2(k^2-1/4)]$ for $k\neq 0$; $1-4/\pi^2$ for $k=0$, we get

$$\begin{aligned}\sum_{k=1}^{l_A} I(k) &= \frac{4}{\pi^2}\sum_{k=1}^{l_A}\frac{1}{4k^2-1} \\ &= \frac{2}{\pi^2}\left(1-\frac{1}{2l_A+1}\right) = \frac{2}{\pi^2}+\mathcal{O}(l_A^{-1}),\end{aligned} \tag{F.3}$$

$$\sum_{k=1}^{l_A} kI(k) = \frac{1}{\pi^2}\sum_{k=1}^{l_A} 2k\left(\frac{1}{2k-1}-\frac{1}{2k+1}\right)$$
$$= \frac{1}{\pi^2}\sum_{k=1}^{2l_A}\left(\frac{k+1}{k}-\frac{k-1}{k}\right)\sigma_k - \frac{l_A}{2l_A+1}$$
$$= \frac{2}{\pi^2}\sum_{k=1}^{2l_A}\frac{\sigma_k}{k} - \frac{l_A}{2l_A+1}, \tag{F.4}$$

with $\sigma_k = 1$ for $k =$ odd and $\sigma_k = 0$ for $k =$ even. It is convenient to re-express the finite sum in terms of the difference of two infinite sums

$$\sum_{k=1}^{2l_A}\frac{\sigma_k}{k} = \sum_{k=1}^{\infty}\frac{\sigma_k}{k} - \frac{\sigma_{k+2l_A}}{k+2l_A}$$
$$= \sum_{k=1}^{\infty}\left(\frac{1}{k}-\frac{1}{2k}\right) - \left(\frac{1}{k+2l_A}-\frac{1}{2k+2l_A}\right). \tag{F.5}$$

In the second equality, we have also used the relation: (odd terms) = (all terms) − (even terms). Now we can apply the properties of the digamma function, which shares the series representation related to the Euler's constant $\gamma \simeq 0.57721$, as well as the asymptotic expansion

$$\psi(x) = -\gamma + \sum_{k=1}^{\infty}\left(\frac{1}{k}-\frac{1}{k+x-1}\right),$$
$$\psi(x\to\infty) = \ln x - \frac{1}{2x} - \frac{1}{12x^2} + \mathcal{O}(x^{-4}). \tag{F.6}$$

Therefore,

$$\sum_{k=1}^{2l_A}\frac{\sigma_k}{k} = \psi(2l_A+1) + \gamma - \frac{1}{2}\left(\psi(l_A+1)+\gamma\right)$$
$$= \frac{1}{2}\ln l_A + \frac{\gamma}{2} + \ln 2 + \mathcal{O}(l_A^{-1}). \tag{F.7}$$

For a bipartition $l_A = l_B = L/2$, we then get the critical scaling of $\mathcal{F}_A$ and at the same time, $\mathcal{F}_{AB}$ from their relation (3.6)

$$\mathcal{F}_A = l_A - \frac{2}{\pi^2}\ln l_A - \frac{2}{\pi^2}\left(\gamma + 2\ln 2 - \frac{1}{2}\right) + \mathcal{O}(l_A^{-1}),$$
$$\mathcal{F}_{AB} = \frac{1}{\pi^2}\ln l_A + \frac{1}{\pi^2}\left(\gamma + \ln 2 - \frac{1}{2}\right) + \mathcal{O}(l_A^{-1}). \tag{F.8}$$

We continue to study the gapped phase of the Kitaev spin chain with negative exchanges such that $|J_1| > |J_2|$, such that the strong bonds occur on the x-links. In Eq. (3.32) and Eq. (3.33), we predict that the bond correlator behaves as $I(i,j) = c_1|i-j|^{-2}$ for $|i-j| \leq \xi$ and $I(i,j) = c_2 e^{-|i-j|/\xi}$ for $|i-j| > \xi$, with a correlation length $\xi \sim |J_2 - J_1|^{-1}$. For $1 < \xi < l_A = l_B = L/2$, the valence bond fluctuations between two subregions become

$$\begin{aligned}\mathcal{F}_{AB} &= \sum_{i=1}^{L/2} \sum_{j=L/2+1}^{L} I(i,j) \\ &= \sum_{k=1}^{\xi} k \frac{c_1}{k^2} + \sum_{k=\xi+1}^{L/2} k c_2 e^{-\frac{k}{\xi}} + \sum_{k=L/2+1}^{L} (L-k)\, c_2 e^{-\frac{k}{\xi}}. \end{aligned} \tag{F.9}$$

Approximating the single summation by an integral and supposing $\xi \ll L$, one obtains

$$\mathcal{F}_{AB} = c_1 \ln \xi + c_2 e^{-1} \left(2\xi^2 - \xi\right) + \mathcal{O}(1). \tag{F.10}$$

Appendix G

Asymptotic form of bond correlator in the B phase

Here, we derive the power-law behavior of bond correlation functions in the intermediate gapless spin liquid phase of the Kitaev honeycomb model. We assume a simple case where three Ising couplings share the same strength: $J_x = J_y = J_z = J$.

When $\kappa = 0$, the valence bond correlator (3.39) can be re-expressed as the product of two sums

$$\begin{aligned} I(i,j) &= -\langle -ic_{i,1}c_{j,2}\rangle\langle -ic_{j,1}c_{i,2}\rangle, \\ \langle -ic_{i,1}c_{j,2}\rangle &= \frac{1}{N}\sum_{\vec{k}} e^{i\vec{k}\cdot(\vec{r}_j-\vec{r}_i)}\frac{f(k)^*}{|f(k)|}, \\ \langle -ic_{j,1}c_{i,2}\rangle &= \frac{1}{N}\sum_{\vec{q}} e^{-i\vec{q}\cdot(\vec{r}_j-\vec{r}_i)}\frac{f(q)^*}{|f(q)|}. \end{aligned} \tag{G.1}$$

The main contribution comes from the two Dirac points $\pm\vec{k}^* = \pm(k_x^*, k_y^*) = \mp(4\pi/3, 0)$ which satisfy $|f(\pm\vec{k}^*)| = 0$. It allows us to approximate the summation by an expansion around each Dirac point within a small radius ξ: $\vec{k} \in \Omega(\pm\vec{k}^*, \xi)$.

For the first sum in Eq. (G.1), around one Dirac point $\vec{k}^* = (-4\pi/3, 0)$ we get

$$\frac{f(\vec{k})^*}{|f(\vec{k})|} = -\cos\theta' + i\sin\theta'. \tag{G.2}$$

Here θ' is the angle between the relative vector around the Dirac cone $\delta\vec{k} = \vec{k} - \vec{k}^*$ and the x axis. It is clear to see that $I(i,j)$ is anisotropic. To simplify the exponential,

we denote the direction of the two unit cells as $\vec{r} = \vec{r}_j - \vec{r}_i = (r\cos\theta^*, r\sin\theta^*)$ with θ^* the angle between vectors $\vec{r}$ and $\vec{k}^*$. Then,

$$e^{i\vec{k}\cdot(\vec{r}_j-\vec{r}_i)} = e^{i\vec{k}^*\cdot\vec{r}}e^{i\delta\vec{k}\cdot\vec{r}} = e^{i\vec{k}^*\cdot\vec{r}}e^{i\delta kr\cos\theta}, \tag{G.3}$$

with θ the relative angle between $\delta\vec{k}$ and $\vec{r}_j - \vec{r}_i$.

Now we can evaluate the summation by taking the continuum limit

$$\begin{aligned}\langle -ic_{i,1}c_{j,2}\rangle_{\vec{k}^*} =& \frac{(-1)}{(2\pi)^2}\cdot\frac{\sqrt{3}}{2}\int_0^{\xi} kdk\int_0^{2\pi} e^{ikr\cos\theta} \\ &\times e^{i(\vec{k}^*\cdot\vec{r}-\theta^*)}(\cos\theta + i\sin\theta)d\theta.\end{aligned} \tag{G.4}$$

The factor 2 comes from the contribution of two Dirac points. The other factor $\sqrt{3}/2$ originates from a change of basis from dk_1dk_2 in the Brillouin zone (with unit vectors $\vec{n}_1$ and $\vec{n}_2$) to dk_xdk_y. We have also used the relation $\theta + \theta' = \theta^*$.

Via a change of variables $k' = kr$, one reaches

$$\begin{aligned}\langle -ic_{i,1}c_{j,2}\rangle_{\vec{k}^*} &= -\frac{\sqrt{3}}{8\pi^2}e^{i(\vec{k}^*\cdot\vec{r}-\theta^*)}\int_0^{\Lambda}\frac{kdk}{r^2}\int_0^{2\pi}\cos\theta e^{ik\cos\theta}d\theta \\ &= -\frac{t(\Lambda)}{2r^2}ie^{i(\vec{k}^*\cdot\vec{r}-\theta^*)},\end{aligned} \tag{G.5}$$

where $t(\Lambda) = \sqrt{3}/(2\pi)\cdot\int_0^{\Lambda} J_1(k)kdk$ with a cutoff $\Lambda = \xi r$ and inside the integral $J_1(k)$ denotes the Bessel function of the first kind.

A similar expansion around the other Dirac point $-\vec{k}^* = (4\pi/3, 0)$ would give an additional phase factor $e^{i(-\vec{k}^*\cdot\vec{r}-(\pi-\theta^*))}$. Thus, the total contribution reads

$$\begin{aligned}\langle -ic_{i,1}c_{j,2}\rangle &= \langle -ic_{i,1}c_{j,2}\rangle_{\vec{k}^*} + \langle -ic_{i,1}c_{j,2}\rangle_{-\vec{k}^*} \\ &= \frac{t(\Lambda)}{r^2}\sin(\vec{k}^*\cdot\vec{r} - \theta^*).\end{aligned} \tag{G.6}$$

For the second sum in Eq. (G.1), we only need to change $\vec{r}$ to $-\vec{r}$ and adjust the relative angle from θ^* to $\theta^* - \pi$:

$$\langle -ic_{j,1}c_{i,2}\rangle = \frac{t(\Lambda)}{r^2}\sin(\vec{k}^*\cdot\vec{r} + \theta^*). \tag{G.7}$$

Combining Eqs. (G.1), (G.6) and (G.7), we then recover the r^{-4} scaling of the bond correlator in the gapless phase [279]:

$$I(i,j) = \frac{\widetilde{c}_1}{r^4}. \tag{G.8}$$

Furthermore, from our calculations the amplitude $\widetilde{c}_1$ retrieves an anisotropic factor $Y(\vec{r})$:

$$\begin{aligned} \widetilde{c}_1 &= t^2(\Lambda) \cdot Y(\vec{r}), \\ Y(\vec{r}) &= \cos^2(\vec{k}^* \cdot \vec{r}) - \cos^2(\theta^*). \end{aligned} \tag{G.9}$$

One can also verify that the forms of $\tilde{c}_1$ and of the anisotropic Y-function in Eq. (G.9) are valid for the whole gapless region.

Appendix H

Bipartite fluctuations on honeycomb geometry

We evaluate here the bipartite fluctuations on the honeycomb lattice, involving the lattice summation.

H.1 General scaling rule

Consider a bipartition on the honeycomb lattice shown in Fig. 3.3a. The parallelogram is expanded by two unit vectors $\vec{n}_1 = (1/2, \sqrt{3}/2)$ and $\vec{n}_2 = (-1/2, \sqrt{3}/2)$ with a total size $\Omega = l_x \times l_y$ and the subsystems are chosen as $A = B = (l_x/2) \times l_y = (L/2) \times L$. For convenience, we adopt new coordinates $\vec{r} = x\vec{n}_1 + y\vec{n}_2 : x = 1, 2, \ldots, l_x, y = 1, 2, \ldots, l_y$. The summation in the bipartite fluctuations can then be re-expressed into

$$\mathcal{F}_\Omega = \sum_{\vec{r},\vec{r}' \in \Omega} I(\vec{r}' - \vec{r}) = \sum_{x,x'=1}^{l_x} \sum_{y,y'=1}^{l_y} I(x' - x, y' - y). \tag{H.1}$$

To derive general scaling arguments in a 'simple' way, we only consider the case where $I(\vec{r})$ is an isotropic function of the distance $|\vec{r}| = \sqrt{x^2 + xy + y^2}$. By analogy to Eq. (F.2), a relation between the double and single sums can be established

$$\begin{aligned} &\sum_{x,x'=1}^{l_x} I(x' - x, y) \\ &= l_x I(0, y) + \sum_{x=1}^{l_x} (l_x - x) \left[I(x, y) + I(-x, y) \right] \end{aligned} \tag{H.2}$$

and the same for $\sum_{y,y'=1}^{l_y} I(x, y'-y)$. Then the bipartite fluctuation function can be grouped into four parts:

$$\mathcal{F}_\Omega = l_x l_y I_1 + l_x I_2 + I_y I_3 + I_4, \tag{H.3}$$

with

$$\begin{aligned}
I_1 &= I(0,0) + 2\sum_{x=1}^{l_x} I(x,0) + 2\sum_{y=1}^{l_y} I(0,y) \\
&\quad + 2\sum_{x=1}^{l_x}\sum_{y=1}^{l_y} \left[I(x,y) + I(-x,y)\right], \\
I_2 &= -2\sum_{y=1}^{l_y} yI(0,y) - 2\sum_{x=1}^{l_x}\sum_{y=1}^{l_y} y\left[I(x,y) + I(-x,y)\right], \\
I_3 &= -2\sum_{x=1}^{l_x} xI(x,0) - 2\sum_{x=1}^{l_x}\sum_{y=1}^{l_y} x\left[I(x,y) + I(-x,y)\right], \\
I_4 &= 2\sum_{x=1}^{l_x}\sum_{y=1}^{l_y} xy\left[I(x,y) + I(-x,y)\right].
\end{aligned} \tag{H.4}$$

The dominant scaling terms in $\mathcal{F}_\Omega$ depend on the particular form of $I(r)$. Suppose a general case where $I(r) \propto r^{-\alpha}$ and l_x, l_y are of the same order as L:

$$\begin{aligned}
I_1 &\sim \mathcal{O}(1) + \mathcal{O}(\frac{1}{L^{\alpha-1}}) + \mathcal{O}(\frac{1}{L^{\alpha-2}}), \\
I_2, I_3 &\sim \mathcal{O}(1) + \mathcal{O}(\frac{1}{L^{\alpha-2}}) + \mathcal{O}(\frac{1}{L^{\alpha-3}}), \\
I_4 &\sim \mathcal{O}(1) + \mathcal{O}(\frac{1}{L^{\alpha-4}}),
\end{aligned} \tag{H.5}$$

where $\mathcal{O}(1/L^0) \sim \mathcal{O}(\ln L)$. The leading-order scaling in $\mathcal{F}_\Omega$ becomes

$$I(r) \propto \frac{1}{r^\alpha}, \quad \mathcal{F}_\Omega \propto \begin{cases} L^4, & \alpha = 0; \\ L^3, & \alpha = 1; \\ L^2, & \alpha \geq 2. \end{cases} \tag{H.6}$$

When $I(r) \propto e^{-r/\xi}$, $\alpha \to \infty$, $\mathcal{F}_\Omega$ still show the volume law: $\mathcal{F}_\Omega \propto L^2 = \mathcal{V}$. Besides, after the subtraction: $\left|\mathcal{F}_{A\cup B} - \mathcal{F}_A - \mathcal{F}_B\right|/2$, while the higher order terms L^4 and L^3

survive in $\mathcal{F}_{AB}$, the square term L^2 always vanishes, which leads to an area law in $\mathcal{F}_{AB} \propto L = \mathcal{A}$.

To evaluate $\mathcal{F}_{AB}$ more precisely, we are going to study next-leading order terms in $\mathcal{F}_{\Omega}$ case by case.

H.2 Kitaev model: the gapless phase

For the gapless phase of the Kitaev honeycomb model, first we consider an isotropic form of the valence bond correlator in Eq. (3.42)

$$I(x,y) = \frac{\tilde{c}_1}{(x^2+xy+y^2)^2}, \tag{H.7}$$

where $\tilde{c}_1$ is a constant for a given $J_z \in [0, 0.50]$ in our convention.

As $\alpha = 4$, from the general scaling rule in Eq. (H.5) we get $I_i (i = 1, 2, 3) \propto \mathcal{O}(1)$ and $I_4 \propto \mathcal{O}(\ln L)$. In particular, due to the convergence of the lattice summations in $I_i (i = 1, 2, 3)$ in Eq. (H.4), we can introduce a cutoff $l_x = l_y = \Lambda = 10^3$ to approximate these pre-factors:

$$\begin{aligned} I_1 &\simeq I(0,0) + 2\sum_{x=1}^{\Lambda} I(x,0) + 2\sum_{y=1}^{\Lambda} I(0,y) \\ &\quad + 2\sum_{x=1}^{\Lambda}\sum_{y=1}^{\Lambda} [I(x,y) + I(-x,y)] \\ &= I(0) + 7.32\widetilde{c}_1, \\ I_2 = I_3 &\simeq -2\sum_{y=1}^{\Lambda} y I(0,y) - 2\sum_{x=1}^{\Lambda}\sum_{y=1}^{\Lambda} y\,[I(x,y) + I(-x,y)] \\ &= -7.68\widetilde{c}_1. \end{aligned} \tag{H.8}$$

Here $I(0)$ denotes the on-site contribution and has the value

$$I(0) = 1 - \langle Q_i \rangle^2. \tag{H.9}$$

$\langle Q_i \rangle = \langle \sigma^z_{i_1} \sigma^z_{i_2} \rangle$ represents the integral over the Brillouin zone:

$$\langle Q_i \rangle = (2\pi)^{-2} \int_{-\pi}^{\pi}\int_{-\pi}^{\pi} dk_1 k_2 \cos\theta(k_1, k_2), \tag{H.10}$$

with $\cos\theta(k_1,k_2) = a/\sqrt{a^2+b^2}$ and $f(k) = a + bi = J_x e^{ik_1} + J_y e^{ik_2} + J_z$. Combined with the general expression of $\mathcal{F}_\Omega$ in Eq. (H.3), we arrive at

$$\begin{aligned} \mathcal{F}_A &= \alpha L^2 + \beta L + \mathcal{O}(\ln L), \\ \mathcal{F}_{AB} &= \alpha_{\mathcal{F}} L + \mathcal{O}(\ln L), \end{aligned} \tag{H.11}$$

where

$$\begin{aligned} \alpha &= I_1/2 = I(0)/2 + 3.66\tilde{c}_1, \\ \beta &= 3I_2/2 = -11.5\tilde{c}_1, \\ \alpha_{\mathcal{F}} &= |I_2|/2 = 3.84\widetilde{c}_1. \end{aligned} \tag{H.12}$$

In the special case $J_x = J_y = J_z = 1/3$, we have

$$\langle Q_i \rangle \simeq 0.525, \quad I(0)/2 \simeq 0.362. \tag{H.13}$$

As indicated by the inset of Fig. 3.3b, the pre-factor of the L^2 term in $\mathcal{F}_A$ takes the value $\alpha = 0.391$ close to $I(0)/2$. We conclude that the major contribution to $\mathcal{F}_A$ comes from the on-site interactions.

H.3 Kitaev model: the gapped phases

In the gapped phases, the bond correlation function decays exponentially and there is less anisotropy observed in Fig. 3.2b. We can safely start with an isotropic form

$$I(x,y) = c_2 e^{-\sqrt{x^2+xy+y^2}/\xi}. \tag{H.14}$$

For $\alpha = \infty$ in Eq. (H.5), all of the amplitudes $I_i (i = 1,2,3,4) \propto \mathcal{O}(1)$. Yet we can still relate them to the powers of the finite correlation length ξ. The following assumption is taken

$$\xi \sim L^{1/p}, \qquad p \geq 5, \tag{H.15}$$

such that when $n < 5$,

$$L/\xi \to \infty, \quad 1/\xi \to 0, \quad \xi^n < L. \tag{H.16}$$

Back to Eq. (H.4), we can then replace the summations on the lattice with integrals

$$\begin{aligned}
&\sum_{x=1}^{l_x} I(x,0) = c_2\xi \int_{1/\xi}^{l_x/\xi} dx e^{-x} = c_2\xi \int_0^{\infty} dx e^{-x} = c_2\xi, \\
&\sum_{y=1}^{l_y} yI(0,y) = c_2\xi^2 \int_0^{\infty} ye^{-y} = c_2\xi^2, \\
&\sum_{x=1}^{l_x}\sum_{y=1}^{l_y} [I(x,y) + I(-x,y)] = 3.63c_2\xi^2 \\
&= c_2\xi^2 \int_0^{\infty}\int_0^{\infty} dxdy \left(e^{-\sqrt{x^2+xy+y^2}} + e^{-\sqrt{x^2-xy+y^2}}\right), \\
&\sum_{x=1}^{l_x}\sum_{y=1}^{l_y} y\,[I(x,y) + I(-x,y)] = 5.33c_2\xi^3 \\
&= c_2\xi^3 \int_0^{\infty}\int_0^{\infty} dxdy \left(e^{-\sqrt{x^2+xy+y^2}} + e^{-\sqrt{x^2-xy+y^2}}\right) y, \\
&\sum_{x=1}^{l_x}\sum_{y=1}^{l_y} xy\,[I(x,y) + I(-x,y)] = 10.4c_2\xi^4 \\
&= c_2\xi^4 \int_0^{\infty}\int_0^{\infty} dxdy \left(e^{-\sqrt{x^2+xy+y^2}} + e^{-\sqrt{x^2-xy+y^2}}\right) xy.
\end{aligned} \tag{H.17}$$

The pre-factors now read

$$\begin{aligned}
I_1 &= I(0) + 7.26c_2\xi^2 + 4c_2\xi, \\
I_2 &= I_3 = -10.7c_2\xi^3 - 2c_2\xi^2, \\
I_4 &= 20.8c_2\xi^4.
\end{aligned} \tag{H.18}$$

Correspondingly, the bipartite fluctuations share the quadratic and linear forms respectively

$$\begin{aligned}
\mathcal{F}_A &= \alpha L^2 + \beta L + \mathcal{O}(1), \\
\mathcal{F}_{AB} &= \alpha_{\mathcal{F}} L + \mathcal{O}(1),
\end{aligned} \tag{H.19}$$

with

$$\alpha = I_1/2 \propto \xi^2,$$
$$\beta = 3I_2/2 \propto \xi^3,$$
$$\alpha_{\mathcal{F}} = |I_2|/2 \propto \xi^3. \tag{H.20}$$

It indicates that in gapped phases, $\alpha_{\mathcal{F}}$ increases at the transition towards the intermediate gapless phase.

Appendix I

Heisenberg antiferromagnet on honeycomb lattice

First, we give a review of the modified spin-wave theory on a two-dimensional Heisenberg antiferromagnet. We then analyze the asymptotic behavior of the two-spin correlation function on the honeycomb lattice. Later, a closed form of the valence bond correlator is derived and the r^{-1} scaling is verified both analytically and numerically.

I.1 Modified spin-wave theory

For an antiferromagnetic Heisenberg model on the honeycomb lattice, we can reach the Néel state by applying a staggered magnetic field [287, 294].

The Hamiltonian reads

$$\hat{H} = \frac{J}{2} \sum_{\vec{r},\vec{\delta}} \hat{S}_{\vec{r}} \cdot \hat{S}_{\vec{r}+\vec{\delta}} - h \sum_{\vec{r}} (-1)^{|\vec{r}|} \hat{S}^z_{\vec{r}}. \tag{I.1}$$

Two sets of sublattices $\{1, 2\}$ are differentiated by $(-1)^{|\vec{r}|} = 1$ for $\vec{r} \in 1$ and $(-1)^{|\vec{r}|} = -1$ for $\vec{r} \in 2$. Vectors $\vec{\delta}$ connect each site to its nearest neighbors, with the total number of nearest neighbor sites denoted by z. The introduction of the staggered field breaks the $O(3)$ spin-rotational symmetry and helps to repair the divergence in Green functions arising from the zero mode (or the Goldstone mode).

In the modified spin-wave theory [294], one can map spin operators to bosonic operators: $\vec{r} \in 1$, $S^+_r = \sqrt{2S - a^\dagger_r a_r}\ a_r$, $S^-_r = a^\dagger_r \sqrt{2S - a^\dagger_r a_r}$, $S^z_r = S - a^\dagger_r a_r$; $\vec{r} \in 2$,

$S_r^+ = b_r^\dagger \sqrt{2S - b_r^\dagger b_r}$, $S_r^- = \sqrt{2S - b_r^\dagger b_r}\, b_r$, $S_r^z = -\left(S - b_r^\dagger b_r\right)$ with $[a_r, a_{r'}^\dagger] = [b_r, b_{r'}^\dagger] = \delta_{r,r'}$. Expansion around large S then gives the Hamiltonian of the order $\mathcal{O}(S^2)$ and $\mathcal{O}(S)$.

Combining Fourier transform and Bogoliubov transformation, it is straightforward to obtain single-particle expectation values

$$\begin{aligned} \langle a_{\vec{r}}^\dagger a_{\vec{r}} \rangle = \langle b_{\vec{r}}^\dagger b_{\vec{r}} \rangle &= -\frac{1}{2}\delta_{\vec{r},\vec{r}'} + f\left(\vec{r} - \vec{r}'\right), \\ \langle a_{\vec{r}}^\dagger b_{\vec{r}'}^\dagger \rangle = \langle a_{\vec{r}} b_{\vec{r}'} \rangle &= g\left(\vec{r} - \vec{r}'\right), \end{aligned} \tag{I.2}$$

with

$$\begin{aligned} f\left(\vec{r}\right) &= \frac{1}{N}\sum_{\vec{k}} \cos(\vec{k}\cdot\vec{r}) \frac{1}{\sqrt{1-(\eta\gamma_k)^2}}, \\ g\left(\vec{r}\right) &= \frac{1}{N}\sum_{\vec{k}} \cos(\vec{k}\cdot\vec{r}) \frac{(-\eta\gamma_k)}{\sqrt{1-(\eta\gamma_k)^2}}, \end{aligned} \tag{I.3}$$

and others all vanish. Here, N denotes the total number of lattice sites. η and γ_k are functions depending on the geometry of the lattice

$$\begin{aligned} \eta &= \left(1 + \frac{h}{zJS}\right)^{-1}, \\ \gamma_k &= \frac{1}{z}\sum_{\vec{\delta}} \cos(\vec{k}\cdot\vec{\delta}). \end{aligned} \tag{I.4}$$

Let us take a closer look at a finite honeycomb lattice. The geometric function reads

$$\gamma_k = \frac{1}{3}\left[\cos\left(k_y/\sqrt{3}\right) + 2\cos\left(k_x/2\right)\cos(\sqrt{3}k_y/6)\right]. \tag{I.5}$$

When $h \to 0$, $\eta \to 1$, there exists one zero mode $\vec{k}_0 = (0,0)$ making $f(\vec{r})$ and $g(\vec{r})$ divergent.

Following Ref. [294], one repairs the divergence by adjusting the strength h of the local staggered magnetic field such that the magnetization becomes zero

$$\langle S_r^z \rangle = (-1)^{|\vec{r}|}\left(S - \langle n_r \rangle\right) = 0 \Longleftrightarrow f(\vec{0}) = S + 1/2. \tag{I.6}$$

It is noted that only the zero mode is regularized by $h \neq 0$ and the sum over the remaining region can be safely approximated by a finite integral at $h = 0$. One arrives at

$$f(\vec{0}) = \frac{1}{N}\frac{1}{\sqrt{1-\eta^2}} + \frac{1}{2}\int \frac{d\vec{k}}{(2\pi)^2}\frac{1}{\sqrt{1-\gamma_k^2}} = m_0 + 0.754. \tag{I.7}$$

Taking $S = 1/2$ in Eq. (I.6), we get

$$m_0 = \frac{1}{N}\frac{1}{\sqrt{1-\eta^2}} = 0.246. \tag{I.8}$$

In the same manner,

$$g(\vec{0}) = \frac{1}{N}\frac{(-\eta)}{\sqrt{1-\eta^2}} + \frac{1}{2}\int \frac{d\vec{k}}{(2\pi)^2}\frac{(-\gamma_k)}{\sqrt{1-\gamma_k^2}} \simeq -0.692. \tag{I.9}$$

I.2 Asymptotic behavior of spin-spin correlation

Now, we can evaluate the behavior of the two-spin correlation function. From Wick's theorem, it differs between sites

$$\begin{aligned}
&\langle S^z_{\vec{r}} S^z_{\vec{r}'}\rangle - \langle S^z_{\vec{r}}\rangle\langle S^z_{\vec{r}'}\rangle \\
&= \begin{cases} 1/4, & \vec{r} = \vec{r}'; \\ f^2(\vec{r}-\vec{r}')/3, & \vec{r} \neq \vec{r}' \text{ and } \vec{r}, \vec{r}' \in \text{ same sublattice}; \\ -g^2(\vec{r}-\vec{r}')/3, & \text{otherwise.} \end{cases}
\end{aligned} \tag{I.10}$$

To restore the spin-rotational symmetry at zero magnetic field, we have introduced an extra factor 1/3 to Eq. (I.10).

At large distances, an expansion of $f(\vec{r})$ around $\vec{k}_0 = (0, 0)$ within radius ξ leads to

$$f(\vec{r}) \simeq m_0 + \frac{1}{2}\cdot\frac{\sqrt{3}}{2}\int_0^{\xi}\frac{kdk}{(2\pi)^2}\int_0^{2\pi} d\theta \frac{e^{ikr\cos\theta}}{k/\sqrt{3}}. \tag{I.11}$$

Once we take $r \to \infty$,

$$f(\vec{r}) = c_0 + \frac{c_1}{r}, \tag{I.12}$$

with $c_0 = m_0 \simeq 0.246$, $c_1 = 3/(8\pi) \simeq 0.119$.

Since the approximation $(-\eta\gamma_k) \simeq -1$ is still valid for $\vec{k} \in \Omega\,(0, \xi)$, one finds over a long distance

$$g(\vec{r}) = -f(\vec{r}). \tag{I.13}$$

The two-spin correlation function then reveal a power-law r^{-1} decay with alternating signs on the same and different sublattices.

I.3 Closed form of the valence bond correlator

Next, we study the response of valence bond correlation functions in the Néel state. We adopt the same definition as the Kitaev honeycomb model

$$I(i,j) = \langle Q_i Q_j \rangle - \langle Q_i \rangle \langle Q_j \rangle, \quad Q_i = S^z_{i_1} S^z_{i_2}. \tag{I.14}$$

The bond index $\langle i_1 i_2 \rangle$ denotes two sites in the i-th unit cell of the sublattice $\{1\}$ and $\{2\}$. In the modified spin-wave theory, $S^z_{i_1} = 1/2 - a^\dagger_i a_i$, $S^z_{i,2} = -(1/2 - b^\dagger_i b_i)$. Reassembling different terms, we reach

$$\begin{aligned} & 16 I(i,j) \\ & = \sum_{k,l=1,2} \langle \hat{n}_k \hat{m}_l \rangle + \left[2 \left(\langle \hat{n}_1 \hat{n}_2 \rangle + \langle \hat{m}_1 \hat{m}_2 \rangle \right) - \langle \hat{n}_1 \hat{n}_2 \rangle \langle \hat{m}_1 \hat{m}_2 \rangle \right] \\ & \quad - \sum_{k=1,2} \left[\langle \hat{n}_k \hat{m}_1 \hat{m}_2 \rangle + \langle \hat{n}_1 \hat{n}_2 \hat{m}_k \rangle \right] + \langle \hat{n}_1 \hat{n}_2 \hat{m}_1 \hat{m}_2 \rangle - 4. \end{aligned} \tag{I.15}$$

To simplify the notation, we have introduced a new set of number operators

$$\begin{aligned} \hat{n}_1 = 2 a^\dagger_i a_i, \quad \hat{n}_2 = 2 b^\dagger_i b_i, \\ \hat{m}_1 = 2 a^\dagger_j a_j, \quad \hat{m}_2 = 2 b^\dagger_j b_j. \end{aligned} \tag{I.16}$$

First, taking into account $\langle a^\dagger_i a_i \rangle = \langle b^\dagger_i b_i \rangle = -1/2 + f(\vec{0}) = 1/2$, the single-particle expectation values become

$$\langle \hat{n}_1 \rangle = \langle \hat{n}_2 \rangle = \langle \hat{m}_1 \rangle = \langle \hat{m}_2 \rangle = 1. \tag{I.17}$$

.

Then, Wick's theorem can be applied to calculate the remaining terms involving (2,3,4)-particle expectation values. Before proceeding, from Eq. (I.3) we identify three useful functions

$$
\begin{aligned}
&i \neq j, \\
&\qquad f = f(|\vec{r}_i - \vec{r}_j|) = \langle a_i^\dagger a_j \rangle = \langle b_i^\dagger b_j \rangle = \langle a_j^\dagger a_i \rangle = \langle b_j^\dagger b_i \rangle; \\
&\qquad g = g(|\vec{r}_i - \vec{r}_j|) = \langle a_i^\dagger b_j^\dagger \rangle = \langle a_i b_j \rangle = \langle a_j^\dagger b_i^\dagger \rangle = \langle a_j b_i \rangle; \\
&i = j, \\
&\qquad g_0 = \langle a_i^\dagger b_i^\dagger \rangle = \langle a_i b_i \rangle = -0.692.
\end{aligned} \tag{I.18}
$$

All the other terms like $\langle a_i^\dagger a_j^\dagger \rangle$ and $\langle a_i^\dagger b_j \rangle$ vanish in the ground state. Two-particle expectation values then read

$$
\begin{aligned}
\langle \hat{n}_1 \hat{m}_1 \rangle &= 1 + 4f^2 = \langle \hat{n}_2 \hat{m}_2 \rangle, \\
\langle \hat{n}_1 \hat{m}_2 \rangle &= 1 + 4g^2 = \langle \hat{n}_2 \hat{m}_1 \rangle, \\
\langle \hat{n}_1 \hat{n}_2 \rangle &= 1 + 4g_0^2 = \langle \hat{m}_1 \hat{m}_2 \rangle.
\end{aligned} \tag{I.19}
$$

The three-particle expectation value takes the form

$$
\langle \hat{n}_1 \hat{m}_1 \hat{m}_2 \rangle = 1 + 4g_0^2 + 4(f^2 + g^2) + 16 g_0 f g. \tag{I.20}
$$

The summation is invariant under the exchange of $(i \leftrightarrow j)$. Combined with the sublattice symmetries, we have

$$
\langle \hat{n}_1 \hat{m}_1 \hat{m}_2 \rangle = \langle \hat{n}_1 \hat{n}_2 \hat{m}_1 \rangle = \langle \hat{n}_1 \hat{n}_2 \hat{m}_2 \rangle = \langle \hat{n}_2 \hat{m}_1 \hat{m}_2 \rangle. \tag{I.21}
$$

For the four-particle expectation value, we verify

$$
\langle \hat{n}_1 \hat{n}_2 \hat{m}_1 \hat{m}_2 \rangle = \left[(1 + 4g_0^2) + 4(f^2 + g^2) \right]^2 + 64 g_0 f g. \tag{I.22}
$$

Therefore, we arrive at a closed form of the bond-bond correlators

$$
I(i,j) = 2g_0^2(f^2 + g^2) + (f^2 + g^2)^2. \tag{I.23}
$$

Considering the asymptotic behaviors of $f(\vec{r})$ and $g(\vec{r})$ functions in Eq. (I.12) and Eq. (I.13), we establish

$$I(i,j) = c_0 + \frac{c_1}{r} + \mathcal{O}(r^{-2}), \tag{I.24}$$

where $c_0 = 4m_0^2(g_0^2 + m_0^2) \simeq 0.131$ and $c_1 = m_0(3g_0^2 + 6m_0^2)/\pi \simeq 0.141$.

In the end, we find for the Néel state supported by strong antiferromagnetic Heisenberg exchanges, that the valence bond correlator gives a signature of the r^{-1} scaling accompanied by a non-vanishing constant from finite-size effects (the regularization of the zero mode). This is clearly distinct from the pure r^{-4} scaling in the gapless Kitaev spin liquid phase.

Bibliography

[1] J. Alicea, Y. Oreg, G. Refael, F. Von Oppen, and M. P. A. Fisher, "Non-Abelian statistics and topological quantum information processing in 1D wire networks", *Nature Physics*, vol. 7, no. 5, pp. 412–417, 2011.

[2] B. I. Halperin, Y. Oreg, A. Stern, G. Refael, J. Alicea, and F. von Oppen, "Adiabatic manipulations of Majorana fermions in a three-dimensional network of quantum wires", *Physical Review B*, vol. 85, no. 14, p. 144 501, 2012.

[3] S. Nadj-Perge, I. K. Drozdov, J. Li, H. Chen, S. Jeon, J. Seo, A. H. MacDonald, B. A. Bernevig, and A. Yazdani, "Observation of Majorana fermions in ferromagnetic atomic chains on a superconductor", *Science*, vol. 346, no. 6209, pp. 602–607, 2014.

[4] S. R. Elliott and M. Franz, "Colloquium: Majorana fermions in nuclear, particle, and solid-state physics", *Reviews of Modern Physics*, vol. 87, no. 1, p. 137, 2015.

[5] S. D. Sarma, M. Freedman, and C. Nayak, "Majorana zero modes and topological quantum computation", *npj Quantum Information*, vol. 1, no. 1, pp. 1–13, 2015.

[6] C. Beenakker and L. Kouwenhoven, "A road to reality with topological superconductors", *Nature Physics*, vol. 12, no. 7, pp. 618–621, 2016.

[7] T. Karzig, C. Knapp, R. M. Lutchyn, P. Bonderson, M. B. Hastings, C. Nayak, J. Alicea, K. Flensberg, S. Plugge, Y. Oreg, *et al.*, "Scalable designs for quasiparticle-poisoning-protected topological quantum computation with Majorana zero modes", *Physical Review B*, vol. 95, no. 23, p. 235 305, 2017.

[8] B. M. Terhal, F. Hassler, and D. P. DiVincenzo, "From Majorana fermions to topological order", *Physical Review Letters*, vol. 108, no. 26, p. 260 504, 2012.

[9] S. Vijay, T. H. Hsieh, and L. Fu, "Majorana fermion surface code for universal quantum computation", *Physical Review X*, vol. 5, no. 4, p. 041 038, 2015.

[10] L. A. Landau, S. Plugge, E. Sela, A. Altland, S. M. Albrecht, and R. Egger, "Towards realistic implementations of a Majorana surface code", *Physical Review Letters*, vol. 116, no. 5, p. 050 501, 2016.

[11] S. Plugge, L. A. Landau, E. Sela, A. Altland, K. Flensberg, and R. Egger, "Roadmap to Majorana surface codes", *Physical Review B*, vol. 94, no. 17, p. 174 514, 2016.

[12] A. Roy, B. M. Terhal, and F. Hassler, "Quantum phase transitions of the Majorana toric code in the presence of finite Cooper-pair tunneling", *Physical Review Letters*, vol. 119, no. 18, p. 180 508, 2017.

[13] G. Moore and N. Read, "Nonabelions in the fractional quantum Hall effect", *Nuclear Physics B*, vol. 360, no. 2-3, pp. 362–396, 1991.

[14] N. Read and D. Green, "Paired states of fermions in two dimensions with breaking of parity and time-reversal symmetries and the fractional quantum Hall effect", *Physical Review B*, vol. 61, no. 15, p. 10 267, 2000.

[15] C. Nayak, S. H. Simon, A. Stern, M. Freedman, and S. D. Sarma, "Non-Abelian anyons and topological quantum computation", *Reviews of Modern Physics*, vol. 80, no. 3, p. 1083, 2008.

[16] L. Savary and L. Balents, "Quantum spin liquids: A review", *Reports on Progress in Physics*, vol. 80, no. 1, p. 016 502, 2016.

[17] C. Broholm, R. J. Cava, S. A. Kivelson, D. G. Nocera, M. R. Norman, and T. Senthil, "Quantum spin liquids", *Science*, vol. 367, no. 6475, 2020.

[18] A. Kitaev, "Anyons in an exactly solved model and beyond", *Annals of Physics*, vol. 321, no. 1, pp. 2–111, 2006.

[19] K. v. Klitzing, G. Dorda, and M. Pepper, "New method for high-accuracy determination of the fine-structure constant based on quantized Hall resistance", *Physical Review Letters*, vol. 45, no. 6, p. 494, 1980.

[20] D. C. Tsui, H. L. Stormer, and A. C. Gossard, "Two-dimensional magnetotransport in the extreme quantum limit", *Physical Review Letters*, vol. 48, no. 22, p. 1559, 1982.

[21] F. D. M. Haldane, "Model for a quantum Hall effect without Landau levels: Condensed-matter realization of the parity anomaly", *Physical Review Letters*, vol. 61, no. 18, p. 2015, 1988.

[22] B. I. Halperin, "Quantized Hall conductance, current-carrying edge states, and the existence of extended states in a two-dimensional disordered potential", *Physical Review B*, vol. 25, no. 4, p. 2185, 1982.

[23] M. Büttiker, "Absence of backscattering in the quantum Hall effect in multiprobe conductors", *Physical Review B*, vol. 38, no. 14, p. 9375, 1988.

[24] R. B. Laughlin, "Anomalous quantum Hall effect: An incompressible quantum fluid with fractionally charged excitations", *Physical Review Letters*, vol. 50, no. 18, p. 1395, 1983.

[25] M. Stone and M. P. Fisher, "Laughlin states at the edge", *International Journal of Modern Physics B*, vol. 8, no. 18, pp. 2539–2553, 1994.

[26] X.-G. Wen, *Quantum field theory of many-body systems: from the origin of sound to an origin of light and electrons*. Oxford University Press, 2004.

[27] T. H. Hansson, M. Hermanns, S. H. Simon, and S. F. Viefers, "Quantum Hall physics: Hierarchies and conformal field theory techniques", *Reviews of Modern Physics*, vol. 89, no. 2, p. 025 005, 2017.

[28] C. L. Kane, R. Mukhopadhyay, and T. C. Lubensky, "Fractional quantum Hall effect in an array of quantum wires", *Physical Review Letters*, vol. 88, no. 3, p. 036 401, 2002.

[29] J. C. Teo and C. Kane, "From Luttinger liquid to non-Abelian quantum Hall states", *Physical Review B*, vol. 89, no. 8, p. 085 101, 2014.

[30] C. L. Kane, A. Stern, and B. I. Halperin, "Pairing in Luttinger liquids and quantum Hall states", *Physical Review X*, vol. 7, no. 3, p. 031 009, 2017.

[31] L. Herviou, C. Mora, and K. Le Hur, "Phase diagram and entanglement of two interacting topological Kitaev chains", *Physical Review B*, vol. 93, no. 16, p. 165 142, 2016.

[32] E. Sagi, A. Haim, E. Berg, F. von Oppen, and Y. Oreg, "Fractional chiral superconductors", *Physical Review B*, vol. 96, no. 23, p. 235 144, 2017.

[33] J. Klinovaja, A. Yacoby, and D. Loss, "Kramers pairs of Majorana fermions and parafermions in fractional topological insulators", *Physical Review B*, vol. 90, no. 15, p. 155 447, 2014.

[34] F. D. M. Haldane, "'Luttinger liquid theory' of one-dimensional quantum fluids. I. Properties of the Luttinger model and their extension to the general 1D interacting spinless Fermi gas", *Journal of Physics C: Solid State Physics*, vol. 14, no. 19, p. 2585, 1981.

[35] H. J. Schulz, G. Cuniberti, and P. Pieri, "Fermi liquids and Luttinger liquids", in *Field theories for low-dimensional condensed matter systems*, Springer, 2000, pp. 9–81.

[36] F. D. M. Haldane, "Continuum dynamics of the 1-D Heisenberg antiferromagnet: Identification with the O(3) nonlinear sigma model", *Physics Letters A*, vol. 93, no. 9, pp. 464–468, 1983.

[37] F. D. M. Haldane, "Nonlinear field theory of large-spin Heisenberg antiferromagnets: Semiclassically quantized solitons of the one-dimensional easy-axis Néel state", *Physical Review Letters*, vol. 50, no. 15, p. 1153, 1983.

[38] P. W. Anderson, "The resonating valence bond state in La_2CuO_4 and superconductivity", *science*, vol. 235, no. 4793, pp. 1196–1198, 1987.

[39] I. Affleck, T. Kennedy, E. H. Lieb, and H. Tasaki, "Rigorous results on valence-bond ground states in antiferromagnets", in *Condensed Matter Physics and Exactly Soluble Models*, Springer, 2004, pp. 249–252.

[40] L. Balents, "Spin liquids in frustrated magnets", *Nature*, vol. 464, no. 7286, pp. 199–208, 2010.

[41] F. Pollmann, E. Berg, A. M. Turner, and M. Oshikawa, "Symmetry protection of topological phases in one-dimensional quantum spin systems", *Physical Review B*, vol. 85, no. 7, p. 075 125, 2012.

[42] J. P. Renard, M. Verdaguer, L. P. Regnault, W. A. C. Erkelens, J. Rossat-Mignod, J. Ribas, W. G. Stirling, and C. Vettier, "Quantum energy gap in two quasi-one-dimensional S=1 Heisenberg antiferromagnets", *Journal of Applied Physics*, vol. 63, no. 8, pp. 3538–3542, 1988.

[43] H. Alloul, T. Ohno, and P. Mendels, "^{89}Y NMR evidence for a fermi-liquid behavior in $YBa_2Cu_3\ O_{6+x}$", *Physical Review Letters*, vol. 63, no. 16, p. 1700, 1989.

[44] D. C. Johnston, "Magnetic susceptibility scaling in $La_{2-x}Sr_xCuO_{4-y}$", *Physical Review Letters*, vol. 62, no. 8, p. 957, 1989.

[45] M. Hagiwara, K. Katsumata, I. Affleck, B. I. Halperin, and J. P. Renard, "Observation of S=1/2 degrees of freedom in an S=1 linear-chain Heisenberg antiferromagnet", *Physical Review Letters*, vol. 65, no. 25, p. 3181, 1990.

[46] R. Coldea, D. A. Tennant, A. M. Tsvelik, and Z. Tylczynski, "Experimental realization of a 2D fractional quantum spin liquid", *Physical Review Letters*, vol. 86, no. 7, p. 1335, 2001.

[47] Y. Shimizu, K. Miyagawa, K. Kanoda, M. Maesato, and G. Saito, "Spin liquid state in an organic Mott insulator with a triangular lattice", *Physical Review Letters*, vol. 91, no. 10, p. 107 001, 2003.

[48] P. Mendels and F. Bert, "Quantum kagome antiferromagnet $ZnCu_3(OH)_6Cl_2$", *Journal of the Physical Society of Japan*, vol. 79, no. 1, p. 011 001, 2010.

[49] P. Mendels and F. Bert, "Quantum kagome frustrated antiferromagnets: One route to quantum spin liquids", *Comptes Rendus Physique*, vol. 17, no. 3-4, pp. 455–470, 2016.

[50] H. Takagi, T. Takayama, G. Jackeli, G. Khaliullin, and S. E. Nagler, "Concept and realization of Kitaev quantum spin liquids", *Nature Reviews Physics*, vol. 1, no. 4, pp. 264–280, 2019.

[51] V. Kalmeyer and R. B. Laughlin, "Equivalence of the resonating-valence-bond and fractional quantum Hall states", *Physical Review Letters*, vol. 59, no. 18, p. 2095, 1987.

[52] S. A. Kivelson, D. S. Rokhsar, and J. P. Sethna, "Topology of the resonating valence-bond state: Solitons and high-T_c superconductivity", *Physical Review B*, vol. 35, no. 16, p. 8865, 1987.

[53] X.-G. Wen, F. Wilczek, and A. Zee, "Chiral spin states and superconductivity", *Physical Review B*, vol. 39, no. 16, p. 11 413, 1989.

[54] N. Read and S. Sachdev, "Large-N expansion for frustrated quantum antiferromagnets", *Physical Review Letters*, vol. 66, no. 13, p. 1773, 1991.

[55] A. Kitaev and C. Laumann, "Topological phases and quantum computation", *arXiv:0904.2771*, 2009.

[56] H. Yao and S. A. Kivelson, "Exact chiral spin liquid with non-Abelian anyons", *Physical Review Letters*, vol. 99, no. 24, p. 247 203, 2007.

[57] T. Meng, T. Neupert, M. Greiter, and R. Thomale, "Coupled-wire construction of chiral spin liquids", *Physical Review B*, vol. 91, no. 24, p. 241 106, 2015.

[58] P. Roushan, C. Neill, A. Megrant, Y. Chen, R. Babbush, R. Barends, B. Campbell, Z. Chen, B. Chiaro, A. Dunsworth, *et al.*, "Chiral ground-state currents of interacting photons in a synthetic magnetic field", *Nature Physics*, vol. 13, no. 2, pp. 146–151, 2017.

[59] J. Koch, A. A. Houck, K. Le Hur, and S. M. Girvin, "Time-reversal-symmetry breaking in circuit-QED-based photon lattices", *Physical Review A*, vol. 82, no. 4, p. 043 811, 2010.

[60] K. Le Hur, L. Henriet, A. Petrescu, K. Plekhanov, G. Roux, and M. Schiró, "Many-body quantum electrodynamics networks: Non-equilibrium condensed matter physics with light", *Comptes Rendus Physique*, vol. 17, no. 8, pp. 808–835, 2016.

[61] S. Nascimbene, Y.-A. Chen, M. Atala, M. Aidelsburger, S. Trotzky, B. Paredes, and I. Bloch, "Experimental realization of plaquette resonating valence-bond states with ultracold atoms in optical superlattices", *Physical Review Letters*, vol. 108, no. 20, p. 205 301, 2012.

[62] P. W. Anderson, "Resonating valence bonds: A new kind of insulator?", *Materials Research Bulletin*, vol. 8, no. 2, pp. 153–160, 1973.

[63] K. Le Hur and T. M. Rice, "Superconductivity close to the Mott state: From condensed-matter systems to superfluidity in optical lattices", *Annals of Physics*, vol. 324, no. 7, pp. 1452–1515, 2009.

[64] Y.-P. Zhong, D. Xu, P. Wang, C. Song, Q. J. Guo, W. X. Liu, K. Xu, B. X. Xia, C.-Y. Lu, S. Han, *et al.*, "Emulating anyonic fractional statistical behavior in a superconducting quantum circuit", *Physical Review Letters*, vol. 117, no. 11, p. 110 501, 2016.

[65] H.-N. Dai, B. Yang, A. Reingruber, H. Sun, X.-F. Xu, Y.-A. Chen, Z.-S. Yuan, and J.-W. Pan, "Observation of four-body ring-exchange interactions and anyonic fractional statistics", *arXiv:1602.05709*, 2016.

[66] H. P. Büchler, M. Hermele, S. D. Huber, M. P. A. Fisher, and P. Zoller, "Atomic quantum simulator for lattice gauge theories and ring exchange models", *Physical Review Letters*, vol. 95, no. 4, p. 040 402, 2005.

[67] M. Sameti, A. Potočnik, D. E. Browne, A. Wallraff, and M. J. Hartmann, "Superconducting quantum simulator for topological order and the toric code", *Physical Review A*, vol. 95, no. 4, p. 042 330, 2017.

[68] A. Petrescu and K. Le Hur, "Chiral Mott insulators, Meissner effect, and Laughlin states in quantum ladders", *Physical Review B*, vol. 91, no. 5, p. 054 520, 2015.

[69] C.-K. Chiu, J. C. Teo, A. P. Schnyder, and S. Ryu, "Classification of topological quantum matter with symmetries", *Reviews of Modern Physics*, vol. 88, no. 3, p. 035 005, 2016.

[70] A. Bernevig and T. Neupert, "Topological superconductors and category theory", *Lecture Notes of the Les Houches Summer School: Topological Aspects of Condensed Matter Physics*, pp. 63–121, 2017.

[71] A. Kitaev, "Periodic table for topological insulators and superconductors", *AIP Conference Proceedings*, vol. 1134, no. 1, pp. 22–30, 2009.

[72] A. Kitaev, "Unpaired Majorana fermions in quantum wires", *Physics-Uspekhi*, vol. 44, no. 10S, p. 131, 2001.

[73] B. A. Bernevig, T. L. Hughes, and S.-C. Zhang, "Quantum spin Hall effect and topological phase transition in HgTe quantum wells", *Science*, vol. 314, no. 5806, pp. 1757–1761, 2006.

[74] D. Hsieh, D. Qian, L. Wray, Y. Xia, Y. S. Hor, R. J. Cava, and M. Z. Hasan, "A topological Dirac insulator in a quantum spin Hall phase", *Nature*, vol. 452, no. 7190, pp. 970–974, 2008.

[75] I. Knez, R.-R. Du, and G. Sullivan, "Evidence for helical edge modes in inverted InAs/GaSb quantum wells", *Physical Review Letters*, vol. 107, no. 13, p. 136 603, 2011.

[76] J. Alicea, "New directions in the pursuit of Majorana fermions in solid state systems", *Reports on Progress in Physics*, vol. 75, no. 7, p. 076 501, 2012.

[77] S Murakawa, Y Tamura, Y Wada, M Wasai, M Saitoh, Y Aoki, R Nomura, Y Okuda, Y Nagato, M Yamamoto, *et al.*, "New anomaly in the transverse acoustic impedance of superfluid ^{3}He-B with a wall coated by several layers of ^{4}He", *Physical Review Letters*, vol. 103, no. 15, p. 155 301, 2009.

[78] Z. Wang, Y. Sun, X.-Q. Chen, C. Franchini, G. Xu, H. Weng, X. Dai, and Z. Fang, "Dirac semimetal and topological phase transitions in A_3Bi (A = Na, K, Rb)", *Physical Review B*, vol. 85, no. 19, p. 195 320, 2012.

[79] X. Wan, A. M. Turner, A. Vishwanath, and S. Y. Savrasov, "Topological semimetal and Fermi-arc surface states in the electronic structure of pyrochlore iridates", *Physical Review B*, vol. 83, no. 20, p. 205 101, 2011.

[80] P. Brydon, A. P. Schnyder, and C. Timm, "Topologically protected flat zero-energy surface bands in noncentrosymmetric superconductors", *Physical Review B*, vol. 84, no. 2, p. 020 501, 2011.

[81] A. P. Schnyder and S. Ryu, "Topological phases and surface flat bands in superconductors without inversion symmetry", *Physical Review B*, vol. 84, no. 6, p. 060 504, 2011.

[82] K. G. Wilson and J. Kogut, "The renormalization group and the ϵ expansion", *Physics Reports*, vol. 12, no. 2, pp. 75–199, 1974.

[83] E. M. Lifshitz and L. P. Pitaevskii, *Statistical physics: theory of the condensed state*. Elsevier, 2013, vol. 9.

[84] Z.-C. Gu and X.-G. Wen, "Tensor-entanglement-filtering renormalization approach and symmetry-protected topological order", *Physical Review B*, vol. 80, no. 15, p. 155 131, 2009.

[85] J. C. Teo and C. L. Kane, "Topological defects and gapless modes in insulators and superconductors", *Physical Review B*, vol. 82, no. 11, p. 115 120, 2010.

[86] F. J. Dyson, "The threefold way. Algebraic structure of symmetry groups and ensembles in quantum mechanics", *Journal of Mathematical Physics*, vol. 3, no. 6, pp. 1199–1215, 1962.

[87] M. R. Zirnbauer, "Riemannian symmetric superspaces and their origin in random-matrix theory", *Journal of Mathematical Physics*, vol. 37, no. 10, pp. 4986–5018, 1996.

[88] A. Altland and M. R. Zirnbauer, "Nonstandard symmetry classes in mesoscopic normal-superconducting hybrid structures", *Physical Review B*, vol. 55, no. 2, p. 1142, 1997.

[89] W.-P. Su, J. Schrieffer, and A. Heeger, "Soliton excitations in polyacetylene", *Physical Review B*, vol. 22, no. 4, p. 2099, 1980.

[90] A. J. Heeger, S Kivelson, J. Schrieffer, and W.-P. Su, "Solitons in conducting polymers", *Reviews of Modern Physics*, vol. 60, no. 3, p. 781, 1988.

[91] M. F. Atiyah, R. Bott, and A. Shapiro, "Clifford modules", *Topology*, vol. 3, pp. 3–38, 1964.

[92] M. Karoubi, *K-theory: An introduction*. Springer Science & Business Media, 2008, vol. 226.

[93] G. Abramovici and P. Kalugin, "Clifford modules and symmetries of topological insulators", *International Journal of Geometric Methods in Modern Physics*, vol. 9, no. 03, p. 1 250 023, 2012.

[94] T. Morimoto and A. Furusaki, "Topological classification with additional symmetries from Clifford algebras", *Physical Review B*, vol. 88, no. 12, p. 125 129, 2013.

[95] M. Freedman, M. B. Hastings, C. Nayak, X.-L. Qi, K. Walker, and Z. Wang, "Projective ribbon permutation statistics: A remnant of non-Abelian braiding in higher dimensions", *Physical Review B*, vol. 83, no. 11, p. 115 132, 2011.

[96] N. Nagaosa, J. Sinova, S. Onoda, A. H. MacDonald, and N. P. Ong, "Anomalous Hall effect", *Reviews of Modern Physics*, vol. 82, no. 2, p. 1539, 2010.

[97] J Zak, "Berry's phase for energy bands in solids", *Physical Review Letters*, vol. 62, no. 23, p. 2747, 1989.

[98] M. Atala, M. Aidelsburger, J. T. Barreiro, D. Abanin, T. Kitagawa, E. Demler, and I. Bloch, "Direct measurement of the Zak phase in topological Bloch bands", *Nature Physics*, vol. 9, no. 12, pp. 795–800, 2013.

[99] E. Majorana, "Nuovo cim. 14, 171 (1937)", *Maiani's English translation can be found in Soryushiron Kenkyu*, vol. 63, pp. 149–162, 1981.

[100] L. N. Cooper, "Bound electron pairs in a degenerate Fermi gas", *Physical Review*, vol. 104, no. 4, p. 1189, 1956.

[101] J. Bardeen, L. N. Cooper, and J. R. Schrieffer, "Microscopic theory of superconductivity", *Physical Review*, vol. 106, no. 1, p. 162, 1957.

[102] J. Bardeen, L. N. Cooper, and J. R. Schrieffer, "Theory of superconductivity", *Physical Review*, vol. 108, no. 5, p. 1175, 1957.

[103] P. A. M. Dirac, "The quantum theory of the electron", *Proceedings of the Royal Society of London. Series A, Containing Papers of a Mathematical and Physical Character*, vol. 117, no. 778, pp. 610–624, 1928.

[104] P. Minkowski, "$\mu \to e\gamma$ at a rate of one out of 10^9 muon decays", *Physics Letters B*, vol. 67, no. 4, pp. 421–428, 1977.

[105] M. Gell-Mann, P. Ramond, and R. Slansky, "Supergravity", *Amsterdam: North-Holland*, vol. 315, pp. 79–18, 1979.

[106] T. Yanagida, "Horizontal symmetry and masses of neutrinos", *Progress of Theoretical Physics*, vol. 64, no. 3, pp. 1103–1105, 1980.

[107] R. N. Mohapatra and G. Senjanović, "Neutrino mass and spontaneous parity nonconservation", *Physical Review Letters*, vol. 44, no. 14, p. 912, 1980.

[108] J. Vergados, H Ejiri, and F Šimkovic, "Theory of neutrinoless double-beta decay", *Reports on Progress in Physics*, vol. 75, no. 10, p. 106 301, 2012.

[109] B. Schwingenheuer, "Status and prospects of searches for neutrinoless double beta decay", *Annalen der Physik*, vol. 525, no. 4, pp. 269–280, 2013.

[110] K. S. Babu and R. N. Mohapatra, "Determining Majorana nature of neutrino from nucleon decays and $n - \overline{n}$ oscillations", *Physical Review D*, vol. 91, p. 013 008, 1 2015.

[111] G. Jungman, M. Kamionkowski, and K. Griest, "Supersymmetric dark matter", *Physics Reports*, vol. 267, no. 5-6, pp. 195–373, 1996.

[112] M. Schumann, "Dark matter 2013", *Brazilian Journal of Physics*, vol. 44, no. 5, pp. 483–493, 2014.

[113] D. S. Akerib, H. Araújo, X Bai, A. Bailey, J Balajthy, S Bedikian, E Bernard, A Bernstein, A Bolozdynya, A Bradley, *et al.*, "First results from the LUX dark matter experiment at the Sanford Underground Research Facility", *Physical Review Letters*, vol. 112, no. 9, p. 091 303, 2014.

[114] P.-G. De Gennes, *Superconductivity of metals and alloys*. CRC Press, 2018.

[115] R. Kennedy and M. R. Zirnbauer, "Bott periodicity for $\mathbb{Z}_2$ symmetric ground states of gapped free-Fermion systems", *Communications in Mathematical Physics*, vol. 342, no. 3, pp. 909–963, 2016.

[116] L. Fidkowski and A. Kitaev, "Topological phases of fermions in one dimension", *Physical Review B*, vol. 83, p. 075 103, 7 2011.

[117] A. M. Turner, F. Pollmann, and E. Berg, "Topological phases of one-dimensional fermions: An entanglement point of view", *Physical Review B*, vol. 83, no. 7, p. 075 102, 2011.

[118] A. M. Essin and V. Gurarie, "Bulk-boundary correspondence of topological insulators from their respective Green's functions", *Physical Review B*, vol. 84, no. 12, p. 125 132, 2011.

[119] G. M. Graf and M. Porta, "Bulk-edge correspondence for two-dimensional topological insulators", *Communications in Mathematical Physics*, vol. 324, no. 3, pp. 851–895, 2013.

[120] M. F. Atiyah and I. M. Singer, "The index of elliptic operators on compact manifolds", *Bulletin of the American Mathematical Society*, vol. 69, no. 3, pp. 422–433, 1963.

[121] R. Jackiw and C. Rebbi, "Solitons with fermion number 1/2", *Physical Review D*, vol. 13, no. 12, p. 3398, 1976.

[122] R Jackiw and P. Rossi, "Zero modes of the vortex-fermion system", *Nuclear Physics B*, vol. 190, no. 4, pp. 681–691, 1981.

[123] E. J. Weinberg, "Index calculations for the fermion-vortex system", *Physical Review D*, vol. 24, no. 10, p. 2669, 1981.

[124] N. Berline, E. Getzler, and M. Vergne, *Heat kernels and Dirac operators*. Springer Science & Business Media, 2003.

[125] M. Stone and R. Roy, "Edge modes, edge currents, and gauge invariance in $p_x + ip_y$ superfluids and superconductors", *Physical Review B*, vol. 69, no. 18, p. 184 511, 2004.

[126] D. A. Huse and V. Elser, "Simple variational wave functions for two-dimensional Heisenberg spin-1/2 antiferromagnets", *Physical Review Letters*, vol. 60, no. 24, p. 2531, 1988.

[127] G. Jackeli and G. Khaliullin, "Mott insulators in the strong spin-orbit coupling limit: From Heisenberg to a quantum compass and Kitaev models", *Physical Review Letters*, vol. 102, no. 1, p. 017 205, 2009.

[128] J. Chaloupka, G. Jackeli, and G. Khaliullin, "Zigzag magnetic order in the iridium oxide Na_2IrO_3", *Physical Review Letters*, vol. 110, no. 9, p. 097 204, 2013.

[129] K. Plumb, J. Clancy, L. Sandilands, V. V. Shankar, Y. Hu, K. Burch, H.-Y. Kee, and Y.-J. Kim, "α-$RuCl_3$: A spin-orbit assisted Mott insulator on a honeycomb lattice", *Physical Review B*, vol. 90, no. 4, p. 041 112, 2014.

[130] G. B. Halász, J. Chalker, and R Moessner, "Doping a topological quantum spin liquid: Slow holes in the Kitaev honeycomb model", *Physical Review B*, vol. 90, no. 3, p. 035 145, 2014.

[131] E. H. Lieb, "Flux phase of the half-filled band", *Physical Review Letters*, vol. 73, pp. 2158–2161, 16 1994.

[132] J. Eisert, M. Cramer, and M. B. Plenio, "Colloquium: Area laws for the entanglement entropy", *Reviews of Modern Physics*, vol. 82, no. 1, p. 277, 2010.

[133] H. Yao and X.-L. Qi, "Entanglement entropy and entanglement spectrum of the Kitaev model", *Physical Review Letters*, vol. 105, no. 8, p. 080 501, 2010.

[134] F. Wilczek, *Fractional statistics and anyon superconductivity*. World scientific, 1990, vol. 5.

[135] J. M. Leinaas and J. Myrheim, "On the theory of identical particles", *Il Nuovo Cimento B (1971-1996)*, vol. 37, no. 1, pp. 1–23, 1977.

[136] F. Wilczek, "Magnetic flux, angular momentum, and statistics", *Physical Review Letters*, vol. 48, no. 17, p. 1144, 1982.

[137] A. Kitaev, "Fault-tolerant quantum computation by anyons", *Annals of Physics*, vol. 303, no. 1, pp. 2–30, 2003.

[138] G. Baskaran, S. Mandal, and R. Shankar, "Exact results for spin dynamics and fractionalization in the Kitaev model", *Physical Review Letters*, vol. 98, no. 24, p. 247 201, 2007.

[139] R. B. Laughlin, "Quantized Hall conductivity in two dimensions", *Physical Review B*, vol. 23, no. 10, p. 5632, 1981.

[140] G. Volovik, "Quantum Hall state and chiral edge state in thin ^{3}He-A film", *JETP Letters*, vol. 55, no. 6, 1992.

[141] Y. Hatsugai, "Chern number and edge states in the integer quantum Hall effect", *Physical Review Letters*, vol. 71, no. 22, p. 3697, 1993.

[142] J. Luttinger, "Theory of thermal transport coefficients", *Physical Review*, vol. 135, no. 6A, A1505, 1964.

[143] C. Kane and M. P. Fisher, "Quantized thermal transport in the fractional quantum Hall effect", *Physical Review B*, vol. 55, no. 23, p. 15 832, 1997.

[144] A. Cappelli, M. Huerta, and G. R. Zemba, "Thermal transport in chiral conformal theories and hierarchical quantum Hall states", *Nuclear Physics B*, vol. 636, no. 3, pp. 568–582, 2002.

[145] F. Yang, K. Plekhanov, and K. Le Hur, "Valence bond fluctuations in the Kitaev spin model", *Physical Review Research*, vol. 2, no. 1, p. 013 005, 2020.

[146] X.-Y. Feng, G.-M. Zhang, and T. Xiang, "Topological characterization of quantum phase transitions in a spin-1/2 model", *Physical Review Letters*, vol. 98, no. 8, p. 087 204, 2007.

[147] K. Le Hur, A. Soret, and F. Yang, "Majorana spin liquids, topology, and superconductivity in ladders", *Physical Review B*, vol. 96, no. 20, p. 205 109, 2017.

[148] I. Affleck and A. W. W. Ludwig, "Universal noninteger "ground-state degeneracy" in critical quantum systems", *Physical Review Letters*, vol. 67, no. 2, p. 161, 1991.

[149] B. Alkurtass, A. Bayat, I. Affleck, S. Bose, H. Johannesson, P. Sodano, E. S. Sørensen, and K. Le Hur, "Entanglement structure of the two-channel Kondo model", *Physical Review B*, vol. 93, no. 8, p. 081 106, 2016.

[150] S. R. Lee, P. A. Sharma, A. L. Lima-Sharma, W. Pan, and T. M. Nenoff, "Topological quantum materials for realizing Majorana quasiparticles", *Chemistry of Materials*, vol. 31, no. 1, pp. 26–51, 2018.

[151] R. Prange and S. Girvin, *The quantum Hall effect*. Springer-Verlag, New York, 1990.

[152] S. D. Sarma and A. Pinczuk, *Perspectives in quantum Hall effects: Novel quantum liquids in low-dimensional semiconductor structures*. Wiley, New York, 1997.

[153] J. Nakamura, S. Liang, G. C. Gardner, and M. J. Manfra, "Direct observation of anyonic braiding statistics", *Nature Physics*, vol. 16, no. 9, pp. 931–936, 2020.

[154] B. Rosenow and A. Stern, "Flux superperiods and periodicity transitions in quantum Hall interferometers", *Physical Review Letters*, vol. 124, no. 10, p. 106 805, 2020.

[155] H. Bartolomei, M. Kumar, R. Bisognin, A. Marguerite, J.-M. Berroir, E. Bocquillon, B. Placais, A. Cavanna, Q Dong, U. Gennser, *et al.*, "Fractional statistics in anyon collisions", *Science*, vol. 368, no. 6487, pp. 173–177, 2020.

[156] M. Greiter, X.-G. Wen, and F. Wilczek, "Paired Hall states", *Nuclear Physics B*, vol. 374, no. 3, pp. 567–614, 1992.

[157] M. Banerjee, M. Heiblum, V. Umansky, D. E. Feldman, Y. Oreg, and A. Stern, "Observation of half-integer thermal Hall conductance", *Nature*, vol. 559, no. 7713, pp. 205–210, 2018.

[158] J. Li, C Tan, S Chen, Y Zeng, T Taniguchi, K Watanabe, J Hone, and C. Dean, "Even-denominator fractional quantum Hall states in bilayer graphene", *Science*, vol. 358, no. 6363, pp. 648–652, 2017.

[159] X.-G. Wen, "Edge transport properties of the fractional quantum Hall states and weak-impurity scattering of a one-dimensional charge-density wave", *Physical Review B*, vol. 44, no. 11, p. 5708, 1991.

[160] C. d. C. Chamon, D. Freed, and X. Wen, "Tunneling and quantum noise in one-dimensional Luttinger liquids", *Physical Review B*, vol. 51, no. 4, p. 2363, 1995.

[161] J. Rech, D. Ferraro, T. Jonckheere, L. Vannucci, M. Sassetti, and T. Martin, "Minimal excitations in the fractional quantum Hall regime", *Physical Review Letters*, vol. 118, no. 7, p. 076 801, 2017.

[162] M. Kapfer, P. Roulleau, M. Santin, I. Farrer, D. A. Ritchie, and D. C. Glattli, "A Josephson relation for fractionally charged anyons", *Science*, vol. 363, no. 6429, pp. 846–849, 2019.

[163] T. Goren and K. Le Hur, "Real-time Ramsey interferometry in fractional quantum Hall states", *Physical Review B*, vol. 99, no. 16, p. 161 109, 2019.

[164] A. Petrescu, H. F. Song, S. Rachel, Z. Ristivojevic, C. Flindt, N. Laflorencie, I. Klich, N. Regnault, and K. Le Hur, "Fluctuations and entanglement spectrum in quantum Hall states", *Journal of Statistical Mechanics: Theory and Experiment*, vol. 2014, no. 10, P10005, 2014.

[165] C. Beenakker, "Search for Majorana fermions in superconductors", *Annual Review of Condensed Matter Physics*, vol. 4, no. 1, pp. 113–136, 2013.

[166] T. D. Stanescu and S. Tewari, "Majorana fermions in semiconductor nanowires: Fundamentals, modeling, and experiment", *Journal of Physics: Condensed Matter*, vol. 25, no. 23, p. 233 201, 2013.

[167] R. M. Lutchyn, J. D. Sau, and S. D. Sarma, "Majorana fermions and a topological phase transition in semiconductor-superconductor heterostructures", *Physical Review Letters*, vol. 105, no. 7, p. 077 001, 2010.

[168] Y. Oreg, G. Refael, and F. Von Oppen, "Helical liquids and Majorana bound states in quantum wires", *Physical Review Letters*, vol. 105, no. 17, p. 177 002, 2010.

[169] V. Mourik, K. Zuo, S. M. Frolov, S. Plissard, E. P. Bakkers, and L. P. Kouwenhoven, "Signatures of Majorana fermions in hybrid superconductor-semiconductor nanowire devices", *Science*, vol. 336, no. 6084, pp. 1003–1007, 2012.

[170] L. Fu and C. L. Kane, "Josephson current and noise at a superconductor/quantum-spin-Hall-insulator/superconductor junction", *Physical Review B*, vol. 79, no. 16, p. 161 408, 2009.

[171] A. Cook and M. Franz, "Majorana fermions in a topological-insulator nanowire proximity-coupled to an s-wave superconductor", *Physical Review B*, vol. 84, no. 20, p. 201 105, 2011.

[172] L. Fu and C. L. Kane, "Superconducting proximity effect and Majorana fermions at the surface of a topological insulator", *Physical Review Letters*, vol. 100, no. 9, p. 096 407, 2008.

[173] C.-K. Chiu, M. J. Gilbert, and T. L. Hughes, "Vortex lines in topological insulator-superconductor heterostructures", *Physical Review B*, vol. 84, no. 14, p. 144 507, 2011.

[174] J.-P. Xu, M.-X. Wang, Z. L. Liu, J.-F. Ge, X. Yang, C. Liu, Z. A. Xu, D. Guan, C. L. Gao, D. Qian, *et al.*, "Experimental detection of a Majorana mode in the core of a magnetic vortex inside a topological insulator-superconductor $Bi_2Te_3/NbSe_2$ heterostructure", *Physical Review Letters*, vol. 114, no. 1, p. 017 001, 2015.

[175] T. D. Stanescu, J. D. Sau, R. M. Lutchyn, and S. D. Sarma, "Proximity effect at the superconductor-topological insulator interface", *Physical Review B*, vol. 81, no. 24, p. 241 310, 2010.

[176] A. C. Potter and P. A. Lee, "Engineering a $p+ip$ superconductor: Comparison of topological insulator and Rashba spin-orbit-coupled materials", *Physical Review B*, vol. 83, no. 18, p. 184 520, 2011.

[177] J. D. Sau, R. M. Lutchyn, S. Tewari, and S. D. Sarma, "Generic new platform for topological quantum computation using semiconductor heterostructures", *Physical Review Letters*, vol. 104, no. 4, p. 040 502, 2010.

[178] J. Alicea, "Majorana fermions in a tunable semiconductor device", *Physical Review B*, vol. 81, no. 12, p. 125 318, 2010.

[179] P. Hosur, P. Ghaemi, R. S. Mong, and A. Vishwanath, "Majorana modes at the ends of superconductor vortices in doped topological insulators", *Physical Review Letters*, vol. 107, no. 9, p. 097 001, 2011.

[180] D. Wang, L. Kong, P. Fan, H. Chen, S. Zhu, W. Liu, L. Cao, Y. Sun, S. Du, J. Schneeloch, *et al.*, "Evidence for Majorana bound states in an iron-based superconductor", *Science*, vol. 362, no. 6412, pp. 333–335, 2018.

[181] J. D. Cain, E. D. Hanson, F. Shi, and V. P. Dravid, "Emerging opportunities in the two-dimensional chalcogenide systems and architecture", *Current Opinion in Solid State and Materials Science*, vol. 20, no. 6, pp. 374–387, 2016.

[182] S. Manzeli, D. Ovchinnikov, D. Pasquier, O. V. Yazyev, and A. Kis, "2D transition metal dichalcogenides", *Nature Reviews Materials*, vol. 2, no. 8, pp. 1–15, 2017.

[183] W.-Y. He, B. T. Zhou, J. J. He, N. F. Yuan, T. Zhang, and K. T. Law, "Magnetic field driven nodal topological superconductivity in monolayer transition metal dichalcogenides", *Communications Physics*, vol. 1, no. 1, pp. 1–7, 2018.

[184] C. L. Wong, J. Liu, K. T. Law, and P. A. Lee, "Majorana flat bands and unidirectional Majorana edge states in gapless topological superconductors", *Physical Review B*, vol. 88, no. 6, p. 060 504, 2013.

[185] D. Shaffer, J. Kang, F. Burnell, and R. M. Fernandes, "Crystalline nodal topological superconductivity and Bogolyubov Fermi surfaces in monolayer $NbSe_2$", *Physical Review B*, vol. 101, no. 22, p. 224 503, 2020.

[186] C. Schrade, M. Thakurathi, C. Reeg, S. Hoffman, J. Klinovaja, and D. Loss, "Low-field topological threshold in Majorana double nanowires", *Physical Review B*, vol. 96, no. 3, p. 035 306, 2017.

[187] F. Yang, V. Perrin, A. Petrescu, I. Garate, and K. Le Hur, "From topological superconductivity to quantum Hall states in coupled wires", *Physical Review B*, vol. 101, no. 8, p. 085 116, 2020.

[188] T. Tummuru, O. Can, and M. Franz, "Chiral p-wave superconductivity in a twisted array of proximitized quantum wires", *arXiv:2012.03986*, 2020.

[189] S Vaitiekėnas, G. Winkler, B van Heck, T Karzig, M.-T. Deng, K Flensberg, L. Glazman, C Nayak, P Krogstrup, R. Lutchyn, *et al.*, "Flux-induced topological superconductivity in full-shell nanowires", *Science*, vol. 367, no. 6485, 2020.

[190] P. Bonderson, V. Gurarie, and C. Nayak, "Plasma analogy and non-Abelian statistics for Ising-type quantum Hall states", *Physical Review B*, vol. 83, no. 7, p. 075 303, 2011.

[191] D. A. Ivanov, "Non-abelian statistics of half-quantum vortices in p-wave superconductors", *Physical Review Letters*, vol. 86, no. 2, p. 268, 2001.

[192] D. Litinski and F. von Oppen, "Quantum computing with Majorana fermion codes", *Physical Review B*, vol. 97, no. 20, p. 205 404, 2018.

[193] J. G. Rau, E. K.-H. Lee, and H.-Y. Kee, "Spin-orbit physics giving rise to novel phases in correlated systems: Iridates and related materials", *Annual Review of Condensed Matter Physics*, vol. 7, no. 1, pp. 195–221, 2016.

[194] S. Trebst, "Kitaev materials", *arXiv:1701.07056*, 2017.

[195] M. Hermanns, I. Kimchi, and J. Knolle, "Physics of the Kitaev model: Fractionalization, dynamic correlations, and material connections", *Annual Review of Condensed Matter Physics*, vol. 9, pp. 17–33, 2018.

[196] K. Kitagawa, T. Takayama, Y. Matsumoto, A. Kato, R. Takano, Y. Kishimoto, S. Bette, R. Dinnebier, G. Jackeli, and H. Takagi, "A spin-orbital-entangled quantum liquid on a honeycomb lattice", *Nature*, vol. 554, no. 7692, pp. 341–345, 2018.

[197] J. Knolle and R. Moessner, "A field guide to spin liquids", *Annual Review of Condensed Matter Physics*, vol. 10, pp. 451–472, 2019.

[198] Y. Motome and J. Nasu, "Hunting Majorana fermions in Kitaev magnets", *Journal of the Physical Society of Japan*, vol. 89, no. 1, p. 012 002, 2020.

[199] H.-S. Kim and H.-Y. Kee, "Crystal structure and magnetism in α-$RuCl_3$: An ab-initio study", *Physical Review B*, vol. 93, no. 15, p. 155 143, 2016.

[200] L. Janssen, E. C. Andrade, and M. Vojta, "Magnetization processes of zigzag states on the honeycomb lattice: Identifying spin models for α-$RuCl_3$ and Na_2IrO_3", *Physical Review B*, vol. 96, no. 6, p. 064 430, 2017.

[201] J. Cookmeyer and J. E. Moore, "Spin-wave analysis of the low-temperature thermal Hall effect in the candidate Kitaev spin liquid α-$RuCl_3$", *Physical Review B*, vol. 98, no. 6, p. 060 412, 2018.

[202] J. Nasu, J. Knolle, D. L. Kovrizhin, Y. Motome, and R. Moessner, "Fermionic response from fractionalization in an insulating two-dimensional magnet", *Nature Physics*, vol. 12, no. 10, pp. 912–915, 2016.

[203] A. Banerjee, J. Yan, J. Knolle, C. A. Bridges, M. B. Stone, M. D. Lumsden, D. G. Mandrus, D. A. Tennant, R. Moessner, and S. E. Nagler, "Neutron scattering in the proximate quantum spin liquid α-$Rucl_3$", *Science*, vol. 356, no. 6342, pp. 1055–1059, 2017.

[204] N. Janša, A. Zorko, M. Gomilšek, M. Pregelj, K. W. Krämer, D. Biner, A. Biffin, C. Rüegg, and M. Klanjšek, "Observation of two types of fractional excitation in the Kitaev honeycomb magnet", *Nature Physics*, vol. 14, no. 8, pp. 786–790, 2018.

[205] J. Nasu, J. Yoshitake, and Y. Motome, "Thermal transport in the Kitaev model", *Physical Review Letters*, vol. 119, no. 12, p. 127 204, 2017.

[206] Y. Kasahara, K. Sugii, T. Ohnishi, M. Shimozawa, M. Yamashita, N. Kurita, H. Tanaka, J. Nasu, Y. Motome, T. Shibauchi, *et al.*, "Unusual thermal Hall effect in a Kitaev spin liquid candidate α-$RuCl_3$", *Physical Review Letters*, vol. 120, no. 21, p. 217 205, 2018.

[207] Y. Kasahara, T. Ohnishi, Y. Mizukami, O. Tanaka, S. Ma, K. Sugii, N. Kurita, H. Tanaka, J. Nasu, Y. Motome, *et al.*, "Majorana quantization and half-integer thermal quantum Hall effect in a Kitaev spin liquid", *Nature*, vol. 559, no. 7713, pp. 227–231, 2018.

[208] Y. Vinkler-Aviv and A. Rosch, "Approximately quantized thermal Hall effect of chiral liquids coupled to phonons", *Physical Review X*, vol. 8, no. 3, p. 031 032, 2018.

[209] M. Ye, G. B. Halász, L. Savary, and L. Balents, "Quantization of the thermal Hall conductivity at small Hall angles", *Physical Review Letters*, vol. 121, no. 14, p. 147 201, 2018.

[210] J. Nasu and Y. Motome, "Thermodynamic and transport properties in disordered Kitaev models", *Physical Review B*, vol. 102, no. 5, p. 054 437, 2020.

[211] M. Gohlke, G. Wachtel, Y. Yamaji, F. Pollmann, and Y. B. Kim, "Quantum spin liquid signatures in Kitaev-like frustrated magnets", *Physical Review B*, vol. 97, no. 7, p. 075 126, 2018.

[212] J. S. Gordon, A. Catuneanu, E. S. Sørensen, and H.-Y. Kee, "Theory of the field-revealed Kitaev spin liquid", *Nature Communications*, vol. 10, no. 1, pp. 1–8, 2019.

[213] K. S. Tikhonov, M. V. Feigel'man, and A. Y. Kitaev, "Power-law spin correlations in a perturbed spin model on a honeycomb lattice", *Physical Review Letters*, vol. 106, no. 6, p. 067 203, 2011.

[214] J. Knolle, D. Kovrizhin, J. Chalker, and R. Moessner, "Dynamics of a two-dimensional quantum spin liquid: Signatures of emergent Majorana fermions and fluxes", *Physical Review Letters*, vol. 112, no. 20, p. 207 203, 2014.

[215] X.-Y. Song, Y.-Z. You, and L. Balents, "Low-energy spin dynamics of the honeycomb spin liquid beyond the Kitaev limit", *Physical Review Letters*, vol. 117, no. 3, p. 037 209, 2016.

[216] M. Gohlke, R. Moessner, and F. Pollmann, "Dynamical and topological properties of the Kitaev model in a [111] magnetic field", *Physical Review B*, vol. 98, no. 1, p. 014 418, 2018.

[217] G. B. Halász, S. Kourtis, J. Knolle, and N. B. Perkins, "Observing spin fractionalization in the Kitaev spin liquid via temperature evolution of indirect resonant inelastic x-ray scattering", *Physical Review B*, vol. 99, no. 18, p. 184 417, 2019.

[218] J. Feldmeier, W. Natori, M. Knap, and J. Knolle, "Local probes for charge-neutral edge states in two-dimensional quantum magnets", *Physical Review B*, vol. 102, no. 13, p. 134 423, 2020.

[219] B. Zhou, J Balgley, P. Lampen-Kelley, J.-Q. Yan, D. G. Mandrus, and E. A. Henriksen, "Evidence for charge transfer and proximate magnetism in graphene–α-$RuCl_3$ heterostructures", *Physical Review B*, vol. 100, no. 16, p. 165 426, 2019.

[220] S. Mashhadi, Y. Kim, J. Kim, D. Weber, T. Taniguchi, K. Watanabe, N. Park, B. Lotsch, J. H. Smet, M. Burghard, *et al.*, "Spin-split band hybridization in graphene proximitized with α-$RuCl_3$ nanosheets", *Nano letters*, vol. 19, no. 7, pp. 4659–4665, 2019.

[221] S. Biswas, Y. Li, S. M. Winter, J. Knolle, and R. Valentí, "Electronic properties of α-$RuCl_3$ in proximity to graphene", *Physical Review Letters*, vol. 123, no. 23, p. 237 201, 2019.

[222] V Leeb, K Polyudov, S Mashhadi, S Biswas, R. Valenti, M Burghard, and J Knolle, "Anomalous quantum oscillations in a heterostructure of graphene on a proximate quantum spin liquid", *arXiv:2010.01649*, 2020.

[223] D. Aasen, R. S. K. Mong, B. M. Hunt, D. Mandrus, and J. Alicea, "Electrical probes of the non-Abelian spin liquid in Kitaev materials", *Physical Review X*, vol. 10, p. 031 014, 3 2020.

[224] K. Klocke, D. Aasen, R. S. Mong, E. A. Demler, and J. Alicea, "Time-domain anyon interferometry in Kitaev honeycomb spin liquids and beyond", *arXiv: 2011.00015*, 2020.

[225] J. Dalibard, F. Gerbier, G. Juzeliūnas, and P. Öhberg, "Colloquium: Artificial gauge potentials for neutral atoms", *Reviews of Modern Physics*, vol. 83, no. 4, p. 1523, 2011.

[226] M. Aidelsburger, S. Nascimbene, and N. Goldman, "Artificial gauge fields in materials and engineered systems", *Comptes Rendus Physique*, vol. 19, no. 6, pp. 394–432, 2018.

[227] L.-M. Duan, E Demler, and M. D. Lukin, "Controlling spin exchange interactions of ultracold atoms in optical lattices", *Physical Review Letters*, vol. 91, no. 9, p. 090 402, 2003.

[228] A. Micheli, G. Brennen, and P. Zoller, "A toolbox for lattice-spin models with polar molecules", *Nature Physics*, vol. 2, no. 5, pp. 341–347, 2006.

[229] C. Zhang, V. W. Scarola, S. Tewari, and S. D. Sarma, "Anyonic braiding in optical lattices", *Proceedings of the National Academy of Sciences*, vol. 104, no. 47, pp. 18 415–18 420, 2007.

[230] F. Yang, L. Henriet, A. Soret, and K. Le Hur, "Engineering quantum spin liquids and many-body Majorana states with a driven superconducting box circuit", *Physical Review B*, vol. 98, no. 3, p. 035 431, 2018.

[231] E. Sagi, H. Ebisu, Y. Tanaka, A. Stern, and Y. Oreg, "Spin liquids from Majorana zero modes in a Cooper-pair box", *Physical Review B*, vol. 99, no. 7, p. 075 107, 2019.

[232] M. Greiner, O. Mandel, T. Esslinger, T. W. Hänsch, and I. Bloch, "Quantum phase transition from a superfluid to a Mott insulator in a gas of ultracold atoms", *Nature*, vol. 415, no. 6867, pp. 39–44, 2002.

[233] A Recati, P. Fedichev, W Zwerger, and P Zoller, "Spin-charge separation in ultracold quantum gases", *Physical Review Letters*, vol. 90, no. 2, p. 020 401, 2003.

[234] B. Paredes and J. I. Cirac, "From Cooper pairs to Luttinger liquids with bosonic atoms in optical lattices", *Physical Review Letters*, vol. 90, no. 15, p. 150 402, 2003.

[235] M. A. Levin and X.-G. Wen, "String-net condensation: A physical mechanism for topological phases", *Physical Review B*, vol. 71, no. 4, p. 045 110, 2005.

[236] M. Levin and X.-G. Wen, "Detecting topological order in a ground state wave function", *Physical Review Letters*, vol. 96, no. 11, p. 110 405, 2006.

[237] N. Bonesteel and D. DiVincenzo, "Quantum circuits for measuring Levin-Wen operators", *Physical Review B*, vol. 86, no. 16, p. 165 113, 2012.

[238] H. Steinberg, G. Barak, A. Yacoby, L. N. Pfeiffer, K. W. West, B. I. Halperin, and K. Le Hur, "Charge fractionalization in quantum wires", *Nature Physics*, vol. 4, no. 2, pp. 116–119, 2008.

[239] M. Aidelsburger, M. Lohse, C. Schweizer, M. Atala, J. T. Barreiro, S. Nascimbène, N. R. Cooper, I. Bloch, and N. Goldman, "Measuring the Chern number of Hofstadter bands with ultracold bosonic atoms", *Nature Physics*, vol. 11, no. 2, pp. 162–166, 2015.

[240] B. K. Stuhl, H.-I. Lu, L. M. Aycock, D Genkina, and I. B. Spielman, "Visualizing edge states with an atomic Bose gas in the quantum Hall regime", *Science*, vol. 349, no. 6255, pp. 1514–1518, 2015.

[241] M. Mancini, G. Pagano, G. Cappellini, L. Livi, M. Rider, J. Catani, C. Sias, P. Zoller, M. Inguscio, M. Dalmonte, *et al.*, "Observation of chiral edge states with neutral fermions in synthetic Hall ribbons", *Science*, vol. 349, no. 6255, pp. 1510–1513, 2015.

[242] F. A. An, E. J. Meier, and B. Gadway, "Direct observation of chiral currents and magnetic reflection in atomic flux lattices", *Science advances*, vol. 3, no. 4, e1602685, 2017.

[243] F. Grusdt and M. Höning, "Realization of fractional Chern insulators in the thin-torus limit with ultracold bosons", *Physical Review A*, vol. 90, no. 5, p. 053 623, 2014.

[244] A. Petrescu, M. Piraud, G. Roux, I. McCulloch, and K. Le Hur, "Precursor of the Laughlin state of hard-core bosons on a two-leg ladder", *Physical Review B*, vol. 96, no. 1, p. 014 524, 2017.

[245] E. Cornfeld and E. Sela, "Chiral currents in one-dimensional fractional quantum Hall states", *Physical Review B*, vol. 92, no. 11, p. 115 446, 2015.

[246] M. C. Strinati, E. Cornfeld, D. Rossini, S. Barbarino, M. Dalmonte, R. Fazio, E. Sela, and L. Mazza, "Laughlin-like states in bosonic and fermionic atomic synthetic ladders", *Physical Review X*, vol. 7, no. 2, p. 021 033, 2017.

[247] S. Greschner, M. Filippone, and T. Giamarchi, "Universal Hall response in interacting quantum systems", *Physical Review Letters*, vol. 122, no. 8, p. 083 402, 2019.

[248] M. C. Strinati, S. Sahoo, K. Shtengel, and E. Sela, "Pretopological fractional excitations in the two-leg flux ladder", *Physical Review B*, vol. 99, no. 24, p. 245 101, 2019.

[249] H. Q. Wang, L. B. Shao, Y. M. Pan, R Shen, L Sheng, and D. Y. Xing, "Flux-driven quantum phase transitions in two-leg Kitaev ladder topological superconductor systems", *Physics Letters A*, vol. 380, no. 46, pp. 3936–3941, 2016.

[250] U. Ledermann and K. Le Hur, "Phases of the two-band model of spinless fermions in one dimension", *Physical Review B*, vol. 61, no. 4, p. 2497, 2000.

[251] K. Le Hur, "Andreev scattering in the asymmetric ladder with preformed bosonic pairs", *Physical Review B*, vol. 64, no. 6, p. 060 502, 2001.

[252] W. Qin, L. Li, and Z. Zhang, "Chiral topological superconductivity arising from the interplay of geometric phase and electron correlation", *Nature Physics*, vol. 15, no. 8, pp. 796–802, 2019.

[253] D. V. Khveshchenko and T. M. Rice, "Spin-gap fixed points in the double-chain problem", *Physical Review B*, vol. 50, no. 1, p. 252, 1994.

[254] H. Katsura, D. Schuricht, and M. Takahashi, "Exact ground states and topological order in interacting Kitaev/Majorana chains", *Physical Review B*, vol. 92, no. 11, p. 115 137, 2015.

[255] Z. Li and Q. Han, "Effect of interaction on the Majorana zero modes in the Kitaev chain at half filling", *Chinese Physics Letters*, vol. 35, no. 4, p. 047 101, 2018.

[256] T. Giamarchi, *Quantum physics in one dimension*. Clarendon Press, 2003, vol. 121.

[257] A. O. Gogolin, A. A. Nersesyan, and A. M. Tsvelik, *Bosonization and strongly correlated systems*. Cambridge University Press, 2004.

[258] A. Petrescu and K. Le Hur, "Bosonic Mott insulator with Meissner currents", *Physical Review Letters*, vol. 111, no. 15, p. 150 601, 2013.

[259] L. Barbiero, C. Schweizer, M. Aidelsburger, E. Demler, N. Goldman, and F. Grusdt, "Coupling ultracold matter to dynamical gauge fields in optical lattices: From flux attachment to $\mathbb{Z}_2$ lattice gauge theories", *Science Advances*, vol. 5, no. 10, eaav7444, 2019.

[260] H. J. Schulz, "Critical behavior of commensurate-incommensurate phase transitions in two dimensions", *Physical Review B*, vol. 22, no. 11, p. 5274, 1980.

[261] S. Nakosai, Y. Tanaka, T. K. Ng, and N. Nagaosa, "Spontaneous modulation of superconducting phase in Kitaev ladder", *Journal of the Physical Society of Japan*, vol. 87, no. 8, p. 083 702, 2018.

[262] L. P. Rokhinson, X. Liu, and J. K. Furdyna, "The fractional a.c. Josephson effect in a semiconductor–superconductor nanowire as a signature of Majorana particles", *Nature Physics*, vol. 8, no. 11, pp. 795–799, 2012.

[263] J. Koch and K. Le Hur, "Discontinuous current-phase relations in small one-dimensional Josephson junction arrays", *Physical Review Letters*, vol. 101, no. 9, p. 097 007, 2008.

[264] L. Fu, "Electron teleportation via Majorana bound states in a mesoscopic superconductor", *Physical Review Letters*, vol. 104, no. 5, p. 056 402, 2010.

[265] D. Thouless, "Quantization of particle transport", *Physical Review B*, vol. 27, no. 10, p. 6083, 1983.

[266] T. Goren and K. Le Hur, "Real-time Ramsey interferometry in fractional quantum Hall states", *Physical Review B*, vol. 99, no. 16, p. 161 109, 2019.

[267] E. Berg, Y. Oreg, E.-A. Kim, and F. Von Oppen, "Fractional charges on an integer quantum Hall edge", *Physical Review Letters*, vol. 102, no. 23, p. 236 402, 2009.

[268] I. Garate and K. Le Hur, "Noninvasive probes of charge fractionalization in quantum spin Hall insulators", *Physical Review B*, vol. 85, no. 19, p. 195 465, 2012.

[269] T. Hyart, B. Van Heck, I. C. Fulga, M. Burrello, A. R. Akhmerov, and C. W. J. Beenakker, "Flux-controlled quantum computation with Majorana fermions", *Physical Review B*, vol. 88, no. 3, p. 035 121, 2013.

[270] D. Asahi and N. Nagaosa, "Topological indices, defects, and Majorana fermions in chiral superconductors", *Physical Review B*, vol. 86, no. 10, p. 100 504, 2012.

[271] I. Seroussi, E. Berg, and Y. Oreg, "Topological superconducting phases of weakly coupled quantum wires", *Physical Review B*, vol. 89, no. 10, p. 104 523, 2014.

[272] C.-E. Bardyn, M. A. Baranov, C. V. Kraus, E. Rico, A İmamoğlu, P. Zoller, and S. Diehl, "Topology by dissipation", *New Journal of Physics*, vol. 15, no. 8, p. 085 001, 2013.

[273] H.-H. Lin, L. Balents, and M. P. A. Fisher, "N-chain Hubbard model in weak coupling", *Physical Review B*, vol. 56, no. 11, p. 6569, 1997.

[274] U. Ledermann, K. Le Hur, and T. Rice, "Successive opening of the Fermi surface in doped N-leg Hubbard ladders", *Physical Review B*, vol. 62, no. 24, p. 16 383, 2000.

[275] E. M. Stoudenmire, J. Alicea, O. A. Starykh, and M. P. A. Fisher, "Interaction effects in topological superconducting wires supporting Majorana fermions", *Physical Review B*, vol. 84, no. 1, p. 014 503, 2011.

[276] A Luther and V. Emery, "Backward scattering in the one-dimensional electron gas", *Physical Review Letters*, vol. 33, no. 10, p. 589, 1974.

[277] T. Neupert, C. Chamon, C. Mudry, and R. Thomale, "Wire deconstructionism of two-dimensional topological phases", *Physical Review B*, vol. 90, no. 20, p. 205 101, 2014.

[278] F. Alet, S. Capponi, N. Laflorencie, and M. Mambrini, "Valence bond entanglement entropy", *Physical Review Letters*, vol. 99, no. 11, p. 117 204, 2007.

[279] S. Yang, S.-J. Gu, C.-P. Sun, and H.-Q. Lin, "Fidelity susceptibility and long-range correlation in the Kitaev honeycomb model", *Physical Review A*, vol. 78, no. 1, p. 012 304, 2008.

[280] C. Hickey and S. Trebst, "Emergence of a field-driven U(1) spin liquid in the Kitaev honeycomb model", *Nature Communications*, vol. 10, no. 1, pp. 1–10, 2019.

[281] H. F. Song, S. Rachel, C. Flindt, I. Klich, N. Laflorencie, and K. Le Hur, "Bipartite fluctuations as a probe of many-body entanglement", *Physical Review B*, vol. 85, no. 3, p. 035 409, 2012.

[282] L. Herviou, C. Mora, and K. Le Hur, "Bipartite charge fluctuations in one-dimensional $\mathbb{Z}_2$ superconductors and insulators", *Physical Review B*, vol. 96, no. 12, p. 121 113, 2017.

[283] J. A. Kjäll, J. H. Bardarson, and F. Pollmann, "Many-body localization in a disordered quantum Ising chain", *Physical Review Letters*, vol. 113, no. 10, p. 107 204, 2014.

[284] M. Ohya and D. Petz, *Quantum entropy and its use*. Springer Science & Business Media, 2004.

[285] T. Nishioka, "Entanglement entropy: Holography and renormalization group", *Reviews of Modern Physics*, vol. 90, no. 3, p. 035 007, 2018.

[286] M. M. Wolf, F. Verstraete, M. B. Hastings, and J. I. Cirac, "Area laws in quantum systems: Mutual information and correlations", *Physical Review Letters*, vol. 100, no. 7, p. 070 502, 2008.

[287] H. F. Song, N. Laflorencie, S. Rachel, and K. Le Hur, "Entanglement entropy of the two-dimensional Heisenberg antiferromagnet", *Physical Review B*, vol. 83, no. 22, p. 224 410, 2011.

[288] S. Rachel, N. Laflorencie, H. F. Song, and K. Le Hur, "Detecting quantum critical points using bipartite fluctuations", *Physical Review Letters*, vol. 108, no. 11, p. 116 401, 2012.

[289] H. Yao and D.-H. Lee, "Fermionic magnons, non-Abelian spinons, and the spin quantum Hall effect from an exactly solvable spin-1/2 Kitaev model with SU(2) symmetry", *Physical Review Letters*, vol. 107, no. 8, p. 087 205, 2011.

[290] H. F. Song, S. Rachel, and K. Le Hur, "General relation between entanglement and fluctuations in one dimension", *Physical Review B*, vol. 82, no. 1, p. 012 405, 2010.

[291] P Calabrese and J Cardy, "J. stat. mech. p06002", 2004.

[292] L. Herviou, K. Le Hur, and C. Mora, "Bipartite fluctuations and topology of Dirac and Weyl systems", *Physical Review B*, vol. 99, no. 7, p. 075 133, 2019.

[293] I. Peschel, "Calculation of reduced density matrices from correlation functions", *Journal of Physics A: Mathematical and General*, vol. 36, no. 14, p. L205, 2003.

[294] M. Takahashi, "Modified spin-wave theory of a square-lattice antiferromagnet", *Physical Review B*, vol. 40, no. 4, p. 2494, 1989.

[295] D. Vion, A Aassime, A. Cottet, P. Joyez, H Pothier, C Urbina, D. Esteve, and M. H. Devoret, "Manipulating the quantum state of an electrical circuit", *Science*, vol. 296, no. 5569, pp. 886–889, 2002.

[296] J. Koch, M. Y. Terri, J. Gambetta, A. A. Houck, D. I. Schuster, J Majer, A. Blais, M. H. Devoret, S. M. Girvin, and R. J. Schoelkopf, "Charge-insensitive qubit design derived from the Cooper pair box", *Physical Review A*, vol. 76, no. 4, p. 042 319, 2007.

[297] W. DeGottardi, D. Sen, and S. Vishveshwara, "Topological phases, Majorana modes and quench dynamics in a spin ladder system", *New Journal of Physics*, vol. 13, no. 6, p. 065 028, 2011.

[298] H.-H. Lai and O. I. Motrunich, "Majorana spin liquids on a two-leg ladder", *Physical Review B*, vol. 84, no. 23, p. 235 148, 2011.

[299] F. L. Pedrocchi, S. Chesi, S. Gangadharaiah, and D. Loss, "Majorana states in inhomogeneous spin ladders", *Physical Review B*, vol. 86, no. 20, p. 205 412, 2012.

[300] A. G. Fowler, M. Mariantoni, J. M. Martinis, and A. N. Cleland, "Surface codes: Towards practical large-scale quantum computation", *Physical Review A*, vol. 86, no. 3, p. 032 324, 2012.

[301] B. Fåk, E. Kermarrec, L. Messio, B. Bernu, C. Lhuillier, F. Bert, P. Mendels, B. Koteswararao, F. Bouquet, J. Ollivier, *et al.*, "Kapellasite: A kagome quantum spin liquid with competing interactions", *Physical Review Letters*, vol. 109, no. 3, p. 037 208, 2012.

[302] A. Scheie, M. Sanders, J. Krizan, Y. Qiu, R. J. Cava, and C. Broholm, "Effective spin-1/2 scalar chiral order on kagome lattices in $Nd_3Sb_3Mg_2O_{14}$", *Physical Review B*, vol. 93, no. 18, p. 180 407, 2016.

[303] A. Banerjee, C. A. Bridges, J.-Q. Yan, A. A. Aczel, L. Li, M. B. Stone, G. E. Granroth, M. D. Lumsden, Y. Yiu, J. Knolle, *et al.*, "Proximate Kitaev quantum spin liquid behaviour in a honeycomb magnet", *Nature Materials*, vol. 15, no. 7, pp. 733–740, 2016.

[304] H. Weimer, M. Müller, I. Lesanovsky, P. Zoller, and H. P. Büchler, "A Rydberg quantum simulator", *Nature Physics*, vol. 6, no. 5, pp. 382–388, 2010.

[305] I. M. Pop, K. Hasselbach, O. Buisson, W. Guichard, B. Pannetier, and I Protopopov, "Measurement of the current-phase relation in Josephson junction rhombi chains", *Physical Review B*, vol. 78, no. 10, p. 104 504, 2008.

[306] B. Douçot and L. B. Ioffe, "Physical implementation of protected qubits", *Reports on Progress in Physics*, vol. 75, no. 7, p. 072 001, 2012.

[307] R. Barends, J. Kelly, A. Megrant, A. Veitia, D. Sank, E. Jeffrey, T. C. White, J. Mutus, A. G. Fowler, B. Campbell, *et al.*, "Superconducting quantum circuits at the surface code threshold for fault tolerance", *Nature*, vol. 508, no. 7497, pp. 500–503, 2014.

[308] S. Sachdev and J. Ye, "Gapless spin-fluid ground state in a random quantum Heisenberg magnet", *Physical Review Letters*, vol. 70, no. 21, p. 3339, 1993.

[309] A. Georges, O. Parcollet, and S. Sachdev, "Quantum fluctuations of a nearly critical Heisenberg spin glass", *Physical Review B*, vol. 63, no. 13, p. 134 406, 2001.

[310] A. Kitaev and S. J. Suh, "The soft mode in the Sachdev-Ye-Kitaev model and its gravity dual", *Journal of High Energy Physics*, vol. 2018, no. 5, p. 183, 2018.

[311] J. Polchinski and V. Rosenhaus, "The spectrum in the Sachdev-Ye-Kitaev model", *Journal of High Energy Physics*, vol. 2016, no. 4, p. 1, 2016.

[312] J. Maldacena and D. Stanford, "Remarks on the Sachdev-Ye-Kitaev model", *Physical Review D*, vol. 94, no. 10, p. 106 002, 2016.

[313] E. Witten, "An SYK-like model without disorder", *Journal of Physics A: Mathematical and Theoretical*, vol. 52, no. 47, p. 474 002, 2019.

[314] D. I. Pikulin and M. Franz, "Black hole on a chip: Proposal for a physical realization of the Sachdev-Ye-Kitaev model in a solid-state system", *Physical Review X*, vol. 7, no. 3, p. 031 006, 2017.

[315] A. Chew, A. Essin, and J. Alicea, "Approximating the Sachdev-Ye-Kitaev model with Majorana wires", *Physical Review B*, vol. 96, no. 12, p. 121 119, 2017.

[316] Z. Luo, Y.-Z. You, J. Li, C.-M. Jian, D. Lu, C. Xu, B. Zeng, and R. Laflamme, "Quantum simulation of the non-fermi-liquid state of Sachdev-Ye-Kitaev model", *npj Quantum Information*, vol. 5, no. 1, pp. 1–6, 2019.

[317] Y. Gu, X.-L. Qi, and D. Stanford, "Local criticality, diffusion and chaos in generalized Sachdev-Ye-Kitaev models", *Journal of High Energy Physics*, vol. 2017, no. 5, p. 125, 2017.

[318] X.-G. Wen, "Quantum orders in an exact soluble model", *Physical Review Letters*, vol. 90, no. 1, p. 016 803, 2003.

[319] N. Wu, "Topological phases of the two-leg Kitaev ladder", *Physics Letters A*, vol. 376, no. 46, pp. 3530–3534, 2012.

[320] A. Dutta, G. Aeppli, B. K. Chakrabarti, U. Divakaran, T. F. Rosenbaum, and D. Sen, *Quantum phase transitions in transverse field spin models: from statistical physics to quantum information*. Cambridge University Press, 2015.

[321] I. Affleck and J. B. Marston, "Large-n limit of the Heisenberg-Hubbard model: Implications for high-T_c superconductors", *Physical Review B*, vol. 37, no. 7, p. 3774, 1988.

[322] J. B. Marston and I. Affleck, "Large-n limit of the Hubbard-Heisenberg model", *Physical Review B*, vol. 39, no. 16, p. 11 538, 1989.

[323] P. W. Anderson, P. Lee, M Randeria, T. Rice, N Trivedi, and F. Zhang, "The physics behind high-temperature superconducting cuprates: The 'plain vanilla' version of RVB", *Journal of Physics: Condensed Matter*, vol. 16, no. 24, R755, 2004.

[324] J. Jeong, Y. Sidis, A. Louat, V. Brouet, and P. Bourges, "Time-reversal symmetry breaking hidden order in $Sr_2(Ir,Rh)O_4$", *Nature Communications*, vol. 8, no. 1, pp. 1–6, 2017.

[325] P. Bourges and Y. Sidis, "Novel magnetic order in the pseudogap state of high-T_c copper oxides superconductors", *Comptes Rendus Physique*, vol. 12, no. 5-6, pp. 461–479, 2011.

[326] J. H. Shirley, "Solution of the Schrödinger equation with a Hamiltonian periodic in time", *Physical Review*, vol. 138, B979–B987, 4B 1965.

[327] H. Sambe, "Steady states and quasienergies of a quantum-mechanical system in an oscillating field", *Physical Review A*, vol. 7, pp. 2203–2213, 6 1973.

[328] F Gesztesy and H Mitter, "A note on quasi-periodic states", *Journal of Physics A: Mathematical and General*, vol. 14, no. 4, p. L79, 1981.

[329] S. Rahav, I. Gilary, and S. Fishman, "Effective Hamiltonians for periodically driven systems", *Physical Review A*, vol. 68, p. 013 820, 1 2003.

[330] C. Neill, P. Roushan, M. Fang, Y. Chen, M. Kolodrubetz, Z. Chen, A. Megrant, R. Barends, B. Campbell, B. Chiaro, *et al.*, "Ergodic dynamics and thermalization in an isolated quantum system", *Nature Physics*, vol. 12, no. 11, pp. 1037–1041, 2016.

[331] V. J. Emery and S. Kivelson, "Mapping of the two-channel Kondo problem to a resonant-level model", *Physical Review B*, vol. 46, no. 17, p. 10 812, 1992.

[332] D. G. Clarke, T. Giamarchi, and B. I. Shraiman, "Curie and non-Curie behavior of impurity spins in quantum antiferromagnets", *Physical Review B*, vol. 48, no. 10, p. 7070, 1993.

[333] A. M. Sengupta and A. Georges, "Emery-Kivelson solution of the two-channel Kondo problem", *Physical Review B*, vol. 49, no. 14, p. 10 020, 1994.

[334] K. Le Hur and B. Coqblin, "Underscreened Kondo effect: A two S=1 impurity model", *Physical Review B*, vol. 56, no. 2, p. 668, 1997.

[335] A. Petrescu, H. E. Türeci, A. V. Ustinov, and I. M. Pop, "Fluxon-based quantum simulation in circuit QED", *Physical Review B*, vol. 98, no. 17, p. 174 505, 2018.

[336] K. Le Hur, L. Henriet, L. Herviou, K. Plekhanov, A. Petrescu, T. Goren, M. Schiro, C. Mora, and P. P. Orth, "Driven dissipative dynamics and topology of quantum impurity systems", *Comptes Rendus Physique*, vol. 19, no. 6, pp. 451–483, 2018.

[337] S. F. Edwards and P. W. Anderson, "Theory of spin glasses", *Journal of Physics F: Metal Physics*, vol. 5, no. 5, p. 965, 1975.

[338] M. Schmitt, D. Sels, S. Kehrein, and A. Polkovnikov, "Semiclassical echo dynamics in the Sachdev-Ye-Kitaev model", *Physical Review B*, vol. 99, no. 13, p. 134 301, 2019.

[339] H. Hu, E. Zhao, and I. I. Satija, "Tuning the topology of p-wave superconductivity in an analytically solvable two-band model", *Physical Review B*, vol. 102, no. 23, p. 235 156, 2020.

[340] U. Dorner, P. Fedichev, D. Jaksch, M. Lewenstein, and P. Zoller, "Entangling strings of neutral atoms in 1D atomic pipeline structures", *Physical Review Letters*, vol. 91, no. 7, p. 073 601, 2003.

[341] L. S. Levitov, T. P. Orlando, J. B. Majer, and J. E. Mooij, "Quantum spin chains and Majorana states in arrays of coupled qubits", *arXiv preprint cond-mat/0108266*, 2001.

[342] H. Ebisu, R. R. Kalloor, A. M. Tsvelik, and Y. Oreg, "Chiral topologically ordered insulating phases in arrays of interacting integer quantum Hall islands", *arXiv:2005.06574*, 2020.

[343] T Senthil and M. P. A. Fisher, "$\mathcal{Z}_2$ gauge theory of electron fractionalization in strongly correlated systems", *Physical Review B*, vol. 62, no. 12, p. 7850, 2000.

[344] L. Balents, L. Bartosch, A. Burkov, S. Sachdev, and K. Sengupta, "Putting competing orders in their place near the Mott transition", *Physical Review B*, vol. 71, no. 14, p. 144 508, 2005.

[345] T Senthil and P. A. Lee, "Cuprates as doped $U(1)$ spin liquids", *Physical Review B*, vol. 71, no. 17, p. 174 515, 2005.

[346] M. J. Lawler, A. Paramekanti, Y. B. Kim, and L. Balents, "Gapless spin liquids on the three-dimensional hyperkagome lattice of na4ir3o8", *Physical Review Letters*, vol. 101, p. 197 202, 19 2008.

[347] Y.-Z. You, I. Kimchi, and A. Vishwanath, "Doping a spin-orbit Mott insulator: Topological superconductivity from the Kitaev-Heisenberg model and possible application to $(Na_2/Li_2)IrO_3$", *Physical Review B*, vol. 86, p. 085 145, 8 2012.

[348] M. Hermanns and S. Trebst, "Quantum spin liquid with a Majorana Fermi surface on the three-dimensional hyperoctagon lattice", *Physical Review B*, vol. 89, no. 23, p. 235 102, 2014.

[349] S. Puri, C. K. Andersen, A. L. Grimsmo, and A. Blais, "Quantum annealing with all-to-all connected nonlinear oscillators", *Nature Communications*, vol. 8, no. 1, pp. 1–9, 2017.

[350] J. Struck, M. Weinberg, C. Ölschläger, P. Windpassinger, J. Simonet, K. Sengstock, R. Höppner, P. Hauke, A. Eckardt, M. Lewenstein, *et al.*, "Engineering Ising-XY spin-models in a triangular lattice using tunable artificial gauge fields", *Nature Physics*, vol. 9, no. 11, pp. 738–743, 2013.

[351] B. Bauer, T Pereg-Barnea, T. Karzig, M.-T. Rieder, G. Refael, E. Berg, and Y. Oreg, "Topologically protected braiding in a single wire using Floquet Majorana modes", *Physical Review B*, vol. 100, no. 4, p. 041 102, 2019.

[352] S. Gangadharaiah, B. Braunecker, P. Simon, and D. Loss, "Majorana edge states in interacting one-dimensional systems", *Physical Review Letters*, vol. 107, no. 3, p. 036 801, 2011.

[353] E. Stoudenmire, J. Alicea, O. A. Starykh, and M. P. Fisher, "Interaction effects in topological superconducting wires supporting Majorana fermions", *Physical Review B*, vol. 84, no. 1, p. 014 503, 2011.

[354] H. Katsura, D. Schuricht, and M. Takahashi, "Exact ground states and topological order in interacting Kitaev/Majorana chains", *Physical Review B*, vol. 92, no. 11, p. 115 137, 2015.

[355] N. M. Gergs, L. Fritz, and D. Schuricht, "Topological order in the Kitaev/Majorana chain in the presence of disorder and interactions", *Physical Review B*, vol. 93, no. 7, p. 075 129, 2016.

[356] A. Haim and Y. Oreg, "Time-reversal-invariant topological superconductivity in one and two dimensions", *Physics Reports*, vol. 825, pp. 1–48, 2019.

[357] F. Zhang, C. Kane, and E. Mele, "Time-reversal-invariant topological superconductivity and Majorana Kramers pairs", *Physical Review Letters*, vol. 111, no. 5, p. 056 402, 2013.

[358] N. Laflorencie and S. Rachel, "Spin-resolved entanglement spectroscopy of critical spin chains and Luttinger liquids", *Journal of Statistical Mechanics: Theory and Experiment*, vol. 2014, no. 11, P11013, 2014.

[359] M. Goldstein and E. Sela, "Symmetry-resolved entanglement in many-body systems", *Physical Review Letters*, vol. 120, no. 20, p. 200 602, 2018.

[360] E. Cornfeld, M. Goldstein, and E. Sela, "Imbalance entanglement: Symmetry decomposition of negativity", *Physical Review A*, vol. 98, no. 3, p. 032 302, 2018.

[361] A. Lukin, M. Rispoli, R. Schittko, M. E. Tai, A. M. Kaufman, S. Choi, V. Khemani, J. Léonard, and M. Greiner, "Probing entanglement in a many-body localized system", *Science*, vol. 364, no. 6437, pp. 256–260, 2019.

[362] D. X. Horváth and P. Calabrese, "Symmetry resolved entanglement in integrable field theories via form factor bootstrap", *Journal of High Energy Physics*, vol. 2020, no. 11, pp. 1–45, 2020.

[363] S. Fraenkel and M. Goldstein, "Symmetry resolved entanglement: Exact results in 1D and beyond", *Journal of Statistical Mechanics: Theory and Experiment*, vol. 2020, no. 3, p. 033 106, 2020.

[364] M. T. Tan and S. Ryu, "Particle number fluctuations, Rényi entropy, and symmetry-resolved entanglement entropy in a two-dimensional Fermi gas from multidimensional bosonization", *Physical Review B*, vol. 101, no. 23, p. 235 169, 2020.

[365] W. Yang, A. Nocera, E. S. Sørensen, H.-Y. Kee, and I. Affleck, "Spin-nematic order in the spin-1/2 Kitaev-Gamma chain", *arXiv:2004.06074*, 2020.

[366] E. S. Sørensen, A. Catuneanu, J. S. Gordon, and H.-Y. Kee, "Heart of entanglement: Chiral, nematic, and incommensurate phases in the Kitaev-Gamma ladder in a field", *Physical Review X*, vol. 11, no. 1, p. 011 013, 2021.

[367] K. Yang, S. C. Morampudi, and E. J. Bergholtz, "Exceptional spin liquids", *arXiv: 2007.04329*, 2020.

[368] J. May-Mann and T. L. Hughes, "Twisted Kitaev bilayers and the moiré Ising model", *Physical Review B*, vol. 101, no. 24, p. 245 126, 2020.

[369] A. Rahmani, X. Zhu, M. Franz, and I. Affleck, "Emergent supersymmetry from strongly interacting Majorana zero modes", *Physical Review Letters*, vol. 115, no. 16, p. 166 401, 2015.

[370] A. Rahmani, X. Zhu, M. Franz, and I. Affleck, "Phase diagram of the interacting Majorana chain model", *Physical Review B*, vol. 92, no. 23, p. 235 123, 2015.

[371] I. Affleck, A. Rahmani, and D. Pikulin, "Majorana-Hubbard model on the square lattice", *Physical Review B*, vol. 96, no. 12, p. 125 121, 2017.

[372] K. Wamer and I. Affleck, "Renormalization group analysis of phase transitions in the two-dimensional Majorana-Hubbard model", *Physical Review B*, vol. 98, no. 24, p. 245 120, 2018.

[373] A. Rahmani, D. Pikulin, and I. Affleck, "Phase diagrams of Majorana-Hubbard ladders", *Physical Review B*, vol. 99, no. 8, p. 085 110, 2019.

[374] A. Rahmani and M. Franz, "Interacting Majorana fermions", *Reports on Progress in Physics*, vol. 82, no. 8, p. 084 501, 2019.

[375] R. D. King-Smith and D. Vanderbilt, "Theory of polarization of crystalline solids", *Physical Review B*, vol. 47, no. 3, p. 1651, 1993.

[376] D. Xiao, M.-C. Chang, and Q. Niu, "Berry phase effects on electronic properties", *Reviews of Modern Physics*, vol. 82, no. 3, p. 1959, 2010.

ECOLE DOCTORALE

Titre : Modèles topologiques de Majorana fermions et nouvelles applications

Mots clés : Supraconductivité topologique, liquides de spin quantique, fermions de Majorana, intrication, ingénierie quantique

Résumé : Dans cette thèse, nous présentons une étude théorique des modèles topologiques révélant des fermions de Majorana qui sont leurs propres anti-particules, avec des sondes de l'intrication quantique et des protocoles expérimentaux d'ingénierie quantique en cQED.
Dans la première partie, par des effets de proximité, nous abordons le supraconducteur topologique dans des systèmes de fil, où les fermions de Majorana émergent comme modes à énergie nulle sur les bords. En faisant varier les forces des couplages inter-fils et l'évolution des flux dus aux champs magnétiques orbitaux, nous montrons une interaction entre la supraconductivité topologique des ondes p et les états Hall quantiques.
Pour les deux autres parties de la thèse, nous nous concentrons sur les liquides de spin de Kitaev qui peuvent être résolus exactement dans une représentation de fermions de Majorana. Nous présentons une solution dans des géométries de type échelle. Nous introduisons les fluctuations des liens de valence pour caractériser les transitions de phase entre les phases abélienne et non abélienne, et trouver une relation générale avec l'entropie d'enchevêtrement. Pour simuler ces états Majorana à plusieurs corps, nous proposons un circuit en caisson supraconducteur puis des généralisations pour des ensembles de boîtes couplées. Là, une variété de modèles peut être implémentée, y compris le code torique, la chaîne d'Ising aléatoire ainsi que le modèle SYK Majorana.

Title : Topological Majorana fermions models and new applications

Keywords : Topological superconductivity, quantum spin liquids, Majorana fermions, entanglement, quantum engineering

Abstract : In this thesis, we present a theoretical study of topological models hosting Majorana fermions which are their own anti-particles, with relevant probes of quantum entanglement and experimental protocols for quantum engineering in cQED.
In the first part, by proximity effects we address the topological superconducting wire systems, where Majorana fermions emerge as zero-energy modes at the edges. By varying strengths of inter-wire couplings and changing fluxes of orbital magnetic fields, we show an interplay between topological p-wave superconductivity and quantum Hall states.
For the remaining two parts of the thesis, we focus on Kitaev spin liquids that can be exactly solved in a Majorana fermion representation. We present a solution for tunable square and brickwall ladder systems. We introduce valence bond fluctuations to characterize phase transitions between Abelian and non-Abelian phases, and find a general relation with the entanglement entropy. To simulate these many-body Majorana states, we propose a driven superconducting box circuit with generalizations to coupled box ensembles. There, a variety of models can be implemented including the toric code, the random Ising chain as well as the SYK Majorana model.

Institut Polytechnique de Paris
91120 Palaiseau, France